

Cranfield University

F. Dauchy

Stress Analysis, Dielectric,
Piezoelectric, and Ferroelectric
Properties of PZT Thick Films.

Fabrication of a 50MHz Tm-pMUT
Annular Array.

School of Applied Science

PhD Thesis

Cranfield University

School of Applied Science

PhD Thesis
2007

Florent Dauchy

***Stress Analysis, Dielectric, Piezoelectric, and
Ferroelectric Properties of PZT Thick Films.***

Fabrication of a 50MHz Tm-pMUT Annular Array.

Supervisor: Dr Robert Dorey

2007

This thesis is submitted in partial fulfilment of the requirements for the degree Doctor of
Philosophy

© Cranfield University, 2007. All rights reserved. No part of this publication may be
reproduced without the written permission of the copyright holder.

To friends and family...

Abstract

PZT films up to 35 μm thick were fabricated, using a composite sol gel route combining a PZT powder and a PZT sol. The maximum temperature for the process was 710°C. A demonstration of single layer and multilayer structures was given to show the flexibility of this technology. With Stoney's Equation, studies of the in-situ film stress development as a function of the film thickness and density was effectuated. It helped to understand that the internal forces increase considerably with the film thickness and density. This study yields to set up experimental conditions in which a crack free surface finish of a 28 μm thick film revealed the adaptability of the spin coating technique to fabricate thick films.

The wet etching technology revealed the possibility of a great adaptability to pattern and shape innovative devices such as bars 10 μm wide of 21 μm PZT thick film. The results open the way to a wide range of new industrial application requiring small features and/or multilayer PZT thick film with embedded electrodes.

The single element and annular array devices have been shown to resonate at approximately 60MHz in air and 50 MHz in water. Three types of the composite thick film – 2C+4S, 2C+5S and 2C+6S – were used to fabricate the Tm-pMUT devices. In each case the most effective poling was obtained by maintaining the poling field of 8.4V/ μm during cooling from the poling temperature (200°C) to 'freeze' poled domains in place. This 'freezing' was required to prevent the tensile stresses within the film from reorienting the domains at high temperatures when the poling field is removed.

Increasing values of thickness mode coupling coefficient (k_t) were observed with increasing levels of sol infiltration (decreasing density). Such behaviour is thought to be due to non linear effects on the piezoelectric coefficient (e_{33}) at high levels of porosity. For very dense thick film material a k_t of 0.47 was observed which is comparable to that observed for the bulk material.

Acknowledgments

I would like to thank the European Community MUSTWIN project (NMP2-CT-2003-505630) for funding this project.

I would also like to thank the whole community of Professors, lecturers, postdoctorals and PhD students of the Microsystems and Nanotechnology Centre for their moral support and scientific conversations.

I would like to thank particularly Professor Roger Whatmore for inviting me to play, to sing and to dance on stage at the Gilbert and Sullivan Company.

Most importantly, I would like to thank Dr. Robert Dorey who was an exceptional supervisor. The conversations exchanged during this work were of an outstanding standard. I will remember his calm during hard moments, and his kindness and friendship during all the other moments.

CONTENTS

Chapter 1: Introduction	1
1.1 Project background	2
1.2 Thesis outline	3
Chapter2: Litterature review	4
2.1 Introduction	5
2.2 Dielectric material behaviour	6
2.2.1 Introduction to dielectrics	6
2.2.2 Capacitance	7
2.2.3 Relative permittivity	7
2.2.4 Fringe effect	8
2.2.5 Breakdown and degradation	10
2.2.6 Resistivity	11
2.2.7 dielectric loss	12
2.2.8 Polarisability	13
2.3 Piezoelectric materials	16
2.3.1 Piezoelectricity	16
2.3.2 Notation simplifications of the formulation	17
2.3.3 Constitutive relations	19
2.4 Ferroelectric material	21
2.4.1 ferroelectricity	21
2.4.2 Spontaneous and remanent polarisation	21
2.4.3 Hysteresis loop	24
2.4.4 Precision on the polarisation of ferroelectric ceramics	26
2.4.5 Shottky-Bradeen barrier (depletion barrier) effect on the coercive field	27
2.5. Stress and strain	31
2.5.1 Introduction	31
2.5.2 Stoney's Equation	31

2.5.3 Improvement of Stoney's equation	33
2.6 Ultrasonic piezoelectric thickness mode transducer: fabrication	35
2.6.1 Introduction to the ceramic fabrication	35
2.6.2 Sol-gel method and sintering process	36
2.6.3 Coating	37
2.6.3.1 Introduction to the sol-gel technique: manufacturing routes	37
2.6.3.2 Screen-printing	38
2.6.3.3 Tape casting	40
2.6.3.4 Spin coating	42
2.6.4 Photolithography	46
2.7 Ultrasonic transducer structure	48
2.7.1 Introduction	48
2.7.2 Capacitive Micro-machined Ultrasonic Transducer (CMUT).	49
2.7.3 Piezoelectricity in ultrasonic transducer	50
2.7.3.1. Thickness mode piezoelectric Micro-machined Ultrasonic Transducer (tm-PMUT)	50
2.7.3.2 Flexural mode piezoelectric Micro-machined Ultrasonic Transducer (PMUT).	51
2.7.4. Choice the tm-pMUT structure for high frequency application	52
2.8 Thickness mode piezoelectric transducer theory	53
2.8.1 Introduction	53
2.8.2 Acoustic waves - Basic equations	53
2.8.3 Piezoelectric transducer	57
2.8.4 Transducers as a three port-network	58
2.8.4.1 introduction	58
2.8.4.2 Mason model	58
2.9 Summary	63
Chapter 3: Experimental procedure	64
3.1 Introduction	65
3.2 PZT sol and PZT composite	67
3.2.1 PZT Sol	67
3.2.2. Composite slurry	70
3.3 Sol and composite rheology	70
3.3.1 Sol rheology	70

3.3.2 Composite slurry rheology	71
3.4 Film and electrode deposition	71
3.4.1 Silicon wafer cleaning	71
3.4.2 ZrO ₂ diffusion barrier deposition	72
3.4.3 Electrode deposition	72
3.4.4 Thick film deposition	73
3.5 Device micro-fabrication	75
3.5.1 Introduction	75
3.5.2 PZT wet etching	75
3.5.3 SiO ₂ dry etching	75
3.5.4 Silicon dry etching	76
3.6 Microstructural evaluation	77
3.6.1 Introduction	77
3.6.2 Scanning Electron Micrograph	77
3.6.3 Scanning Field Emission Gun microscope (SFEG)	77
3.6.4 X-Ray Diffraction	78
3.6.5 Images analysis	78
3.6.6 The Dektak® Surface Profiler.	78
3.7 Poling	78
3.7.1 Contact poling	78
3.7.2 Corona poling	78
3.8 Measurements of device properties	79
3.8.1 Dielectric properties	79
3.8.2 Piezoelectric Measurement	79
3.8.3 Resonance frequency measurement	80
3.8.3.1 introduction to S-parameter	80
3.8.3.2 S ₂₁ Parameter	82
3.8.3.3 S ₁₁ measurement	83
Chapter 4: Material design and thick film development	85
4.1 Introduction	86
4.2 PZT material	86
4.2.1 PZT Powder	86
4.2.2 Sol and slurry viscosities	87
4.3 PZT Composite-Infiltration	88
4.4 PZT thick film fabrication, 35 μm the state of the art via the spin coating technique	94
4.5 Evaluation of different substrate	96
4.6 Improvement of the ceramic surface finish	99
4.7 Microstructure of sintered films	103

4.8 PZT wet etching	107
4.8.1 PbClF Residue	107
4.8.2 Etching of PZT thick film ([C+4S])	109
4.8.2.1 Using with the photoresist S1818	109
4.8.2.2 AZ4562 photoresist etch mask	110
4.8.2.3 Etching process of [2C+4S] PZT thick film	111
4.9 Summary on the device fabrication	112
Chapter 5: PZT thick film stress development	114
5.1 Introduction	115
5.2. Stress calculation from the curvature of the wafer	115
5.3. Stress due to the platinum layer and validation of Stoney's equation	116
5.4. Stress measurement of a PZT thick film on a Pt coated silicon substrate	120
5.5 Effect of drying and pyrolysing of PZT thick film on in-situ stress	126
5.6. Stress added via the PZT sol infiltration steps	127
5.7 Effect of PZT film thickness on in situ stress	130
5.8 PZT thickness effect on the In-situ stress on alumina different substrates	132
5.9 Summary	134
Chapter 6: Dielectric, piezoelectric and ferroelectric properties of PZT thick films	135
6.1 Introduction	136
6.2 Experimental set up	136
6.3 Effect of the sintering temperature	138
6.5 Cylinder device: relative permittivity of free standing elements	143
6.5.1 Cylinder device design	143
6.5.2 Capacitance and relative permittivity	144
6.5.2.1 Effect of electrode size on capacitance	144
6.5.2.2 Stray capacitance	146
6.5.2.3 Thickness variation due to the spin coating technique for thick film	149
6.5.2.4 Thickness correction of the relative permittivity	150
6.6 Capacitance on an alumina substrate and fringing fields	153
6.7 Dielectric loss	154
6.8 PZT composite piezoelectric coefficient results for the test structure	156
6.9 Piezoelectric coefficient versus poling temperature / Poling	158
6.10 Ferroelectric properties	159
6.10.1 Presentation of the PZT composite thick film hysteresis loop	159
6.10.2 Hysteresis loop of the 8 μm thick film of 4[C+4S]	160
6.10.3 Effect of stress on the hysteresis loop	162

6.11 Summary	165
Chapter 7: TmpMUT: Thickness mode piezoelectric micromachined ultrasonic transducer	166
7.1 Introduction to high frequency transducer	167
7.2. Thickness mode of excitation	168
7.3 S_{21} parameters results	169
7.4 S_{11} parameter results	171
7.5 Modelling the resonant frequency	173
7.5.1 Impedance	173
7.5.2 Influence of the load (SiO_2 , Pt, ZrO_2)	175
a) Influence of the backing on the resonant frequency predicted by Equation 7.1	175
b) Influence of the backing on the resonant frequency predicted by the Mason model	175
7.5.3 Influence of the porosity on Equation 7.1 and on the Mason model	176
a) Influence of the porosity on the resonant frequency predicted by Equation 7.1	176
b) Influence of the porosity on the resonant frequency predicted by the Mason model	177
7.5.4 Discussion and precision of this observed difference between a porous PZ26 and the composite [C+4S] films.	180
7.5.5 Effect of the relative permittivity on the Mason model	181
7.5.6 Dielectric Loss in the Mason model	182
7.6 The thickness mode of excitation	184
7.6.1 Thickness effect on the thickness mode of excitation	184
7.6.2 Electrode area /PZT thickness ratio effect on the resonant frequency intensity	186
7.6.2.1 First approach of the variation of the ratio electrode radius/ thickness	186
7.6 Effect of infiltration steps on the electromechanical behaviour of the transducer	189
7.7 Summary	193
Chapter 8: Prototype presentation: Annular array	195
8.1 Introduction	196
8.2 Annular array prototypes	196
8.3 Dielectric properties of the annular array	199
8.4 Acoustic behaviour of the tmpMUT annular array	200
8.5 Summary	202

Chapter 9: Conclusion And Future work	203
9.1 Introduction	204
9.2 Next generation of high frequency transducers	204
9.2.1 PZT [2C+6S] thick films on alumina substrates	204
9.2.2 Multilayer piezoelectric structure	205
9.2.2.1 Advantage of a multilayer	205
9.2.2.2 Electrical characterization	206
9.2.2.2 Bi-layer transducer: Single layer resonance	207
9.2.2.3 Bi-layer transducer poled in parallel	208
9.2.2.3 Bi-layer transducer poled in anti-parallel	209
9.3 General conclusion	210
9.3.1 A new fabrication technique	210
9.3.2 stress development	211
9.3.3 Dielectric, piezoelectric, and ferroelectric properties of thick film	211
9.3.4 Characterise and model the acoustic properties of a single element	211
9.3.5 High frequency annular array working at 50MHz	212
9.3.6 Next generation of transducer	212
References	213
Appendix	220

FIGURES TABLE

Figure 2.1: classification of dielectric materials	6
Figure 2.2: Schematic of fringing fields for various capacitor structures.	8
Figure 2.3: Schematic representation of the guard-ring electrodes or guarding electrodes, which blocked the effect of the fringing fields, by confining the active electric field inside the capacitor.	9
Figure 2.4: Graphic representation of the polarisability as a function of the driving frequency	15
Figure 2.5. Schematic representation of interfaces discontinuity generating charges in a dielectric.	16
Figure 2.6: schematic representations of the subscripts definition for the stress matrices.	17
Figure 2.7 Simplification of d_{ijk} parameters for the crystallographic class $6mm$ of the hexagonal polarised crystal system.	19
Figure 2.8 Displays a characteristic hysteresis loop occurring during the reversal of the polarization in a ferroelectric. [Bottger, 2005].	21
Figure 2.9: Schematic of domain pattern of fine-grained ferroelectric ceramic	22
Figure 2.10: Schematic illustration of <i>a</i>) 180° and <i>b</i>) 90° ferroelectric domains and domain-wall regions in a tetragonal perovskite ferroelectric (as PZT) [Damjanovic, 1998].	23
Figure 2.11 Phase diagram of PZT.	24
Figure 2.12 The relations between hysteresis geometry and complex amplitudes of P(E) dependence [Morosov, 2005].	25
Figure 2.13: Schematic of the poling process in ferroelectric material, showing an unpoled ceramic with a zero net polarisation (1), and a poled ceramic with a net polarisation (2) [Damjanovic, 1998].	26

Figure 2.14 Illustration of the linear and the non linear relation between the polarisation of a ferroelectric ceramic and the applied electric field. This generates the hysteresis loop configuration illustrating the switch of domains [Damjanovic, 1998].	26
Figure 2.15: Representation of the energy levels of a metal and a semi-conductor.	28
Figure 2.16: Schematic level interface metal semiconductor in the Shottky hypothesis.	29
Figure 2.17: Schematic representation of states levels for the contact metal-semiconductor, hypothesis of Shottky-Bradeen.	30
Figure 2.18: Illustration of the curvature of a substrate due to a stressed film deposited on it. A compressed film deposited on rigid substrate will apply forces in the radial direction oriented toward the edge of the substrate. The substrate tries to release that added stress and bend. A tensile film will have the opposite effect, <i>i.e.</i> the curvature of the substrate will have been negative.	32
Figure 2.19: illustration of the sol-gel basic principle.	35
Figure 2.20: Illustration of the different uses, and products of sol gel technologies: from the simple application of an aero-gel to the complex creation of dense ceramic film and fibres.	38
Figure 2.21: Schematic steps of the screen printing process.	39
Figure 2.22: Illustration of the tape casting technology.	40
Figure 2.23: Outline of the fabrication process for the multilayer ceramic capacitor (This schematic is adapted from [Moulson <i>et al.</i> 2003]).	41
Figure 2.24: Schematic of a multilayer ceramic capacitor construction [Cannell et al. 1990].	41
Figure 2.25: Construction and cross section of a multilayer transducer (green stage). [Lilliehorn <i>et al.</i> 2004]	42
Figure 2.26: The four distinct stages to the spin coating process: Stage 1: substrate deposition on the chuck. Stage 2: deposition of the fluid onto the wafer. Stage 3: spinning at constant rate. Stage 4: solvent evaporation during spinning.	43
Figure 2.27: PZT thick film mould technology usable for a single element transducer. [Zhao <i>et al.</i> 2003]	45

Figure 2.28: Typical pictures of micro-molded PZT sol-gel composite structures on a platinum-coated silicon wafer. (a) A 50 μm thick annular pattern with kerfs of 15 μm . The central disk is 100 μm in diameter; the ring is 50 μm wide. Some Su-8 residues trapped on the surface. (b) A linear array (~50 μm thick) of size 23 μm \times 15 μm . The scale is 50 μm . (c) A five-element annular array of ~40- μm thick with kerfs of 20 μm . The outer diameter is 2.0 cm and the scale is 500 μm . (d) A super long linear array of 27,000 μm , 50 μm wide, and 65- μm high. The scale is 500 μm . [Pan <i>et al.</i> 2006]	46
Figure 2.29: Schematic of an etching process using photolithography. Alternatively the etching step can be replaced by a metal deposition to pattern electrode on the substrate.	47
Figure 2.30: Schematic of an example of metal residue after lift off.	47
Figure 2.31: Schematic of a cross section of an ultrasonic transducer.	48
Figure 2.32: Schematic of one element of a CMUT	49
Figure 2.33: Schematic of a piezoelectric transducer working on the thickness mode.	50
Figure 2.34: Schematic cross section through a pMUT. [Murali <i>et al.</i> 2005]	51
Figure 2.35: Schematic illustration of a propagating of a longitudinal wave.	54
Figure 2.36: a) Schematic of piezoelectric resonator of thickness l with top and bottom electrodes, b) schematic of a three port black box, c) relation between the three-port notation and the transducer physical variables.	59
Figure 3.1: Schematic representation of the PZT sol preparation route	68
Figure 3.2: Schematic of the reflux (under nitrogen) experimental set-up	69
Figure 3.3: Schematic of the vacuum distillation experimental set-up	69
Figure 3.4: Schematic of the coaxial cylinder cup and bob configuration used to measure the composite viscosity.	71
Figure 3.5: General schematic of the thick film deposition procedure using sol-gel/composite slurry including the intermediate sol infiltration stages.	74

Figure 3.6: SEM micrograph of a 4[C+4S] PZT thick film cross section: 4 times [1composite layer+ 4 infiltrations sol]	74
Figure 3.7: Silicon wet etching experimental set up.	76
Figure 3.8: Schematic of the corona poling set up	78
Figure 3.9: Schematic diagrams of (a) the test sample with a support ring and (b) the load geometry [Southin <i>et al.</i> 2001].	80
Figure 3.10: Complete representation of the S-parameter involved in a two-port network representing the sample.	82
Figure 3.11: The equivalent circuit of the S_{21} measurement	82
Figure 3.12 Typical result obtained for the S_{21} parameter at the frequency of resonance, (f_r). f_a represents the anti-resonant frequency.	83
Figure 3.13: Two Schematic representation of the S_{11} parameter: a) the electrical equivalent circuit, b) two ports representation.	83
Figure 3.14: probe station developed to measure the S_{11} parameter (B) and typical result obtain for this parameter, f_r is the resonance frequency and f_a the antiresonance frequency (A).	84
Figure 4.1: SEM micrograph and a particle diameter analysis graphic of the PZ26 powder. Mean value of particle diameter is equal to $0.74\mu\text{m}$.	87
Figure 4.2: Viscosity of a 2.2 g.cm^{-3} composite as a function of the shear rate, measured with a parallel plate rheometer.	88
Figure 4.3 X-Ray diffraction pattern of a PZT thick film [C+4S] sintered at 710°C .	88
Figure 4.4: SEM micrographs of fracture cross sections of the PZT composite film infiltrated from 0 to 4 times, images: a, b, c, d, and e respectively.	89
Figure 4.5: Representation of the variation of volume percent of porosity samples infiltrated from 0 to 4 times.	90

Figure 4.6: SEM micrographs of the surfaces of a single layer of PZT composite infiltrated 0 to 4 times. All the pictures were taken after the 450°C temperature treatment.	92
Figure 4.7: Size of pores on the surface of the composite film as a function of the infiltration degree (After the 450°C temperature treatment).	93
Figure 4.8: SEM micrograph of PZT composite cross sections. Showing the non-uniformity of the material density around the cracks. A) Before sintering (after 450°C). B) After sintering. C) After sintering. A dashed line highlights the aureoles of denser material.	94
Figure 4.9: SEM micrographs showing the evolution of the surface of the PZT composite thick film fabricated with the process $x[C+4S]$ when: A) $x=4$, B) $x=8$, C) $x=12$, D) $x=12$. The composite film presented in picture D has been sintered twice: once at $x=8$ and another time at $x=12$.	95
Figure 4.10: Different interfacial layers formed between film and substrate. (1) abrupt interface characterise by a sudden change from the film to the substrate, (1-5 angström), (2) compound interface, a chemical reaction between the film and the substrate form a new layer, (3) diffusion interface characterised by a gradual change in composition between substrate and the film ,(4) mechanical anchoring at interface, characterised by rough surface interfaces [Ohring, 1992].	96
Figure 4.11. Holes produced at the Si/PZT interface due to diffusion of the Pb into the Si substrate during sintering.	98
Figure 4.12: SEM micrograph of PZT thick film composed of $16[C+4S]$ a) cross section, b) surface, c) surface of the same film + 1 layer of pure PZT sol spun leading to a surface with non-critical crack size. Substrate used was Si/SiO ₂ / ZrO ₂ /PZT sol.	100
Figure 4.13: SEM micrograph of a cross section of PZT thick film composed by $16[C+4S]$, highlighting the boundary between composite layers caused by the infiltration.	101
Figure 4.14: SEM micrographs showing the surface finish of the new process $x[2C+4S]$ compared to the surface states of the process $x [C+4S]$.	102
Figure 4.15: SEM micrographs of the PZT thick film cross section of a $7[2C+4S]$ process. The residual infiltration layers are not observable.	103
Figure 4.16: Thermogravimetric analysis (TGA) of a PZT sol / 2ME based: dried and not dried. [Leclerc, 1999]	104

Figure 4.17: SEM micrograph of the surface of a PZT composite layer infiltrated 4 times (1[C+4S]). a) before sintering (after 450°C) and b) after sintering (after 710°C)	105
Figure 4.18: Illustration of processes involved during the sintering process of the PZT composite.	106
Figure 4.19: SEM micrograph of the carbon-coated surface of the PZT composite 1[C+4S], at 200nm and 100 nm magnitude of resolution, showing the columnar crystallisation of the PZT sol on PZT grain.	106
Figure 4.20: a) SEM micrograph of a 110 μm hole in the photoresist. b) Resulting hole in a 35 μm thick PZT film using the HNO ₃ process.	107
Figure 4.21: SEM micrograph of a 21 μm PZT thick film patterned, the device definition illustrates the photoresist delamination due to the ultrasonic agitation every two minutes in order to remove the PbCIF residue.	108
Figure 4.22: SEM micrograph of a 150 μm hole PZT in a 35 μm thick PZT film resulting with a mask of 110μm.	109
Figure 4.23: SEM micrograph of a 21 μm PZT thick film, patterned with features of 10 μm, spun at 2000rpm/30s.	110
Figure 4.24: SEM micrograph of a 21 μm thick PZT film, patterned to a 10 μm wide device.	110
Figure 4.25: SEM micrograph of PZT thick: Comparison between the etching definition of the two process, [2C+4S] (22μm thick) and [C+4S] (21μm thick)	111
Figure 4.26: Laser scan of the (2C+5S) PZT composite showing: undercut characterising an isotropic wet etching, irregularities of the etching due to the non-uniform density of the composite, and that the PZT sol interlayer starts to appear at this degree of infiltration (2C+5S).	112
Figure 5.1: Surface profile in the direction [100] of: A) The substrate SiO ₂ (400nm)/Si (525)/SiO ₂ (400nm)/ZrO ₂ (40nm). B) The same substrate A coated with a 100nm thick Pt layer showing the presence of compressive stress. The curvature is approximated in two ways: 1st) The polynomial function $f(x)$, used to calculate the stress, is represented by the red lines which fits well with the measured data. 2nd) The maximum deflection z , used also to calculate the stress, is represented by the green lines.	117

Figure 5.2: A) Axes of symmetry presents in the silicon unit cell, (diamond structure). B) Young's modulus and Poisson ratio of silicon in different crystal orientation.	118
Figure 5.3: Stress induced by a 100nm thick platinum layer on 525 μ m silicon. Four directions of curvature measurement were probed: [110] & [-110], and, [100] & [010].	119
Figure 5.4 Example of surface profile with the "Dektak" stylus profiler, when the profiled surface contains a comet.	121
Figure 5.5. Surface profile in the direction (100) (plain line) and (010) (dashed line), obtained for a 27 μ m PZT thick film fabricated with the [2C+6S] process. For the stress calculation, the measurement was approximated in 2 ways: The red lines representing an approximation of the measurement, along the (100) plan, by a polynomial function $f(x)$ at the 2nd degree, and the green line representing the maximum deflection of the wafer.	122
Figure 5.6: Hoop stress: A) effect on curvature, B) hoop stress increases from the centre toward the edge of the wafer.	123
Figure 5.7: Surface profiling of the system $x\text{C}/\text{Pt}/\text{SiO}_2/\text{Si}/\text{SiO}_2$: $x=1,2$ and is the number of composite layers, C. Both layers were profiled at 20 $^\circ\text{C}$ after a temperature treatment of 200 $^\circ\text{C}$ and, after a further temperature treatment of 450 $^\circ\text{C}$. (Circle numbers show the succession of the deposition and temperature treatment)	125
Figure 5.8. Surface profile of the system $6[2\text{C}+6\text{S}]/\text{Pt}/\text{SiO}_2/\text{Si}/\text{SiO}_2$: The surface of this system was profiled at 20 $^\circ\text{C}$, after a temperature treatment of 450 $^\circ\text{C}$ and, after a temperature treatment of 710 $^\circ\text{C}$.	127
Figure 5.9: Surfaces profile of system $[2\text{C}+x\text{S}]/\text{Pt}/\text{SiO}_2/\text{Si}/\text{SiO}_2$: where x is the number of infiltrations. The curvature of the system increase but the thickness is considered constant through out the infiltration steps, and equal to 5 μm .	128
Figure 5.10: Stress calculated from the deflection of the surface profiles of system $[2\text{C}+x\text{S}]/\text{Pt}/\text{SiO}_2/\text{Si}/\text{SiO}_2$: where x is the number of infiltration steps (Figure 5.10).	128
Figure 5.11: A) Surfaces profile of system $x[2\text{C}+6\text{S}]/\text{Pt}/\text{SiO}_2/\text{Si}/\text{SiO}_2$: where x is the number of [2C+6S] units. B) Stress calculation from the Stoney's equation and the wafer curvature: The deflection of the system increases with an increase in the thickness.	130

- Figure 5.12: Illustration of the location of the first cracks when a 30 μ m thick PZT composite thick film is spun on a silicon substrate coated with 100nm of Pt (process [2C+6S]). 131
- Figure 5.13: Surface profile of: A) a 27 μ m PZT composite thick film on a silicon substrate. (7[2C+6S]/Pt/SiO₂/Si/SiO₂), B) a 30 μ m PZT composite thick film on an alumina substrate. ([2C+6S]/Pt/AL₂O₃). 132
- Figure 5.14: Stress calculated from the wafer deflection for different thicknesses of PZT composite on alumina and on silicon: a) stress value developed by a increase of PZT thickness on silicon, b) deflection of the silicon wafer, c) stress value developed by a increase of PZT thickness on alumina, b) deflection of the alumina wafer. 133
- Figure 6.1: Test structure use for the relative permittivity, d_{33} , and e_{31} measurements. 137
- Figure 6.2: Relative permittivity and dielectric loss of the [C+4S] PZT composite thick film crystallised with a furnace at 690°C (C) and 710°C (A) (wafer temperature), and an RTA at 710°C (B). 137
- Figure 6.3: Schematic of 2 atomic diffusion processes taking place during the sintering process. 139
- Figure 6.4: Illustration of the PZT composite relative permittivity as function of its porosity using the James Clerk Maxwell equation. The two lowest lines represent the equation 6.2. The highest line represents the same equation applied to an unpoled bulk ceramic. The model is then compared to some experimental data. 141
- Figure 6.5: AutoCAD drawing of the chromium masks used to process the cylinder device and to characterise the PZT composite material. 143
- Figure 6.6: Chromium mask design for the cylinder device presented in Figure 6.7. 144
- Figure 6.7: Schematic of a typical device made with masks. The top electrode on the SEM micrograph has been added for clarity. 144
- Figure 6.8: Capacitance function of the electrode size. On a 24 μ m sample fabricated with the 6[2C+4S] process. [*= experimental data, + = theoretical capacitance calculate with an $\epsilon_r=630$] 145

Figure 6.9: Raw relative permittivity calculated for different electrode sizes. (samples fabricated with 6[2C+4S])	145
Figure 6.10: Extra-capacitance possible in this design.	146
Figure 6.11: Electrical circuit for determining the effect of stray capacitance.	147
Figure 6.12: Relative permittivity corrected assuming an stray capacitance of 50pF	148
Figure 6.13: PZT film thickness variation as a function of the distance from the spin coating centre. The thickness is in μm , the distance in mm.	150
Figure 6.14: Zones where the thickness is influenced by the spin coating effect for a PZT thick film deposition.	150
Figure 6.15: Relative permittivity corrected for the stray capacitance and the thickness variation. 6[2C+4S] sample.	151
Figure 6.16: Theoretical capacitance calculated with $\epsilon_r(\text{PZT})=630$ (dashed lines) versus the thickness corrected capacitance (black square), 6[2C+4S] sample.	152
Figure 6.17: Relative permittivity of thick film fabricated with the [2C+4S] process on alumina substrate. Two film thickness are represented here 30 μm and 40 μm .	153
Figure 6.18: Capacitance and dielectric loss frequency dependence of 6[2C+4S] (24 μm thick), electrodes radius of 350 μm .	155
Figure 6.19: PZT thick film dielectric loss dependence on electrode radius, measure at 1kHz, during the winter.	155
Figure 6.20: Piezoelectric coefficient $d_{33, \text{eff}}$, of a 10 μm 4[C+4S] PZT composite film poled at 130°C/5min and cooled under voltage. 2 samples were sintered at 2 different temperatures (690°C and 710°C).	157
Figure 6.21: Measured $d_{33, \text{eff}}$ as a function of temperature, applied field, and cooling conditions (from (2C+4S) samples).	159
Figure 6.22: Hysteresis loop of PZT composite thick film (8 μm thick).	160

- Figure 6.23: Hysteresis loops of the composite [2C+4S] on silicon substrate, illustrating the influence of tensile stress during fabrication process by applying different maximum electric field during the hysteresis loop experiment, from 11 to 26V/ μm in 1 μm increments. 162
- Figure 6.24: Hysteresis loops of the composite [2C+4S] on alumina substrate, illustrating the influence of a compressive stress during the fabrication process, by applying different maximum electric fields during the hysteresis loop experiment 164
- Figure 6.25: Hysteresis loop of the PZT composite film [2C+4S] on alumina substrate and on silicon substrate. It shows the compressed shape of the hysteresis loop when the film is subjected to a compressive stress, on alumina. 165
- Figure 7.1: Calculated variation in resonant frequency as a function of thickness as predicted by equation 7.1 (PZ26 bulk parameters). 169
- Figure 7.2: Illustration of the measured device design: red lines reveals the location of parasitic capacitances added by the ground signal ground pads, which reduced the measured signal. In the equivalent circuit of the S_{21} parameter measurement, the parasitic impedance $Z_{\text{parasitic } 1}$ and $Z_{\text{parasitic } 2}$ represent this parasitic capacitance. 170
- Figure 7.3: S_{21} characteristic of a 22 μm thick [C+4S] PZT film after and before poling. When poled, it resonates at 77MHz. 171
- Figure 7.4: Electrical equivalent circuit of the S_{11} signal. 171
- Figure 7.5: S_{11} parameter of 600 μm radius electrode of a 22 μm thick PZT [C+4S] device with the backing silicon etched. 172
- Figure 7.6: Variation in resonant frequency as a function of thickness as predicted by equation 7.1 (with PZ26 bulk parameters), in comparison to experimental data obtained for the PZ26 powder/ PZT sol-gel composite thick film (x[C+4S]). 174
- Figure 7.7: red line: Mason model of a simple layer of 22 μm PZT transducer fabricated with PZ26 bulk. Black line: experimental data from the same transducer via the [C+4S] composite route. 174
- Figure 7.8: The red line represents the Mason model prediction for a loaded transducer Pt/PZ26(P=8%, $l=22\mu\text{m}$)/Pt/SiO₂. The black line represents the experimental result for a 10 [C+4S] thick film with 8vol.% of porosity (22 \pm 0.1 μm thick). 179

Figure 7.9: Illustration of the change needed on the stiffness to explain the difference of the resonant frequency between the Mason model of a PZ26 system and the composite system experimental result. Reducing the stiffness of PZ26(P=8%) by $0.2 \cdot 10^{11}$ N/m², shifts the model resonance toward the experimental resonance. 181

Figure 7.10: Variation of the intensity of the modelled resonant frequency for a 22µm thick 10[C+4S] sample, when ϵ^{σ} (PZ26(P=8vol.%)) is reduced from 1150 to 830 (A difference of stiffness does not change the intensity of the resonance) (Figure 7.9). 182

Figure 7.11: Modification of the Mason equivalent circuit presented in Figure 2.30. This figure represents the final Mason equivalent circuit considered in this model. 183

Figure 7.12: Comparison of the modelled S_{11} of PZ26 with 8% of porosity, a stiffness equal 0.87, a relative permittivity equal to 830, and a loss of 0.01 and The measured S_{11} of PZT composite PZ26/sol-gel, 10[C+4S], with 8% of porosity, an unknown stiffness, a relative permittivity equal to 830, and a loss of 0.01. 184

Figure 7.13: S_{11} parameters as a function of frequency for Mason model (A) and experimental data (B). For both A and B, the material considered is the PZT composite PZ26 / PZT sol-gel infiltrated 4 times [C+4S]. 3 different thicknesses of PZT are tested: 7, 22, 32µm. 185

Figure 7.14: Model of 3 PZT composite (P=8%) transducers with 3 different ratios (of electrode radius to film thickness, (r^2/l)). The transducer A, characterised by the ratio R_1 , is 32µm thick. It can be compared with the transducer 1 in Figure 7.13. The transducer B, characterised by the ratio R_3 , is the model presented in figure 7.13 (transducer 2). It is used as reference. The transducer C is characterised by the ratio R_3 and is 32µm thick, it can be compared with the transducer 3 Figure 7.13. 188

Figure 7.15: S_{11} parameter of a 24 µm thick transducer fabricated with the [2C+4S] process (electrodes radius is 320µm). 189

Figure 7.16: Real impedance and real admittance of the 24 µm thick transducer fabricated with the [2C+4S] process (electrode radius is 320µm). 189

Figure 7.17. Analytical model (A) and experimental data (B) of the S_{11} parameter for three different process 2C+4S, 2C+6S, and C+4S. 192

Figure 8.1: Schematic illustration of an array of transducers shape in rings. (cross section of the rings of PZT is represented in blue, the yellow represents the bottom and top electrodes and the grey the 100nm thick silicon oxide membrane and acoustic backing) 196

Figure 8.2: Schematic illustration of the transducer dead area induces by the connection lines. IMASONIC modelled the beam of waves emitted by the annular array demonstrating that the dead area effect on the beam at different distance from the transducer can be neglected (respectively 5, 10, 15, and 20mm, from left to right)	197
Figure 8.4: A) Annular arrays with the PZT etched between annular rings, B) Un-etch annular array with a full un-patterned top electrode. The connections lines of the bottom and top electrodes of the prototype were prepared for a flip-chip packaging design.	199
Figure 8.5: The amplitude and phase of the complex impedance of a [2C+5S] annular array prototype elements 1 (center), 4, 7, are presented. It shows the evolution of resonance behaviour across the device (the optical micrograph picture represented the back electrode observable when the backing Si is removed).	201
Figure 8.6: Pulse-echo responses observed for the 2C+5S based device showing that the TmpMUT devices are able to operate in water.	202
Figure 9.1: S_{11} parameters as function of the frequency, for: A) 42 μm PZT thick film on 500 μm thick alumina substrate, B) 27 μm PZT thick film on 500 μm thick alumina substrate.	205
Figure 9.2: a) Schematic and b) SEM photomicrograph of the multilayer structure with embedded electrode	206
Figure 9.3: the anti-parallel poling and the parallel poling.	207
Figure 9.4: Bi-layer structure transducer of a 30 μm thick PZT film fabricated with the process [2C+6S], the top layer is a 10 μm thick PZT film and the bottom layer is a 20 μm thick PZT film.	208
Figure 9.5. Bi-layer structures transducer of a 30 μm thick PZT film fabricated with the process [2C+6S]: the top layer is a 10 μm thick PZT film and the bottom layer is a 20 μm thick PZT film. The system poled with the parallel technique, and the measurement was taken with the bottom electrode and the top electrode connected with silver paint.	209
Figure 9.6. Bi-layer structure transducer of a 30 μm thick PZT film fabricated with the process [2C+6S]: the top layer is a 10 μm thick PZT film and the bottom layer is a 20 μm thick PZT film. The system poled with the parallel technique, and the measurement was taken with the bottom electrode and the top electrode connected with silver paint.	210

TABLES

Table 2.1: Simplification of tensorial Subscripts based on the space triads (1,2,3) (see Figure 2.6)	18
Table 2.2: Current High frequency transducers	63
Table 3.1: Composition of the slurry used - sintering aid-assisted composite	70
Table 3.2: Composition of the ZrO ₂ diffusion barrier sol	72
Table 3.3: RIE conditions used for silicon oxide	75
Table 4.1: Thickness of PZT achieved until delamination occurred, x = number of infiltrate composite layer spun	97
Table 4.2: EDX composition analyses of 50µm of the PZT composite film surfaces infiltrated 4 times (samples [C+zS] with z=0,1,2,3, exhibit similar analysis).	104
Table 4.3: [C+4S] PZT thick film etch rate by wet etching, (HF (0.5%), H ₂ O (95%), HCl (4.5%))	109
Table 4.4: Etching rate of x[2C+4S] PZT thick film.	111
Table 5.1: Calculated stress of a 100nm thick Pt layer on the substrate: SiO ₂ (400nm)/Si (525)/SiO ₂ (400nm)/ZrO ₂ (40nm).	118
Table 5.2 :Calculated stress of in a 27µm thick PZT layer on the substrate: Pt(100nm) /ZrO ₂ (40nm)/ SiO ₂ (400nm)/Si (525)/SiO ₂ (400nm).	122
Table 5.3: Stress calculation of the system xC/Pt/SiO ₂ /Si/SiO ₂ : x=1, 2 and is the number of composite layers, C. Both layers were profiled at 20°C, after a temperature treatment of 200°C and, after a further temperature treatment of 450°C.	126
Table 6.1: Confirmation of the trend observed in figure 6.2: influence of the temperature and heating-rate on samples prepared with the [C+4S] process.	140

Table 6.2: Piezoelectric properties and dielectric constant of a PZT composite thick film 4[C+4S] process sintered for 30 minutes.	158
Table 7.1: Characteristics specified for the annular array ultrasonic transducers	167
Table 7.2: Bulk (PZ26) material constant parameters input in the Mason model [Ferroperm catalogue] (the thickness of the PZT film was measured by a stylus dektak surface profiler)	173
Table 7.3: e_{33} (C/m ²) values of PZ26, considered to vary like the PZT-5A ceramic with an increase of porosity, revealing a constant k_t with an increase of porosity	178
Table 7.4: Dielectric and mechanical properties of PZ26, PZ26 (with 8% of porosity) that are input in the Mason model. The measured constants characterising the composite PZ26 powder/PZT sol-gel infiltrated 4 times, are also presented.	179
Table 7.5: 3 transducers, (A, B, and C) modelled with three different ratios of r^2/l (electrode radius r and PZT thickness l).	187
Table 7.6: Summary of results obtain for the electro-mechanical coupling coefficient	193
Table 8.1: Measurements and design of each annular	198
Table 8.2: Fringing fields increase the measured capacitance from the central electrode to the external annular electrode. The prototype tested is a 30 μ m thick [2C+4S] annular array on alumina.	200

Chapter 1

Introduction

1.1 Project background

The sensor/transducer market for monitoring and control of discrete and process manufacturing is forecasted to grow to above \$23 billion by 2011. According to the same source, revenues for next-generation biological and chemical sensors will increase to almost \$4 billion in 2011 at a compound annual growth rate of 11.5%. The global market for piezoelectric operated actuators and motors is now worth \$5.27 billion and is expected to reach \$10.66 billion by 2011, with the medical applications alone representing more than 40% for that market. Developing research in new technologies of piezoelectric transducers follows these market trends, especially in the high frequency domains where the research is new and the medical demand, in term of superficial imaging has not been answered by any current technologies (<http://www.caneus.org>).

Piezoelectric micromachined ultrasonic transducers (pMUTs) are being developed as an alternative to transducers fabricated from bulk ceramics as they offer the potential for direct integration of electrical connections, fine scale structuring and batch processing. Traditionally, polishing and dicing of bulk ceramic thick plates is the industrial method to fabricate these ceramic piezoelectric transducers. Such devices resonate in the through-thickness direction (33) and operate at frequencies dictated by their resonance frequency, which is dictated by the thickness of the device. For medical superficial imaging, devices need to operate in the region of 40-60MHz which necessitates a thickness of $\sim 30\mu\text{m}$. Such thicknesses of piezoelectric ceramic can be achieved using bulk ceramic processing but are very difficult to obtain using film forming techniques typically employed for fabrication of pMUTs.

Other pMUT structures, such as the diaphragm type resonators, can be constructed where the resonance is excited using a lateral mode (31) extension. By creating a uni- or bi-morph structure, a bending mode is induced where the resonant frequency is dictated by the diameter and thickness of the diaphragm. In this manner, thin films of lead zirconate titanate (PZT) can be used to produce transducers resonating at high frequency transducer. However, as the size of the diaphragms decrease with an increasing resonant at 50MHz, very small diaphragms are required. This technology faces considerable size limitation for the development of transducer operating at 50MHz and higher.

The goal of this project is to develop a fabrication route to realise a transducer, where the operating frequency is not dependent on the device area, and which can be easily shaped to produce 3D structures, such as annular arrays, or a multilayered structures with embedded electrodes. To do so, ferroelectric thick films are developed with MEMS technology for the fabrication of a transducer working in thickness mode in the high frequency domain (50MHz). Thickness mode (Tm) pMUTs represent the MUT equivalent of the conventional transducer and build on the techniques developed for the fabrication of bending mode pMUTs. To attain such frequency with the thickness mode of excitation a 30 μm thick film is needed. To achieve this thickness, a new PZT powder/fluid composite, deposited with spin coating technology, has been developed to allow one to deposit films with thickness ranging from 2 to 10's of

micrometers when several layers are deposited. This work demonstrates that once shaped using wet chemical etching and sintered at low temperature (710°C), this technology seems to be a candidate for the development of high frequency transducer annular arrays, for the next generation of high frequency transducers such as multilayer transducers with embedded electrodes.

1.2 Thesis outline

This thesis has been divided into nine chapters of which this is the first. The second chapter is a literature review, which addresses separately, the theoretical considerations concerning the fundamental topics of dielectric, piezoelectric and ferroelectric materials and acoustic piezoelectric transducers, as well as presenting a review of the state of the art fabrication techniques. Chapter 3 describes the experimental techniques used to fabricate the patterned PZT thick films presented and qualitatively analysed in Chapter 4. Chapters 5, 6, 7 relate to the main analysis of the in-situ stress of such thick films, their dielectric, piezoelectric and ferroelectric properties, and model their acoustic behavior respectively. Chapter 8 then presents the annular array transducer prototypes for high frequency medical imaging. Finally, Chapter 9 presents the conclusions from this study, and preliminary work conducted multilayer transducers with embedded electrodes.

Chapter 2

Literature review

2.1 Introduction

This literature review mirrors the arrangement of the experimental chapters 4, 5, 6, 7. Describing the content of these chapters becomes then equivalent to describing the sections of this literature review. Some sections just describe the works that has been done around the word on the focused topic of each concerned chapters. Some sections describe more the theory used in our discussions.

The fabrication of thick PZT films, with a thickness of 2 micrometers up to 50 micrometers is detailed in Chapter 4. It will focus on techniques allowing the direct integration of the PZT film onto a silicon substrate or alumina substrate, and on detailing patterning techniques.

While the deposition of different layers is taking place, the *in situ* stress of these layers increases, or decreases. The topic of stress is one of the main issues that have to be understood, when the film develops cracks while its thickness increase. Chapter 5 describes this *in situ* stress variation.

Chapter 6 of this thesis is devoted to the dielectric aspect of our material. As it is a new composite, knowing its dielectrics properties is fundamental for any transducer application.

The last section of this project is dedicated to the production and characterisation of high frequency piezoelectric transducers.

The first half of this chapter is concerned with the basics of dielectric, piezoelectric and stress theories. It introduces the theory needed to understand the core of the discussion: the theory of dielectric materials and polarisability needed to understand Chapter 6 is presented. Basic principles that govern ferroelectricity and piezoelectricity will be then presented: to understand Chapter 6 for its part on the material polarisation, and Chapter 7 for the application of piezoelectricity of transducers. The theory of stress, examined in Chapter 5, is also presented in this part because of its tensorial notation commonality with the piezoelectric system.

The second half of this chapter deals with the fabrication and modelling of ultrasonic piezoelectric thickness mode transducers. It focuses on the PZT thick film fabrication and on explaining the theory of a thickness mode transducers. Different fabrication and shaping technologies found in the literature are presented to complement Chapter 4. This second part also focuses on presenting the literature on high frequency transducers and on modelling ultrasound waves received or emitted by a PZT thick film using the Mason model used in Chapter 7.

2.2 Dielectric material behaviour

2.2.1 Introduction to dielectrics

Dielectrics are not confined to the narrow area of insulators (Figure 2.1), but instead to any non-metal when their interaction with electric or electromagnetic fields is of interest. They are characterised by their polarisation and their dynamics of electric charges.

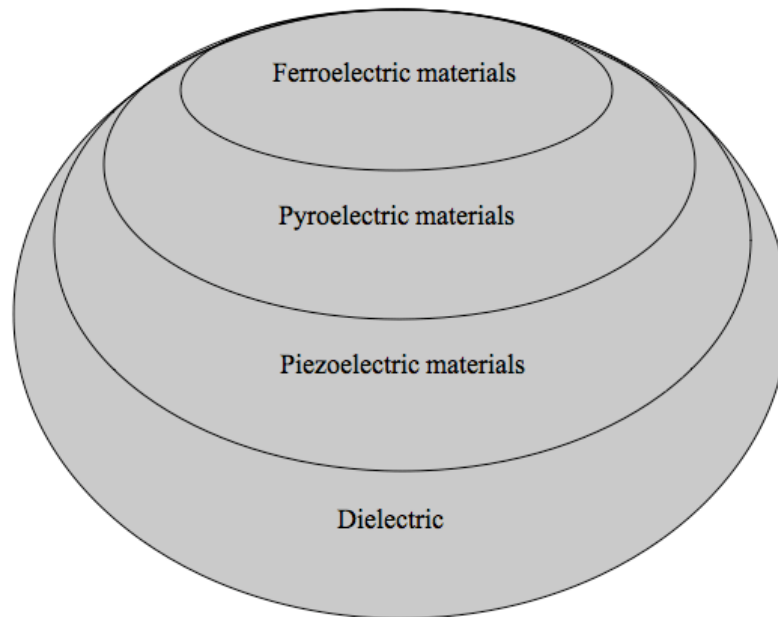


Figure 2.1: classification of dielectric materials

They are often described in terms of macroscopic properties such as permittivity, dielectric loss and breakdown strength. Electrical engineers have characterised dielectrics macroscopically using field vectors, and equivalent circuits. It is interesting to notice that a similar approach is used for transducers. In contrast, the physicist and chemist have pushed forward the understanding of dielectric responses in terms of molecular and structural response and relaxation.

The theory of dielectrics is now well developed, many of the fundamental problems are now understood, and thus it is now possible to move from dielectric analysis to the existing field of dielectric synthesis. This is of considerable interest to most areas of science and demonstrates the cross-disciplinary nature of dielectrics [Von Hippel, 1954]. Some examples include:

- The development of new materials and systems (e.g. non-linear optical, piezoelectric, ferroelectrics, improved insulators, drugs and bio-systems etc.).
- The understanding and predicting of the behaviour of materials and systems to applied electric fields (e.g. mobile phones, power lines, drugs, biological systems etc.)

- Dielectric properties of our composite route are not known, however, for a transducer application, these variables are fundamentals. Dielectric constant, dielectric loss, polarisation, hysteresis loop, piezoelectric and ferroelectric behaviour are then variables that this section presents. Chapter 6 will present the experimental approach of these properties.

As the dielectric material is a complex area, it is impossible to present in detail all the topics involved in this theory. The reader will be redirected to the principal sources used for this section [Herbert, 1985], [Von Hippel, 1954].

2.2.2 Capacitance

The capacitance, C , of a parallel plate capacitor (e.g. ignoring fringe effect etc.), can be defined by Equation 2.1:

$$C = \frac{A\varepsilon}{l} \quad \text{Equation 2.1}$$

Where A is the active electrode area, ε is the permittivity of the material between the parallel plate electrodes, and l is the dielectric material thickness.

2.2.3 Relative permittivity

The relative permittivity, ε_r , is a characteristic quantity for a given dielectric substance, sometimes called dielectric constant. It is generally defined by Equation 2.2 [Bekefi and Barrett 1987, p. 418]:

$$\varepsilon_r = \frac{\varepsilon}{\varepsilon_0} \quad \text{Equation 2.2}$$

Where ε_0 is the permittivity of free space. The relative permittivity, ε_r , therefore defines the permittivity of a material relative to ε_0 .

Then Equation 2.1 becomes Equation 2.3 used in this project:

$$C = \frac{\varepsilon_r \varepsilon_0 A}{l} \quad \text{Equation 2.3}$$

The larger the relative permittivity of a material, the more charge that can be stored. If we considered C_{vac} to be the capacitance measured between 2 parallel plate electrodes in a

vacuum. Completely filling the space between the capacitor plates with a dielectric material increases the capacitance by a factor of the relative permittivity (Equation 2.4). This Equation gives a good insight of what the relative permittivity is: the ratio of the capacity to store (or move) charges between a normal medium with constant medium use as a reference, the vacuum.

$$C = \epsilon_r C_{vac} \quad \text{Equation 2.4}$$

2.2.4 Fringe effect

Equation 2.1 assumes that the edge of the electrodes coincides with the edge of the material, and that flux outside this surface is negligible. Unfortunately, the inter-electrode electric field is not uniform, especially near the electrode edges, where the electric field extends into the space beyond the electrodes. A number of authors have derived functions for the potential distribution between two disc electrodes at equal or opposite potential. The most comprehensive works are by Nicholson [1924], Love [1949] and Sloggett [1986]. These works give numerical solutions to this electrostatic problem.

A brief presentation of the fringing field will be done in this section, without entering into any derivation.

Equation 2.1 is valid for the case described in Figure 2.2.a). In order to simplify the problem, the fringing flux, in the other 2 cases (Figure 2.2.b and c), will be considered to increase according to the ratio of the dielectric constant between the dielectric material (ϵ_1) and the surrounding medium (ϵ_2). The fringing field reaches a maximum when this ratio has the value of unity, as in multilayer capacitors.

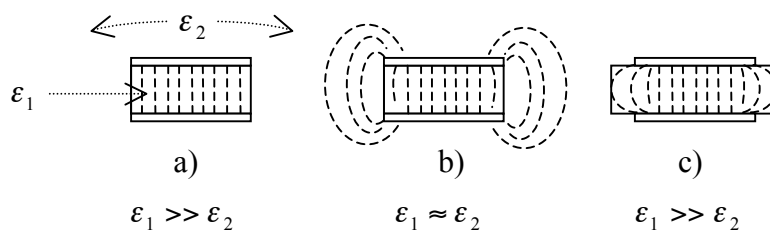


Figure 2.2: Schematic of fringing fields for various capacitor structures.

The effect of the fringing field can be taken into account by considering the effective increase in the area of the electrode, ∂A , such that:

$$\partial A = X2\pi r l \quad \text{Equation 2.5}$$

Where r is the radius of the electrodes and X is a constant that accounts for the derivation treated by Slogett [1986], and includes the ratio of permittivity to the structure of the capacitor. The ratio of the capacitance due to fringing, C_f , with the capacitance due to the area between the electrode, C_e , is given by Equation 2.6:

$$\frac{C_f}{C_e} = \frac{\frac{\epsilon_r \epsilon_0 \partial A}{l}}{\frac{\epsilon_r \epsilon_0 A}{l}} = \frac{\partial A}{A} = \frac{X2l}{r} \quad \text{Equation 2.6}$$

The highest value of X is represented by Figure 2.2 b), and has a maximum value of 0.3. Since l/r is usually less than 0.2, the fringing field rarely adds more than 12% to the capacitance calculated using Equation 2.1. However, when the ratio, l/r , approaches 1 the fringe effect is reported to be more than 20%. [Herbert *et al.* 1985 pp42-48]

There will then not only be a contribution to the capacitance from the fringing field but also a contribution to the dissipation factor. The effect of the fringing field on the capacitance can usually be ignored. However, when the film thickness increases, or when the electrode size decreases, the fringing effect can reach a very high percentage of the measured capacitance. Modelling the fringing effect is complex. The analytical complete potential equation of the capacitor is derived from the Schwartz-Christoffel equation presented by Palmer [1927], and corrected by Wingcho Chew [1980].

In general the easiest and the most efficient way to model the contribution of the fringing effect in an accurate manner, without this X material dependent variable, or without having to solve the 3 dimension integral of potential, is the finite element analysis. In this project the software FEMlab was used to calculate this potential in order to find the influence of the fringing fields on the capacitance.

This fringing effect can be avoided for thick capacitors by the incorporation of guarding electrodes at a constant potential, which will confine the electric field in the desired area (Figure 2.3) [Heerens *et al.* 1986]

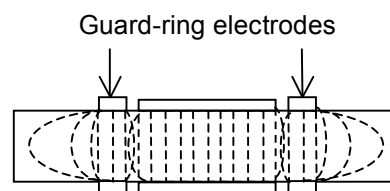


Figure 2.3: Schematic representation of the guard-ring electrodes or guarding electrodes, which blocked the effect of the fringing fields, by confining the active electric field inside the capacitor.

2.2.5 Breakdown and degradation

High voltage can result in an accumulation of charge inducing dielectric breakdown: The increased flux density at the edge of the electrode results in a considerable enhancement of the local field and can lead to breakdown at high voltages.

Dielectrics exhibit what is termed elastic stress, which enables the structure to absorb unusually large quantities of charge. Because of this property, dielectric materials will carry on absorbing charge until a saturation of this capacity to accumulate charge is reached. If the power source is still connected and still trying to apply more charge to the material, it will rupture and a path will be created through the material for charge to discharge. This phenomenon is called dielectric breakdown. If, however, before it ruptures, the charge accumulated within the dielectric rises toward its saturation point and reaches a level of voltage higher than the voltage of the charging circuit, then the dielectric's voltage will discharge itself (just like a short circuit - very violently) back through the power source.

Breakdown results in the rapid discharge of the charge in the capacitor and its conversion to heat and mechanical stress.

The effect of breakdown on a dielectric ceramic is usually to establish a low resistance path between the electrodes due to defects in the microstructures: inclusion, dislocation, or porosity.

The working voltage V_w , is related to the breakdown field, E_b , and the dielectric thickness, l , through the safety factor η_s :

$$V_w = \frac{E_b l}{\eta_s} \quad \text{Equation 2.7}$$

This relation illustrates that for a given working voltage, the thinner the film, the higher the breakdown field because there is a smaller probability that a defect will lead the discharge.

Two types of failure are recognised in dielectrics sometimes distinguished as electrical and electro-thermal breakdown [Wintle 1981] [Herbet 1985].

- Electrical breakdown: The condition for this breakdown is a local field of sufficient magnitude to promote electrons into the conduction band and to impart sufficient energy to them for their impact on other atoms to generate more electrons by ionisation. Thus structural features that lead to a local intensification of an applied field will lower the breakdown strength. Here fringing fields, and cavities, have to be avoided. A crack in the surface may admit metal from the electrode and provide a protruding spike that will have a high field at its tip. A pore may reduce the effective thickness through breakdown across its surface. Conductive impurities may have similar effects
- Electro-thermal breakdown: The term thermal is used as this type of breakdown occurs when high frequency alternating potentials are applied to dielectrics and cause

a rise in temperature through dielectric losses. If the rise in temperature at some point in the dielectric is sufficient to cause an increase in dissipation factor, the rate of temperature rise will be accelerated and become catastrophic. This type of breakdown should be distinguished from degradation or aging which may result in breakdown after a prolonged period of test, or with an old dielectric, but in both of these cases, a fall in capacitance values or resistivity, or an increase of a dissipation factor, is observed before the breakdown. The fall in permittivity and dissipation factor is a few percent per decade and a decrease in compliance at somewhat lower rate.

2.2.6 Resistivity

Through the discussion, the resistivity is often qualitatively described. Equation 2.8 is then necessary to understand the resistivity ρ_r (Ωm), though the DC resistance R_i of the capacitor, its thickness (l) and Area (A):

$$\rho_r = \frac{R_i A}{l} \quad \text{Equation 2.8}$$

Herbet [1985] remind that the high resistivity is a primary requirement for dielectrics since it underlies one of the main functions of a capacitor and transducer, the separation of continuous from alternating forms of electrical energy. The energy gap, between the conduction and the valence bands of the material, controls the resistivity value. This gap may be reduced by the presence of impurities or defects, which can, release electrons into the conduction band, or, add an energy level into the band gap. [Bruggeman *et al.* 1935]

In our case of doped PZT composite, impurity ions with charges greater than those of the ions they replace, i.e. Nb^{5+} on Ti^{4+} sites, act as acceptor: the electron necessary to neutralise the excess positive charge can be promoted into the conduction band. And this effect is reversed for the ions such Mn^{3+} replacing Ti^{4+} , which forms donor centres on Ti^{4+} sites.

To pole the PZT composite, the application of an electric field may not result in the transfer of a carrier from one site to another but simply in the polarisation of an electron-lattice site combination. This induces an increase in the average separation of the two charges. The result will be a contribution to the permittivity and the dissipation factor. There is often a correlation between low resistivity and high dissipation factor through both of them being dependent on a high concentration of donors [Jonsher *et al.* 1975].

High resistivity is best achieved by high purity and a crystal lattice free from defects, but, since defects and impurities are inevitable, an addition of the minimum quantity of a suitable acceptor gives a marked improvement in practical cases. The rutile alumina rubalite 710 reflects this effect with a permittivity close to 10, the highest resistivity ceramics are indeed found among the low permittivity oxides [Harwood *et al.* 1965] [Burn *et al.* 1975]

2.2.7 dielectric loss

A very thorough article, written by Gurevich and Taganstev [1991], shows that the dielectric loss in crystals is a very complex phenomenon. This paragraph presents a very simple approach to it. However, this summary will have to be read in conjunction with the section on dielectric loss in Chapter 6. With both sections, enough details are provided to sense what the dielectric loss is. A high dielectric loss is undesirable in almost all applications. It lowers the quality of the resonant circuit, which is especially undesirable for high frequency ultrasonic transducer applications. It results in the generation of heat and therefore in raising the temperature of a capacitor. The dissipation factor is generally taken as an indication of the quality of a particular type of capacitor. Thus a value of 0.1 might be acceptable for an aluminium electrolytic value, and 0.02 for a high permittivity (high K) capacitor [Abdullah *et al.* 1990], [Fang *et al.* 2006], [Gurevich *et al.* 1991].

In a capacitor, the potential (V_{pot}) is related to the capacitance (C) and the current (I) through Equation 2.9.

$$V_{pot} = \frac{q}{C} = \frac{1}{C} \int Idt \quad \text{Equation 2.9}$$

Where I is defined by the Equation 2.10.

$$I = I_0 \sin(\omega t) \quad \text{Equation 2.10}$$

Integrating I with respect to time Equation 2.9 results in Equation 2.11

$$V_{pot} = -\frac{I_0}{\omega C} \cos(\omega t) = \frac{I_0}{\omega C} \sin\left(\omega t - \frac{\pi}{2}\right) \quad \text{Equation 2.11}$$

This basic equation shows the shift of phase of $\pi/2$ between the current and the voltage in a capacitor. The conversion of the electrical energy to heat in a capacitor is generally expressed by the power of, $\sin \delta$, where $(\pi/2 - \delta)$ is the advance in phase of the current relative to that of an applied alternating voltage. This *dissipation factor* is defined by Equation 2.12.

$$d = \tan(\delta) \quad \text{Equation 2.12}$$

The dielectric loss in a dielectric can also be expressed by considering the permittivity in complex form when the electric field applied is sinusoidal (Equation 2.13 and 2.14)

$$\varepsilon = \varepsilon' - j\varepsilon'' \quad \text{Equation 2.13}$$

$$\frac{\varepsilon''}{\varepsilon'} = d \quad \text{Equation 2.14}$$

Where, d is the dissipation factor when the electrodes and leads do not contribute to the loss. ε' is the real part of the permittivity defining how the material reacts in terms of charge mobility when subjected to an electric field, ε'' represent the dielectric loss ($d\varepsilon'$) which quantifies the conversion of the movement of charges into vibrations of the lattice (phonons). Small simultaneous movements in the charge distribution surrounding each ion of the lattice due electric field are delayed, especially for fields up to the breakdown (see section 2.2.5) and frequencies down to the infrared. These charges follow the field with a little delay and very little conversion of electric energy into other forms. This phenomenon can be from a multiplicity of causes, especially when the microstructure is complex, as it is the case of the PZT sol-gel composite.

In that case the defects in the ceramic (e.g. porosity, dislocations, ion vacancy, impurity) are the most important source of loss. Each defect causes an adjustment in the surrounding ions relative to their state when the defect is absent. This adjustment induces screening charges which act against the polarisation induces by the electric field.

2.2.8 Polarisability

An atom isolated from any external field should have a spherical symmetry, and does not possess a permanent dipole moment. Under the influence of an external electric field the opposite displacements of positive and negative charges induce the apparition of a dipole moment m , proportional to the local electric field E_i , given by Equation 2.15

$$m = pE_i \quad \text{Equation 2.15}$$

Where p is the polarisability of this atom. This parameter applied to a molecule with a spherical symmetry can also be defined in this way. However in the case of non-spherical symmetry Equation 2.15 becomes tensorial and given by Equation 2.16.

$$m_u = p_{ui}E_i \quad \text{Equation 2.16}$$

In the case of a real dielectric, the derivation of the polarisability is not trivial. This section will give a summary of some equations found in the literature. For a precise derivation the work of Mahan [1990] is recommended.

This section has been written with the target to give an insight of how the concept of polarisation is understood in this work. Understanding the link between permittivity, dipole

moment, electric field and polarisation is important as these concepts are often used in the diverse discussions through Chapters 5, 6, and 7. The effective value, or average of each value, will be considered in order to simplify the derivation. In this manner Equation 2.16 can be written as Equation 2.17.

$$\bar{m} = p\bar{E} \quad \text{Equation 2.17}$$

The polarisation, \bar{P} , is equal to the product of the dipole moment and the number of polarisable entities per unit volume, $N = \frac{N_A \rho}{M}$, where ρ is the density, M the molecular weight associated with the polarisable entity and N_A is Avogadro's number. (Equation 2.18)

$$\bar{P} = N\bar{m} \quad \text{Equation 2.18}$$

By definition the polarisation is also given as Equation 2.19 and 2.20 [Damjanovic, 1998].

$$\bar{P} = (\varepsilon - 1)\varepsilon_0 \bar{E} \quad \text{Equation 2.19}$$

$$\bar{P} = \chi \bar{E} \quad \text{Equation 2.20}$$

Where χ is called the susceptibility of the material.

Equalling Equation 2.18 and 2.19 generates Equation 2.21:

$$\bar{m} = \frac{(\varepsilon - 1)\varepsilon_0}{N} \bar{E} \quad \text{Equation 2.21}$$

Equation 2.21 links the permittivity with the dipole moment and the electric field. This Equation shows the linear relation there is between the permittivity and the number of polarisable dipoles, when the electric field is constant through the material. For cubic structures and for induced dipoles (ionic and electronic polarization), the calculation reveals a relation between the atomic polarizability p_i and the macroscopic permittivity ($\varepsilon = \varepsilon_0 \varepsilon_r$) which is referred to the Clausius-Mossotti equation [Feynman, 1989].

$$\varepsilon = \frac{\varepsilon_0 + 2N_i p_i}{\varepsilon_0 - N_i p_i} \quad \text{Equation 2.22}$$

Considering $E = E_0 e^{i\omega t}$ when the driving voltage is alternating, this equation reveals that the polarisability of a dielectric is a function of the frequency of the electric field applied. Figure 2.4 reveals some discontinuities of this function, which indicates that many sources are at the

origin of the polarisation, the *static polarisation* will be the sum of these different contributions when the applied electric field frequency is null: (All of these different polarisation sources are represented during the polarisation of a single crystal, especially under temperature. an important additional sources of piezoelectric material polarisability will be discussed later)

- p_e , electronic (or optical) polarisability, due to the movement of the electron charge cloud relative to the nucleus of the atom.
- p_i , ionic (or infrared) polarisability, due to the movement of ions relative to one another and the accompanying displacement of their electron clouds.
- p_o , orientation (or optical) polarisability, which exist just in polar medium, due to the alignment of the dipoles to the external electric field. At room temperatures, usually all dipole moments have statistical distribution of their directions. An electric field generates a preferred direction for the dipoles, while the thermal movement of the atoms perturbs the alignment.
- p_{sc} , space charge polarisability, exist in dielectric ceramic which shows spatial inhomogeneities of charge carrier densities. This occurs in ceramics when charges are being trapped in insulating grain boundaries,. (so-called Maxwell-Wagner polarization) (Figure 2.5).

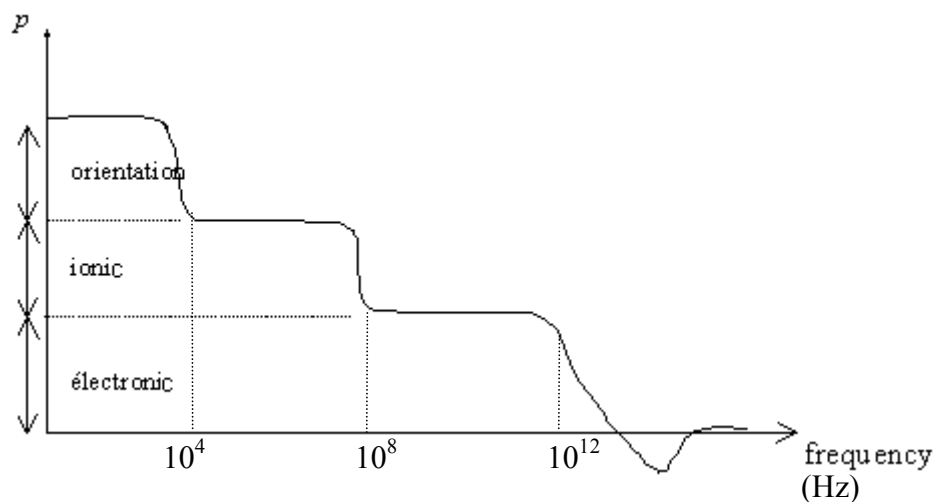


Figure 2.4: Graphic representation of the polarisability as a function of the driving frequency

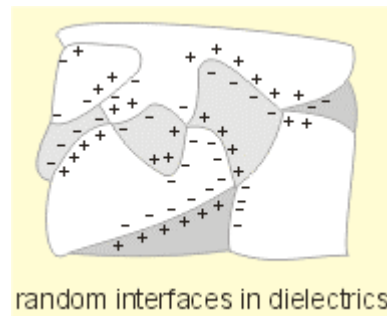


Figure 2.5: Schematic representation of interfaces discontinuity generating charges in a dielectric.

If a material contains polar molecules, they will generally be in random orientations when no electric field is applied. An applied electric field will polarize the material by orienting the dipole moments of polar molecules. This decreases the effective electric field between the plates and will increase the capacitance of the parallel plate structure. The dielectric must be a good electric insulator so as to minimize any DC leakage current through a capacitor, all these charge motion can be phase shifted with the driving voltage as explain in the previous section. The dissipation factor becomes then a measure of in-situ defects of the dielectric.

The polarisability of the dielectric varies directly with the composition of the dielectric. Some materials don't even need an external electric field to be polarized, they only need an application of a simple stress (piezoelectric material), or a variation of temperature (pyroelectric material), and some even are spontaneously polarized (ferroelectric material). The polarisability becomes one of the principal distinctions between different classes of dielectric (Figure 2.1).

This section explains the basic concept of polarisability valid for all dielectric material. As the pyroelectric effect is not used in this project, just the specific polarization of piezoelectric and ferroelectric materials will be presented, even if the composite presented here is also pyroelectric.

For a deeper understanding of these next sections, the reader will be redirected to a non-mathematical paper written by Damjanovic [1998] explaining properties of ferroelectric and piezoelectric material. However, this paper will have to be completed by the book written by Nye [1985] explaining the tensorial algebra used in the strongly recommended IEEE standard of piezoelectricity.

2.3 Piezoelectric materials

2.3.1 Piezoelectricity

The term piezoelectricity is used to describe the properties of this subclass of dielectric materials whose mechanical displacement fields are coupled to some degree to their internal electric fields. A stress applied to a piezoelectric material will result in a net polarisation of the

electric field within it. This is known as the *direct piezoelectric effect*. Similarly, an electric field applied to the material will result in internal stresses, thus deforming the material if its boundaries are free to move. This is known as the *converse piezoelectric effect*. The magnitude of the electric moment per unit volume, or the polarisation charge per unit area is given by Equation 2.23 and 2.26.

$$P_i = d_{ijk} \sigma_{jk} \quad (\text{Direct}) \quad \text{Equation 2.23}$$

$$S_{jk} = d_{ijk} E_i \quad (\text{Converse}) \quad \text{Equation 2.24}$$

$$\forall (i,j,k) \in \{1,2,3\}$$

Here, P_i is the polarization in the direction i , σ_{jk} is the material stress tensor in the direction jk : where k is the direction of the applied stress, this stress is localized on a plane perpendicular to the j direction (Figure 2.5). d_{ijk} is the piezoelectric tensor linking the polarization to the stress tensor, and the material strain tensor S_{jk} to the electric field E_i .

For a piezoelectric material, Equation 2.20 describing the polarization in the 3rd direction becomes Equation 2.25:

$$P_3 = \epsilon_0(\epsilon_{33} - 1)E_3 + d_{333}\sigma_{33} \Leftrightarrow P_3 = \epsilon_0(\epsilon_3 - 1)E_3 + d_{33}\sigma_3 \quad \text{Equation 2.25}$$

2.3.2 Notation simplifications of the formulation

In a single crystal, the base vector (1,2,3) is aligned along the crystal lattice vector (a, b, c). Thus, if we were interested in the component P_3 among the 3rd direction σ_{33} and d_{333} will be the stress and the fully subscripted piezoelectric coefficients. (only the stress tensor can be represented in Figure 2.6)

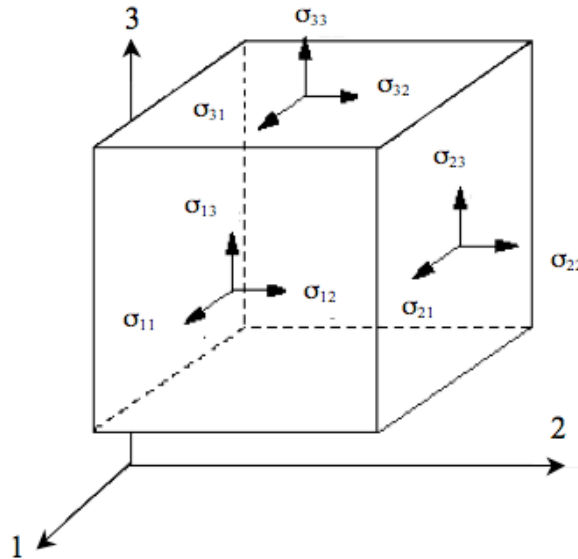


Figure 2.6: schematic representations of the subscripts definition for the stress matrices.

In the case of a ceramic, the crystal lattice is not aligned from one grain to another. In this description, the subscripts i , j and k conserve the same meaning, however, the based $(1,2,3)$ is directed by the 3-direction conventionally parallel to the axis of poling. Thus, the polarization vector throughout this thesis is always among the base vector $(0,0,3)$. Then d_{333} is no longer a piezoelectric coefficient of the PZT crystal, but is, instead, an average of all the d_{ijk} directed along this chosen 3rd direction of each PZT single crystal (grain) composing the ceramic. The 3rd direction of the crystal lattice is not aligned with the 3rd direction of each crystal. d_{333} should be noted as $d_{333,eff}$. The notation was simplified by removing the subscript, eff.

Another simplification of notation, used in crystallography, occurs to reduce the number of independent piezoelectric coefficients from a possible 27 and 9 respectively by the effects of crystal symmetry. This notation occurs to also reduce the number of coefficients of the stress and strain tensor from 9 to 6, and the number of coefficients of the stiffness and compliance tensor from 81 to 36. Any calculation involving these tensors is greatly simplified by this notation. For the piezoelectric d tensor the first index is retained and the remaining two indices are combined into a single index running from 1 to 6. The convention for matrix-notation is summarized in the following Table 2.1.

Table 2.1 Simplification of tensorial Subscripts based on the space triads $(1,2,3)$ (see Figure 2.6)

Tensor Notation	11	22	33	23, 32	31, 13	21, 12
Matrix Notation	1	2	3	4	5	6

Crystal symmetry reduces the number of independent material coefficients significantly. A crystallographic treatment of different crystal structures defines 8 types of crystal symmetries. The symmetry type of polarized polycrystalline ceramic materials such as zinc oxide or lead zirconate titanate ceramics, is associated with the crystallographic class $6mm$ of the hexagonal crystal system in regards to all those physical properties that describe dielectric, piezoelectric and elastic phenomena. These symmetries zero most of the d coefficients. A diagram illustrating the d_{ijk} parameters for with the crystallographic class $6mm$ of the hexagonal polarised crystal system is given in Figure 2.7. Further discussion is given in the IEEE Standard and Nye [1985].

$$\begin{vmatrix} 0 & 0 & 0 & 0 & d_{15} & 0 \\ 0 & 0 & 0 & d_{15} & 0 & 0 \\ d_{31} & d_{31} & d_{33} & 0 & 0 & 0 \end{vmatrix}$$

Figure 2.7 Simplification of d_{ijk} parameters for the crystallographic class $6mm$ of the hexagonal polarised crystal system.

Once again this is only true for single crystals. For ceramics such the PZT composite used in this work, the simplification is kept. However, because the polarisation direction doesn't fit the crystal axes the zero values should not be zero. (IEEE Standard).

2.3.3 Constitutive relations

The constitutive equations are the equations that govern the interaction between the mechanical and electrical fields for a piezoelectrically active material, the 2nd page of the IEEE standard summarises them. They describe how the mechanical stress tensor σ_{ij} (or strain tensor S_{ij}) and electric displacement vector D_i and the electric field vector E_j interact with each other.

In this section all the equations are considered in a linear case to simplify the notation. Piezoelectric materials have an asymmetric atomic lattice. When an electric field is applied to such materials, it changes their mechanical dimensions. It changes also their polarisation such that the change in P can be defined by equation 2.26: [Kino, 1987]

$$\Delta P = PS = eS \quad \text{Equation 2.26}$$

Where e is the piezoelectric stress constant, and S is the macroscopic strain in the material. If the displacement is the measure of the dipole, or charge movement in the piezoelectric

material, the total change in electric displacement, D , in the presence of dielectric field, can then be defined by Equation 2.27 [Kino, 1987].

$$D = \epsilon E + \Delta P = \epsilon E + eS \quad \text{Equation 2.27}$$

Equations 2.28 and 2.29 describe the displacement used for characterising the thickness mode. They describe the importance of this constant in the transducer application: the higher the piezoelectric coefficients, the higher the displacement D , and this will induce a higher polarisation for a defined electric field. The superscript indicates that the value of the associated constant is taken for a constant or null value of the superscript variable [Kino, 1987].

$$D_3 = \epsilon_{33}^S E_3 + e_{33} S_3 \quad \text{Equation 2.28}$$

The Displacement, D_3 can also be described as a function of piezoelectric modulus, d_{33} (Equation 2.29)

$$D_3 = \epsilon_{33}^\sigma E_3 + d_{33} \sigma_3 \quad \text{Equation 2.29}$$

Equation 2.29 shows how the displacement is actually the results of both an action of an electric field and the stress or the strain state of the material. This consistently improves the polarisation of a piezoelectric system.

Equations 2.30 and 2.31 describe the piezoelectric constant e_{ijk} and d_{ijk} for the thickness mode. e_{33} and d_{33} are dependent on each other among these equations [Moulson, 1990].

$$e_{33} = 2d_{31}c_{13}^E + d_{33}c_{33}^E \quad \text{Equation 2.30}$$

And d_{33} and e_{31} are dependent on each other. This is represented by the Equation 2.31 [Moulson, 1990]:

$$e_{31} = d_{31}(c_{11}^E + c_{12}^E) + d_{33}c_{33}^E \quad \text{Equation 2.31}$$

These two last equations demonstrate that the thickness mode of excitation is also influenced by the lateral piezoelectric constants d_{31} and e_{31} .

2.4 Ferroelectric material

2.4.1 ferroelectricity

The phenomenon of ferroelectricity was discovered in 1921 in single-crystal of Rochelle salt (sodium potassium tartrate tetrahydrate). It gave another differentiation of the dielectric material (Figure 2.8). During the second World War, the need to develop high dielectric constant capacitors led to the discovery of a new type of ceramic capacitor which barium titanate (BaTiO_3) was the precursor. The realm of ferroelectric ceramics was definitely consecrated with the last major finding: the spontaneous polarisation.

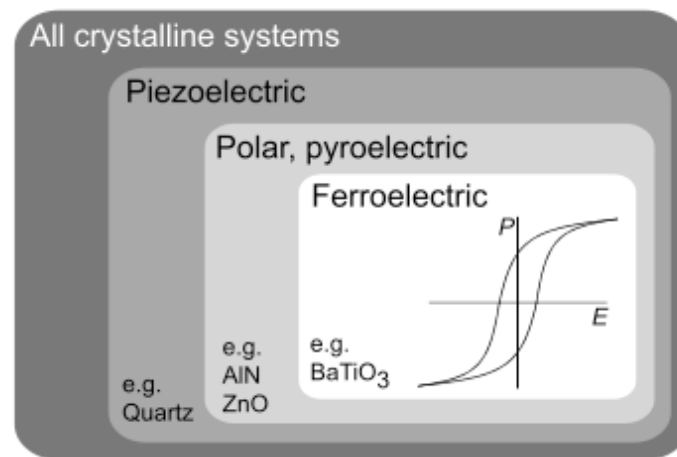


Figure 2.8: Displays a characteristic hysteresis loop occurring during the reversal of the polarization in a ferroelectric. [Bottger, 2005].

It is possible to reorient the spontaneous polarization of a ferroelectric material using an external electric field. The “switchability” by an external field defines, also, a ferroelectric material.

2.4.2 Spontaneous and remanent polarisation

Ferroelectric materials are polar materials. That means that even in the absence of an electric field, a spontaneous polarisation P_S is developed, due to electrical and mechanical boundary conditions. If the boundary conditions change, P_S can change direction:

Considering a single crystal of PZT $\text{Pb}_{1.05}[\text{Nb}_{0.015}\text{Sb}_{0.015}\text{Mn}_{0.015}(\text{Ti}_{0.481}\text{Zr}_{0.472})]\text{O}_3$, material, the high temperature paraelectric phase has a cubic structure, below the Curie temperature, T_C , the low temperature ferroelectric phases are tetragonal and rhombohedral structures. In the cubic system, there are six directions (including positive and negative orientations) along the three

unit cell axes, which are equivalent. The spontaneous polarization may arise with equal probability along any of them when the crystal is cooled through the ferroelectric phase transition temperature. The choice of one direction of spontaneous polarization, over another one, depends on the *in situ* electrical and mechanical boundary conditions imposed on the sample. These conditions generally result in the development of uniformly oriented spontaneous polarization in different regions of the crystal. These regions are called ferroelectric domains, and as the *in situ* conditions vary through a single crystal, it generally includes many domains (Figure 2.9).

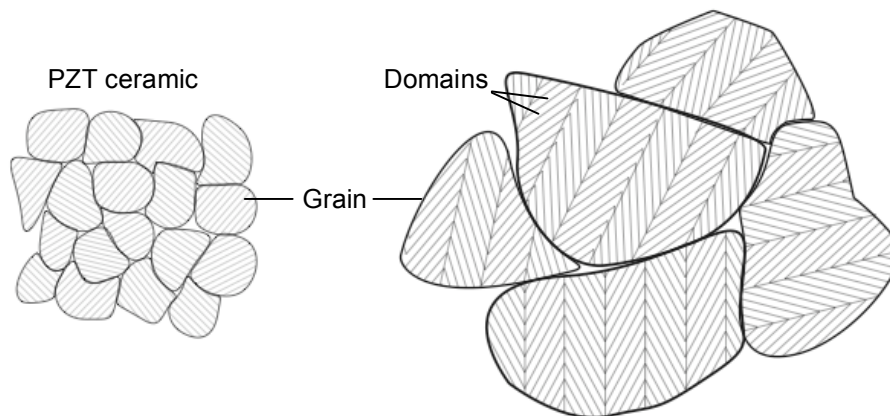


Figure 2.9: Schematic of domain pattern of fine-grained ferroelectric ceramic

When the crystal symmetry changes from cubic to tetragonal, during the transformation from the paraelectric to the tetragonal ferroelectric structure, the crystal lattice is stretched in three different ways among the three unit cell axes. Two are represented in Figure 2.10, the other one not represented, is perpendicular to the plan of the page. When, 2 consecutive domains are stretched in the same direction, their spontaneous polarization will be oppositely orientated. The separation between the two domains is called 180° walls (Figure 2.10.a). Those, which separate regions with mutually perpendicular polarization, are called 90° walls (Figure 2.10.b).

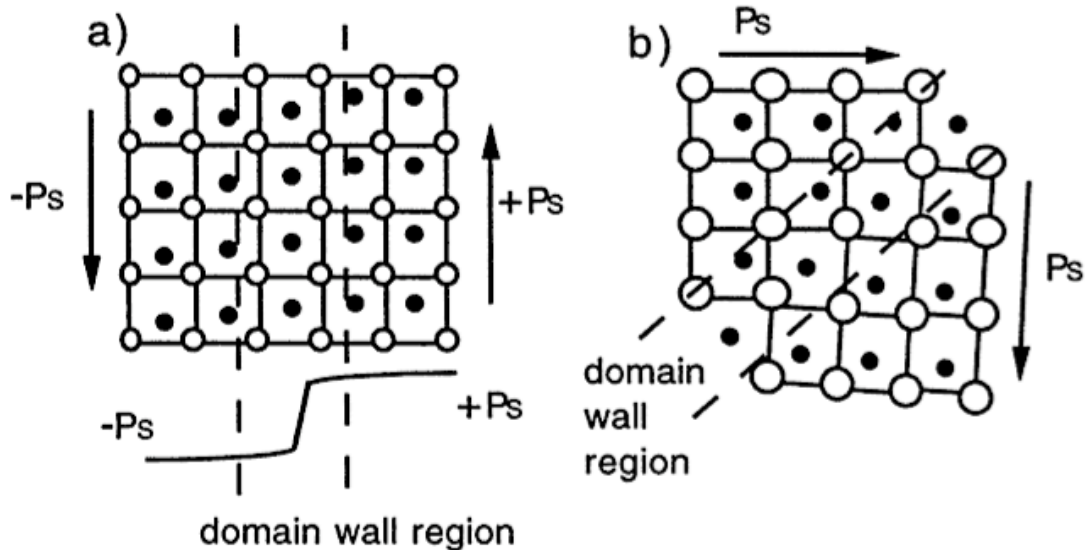


Figure 2.10: Schematic illustration of a) 180° and b) 90° ferroelectric domains and domain-wall regions in a tetragonal perovskite ferroelectric (as PZT) [Damjanovic, 1998].

The mechanical conditions, to which a crystal is subjected during the transition from para to ferroelectric, are generally very complex and lead to a complex domain structures with many 90° and 180° domain walls. Ferroelectric grains in ceramics are then, split into many domains, but also, each grain is randomly oriented and the boundary conditions between each grain are even more complex. This situation illustrates the random distribution of the spontaneous polarization directions, which leads to a case of zero net polarization such that the piezoelectric effects of individual domains will cancel each other (Figure 2.11-1). Such material, as is the PZT composite used in this project, will not exhibit a macroscopic piezoelectric behavior. However, it can be brought into a piezoelectric state by applying a strong electric field. Generally, this action is accompanied by an elevated temperature, which increases the atom mobility, and so, helps the domains to align their polarization directions. This process is called poling. Only domain polarisation can be reoriented in the applied electric field direction, but it is not possible to reorientate the polarisation of a whole grain. Once the ceramic is cooled down, the polarization remaining is called the remanant polarization, P_R (Figure 2.11-2) [Damjanovic, 1998].

At room temperature, PZT ceramics of Ti-rich compositions exhibit a tetragonal phase while the PZT system preferentially has a rhombohedral structure for Zr-rich compositions. These phases are separated by a morphotropic phase boundary (MPB). The presence of a new monoclinic ferroelectric phase close to the MPB has recently been reported [Akhilesh *et al.* 2005]. The phase diagram of PZT is presented in Figure 2.11.

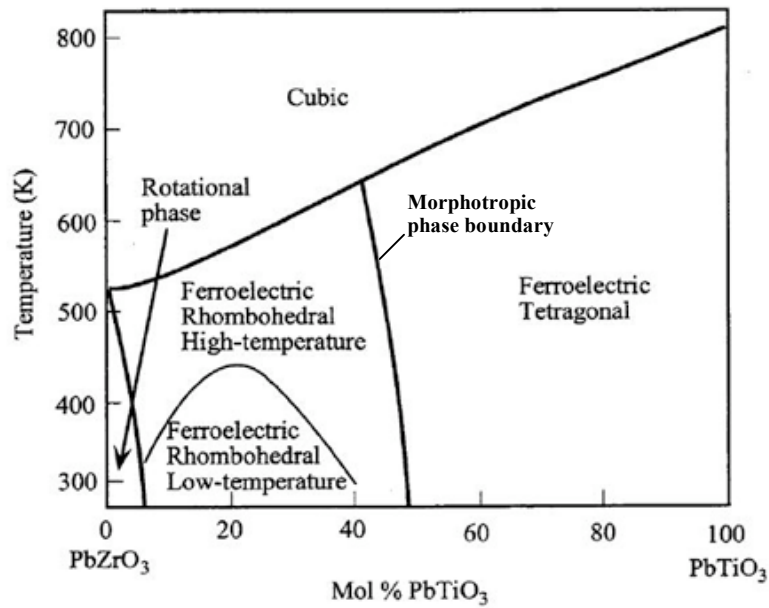


Figure 2.11 Phase diagram of PZT.

[<http://www.doitpoms.ac.uk/tlplib/piezoelectrics/pzt.php?printable=1>]

In the rhombohedral phase of lead zirconate titanate, the direction of the polarization develops along the body diagonals (direction (111)) of the paraelectric cubic unit cell. This gives eight possible directions of the spontaneous polarization with 180°, 71° and 109° domain walls.

Fousek [1971] states that the polarisability of a material, that can occur in a ferroelectric crystal, depends on the symmetry of both the non-ferroelectric and ferroelectric phases of the crystal. In order to summarise, polarisation can take place in 6 crystal directions in the tetragonal phase and 8 crystal directions in the rhombohedral phase. The composition of the PZT presented in this dissertation correspond to that at morphotropic phase boundary (MPB), which is a mix between the tetragonal and rhombohedral. 14 equivalent polarisable directions are then possible in this structural phase. A ceramic based on PZT grains crystallized with the MPB structure, will exhibit a greater ability to have their domains aligned in a given direction than for any other structure available for this system (Figure 2.13). For ceramic crystallised in the MPB structure, it is then easier to reverse (or switch) the polarization of a poled ceramic by applying an electric field oriented in a opposite direction.

2.4.3 Hysteresis loop

The polarization of ferroelectric material is generally modeled via the Rayleigh Equation 2.32 [Preisach, 1935] [Robert *et al.* 2001].

$$P = (\chi + pE_0)E \mp \frac{P}{2}(E_0^2 - E^2) \quad \text{Equation 2.32}$$

Morosov [2005] reviews the papers written Preisach [1935] and Sjöström [1999] which show that developing the Rayleigh Equation 2.31 into fourrier serie of the electric field yields to an equation illustrated by Figure 2.12. It describes the hysteresis loop relation between the polarization and an alternative electric field applied to a ferroelectric field:

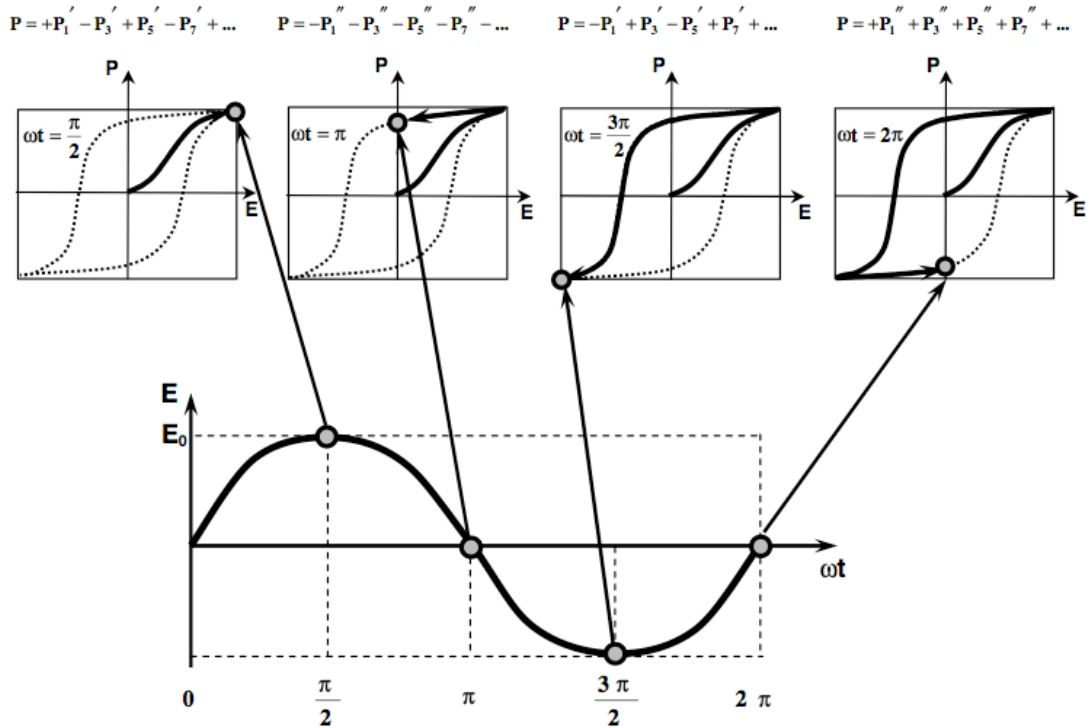
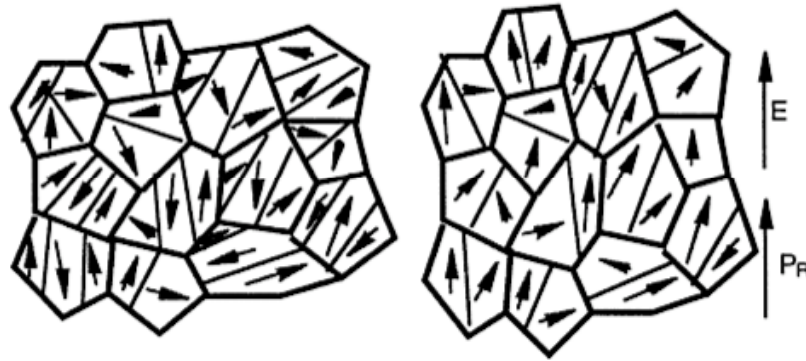


Figure 2.12 The relations between hysteresis geometry and complex amplitudes of P(E) dependence [Morosov, 2005].

The hysteresis loop starts for an unpoled curve at point A with a linear increase of the polarisation until point B in Figure 2.14. In this region Equation 2.19 is valid. Within this region, the domains are not reoriented along the field direction: the increasing electric field just increases the displacement. Domains favourable to a reorientation need a stronger field to switch orientation. This occurs between B and C where Equation 2.19 is no longer valid. Once all the difficult dipoles are switched, the polarisation response becomes linear again with an increase in electric field (between C and D in Figure 2.14). An extrapolation to zero field of this segment gives the value of the spontaneous polarisation P_S . P_S corresponds then to the polarisation maximum achievable by the ideal material without electric field. The remanent polarisation, P_R , is the actual polarisation found at zero electric field (Figure 2.13). For an ideal material, $P_R = P_S$.



1. Unpoled ferroelectric ceramic 2. After poling a ferroelectric ceramic

Figure 2.13: Schematic of the poling process in ferroelectric material, showing an unpoled ceramic with a zero net polarisation (1), and a poled ceramic with a net polarisation (2) [Damjanovic, 1998].

The electric field needs to be reversed to reach the value at the point F to make the polarisation returns to zero. This point is called the coercive field E_c . Moreover, when an electric field greater than E_c is applied, it leads to the reversal of the polarisation by domain switching. An ideal hysteresis loop is centred, and exhibits equal absolute values of $+P_R$ and $-P_R$. It should also exhibit equal absolute values of $+E_c$ and $-E_c$.

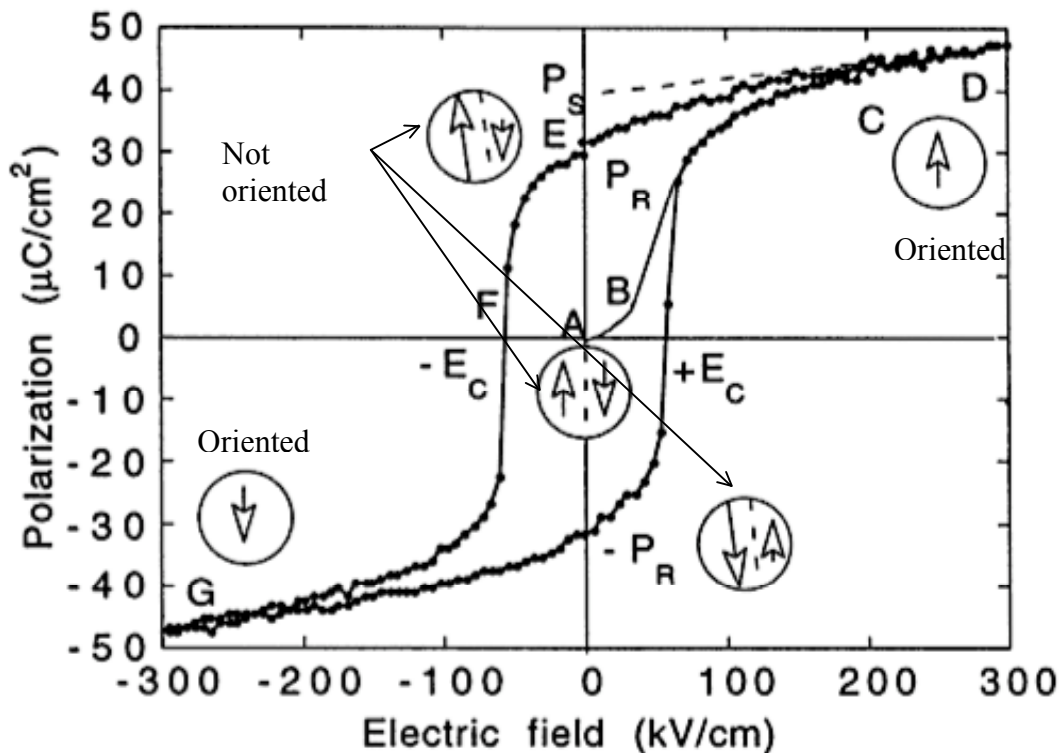


Figure 2.14: Illustration of the linear and the non linear relation between the polarisation of a ferroelectric ceramic and the applied electric field. This generates the hysteresis loop configuration illustrating the switch of domains [Damjanovic, 1998].

2.4.4 Precision on the polarisation of ferroelectric ceramics

In a ferroelectric material when 2 domains align their orientations, they really become 1 single domain. With this point of view, the motion of a domain wall that separates regions of different oriented polarization is the driving phenomenon of this domain polarization. In section 2.2.3, different influences of the total polarisability for a dielectric single crystal were listed. For a ferroelectric ceramic, this important influence of the domain wall motion, was added to this list [Bottger, 2005]. This domain motion is described by a constant called p_{dw} Domain wall polarisability. It plays a decisive role in ferroelectric materials and contributes to the overall dielectric response. It changes radically the understanding of the polarisability in the Rayleigh Equation.

The origins of the hysteresis are complex and can be intrinsic and extrinsic. Intrinsic properties are usually defined in literature as the properties of the crystal lattice of pure material. Extrinsic origins are related to non-lattice contributions, such as movements of defects, grain boundary effects, displacement of interfaces (such as domain walls) and interphase boundaries. In most of ferroelectric materials, especially in ceramics, the extrinsic properties play a major role. Of course, all these surfaces, boundaries, and interface effects are related to the interaction of all defects that can be included in the grain with the domain wall motion. A variety of mechanisms for domain pinning have been proposed, including pinning due to electronic charge trapping, [Brazier, 1999], pinning by oxygen vacancies, [Park *et al.* 1998] as well as pinning by extended defects [Domingos *et al.* 2002][Lee *et al.* 2002]. All these processes are very complex and are still subject to an intense discussion. The domain wall polarisation can either improve or screen the material polarisation by an accumulation of charges inside the material, creating a electric field opposite or not to the one applied.

For a ceramic, another important specification on the motion of domain wall localized closed or in a grain boundary, was revealed by Lee [2002]. It reveals that the motion of the domain walls was harder in these regions of the ceramic. Both the remanent and spontaneous polarization were strongly decreased with an increase of the length of the grain boundary. The main explanation resides in an increase of the concentration of defects (impurities, atomic vacancies and dislocations) in a grain boundary as well as the presence of a liquid phase (sintering aid), which stabilizes the formation of certain domain orientation, which are harder to switch.

For a deeper understanding, the reader will be redirected to the thesis ferroelectric material written by Morozov [2005], which focus on these issues.

Another interface is generally blamed for a decrease in the polarization: The interface between the electrode and the ferroelectric film is thought to also be a source of charges and defects.

2.4.5 Shottky-Bradeen barrier (depletion barrier) effect on the coercive field

Ironically, if the electrodes provide the electric field, the electrode-ferroelectric material interface screens this electric field: charges accumulate at this interface and create an electric field in the opposite direction. Without entering in an exhaustive quantum derivation, this section will introduce in a phenomenological way to examine this problem.

Perovskite structures can be considered as semiconductors with a low mobility of free charges. The problem is now associated to a metal – semiconductor contact (platinum-PZT composite).

First, Figure 2.15 illustrates the energy level situation of a metal such as the platinum, and, semi-conductor or insulating material such as PZT, then Figure 2.16 and Figure 2.17 will illustrate the contact metal-semiconductor.

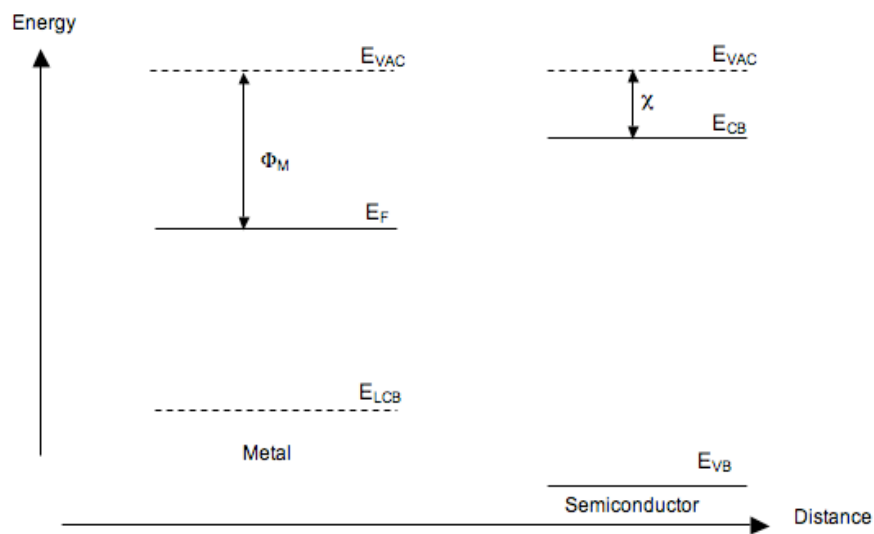


Figure 2.15: Representation of the energy levels of a metal and a semi-conductor

The Fermi level, E_F , of a metal is defined regarding the energy of vacuum E_{VAC} . Φ_M is the metallic potential between E_F and E_{VAC} . For a semiconductor, it is usual to refer to the electronic susceptibility χ to define the difference of the energy of the conduction band E_{CB} and E_{VAC} . In this schematic illustration of band energy, E_{LCB} is the lower levels of the metallic conduction band and E_{VB} is the valence band of the semiconductor.

In 1933, Schottky, proposed a simple model that no electronic transfer occurs at the interface (Figure 2.15): The electrode imposes its Fermi level at whole material, and the barrier potential Φ_B equal to $E_F - \chi$.

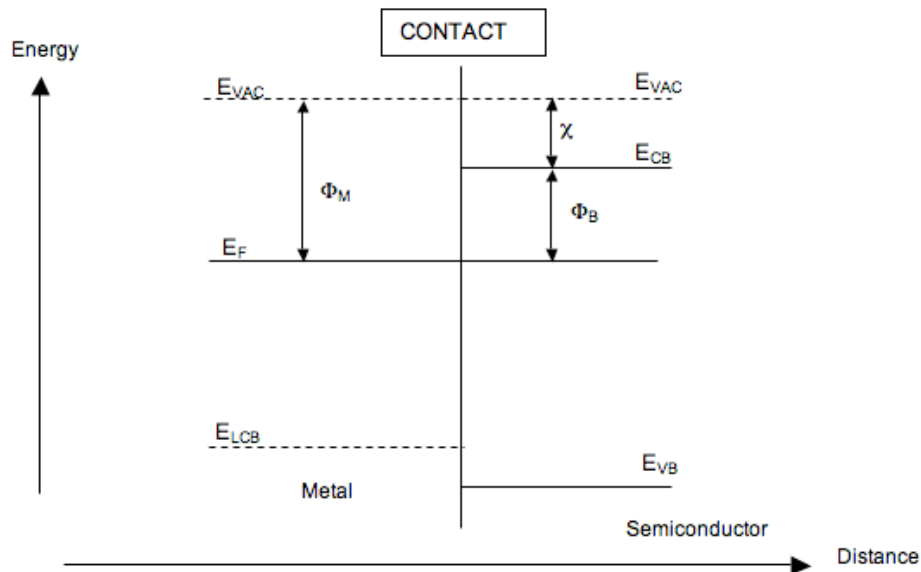


Figure 2.16: Schematic level interface metal semiconductor in the Schottky hypothesis.

Bradeen updated the Schottky model to explain how some charges are accumulated from the electrode to a distance W in the material. He proposed a model based on the existence of a mechanism of charge transfer between the metal and the semiconductor because of the existence of localised surface states on the semiconductor surface (E_{SS}) (or insulant) [Noguera, 1996]. Tagantsev [1996] adds that this role can also be played by state levels added by defects. A charge density will be created to screen this interface electric field. The metallic E_F forms a continuity level with E_{SS} . Φ_B in this Schottky-Bradeen model is just dependent of the semi-conductor: $\Phi_B = E_{CB} - E_{SS}$. It has to be noticed that the charge transfer, which is a necessity for the Fermi levels equalisation bends the metallic and semiconductor bands up to the distance W , where the free charges are accumulated (Figure 2.17).

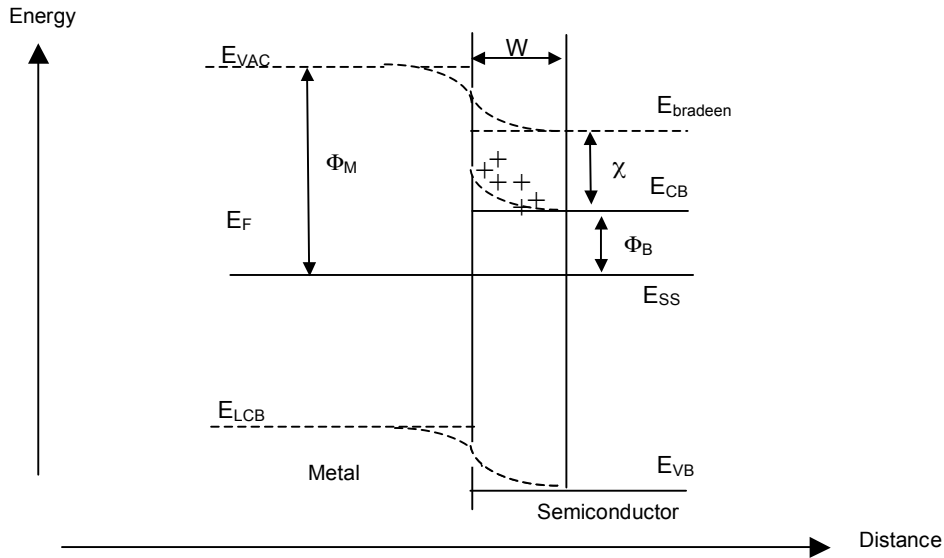


Figure 2.17: Schematic representation of states levels for the contact metal-semiconductor, hypothesis of Shottky-Bradeen.

Tagantsev [1996] and [2001] adds that in a ferroelectrics system, the built-in screening electric field is assisted by the nucleation of domain wall switching against the main applied electric field. He calls this effect “depletion-assisted nucleation of domain walls”. Considering the bottom and top electrode, when the thickness l of the film is smaller than $2W$ (generally below $<1\mu\text{m}$), the screening electric field $E_{\text{screening}}$, is defined by Equation 2.33 [Damjanovic, 1998].

$$E_{\text{screening}} = \frac{eNl}{2\epsilon} \quad \text{Equation 2.33}$$

When the thickness l of the film is larger than the double of W which is the case here ($l=8\mu\text{m}$), the screening field electric field, is defined by Equation 2.34 [Damjanovic, 1998].

$$E_{\text{screening}} = \frac{eNW}{\epsilon} \quad \text{Equation 2.34}$$

Defects increase the mobility of free charges as well as their concentration N , and ceramic thick film include a certain number of different kinds of interfaces. Then, a high screening electric field should be expected, and should be constant when the thickness of the film is above $1\mu\text{m}$.

Mobility of domain wall, dipole orientation, atomic mobility, defects, are generally influenced by the stress states of the film. Actually, the whole mechanical and electrical behaviour of the

film might be influenced by states of compression, or tension of the *in-situ* film presented in next section.

2.5. Stress and strain

The work of Nye [1985] on physical properties of crystals is recommended for a precise mathematical development of the stress.

2.5.1 Introduction

This section on stress mirrors Chapter 5. The state of stress of a film plays a major role in piezoelectric theory (Equation 2.21). It also influences the domain orientation and so the polarization. Then, understanding the *in-situ* stress state of a film seems of a great importance to improve both its piezoelectric and the ferroelectric properties: Tilt of hysteresis loop observed in Chapter 6 between films subjects to compressive and tensile stress. The cracking behaviour controlled by the *in-situ* film stress influences strongly the choice of fabrication techniques used for the PZT thick film presented in this work (Chapters 4 and 5).

There are a number of methods to characterize the residual stress in thin or thick films, such as X-ray diffraction [Fujito *et al.* 2002][Zheng *et al.* 2004], optical interferometry and elipsometry [Ong, 2001] [Padmini *et al.* 2000], and the most used method the curvature measurements [Stoney, 1909] [Ong *et al.* 2005]. Among all these methods for determining stress, the curvature-based techniques are gaining increasingly widespread use because of its experimental simplicity. The work of Stoney was a great support to find the *in-situ* forces, and is described in this section.

2.5.2 Stoney's Equation

A deep understanding of Stoney's Equation will help to evaluate if the equation provides an absolute measure of the *in-situ* stress induced by a thick-film on a rigid substrate, or, if the Stoney equation is just a tool for comparison. The thermo-mechanical mismatched properties between a film and the substrate generates a compressive or tensile curvature of the film/substrate system. However, Stoney simplify the situation by only considering the mechanical behaviour of a stressed film on a rigid substrate (Figure 2.18). The first approximation made by Stoney was then to avoid any thermal argument. He assumed that the wafer curvature was measured before and after the fabrication of the film at the same temperature.

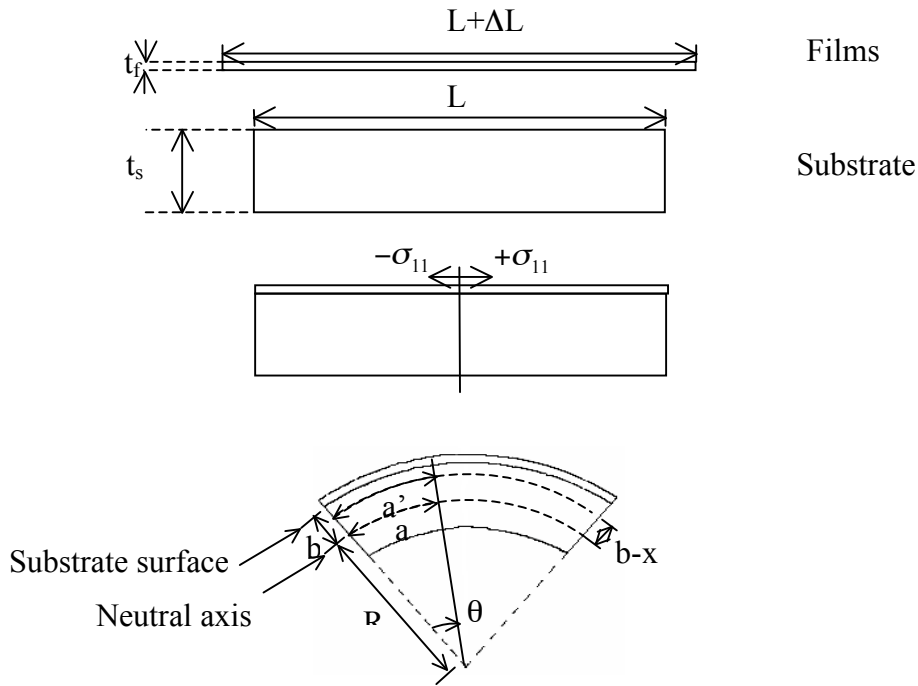


Figure 2.18: Illustration of the curvature of a substrate due to a stressed film deposited on it. A compressed film deposited on rigid substrate will apply forces in the radial direction oriented toward the edge of the substrate. The substrate tries to release that added stress and bend. A tensile film will have the opposite effect, *i.e.* the curvature of the substrate will have been negative.

The tensor σ_{11} induces a relative deformation of the film, in one specific direction, such as, $S_{11} = \frac{\Delta L}{L}$. When the deformation occurs in the elastic domain, the following Hooke's equation describes this phenomenon (Equation 2.35).

$$\sigma_{11} = \frac{F_1}{A_1} = Y \frac{\Delta L}{L} \quad \text{Equation 2.35}$$

Where Y is the Young's modulus, L the length of the considered object, and ΔL its elongation.

The amount of bending combined with the thickness of the film, enables the stress to be evaluated. For a substrate of thickness l_s and width w , curved by a thick film of thickness l_f , results in a radius of curvature R. By considering the thickness of the substrate to be small in comparison with R, the moment M of shear forces applied to the area, A , of the system, can be defined by Equation 2.36.

$$M = \text{Force} \times \text{distance} = \sigma_{11}Ax = \left[wY \left(\frac{b-x}{R} \right) \right] x \quad \text{Equation 2.36}$$

Where b is the depth from the surface of the substrate to the neutral axis of the moments. To find b , Stoney summed the moment applied on the substrate thickness:

$$\int_{l_s}^0 Y \left(\frac{b-x}{R} \right) x dx = 0 \quad \text{Equation 2.37}$$

The sample width, w , has been chosen equal to 1, in order to simplify the derivation. The neutral axis has then been localized at two thirds of l_s , such that $b = (2/3)l_s$.

σ is the stress of section on the PZT film of area $A_1 = wl_f$. Resolving horizontally the force transferred to the substrate by the film can be defined by Equation 2.38.

$$F_1 = \sigma_{11}A_1 = \int_{l_s}^0 Y \left(\frac{b-x}{R} \right) w dx \quad \text{Equation 2.38}$$

Once solved Equation 2.38 becomes Equation 2.39:

$$\sigma_{11}wl_f = Y \left(\frac{bl_s - \frac{l_s^2}{2}}{R} \right) w \quad \text{Equation 2.39}$$

And knowing that $b = (2/3)l_s$, Equation 2.39 becomes the Stoney Equation 2.40:

$$\sigma_{11} = \frac{Y}{6R} \left(\frac{l_s^2}{l_s} \right) \quad \text{Equation 2.40}$$

2.5.3 Improvement of Stoney's equation

Generally, when an anisotropic medium is subjected to a stress σ_{kl} its deformation S_{ij} in the elastic domain follows the generalized Hooke's law:

$$S_{ij} = s_{ijkl} \sigma_{kl} \quad \text{Equation 2.41}$$

Or

$$\sigma_{kl} = c_{kl ij} S_{ij} \quad \text{Equation 2.42}$$

Where s_{ijkl} (compliance) and c_{klij} (stiffness) are 4th rank tensors. By definition for any cubic system, the Young's modulus can be define by Equation 2.43 and 2.44 (the whole derivation can be found in [Nye, 1955]).

$$s_{ii} = \frac{1}{c_{ii}} = \frac{1}{Y} \quad \forall i = 1,2,3 \quad \text{Equation 2.43}$$

And

$$s_{12} = \frac{1}{c_{12}} = \frac{1}{Y} \quad \text{Equation 2.44}$$

Throughout his paper, Stoney never mentioned anything about the connection between the stress and the beam width. In isotropic cubic medium, the lateral deformation is governed by a coefficient of Poisson (ν). For a plate-like structure the width w becomes large in equation 2.40. In that case, Timoshenko [1925] replaced the Young's modulus with a biaxial young Y' represented by Equation 2.45.

$$s_{ii} + s_{i2} = \frac{1-\nu}{Y} = \frac{1}{Y'} \quad \forall i = 1,2,3 \quad \text{Equation 2.45}$$

the Stoney's equation become then equation 2.46.

$$\sigma_{11} = \frac{1}{6R} \frac{Y}{(1-\nu)} \frac{l_s^2}{l_f} \quad \text{Equation 2.46}$$

This equation can correspond to the cap or bowl like deformation of a circular substrate under the influence of intrinsic film stress. Since many solid materials have Poisson's ratios between 0.2 and 0.3, using the biaxial modulus instead of Y yields a modification in the calculated stress values by 25% to 43%. However, the meaning of this percentage has to be taken carefully. Many important assumptions, which can also have strong influence on the calculated stress, have been made by Stoney when he developed his equation:

- Only the mechanical behaviour of the substrate is considered. This could be a major drawback if the film is piezoelectric.
- No thermal consideration.
- Substrate is considered to be infinite, and isotropic.
- Just the radial stress is considered.

Stoney Equation is not the only way to calculate the stress from the radius of curvature. Without entering in this discussion, Weinberg [1999] developed an equation, which takes into account the mechanical behaviour of both the film and of the substrate.

$$\sigma_i = Y_i \left(\frac{b-x}{R} - d_{31i} Y_i - \alpha_i \Delta T \right) \quad \text{Equation 2.49}$$

Where i is the index denoting the films, d_{31i} is the piezoelectric coefficient of the film i , α_i is the thermal expansion coefficient of the film i , and ΔT is the temperature variation from nominal. The extension Weinberg [1999] seems more precise than Stoney. However the material properties of each layer have to be well known. An inaccurate piezoelectric and expansion coefficient has a strong influence on the calculated stress value.

As the composite PZT material piezoelectric and expansion coefficients are not known, the use of the Stoney equation has been chosen. Because of all the assumptions made by Stoney, the stress calculation through the wafer curvature was chosen to be a comparison tool, and not a tool to calculate the exact stress applied at the interface between the film and the substrate.

2.6 Ultrasonic piezoelectric thickness mode transducer: fabrication

2.6.1 Introduction to the ceramic fabrication

This project is about the fabrication of an annular array. The fabrication of this tm-pMUT transducer design is one of the challenges faced. High frequency annular array research started at the beginning of the millennium [Snook 2001], [Brown *et al.* 2004], [Brown *et al.* 2005], [Hu *et al.* 2006], [Snook *et al.* 2006], [Gottlieb *et al.* 2006], [Pan *et al.* 2006]. These papers are from just two different groups. As the technology is new, there is always challenge to stand, also the contribution of this work to this research will be to present different fabrication processes possibly leading to patterned annular arrays. The final product presented in this work presented similar performances. This fabrication processes can allow the fabrication of a single element multilayer system with embedded electrodes working at high frequency (Chapter 9).

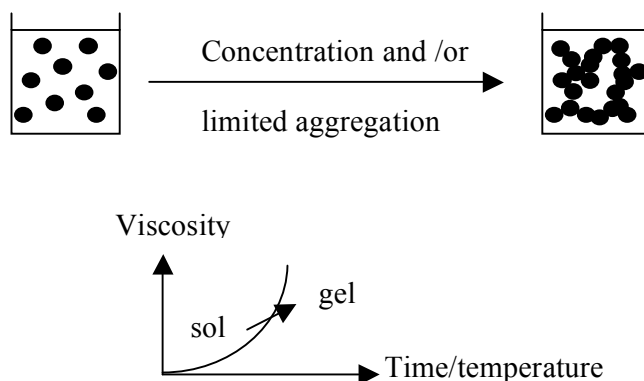
The fabrication of ferroelectric polycrystalline ceramics involves two fabrication steps: the preparation of the ceramic green body and the sintering of the ceramic body. Many procedures are suitable to fabricate such ceramics, ranging from pure physical techniques, such as the ablation technique, to pure chemical routes, such as the sol-gel technique. The most common techniques are the powder routes.

Grain uniformity, in size distribution and composition, is the key factor controlled to realise reproducibility of ceramic characteristics. The sol-gel technique produces good grain uniformity and gives a reproducibility of the piezoelectric characteristics. Also, other methods (e.g. ablation and calcination of a powder) involve solid-state reactions and/or mechanical mixing, and are inevitably accompanied by a compositional fluctuation among the ceramic particles. This technology of sol gel gives also the possibility to achieve the crystallisation at

low temperature ($\sim 500^\circ\text{C}$) [Sakka *et al.* 1999]. However, powder based technologies have the potential to make thicker films. A trade off between the two technologies, such as a composite of PZT powder/PZT sol gel seems to be an ideal candidate for the development of 20-40 μm thick films [Corker *et al.* 2002][Pan *et al.* 2006].

2.6.2 Sol-gel method and sintering process

For a deeper understanding of the sol-gel chemistry, the work of Livage [1992] called “sol gel chemistry” is recommended. It explains that through chains of hydrolysis and condensation reactions, a stable suspension of colloidal particles is transformed into a stable highly-branched macromolecule network, a gel (Figure 2.19). This gel, depending on the sol composition, can be crystallised by heat



treatment.

Sol: stable suspension of a colloidal particles (1 to 1000 nm)

Gel: stable network of particles or highly branched macromolecule, with solvent trapped inside.

Figure 2.19: illustration of the sol-gel basic principle

The sol-gel synthesis can be conducted by non-aqueous or aqueous processes. Both lead to a gel. The route used in this project is strongly involved with metal alkoxides like titanium (IV) isopropoxide and zirconium (IV) propoxide, which react strongly with water. Therefore, the non aqueous route will be described.

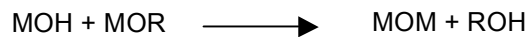
The general sol-gel process is composed of the two mechanisms of hydrolysis and condensation:

The alkoxide hydrolysis :

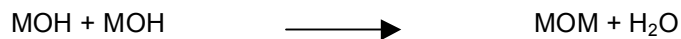


Condensation:

Alkoxilation (removal of H as an alcohol):



Oxolation (removal of H as water):



When the metal alkoxides $M(OR)_x$ (M: metal atom, R: alkyl) are mixed in alcohol in appropriate proportion, and water is added, the hydrolysis reaction produces alcohol and the metal hydrate. High purity can be sustained during the hydrolytic reaction because no other ion doping is necessary [Whatmore *et al.* 2003].

In the case of PZT preparation, Pb alkoxides are relatively difficult to obtain compared to Ti and Zr alkoxides. Thus a more convenient way is to use a two stage method: $(Zr,Ti)O_2$ is first prepared by the alkoxide method stabilised by the nucleophilic character of a 2-methoxyethanol solvent, which avoids all kind of precipitation. Then $Pb(OAc)_2$ is added in order to be used in the solid state reaction: a trans-esterification reaction. If one of the metal alkoxides is used for the PZT routes, the $Ti(OPr^i)$ stays in a monomeric state. A possible reaction could be (between lead acetate and titanium isopropoxide):



Such a reaction can be coupled with the zirconium propoxide to lead to the PZT gel. However this process generates a second phase (pyrochlore) in addition to the perovskite one. To suppress this second phase several mol percentage of Pb in excess is added [Schwarz and Cross 1984], [Schwarz *et al.* 1991], [Huang *et al.* 2004].

A partial sol-gel method combined with PZT micro sized powder will be useful for thick film deposition; this is sometimes called the slurry method [Dorey *et al.* 2002]. This method leads to a composite PZT powder/sol-gel.

After being shaped as desired, the "gel" or the "slurry gel" (if powder is added) is fired at high temperature without reaching the melting temperature. The atoms' diffusion in the gel and/or in the

powder will occur to minimise the surface energy, which promotes crystal bonding at the interface between the two adjacent particles. In the case of a gel, the substrate, generally a Si/SiO₂/Pt wafer, will be the seed inducing the crystallisation. In the case of the slurry, each nanosize PZT grain will act as a nucleation site. This firing process is called sintering. This term is generally used for ceramics processed from the calcination of a crystal powder.

The ceramic density can be increased by adding a little amount of Cu₂O-PbO as well as by repeating sol infiltration filling the porosity during the fabrication process. Cu₂O-PbO is a sintering aid because it forms a low temperature liquid phase during the sintering process, which accelerates the atoms' diffusion [Dorey *et al.* 2002], [Torah *et al.* 2004].

2.6.3 Coating

2.6.3.1 Introduction to the sol-gel technique: manufacturing routes

The PZT slurries were developed originally for tape casting and screen-printing for thick film application [Fernandez *et al.* 1995], [Hrovat *et al.* 2006]. The slurry adapted to the spin coating technology is a more recent development. This kind of slurry is less viscous and generally based on a 2ME solvent for its low evaporation rate, and its stabilisation effect on the sol. [Lukac *et al.* 2000], [Dorey *et al.* 2002].

Three deposition techniques are presented through this section. Two are briefly presented, the screen-printing and the tape casting technique. The third one, the spin coating technique, is the one used in this project. Thus, it will be more deeply presented.

However, many more techniques are available to shape the final desirable body of the gel, or the ceramic. Some are presented in the figure 2.20.

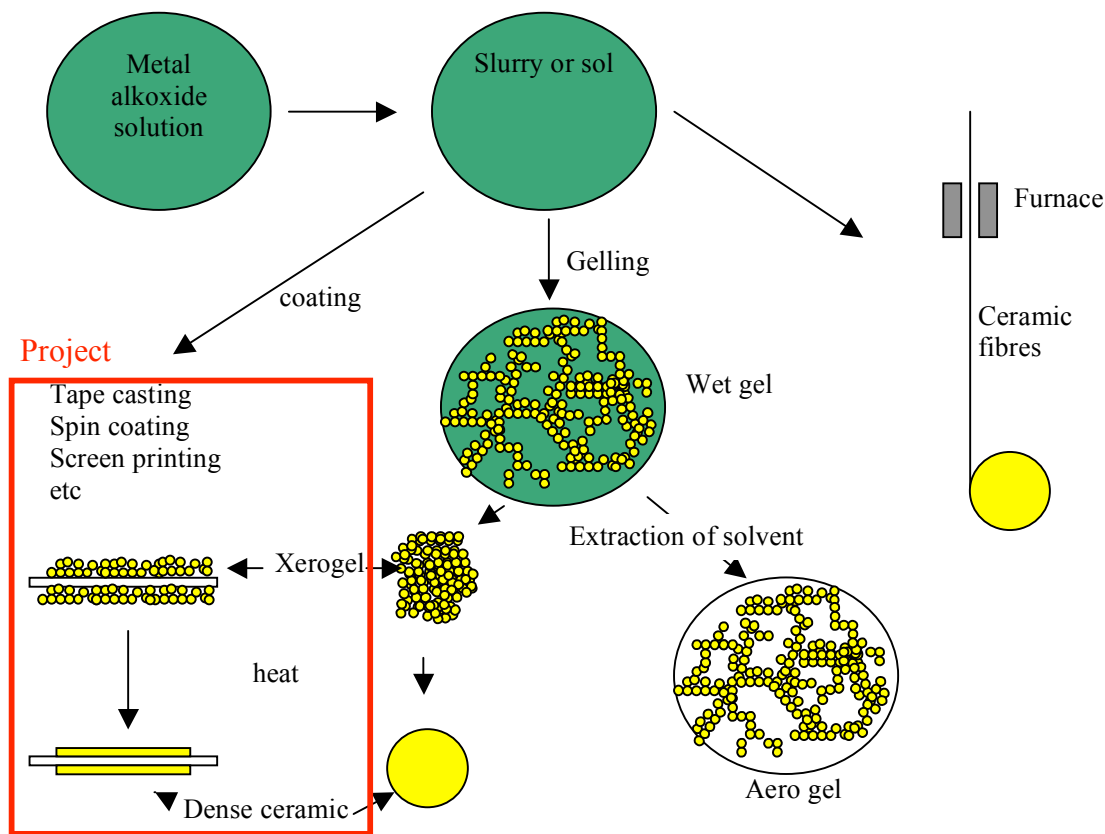


Figure 2.20: Illustration of the different uses, and products of sol gel technologies: from the simple application of an aero-gel to the complex creation of dense ceramic film and fibres.

The main aim of this section is to review the thicknesses achievable by each technique. With the spin coating technology, used in this project, it has been possible to achieve a thickness of 1.5-2 μm per composite layer. This thickness is not ideal for the fabrication of 25-50 μm PZT thick films without embedded electrodes due to the large number of layers required. This required range of thicknesses is more adapted for tape or screen-printing (see next 2 sections). These technologies, as well as the spin-coating technique, produce green ceramics which can be more easily patterned than bulk ceramics. However, a stack of spin coated layers gives flexibility toward the thickness, for more than two layers. Having a large thickness flexibility is crucial for the future development of a multilayer transducer with embedded electrodes. The advantage of stacks of thinner layers gives also the possibility to control the density of the material at different points through the film.

2.6.3.2 Screen-printing

Screen-printing technology is used in the electronics industry for the production of robust and cheap devices. It constitutes one of several thick film deposition techniques used for selective coating of flat surfaces, for example coatings like platinum paste or slurry. It was the first route to be developed for

the fabrication of thick films and it is still widely used. The thickness range easily achievable is from 10 to 100 microns but the typical thickness size is around 20-40 microns [Madou, 2002], [Duval *et al.* 2003], [Hrovat *et al.* 2006]. For thicker films bulk techniques are generally used [Lethiecq *et al.* 2004]. A paste made of the material of interest, for example made of PZT powder and a water based mixture, is pressed on a substrate (silicon wafer) through openings in a stainless steel screen (Figure 2.21). The printed pattern is formed on the substrate. After deposition, the thick film is dried and fired. With this technique the main drawback is the incompatibility of the silicon substrate with the high sintering temperature, around 1200 °C. Alumina, and MgO substrates are generally used. Screen printing is now widely used for patterning electrodes, and/or capacitive ceramics such as PZT, or the making of single or multilayer ceramics [Cannel *et al.* 1990].

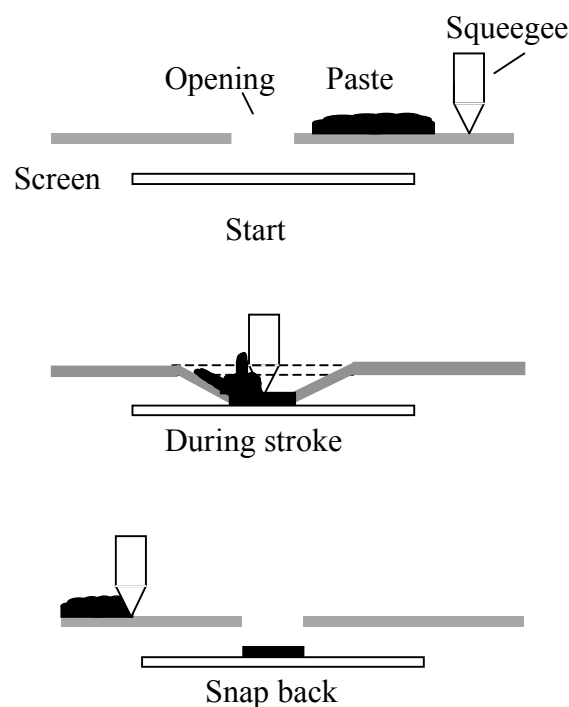


Figure 2.21: Schematic steps of the screen printing process

The thick film is directly patterned onto the wafer, thus avoiding an etching step. This point is the real advantage of this technique. A good introduction to PZT thick film deposition, using this technique for medical imaging application, is given by Kosec [2001].

In this project, the thickness of one PZT film layer must be around 1-2 μ m. In order to develop an imaginative future of the 50MHz transducer techniques, a flexible enough thickness is required to achieve a multilayer structure with embedded electrodes without being limited by the thickness of one layer. The screen-printing technique can achieve 10-30 μ m per thick film layer, requiring just one or two layers for a transducer working at high frequency. This technology can then be an alternative to the spin coating presented hereafter, but has a low possibility to evolve thickness wise. Also,

multilayer actuators are now being reported in the literature for lower frequency <5MHz [Harris *et al.* 2006], [Park *et al.* 2006], [Kwon *et al.* 2006].

The main drawback of the screen-printing technique is its dependence on the grid thickness, as well as the aperture size. The porosity of the screen-printed films is generally above 10-15%, typical example of the state of the art for this technology are the papers by Kwon and Park referred above.

2.6.3.3 Tape casting

Doctor blade technology, or tape casting, is a continuous mechanical fabrication method for producing green ceramic (before sintering) tapes on a moving substrate. A wide choice of substrates can be used for this technique, from steel to glass. A schematic of the tape casting method is represented in Figure 2.22.

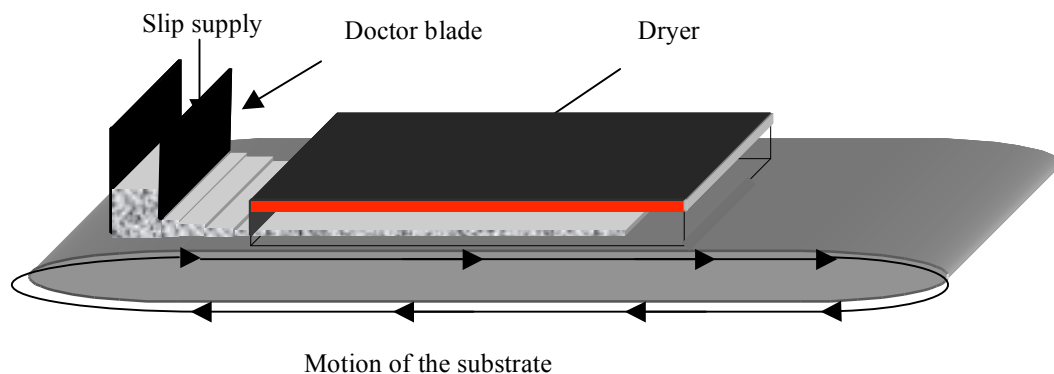


Figure 2.22: Illustration of the tape casting technology.

The ceramic slurry is continuously dispensed onto the moving substrates. The desired thickness is controlled by the *doctor blade*, an horizontal panel which creates a space to let the slurry lay down onto the substrate. This gap between the doctor blade and the substrate is limited by the doctor blade precision. Once dried, the green ceramic is sintered. A tape of ceramic is thus obtained.

This process is well suited for the fabrication of mesoscale devices (layers with a thickness between several 10's microns and millimetres). The viscosity of the slurry should range between 100 and 130 poises (10^{-3}Ns/m^2). Nowadays, regarding the PZT thick film technology, the standard thicknesses are reported to be between 10 μm and several millimetres [Srinivasan *et al.* 2007]. This technique is well known for the fabrication of single or multilayer capacitor fabrication [Schwarzer *et al.* 1999]. This technology presents a possible application for high frequency medical imaging applications, as it is easy to use for films thicker than 10's of micrometers. The drawbacks of this technique are similar to those of the screen-printing technology.

The tape casting method is often coupled with the screen-printing method for the electrode deposition. This mix of techniques is usual for structures such as multilayer transducer and capacitor. Generally, the technique termed cut and bond is used to bind the electrodes (Figures 2.23 and 2.24) [Cannel, 1990, chap 4] [Moulson *et al.*, 2003, p265].

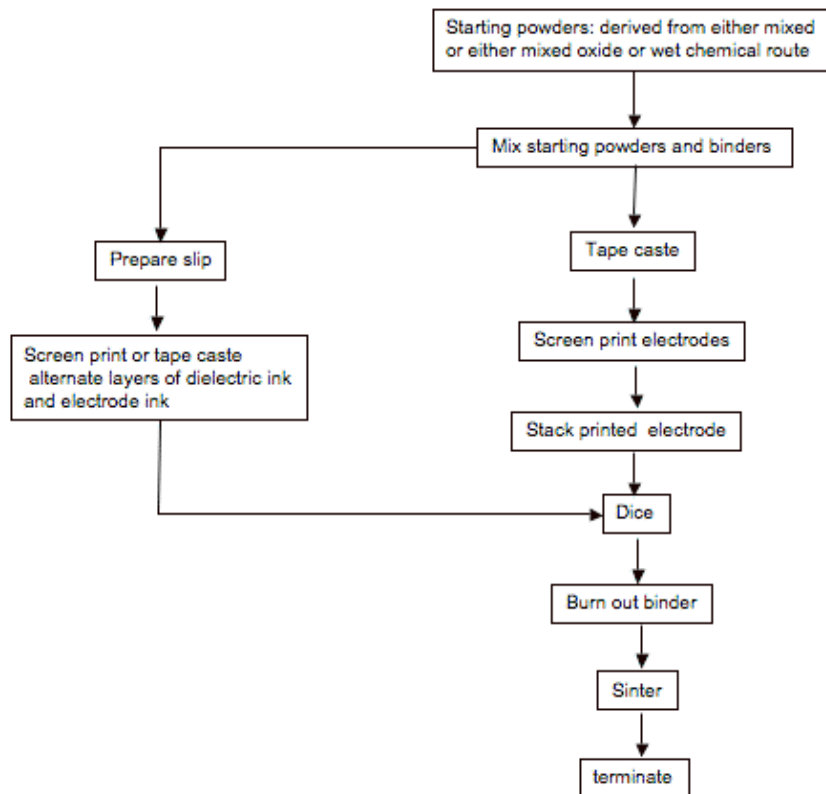


Figure 2.23: Outline of the fabrication process for the multilayer ceramic capacitor (This schematic is adapted from [Moulson *et al.* 2003]).

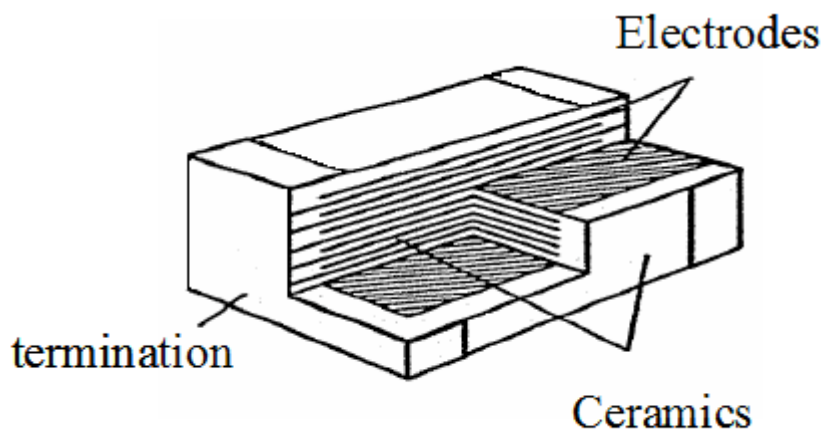


Figure 2.24: Schematic of a multilayer ceramic capacitor construction [Cannell *et al.* 1990].

For 50MHz multilayer transducers in water application, this technology (like the screen printed films) is limited by the inability to incorporate more than one embedded electrode, as the single film thickness is around 15-25 micrometers thick. Lilliehorn [2004] fabricated an example of such a high frequency transducer working at 14MHz, a lower frequency than the transducers presented in this work. This fabrication technique can be applied to a 2D array of individually addressable multilayer elements working at high frequency (Figure 2.25) [Lilliehorn 2004].

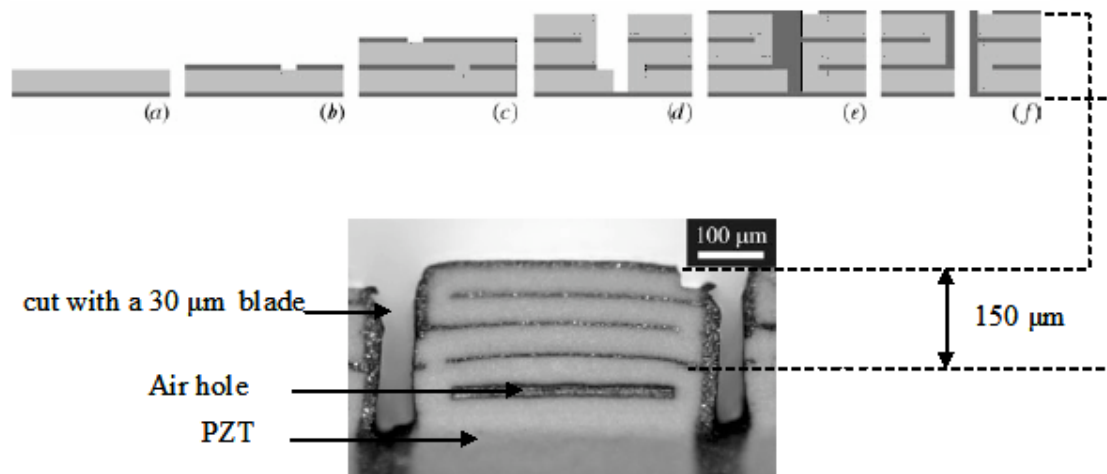


Figure 2.25: Construction and cross section of a multilayer transducer (green stage). [Lilliehorn *et al.* 2004]

A void (air hole) is integrated behind each element to work as an acoustic reflector, with the help of a sacrificial material. The limitation in this work is the thickness per layer. The tape casting seems to give, in this case, a minimum thickness of 50 μm , which limits considerably the range of resonant frequencies achievable. Another limitation in this work is the electrode thickness ($\sim 9\mu\text{m}$); the thinner the electrodes, the lesser their influences on the vibration (from the mechanical and acoustic energy loss point of view) [Harris *et al.* 2006].

2.6.3.4 Spin coating

Spin coating is a complex technique for the film deposition. Many variables need to be controlled to achieve a good surface and thickness uniformity. Figure 2.26 is an illustration of the 4 stages occurring during the spin coating of a layer of a liquid on a substrate.

Stage 1 is one of the critical ones. The centre of the wafer has to coincide with the centre of the chuck. On most spin coaters on the market, this action is done manually. Stage 2: the liquid surface should be perfectly uniform before spinning, as should be the liquid thickness on the substrate. Stages 1 and 2 are important for the film surface finish. The material constituting of the liquid surface is the same as the one constituting the film surface. The film's thickness is controlled principally when

the chuck is spinning at a constant rate (stages 3 and 4). In the ideal case these stages are governed by the following equations. When the centrifugal and viscous forces are in balance, Equation 2.50 must be satisfied.

$$\eta_l \frac{\partial^2 v_l}{\partial z_c^2} = \rho_l \omega_s^2 r_c \quad \text{Equation 2.50}$$

Where z_c and r_c are the cylindrical coordinates system aligned with the axis of substrate rotation, v_l is the fluid velocity in the radial direction, ρ_l is the fluid density, ω_s is the angular velocity (in radians), η_l is the viscosity in poise.

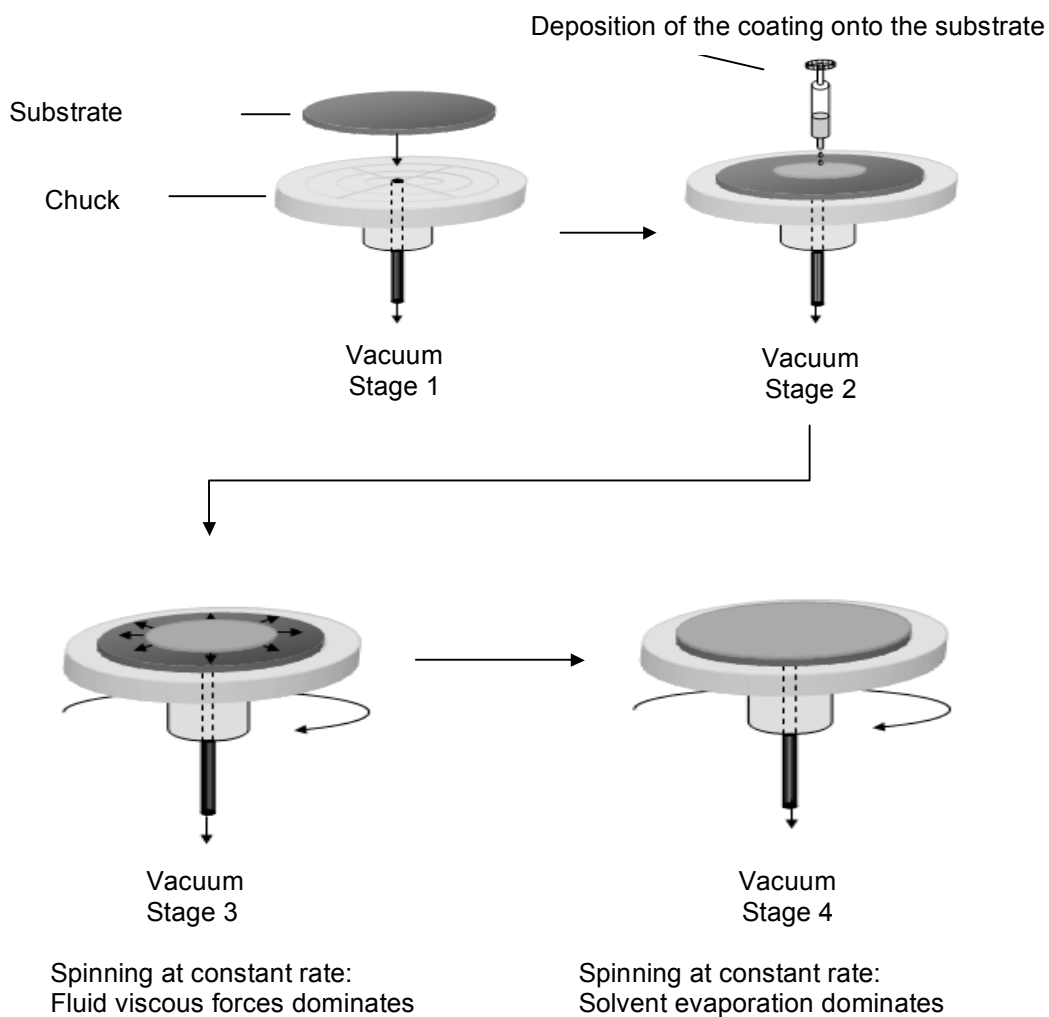


Figure 2.26: The four distinct stages to the spin coating process: Stage 1: substrate deposition on the chuck. Stage 2: deposition of the fluid onto the wafer. Stage 3: spinning at constant rate. Stage 4: solvent evaporation during spinning.

Equations 2.51 and 2.52 describe the spin-coating process during the 3rd stage (ideally, without evaporation of the solvent). Considering appropriate conditions of flow, velocity, and an initially uniform film, the thickness as a function of time can be described by these equations.

$$h = \frac{h_0}{\sqrt{1 + 4Kh_0^2 t}} \quad \text{Equation 2.51}$$

$$K = \frac{\omega_s^2 \rho_l}{3\eta_l} \quad \text{Equation 2.52}$$

Where h_0 is the initial film thickness, before spinning (liquid thickness on the substrate), and t is the spinning time.

In the case of spin coating layers of sol-gel, the viscosity and density are both expected to increase during the evaporation progress. Meyerhofer (1978) showed that the fluid can be described by a volume of solvent (L) which is added to a volume of solid (S). Then the concentration c_0 is defined as $c_0 = S/(S+L)$.

Meyerhofer assumed that the third stage is entirely dominated by the viscous flow rate, and the fourth stage entirely dominated by the evaporation rate. The transition point was set when evaporation rate and the viscous flow both are equal such that Equation 2.53 predicts the final coating thickness.

$$h_f = c_0 \left(\frac{e_s}{2(1-c_0)K} \right)^{1/3} \quad \text{Equation 2.53}$$

Where c_0 is solid concentration in the solution and e_s is the evaporation rate of the solvent [ml/s/cm^2]. It is assumed that the evaporation rate is a function of the spinning condition as described by Equation 2.54 (the airflow above the spinning substrate is considered laminar).

$$e_s = C\sqrt{\omega_s} \quad \text{Equation 2.54}$$

The proportionality constant, C , should be determined by the specific experimental conditions.

This is the chosen project deposition technique, the thickness of layers reported in the literature range between 100nm to $\sim 5 \mu\text{m}$ with good film uniformity, and this thickness could be extended up to $50 \mu\text{m}$ by a multilayered structure, which should give a great adaptability to high frequencies transducer specification [Corker *et al.* 2002].

The thickness mode of excitation of transducers means that device characteristics depend strongly on the film thickness. Because of this thickness flexibility offered by this technology, the spin-coating

technology has been used for the development of 50 MHz ultrasonic transducers [Lukacs *et al.* 2000], [Zhao *et al.* 2003] and [Pan *et al.* 2006]. The use of innovative spin coating techniques for composite PZT powder/ sol gel thick film fabrication has been developed:

- A mould technique [Zhao *et al.* 2003] that uses the spin coating technology.
- The spin coating of a PZT composite for the fabrication of a patterned annular array [Lukacs *et al.* 2000] and [Pan *et al.* 2006]. This technology is similar and now as mature as the one developed in this work. However, the technique to shape the annular array and the material properties are different (see chapter 3 and 8).
- The mould technique

The mould technique is presented to be efficient to spin coat composite sol gel patterned layers [Zhao *et al.* 2003]. This technology uses simply a patterned silicon wafer on top of which the PZT composite is spun (Figure 2.27).

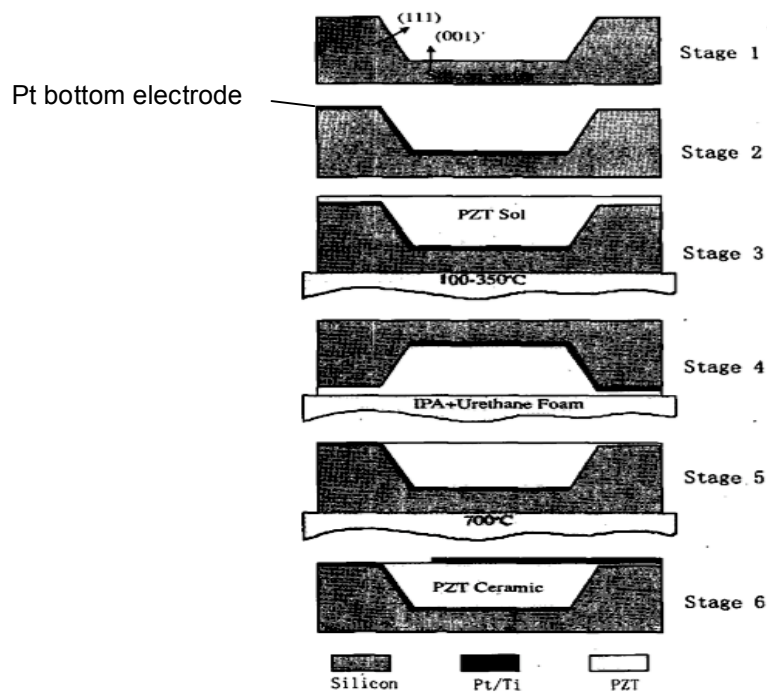


Figure 2.27: PZT thick film mould technology usable for a single element transducer. [Zhao *et al.* 2003]

The depth of the mould dictates the thickness of the mono-film. This technology can achieve PZT films thicker than 50 μm in just one layer [Zhao *et al.* 2003].

- Thick film spun without mould

A PZT composite spun on a silicon substrate can achieve total thickness of 3 μm per layer. A stack of layers can then lead to the fabrication of high frequency transducer (50MHz). This work is the closest to this project [Lukacs *et al.* 2000]. It can be compared to the composite developed in this project (figure 3.1). This composite work was pursued by Pan [2006] and mixed with the mould technique to develop an annular array patterned with kerf at 15-20 μm separating 5 annular arrays, developed to resonate at 50MHz. (Figure 28)

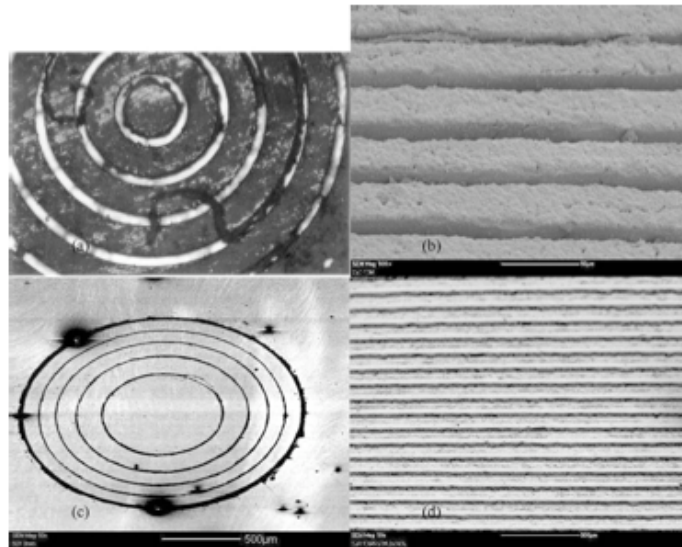


Figure 2.28 :Typical pictures of micromolded PZT sol-gel composite structures on a platinum-coated silicon wafer. (a) A 50- μm thick annular pattern with kerfs of 15 μm . The central disk is 100 μm in diameter; the ring is 50- μm wide. Some Su-8 residues trapped on the surface. (b) A linear array (~50- μm thick) of size 23 μm \times 15 μm . The scale is 50 μm . (c) A five-element annular array of ~40- μm thick with kerfs of 20 μm . The outer diameter is 2.0 cm and the scale is 500 μm . (d) A super long linear array of 27,000 μm , 50- μm wide, and 65- μm high. The scale is 500 μm . [Pan *et.al.* 2006].

This annular is still in development by Pan, and has not yet been analysed. However the same group has developed 50MHz transducer annular arrays based on bulk PZT [Lockwood *et al.* 2004, and 2005].

2.6.4 Photolithography

Photolithography is widely used in this project to define the electrode shape and selectively etch the PZT thick film. Photolithography is used to transfer a geometric shape onto a substrate. MEMS technology uses this technique to shape the most advanced electronic devices. An example of how photolithography is used in an etching procedure is presented in Figure 2.29. The unprotected PZT,

not coated by the photoresist, can be etched by an HF/HCl solution (0.045wt %). This wet process has an etching size limitation equal to the film thickness because of its isotropy.

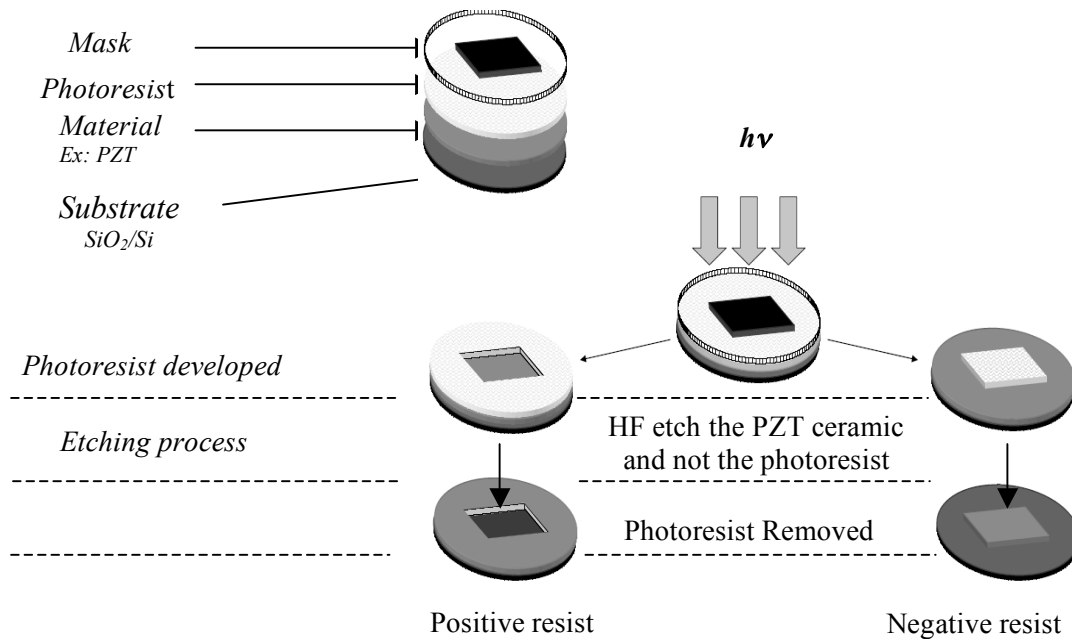


Figure 2.29: Schematic of an etching process using photolithography. Alternatively the etching step can be replaced by a metal deposition to pattern electrode on the substrate.

The lift-off process is the process widely used in MEMS technology to deposit and shape electrodes. The metal is generally sputtered over the whole wafer. The resist can then be removed by a chemical reaction to leave behind only the metal where the photoresist was not present. This technique presents a very good resolution, down to 5 μ m. The lateral definition of these electrodes is entirely limited by the mask quality. A well-known defect is a possible residue on the electrode (Figure 2.30). By disrupting subsequent depositions, the residue may lead to films of poor quality.

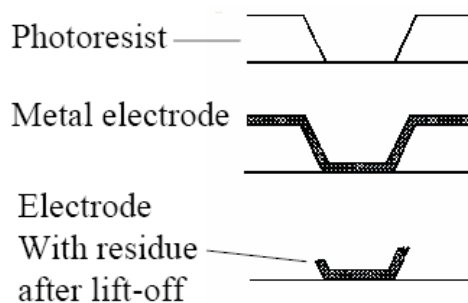


Figure 2.30: Schematic of a example of metal residue after lift off

Now that the main technologies used to fabricate a transducer have been presented through the preceding sections, the next section will focus on how a transducer works, in order to be able to understand, model, and improve it.

2.7 Ultrasonic transducer structure

2.7.1 Introduction

– *Why ultrasounds?*

Ultrasounds are a non-invasive technique used for imaging: nothing has to be inserted into the body unlike fibre-optic endoscopes. Compared to other techniques such as X-Rays and MRI (Magnetic Resonance Imaging), ultrasound examination is relatively inexpensive, quick, convenient and non-ionizing.

– *What is an ultrasonic transducer?*

Ultrasonic Transducers (UT) are usually used with frequencies between 1 and 10MHz. However, as stated in the preceding section, some groups have already presented work on transducers working at 50 MHz since 1996 [section 2.3.1].

Compared to a simple resonator, an ultrasonic transducer is modified to transmit the converted energy in a unique direction (Figure 2.31). To do this, a dense material is placed under the transducer. This kind of structure represents a typical way to maximise the transfer of acoustic energy between the transducer and the medium. In this section it is presented that the index of the active acoustic medium needs to match the index of the medium scanned, in order to optimise the efficiency of the transducer. To do that, layers with an intermediate acoustics index have to be used between the two mediums. In the present case, the index of the PZT has to match with that of water or human body. Usually, this layered structure is obtained by lamination of prepared layers, glued and sliced with a blade into one direction (one dimensional or 1D arrays) or two 2D arrays.

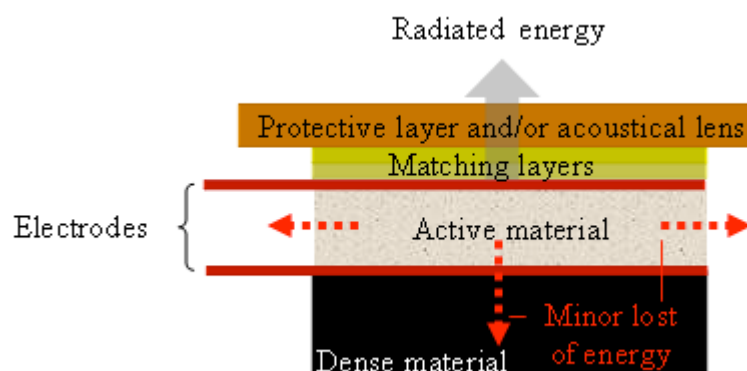


Figure 2.31: Schematic of a cross section of an ultrasonic transducer

Low frequency acoustic waves are used for deep scans (body), and high frequency ones used for superficial scans (eyes, skin). Duval [2004] reported that high frequency applications require thin UTs and 3D imaging 2D arrays and these can only be achieved through micro-fabrication techniques. For these reasons, Micromachined Ultrasonic Transducers (MUT) have received considerable attention.

– *How does an ultrasonic transducer work?*

This introduction treats two important questions of why ultrasounds are needed in medical imaging and what is an ultrasonic transducer. The remaining sections will then focus on the other important questions of how works an ultrasonic transducer, and how to model it.

First the different structures of transducer, which can achieve high frequency will be presented. The main arguments will then be presented, which leads this research toward the use of a piezoelectric transducer. The second part of this section will then present in an exhaustive way, how a thickness mode piezoelectric Micro-machined Ultrasonic Transducer (tm-pMUT) works and how it can be modelled.

2.7.2 Capacitive Micro-machined Ultrasonic Transducer (CMUT)

A Capacitive Micro-machined Ultrasonic Transducer (CMUT) consists of a metalised membranes (top electrode) suspended above a metalised substrate, which consists of a silicon wafer coat with Pt or Au (bottom electrode) [Cianci *et al.* 2004] (Figure 2.32).

When a DC voltage is applied between the two electrodes, Coulomb forces attract them together, while stress within the membrane resists the attraction. If the membrane is driven by an AC voltage, a significant ultrasound is generated. Conversely, if an ultrasound is sent to the transducer, significant currents are produced.

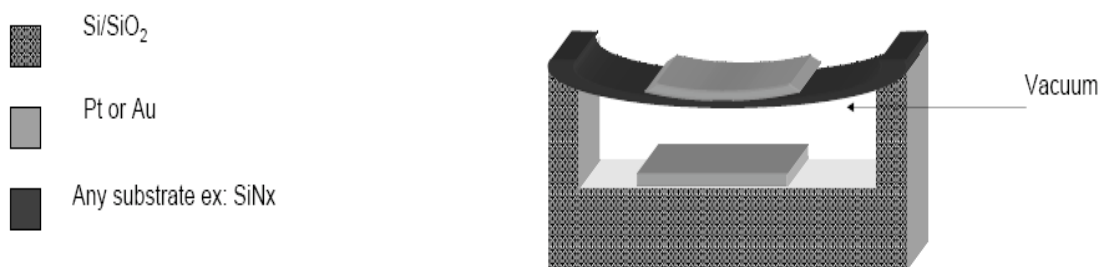


Figure 2.32: Schematic of one element of a CMUT

CMUTs operate typically at a resonant frequency f_r inversely proportional to the membrane radius (r), Equation 2.55.

$$f_r = \frac{2.405}{\pi r} \sqrt{\frac{\sigma}{\rho}} \quad \text{Equation 2.55}$$

Where σ is the applied stress, r the electrode radius and ρ the membrane density. The resonant frequency is dependent on the electrode size which limits considerably the CMUT applications for very high frequency imaging (50MHz) and also induces as well a limitation for an array design. Typically, they operate at few MHz (1-20MHz).

2.7.3 Piezoelectricity in ultrasonic transducer

2.7.3.1. Thickness mode piezoelectric Micro-machined Ultrasonic Transducer (tm-PMUT)

When the displacement used to emit and receive an acoustic wave, happens to be along the thickness of the transducer, the operational mode is termed thickness mode. The piezoelectric constant d_{33} characterises this piezoelectric thickness mode, as describe by Equation 2.24, and Figure 2.33.

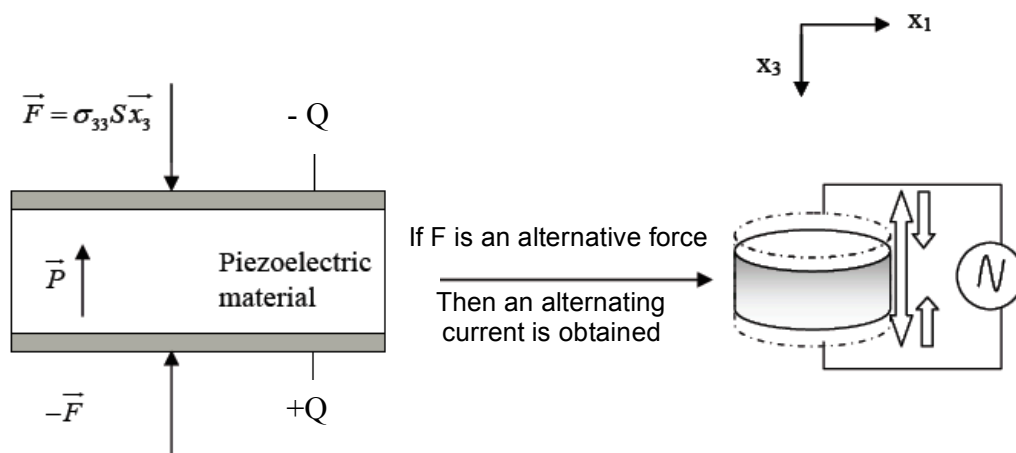


Figure 2.33: Schematic of a piezoelectric transducer working on the thickness mode.

The piezoelectric structure of the transducer described by figure 2.31 will be thick enough that the flexural modes can be neglected. A 10 μ m thick film vibrates at 200 MHz- 300MHz, which is much higher than a typical MUT (CMUT). A thicker film should be able to achieve lower frequencies (25-50MHz) suitable for use as high resolution near surface (Equation 2.56).

$$f_r = \frac{C}{2l_T} = \frac{1}{2l_T} \sqrt{\frac{c_{33}}{\rho}}$$

Equation 2.56

Where C is the acoustic velocity in a thick PZT film, l_T is the total thickness of the device, c_{33} is the material stiffness, ρ is the density.

2.7.3.2 Flexural mode piezoelectric Micro-machined Ultrasonic Transducer (PMUT)

When the displacement used to emit and receive acoustic wave, is along the width of the transducer, the lateral alternating displacement induces an alternating bending of the membrane [Muralt *et al.* 2005]. Such transducer structures are simply termed piezoelectric Micro-machined Ultrasonic Transducer pMUT (Figure 2.34).

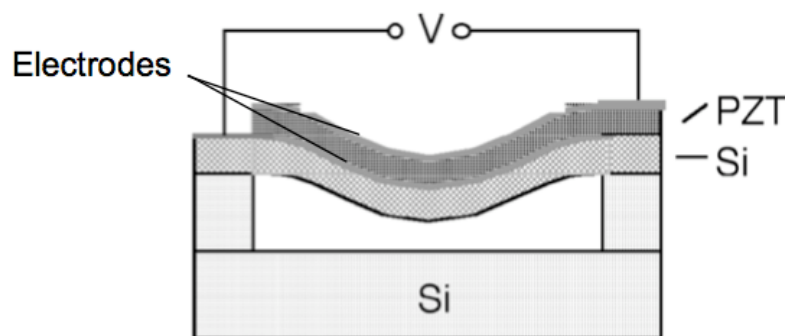


Figure 2.34: Schematic cross section through a pMUT. [Muralt *et al.* 2005]

The resonant frequency of piezoelectric transducer working with the bending mode of excitation is described by Equation 2.57 [Muralt *et al.* 2005].

$$f_r = \frac{(3.19)^2}{2\pi r} \sqrt{\frac{El^2}{12(1-\nu)^2 \rho}} \quad \text{Equation 2.57}$$

Where E and ν are the Young's modulus and Poisson ratio of the membrane, ρ is its density, l is its thickness and r is radius of the active electrodes. Like the CMUT, the resonant frequency is dependent on the electrode size which limits considerably the pMUT applications for very high frequency imaging (50MHz) and induces a limitation for an array design. Typically, they operate at a few MHz (1-20MHz).

2.7.4. Choice the tm-pMUT structure for high frequency application.

The choice of using the tm-pMUT structure as a high frequency transducer came simply from a trade off made between the sensitivity, the bandwidth, and the size of the three transducer structures presented above:

– Sensitivity and dynamics

The gap between the top membrane and the bottom electrode is one of the major characteristics of the CMUT device. It determines the maximum deflection of the membrane under biasing before it collapses on the substrate. This will directly affect the power of the output signal. At equilibrium, the elastic restoring force ($-k.z$) of the CMUT system is equal and opposite of the electrostatic force. The relation between displacement and voltage is non linear and can be describe by Equation 2.58.

$$V = \sqrt{\frac{kz}{\epsilon_0 A_a}} (z_0 - z) \quad \text{Equation 2.58}$$

Where A_a is the device active area, and, $(z_0 - z)$ is the gap between the membrane and the bottom electrode. The collapse of the membrane occurs when $r=2r_0/3$ and the gap becomes zero. By biasing the membrane just below this collapse voltage, the response of the system is very high, (equivalent of a $d_{33}=200\text{nC/N!}$), but the dynamic is very low. The PMUTs design doesn't have this limitation for the acoustic power, but has a lower sensitivity. So there is a trade off between sensitivity and dynamics.

– Bandwidth comparison

Experimentally, the PMUT design has typically a low bandwidth, which is one of the main drawback at this state of the research. The higher the bandwidth is, the higher the range of detected frequencies will be. The CMUT system typically exhibits a wide bandwidth (in excess of 100%) which is the real advantage of CMUT for application such as Doppler imaging. For further details on PMUT and CMUT, see [Gaucher 1999], [Duval *et al.* 2004] and [Cianci *et al.* 2002]

– Electrode Size

PMUT and CMUT structure exhibit a resonant frequency inversely proportional the electrode size: the higher the frequency, the smallest their electrode size. This makes their fabrication difficult. In addition the active area decreases as the connection lines are not reduced in size in line with the size of the electrodes. However, for a tm-pMUT structure, the frequency of resonance is completely independent of the electrodes surface.

The size consideration is the main argument for using the thickness mode of excitation for high frequency transducer application. It allows a large flexibility in the fabrication of one element and simplifies considerably the array design.

2.8 Thickness mode piezoelectric transducer theory

2.8.1 Introduction

This section gives the basic equations needed to give an insight into the key points needed to understand transducer operation and modelling. A short overview of equations will be given. For a deeper understanding the reader should consult the textbooks by Rosenbaum [1988], Kino [1987], and Mason [1945].

For simplicity, it will be assumed that all quantities (particle displacement, particle velocity, stress, strain, elasticity, coupling coefficient...etc) can be expressed in one-dimensional form and the material will be considered to be isotropic. Plane longitudinal wave propagation only will be considered, in order to reduce the problem from three to one dimension. The general behaviour found with these approximations are comparable to a more complete treatment for isotropic material.

2.8.2 Acoustic waves - Basic equations

A longitudinal wave propagating in a material induces motion of the particles within the medium. The propagation of the particle displacement is described by the equation of motion dependent on the particle velocity. While this motion follows the law of mass conservation, the wave is subject to acoustic losses which attenuate the wave power by a constant called the attenuation constant.

The acoustic impedance of a material is the ratio between the transmitted force and the particle velocity of the transmitting wave. Often this constant is used to describe the matching between mediums where the acoustic wave is transmitted (matching layers). To understand a model of piezoelectric transducer, all these important quantities are presented in this section.

A longitudinal wave induces a short-range particle motion in the medium. This particle motion will push the neighbouring particles, which in turn will transmit the motion to their own neighbours. By this short-range particle motion the acoustic wave moves only in the direction of propagation (z). This kind of wave expands or contracts the acoustic medium in which it travels. (Figure 2.35)

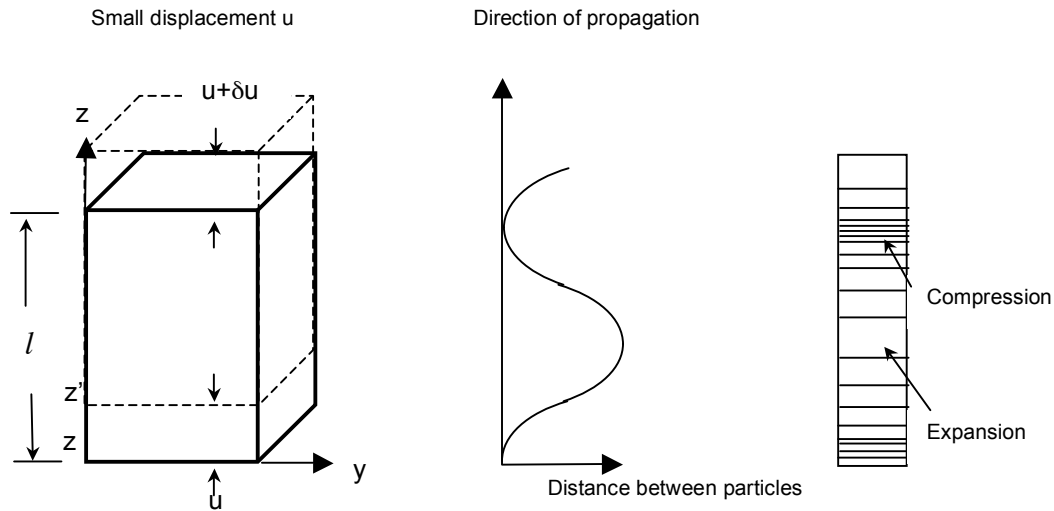


Figure 2.35: Schematic illustration of a propagating of a longitudinal wave

The particle motion induces strain and stress inside the medium. For this chapter the simplified version of Equation 2.44 will be considered as shown by Equation 2.59.

$$\sigma = c \cdot S \quad \text{Equation 2.59}$$

Where c is the elastic stiffness of the material, S is the strain and σ is the stress. S and σ won't be considered as tensor, but as one component for one direction.

The strain in equation 2.59 describes the change of particle displacement (δu) as a function of z as shown by Equation 2.60.

$$\delta u = \frac{\partial u}{\partial z} l = Sl \quad \text{Equation 2.60}$$

Where l is the PZT thickness, and z the direction of propagation of the wave (Figure 2.30).

This variation of particle displacement helps to determine the equation of motion from Newton's 2nd law. The force per unit of area transmitted to the material, for example by an acoustic wave, is given by Equation 2.61.

$$\frac{F}{A} = \frac{\partial \sigma}{\partial z} l \quad \text{Equation 2.61}$$

Where the force F is equal to mass (m_0) times acceleration (\ddot{u}) such that Equation 2.61 can be written as Equation 2.62.

$$\frac{\partial \sigma}{\partial z} = \frac{1}{l} \frac{m_0 \ddot{u}}{A} = \frac{m_0}{V} \ddot{u} \quad \text{Equation 2.62}$$

The motion equation of a particle in a material subject to an acoustic wave can then be describe by Equation 2.63.

$$\frac{\partial \sigma}{\partial z} = \rho_{mo} \ddot{u} = \rho_{mo} \dot{v} \quad \text{Equation 2.63}$$

Where v is the particle velocity, and ρ_{mo} is the mass density in the stationary state.

This motion is governed by the conservation of mass, i.e. during the transmission of energy between the particles during motion no mass is loss. From Equation 2.60 and the fact that the change of a particle velocity in the material is given by $\delta v = \frac{\partial v}{\partial z}$, Equation 2.64 can be derivate.

$$\frac{\partial S}{\partial t} = \frac{\partial v}{\partial z} \quad \text{Equation 2.64}$$

(Remembering that $\delta v = \frac{\partial}{\partial t} \delta u$)

Which leads to the wave equation and the propagation constant of the acoustic wave by the following path:

From Equations 2.59, 2.63, and 2.64, and $v = \delta u / \delta t$, Equation 2.65, describing the sound wave propagation, can be obtain.

$$\frac{\partial^2 \sigma}{\partial z^2} = \rho_{mo} \frac{\partial^2 S}{\partial t^2} = \frac{\rho_{mo}}{c} \frac{\partial^2 \sigma}{\partial t^2} \quad \text{Equation 2.65}$$

For a wave of radian frequency f , the solution of this equation is of the form of $\exp[j\omega t \pm \beta_a z]$. Where β_a is the propagation constants given by Equation 2.66. For wave propagating in a forward direction the sign will be negative, and positive for a backward propagating wave.

$$\beta_a = \omega \left(\frac{\rho_{mo}}{c} \right)^{1/2} = \frac{\omega}{V_a} \quad \text{Equation 2.66}$$

Where V_a is the acoustic velocity.

The acoustic wave propagating equations are often subject to acoustic losses in their power. Ideally, the system won't dissipate energy from the mechanical energy due to the acoustic wave propagation

as the system is purely elastic. In a real system, viscous forces between neighbouring particles attenuate considerably the wave propagation distance. Actually, a viscous term $\eta \frac{\partial S}{\partial t}$ should be added to Hooke's law (equation 2.59). Where η is the coefficient of viscosity of the medium. Considering this coefficient, the power flow per unit area in the acoustic wave is defined as Equation 2.67.

$$P_a = P_o \exp(-2\alpha z) \quad \text{Equation 2.67}$$

Where α is the attenuation constant of the wave described by Equation 2.68, and P_o is a constant.

$$\alpha = \frac{\eta \omega^2}{2V_a^3 \rho_{mo}} \quad \text{Equation 2.68}$$

Equation 2.68 reveals that for a longitudinal wave the attenuation varies as the square of the frequency and the cubed root of the acoustic velocity. In the case of water at room temperature, α is equal to 0.22 db/m at 1 MHz and at 50Mhz its equal to 5.5 db/cm.

During this periodical expansion and compression of the material, thermal conduction becomes another source of acoustic loss. Another well-known source of acoustic loss are the defects of the medium, which can scatter or absorb the acoustic wave. For example in ceramics or crystals waves can be scattered by fine grains, porosity, or dislocations.

The last important concepts described in this short list will be the Acoustic impedance and matching layers. Equation 2.69 defines the acoustic impedance.

$$Z = -\frac{\sigma}{v} \quad \text{Equation 2.69}$$

In order to understand the concept of matching layers the general case of an acoustic wave transmitted from one material to another will be consider.

The general case of a layer of impedance Z_0 , propagation constant β and thickness l , placed in contact with another layer presenting an impedance of Z_L (Z load), the acoustic wave will be partly transmitted to the load, and another part will be reflected. This is represented by the reflection coefficient, Γ , equal to $(Z_L - Z_0) / (Z_L + Z_0)$. If Z_L is at $z=0$, the input impedance of the layer of thickness l is defined by Equation 2.70:

$$Z_{in} = Z_0 \frac{e^{j\beta l} + \Gamma e^{-j\beta l}}{e^{j\beta l} - \Gamma e^{-j\beta l}} \quad \text{Equation 2.70}$$

Thus, with the trigonometric definition of $e^{i\beta l}$:

$$Z_{in} = Z_0 \frac{Z_L \cos \beta l + jZ_0 \sin \beta l}{Z_0 \cos \beta l + jZ_L \sin \beta l} \quad \text{Equation 2.71}$$

Then a good matching layer will be $\lambda/4$ thick (i.e. $\beta l = \pi/2$) where $Z_{in} = Z_0^2/Z_L$. Two very different mediums can match in impedance by choosing a good interlayer. Also perfect matching occurs just at one frequency. [Kino,1987]

2.8.3 Piezoelectric transducer.

Because a transducer emits and receives acoustic waves, interactions between the transducer material, the acoustic waves and load mediums have to be included in a model of the transducer. The definitions of the quantities described above have to be adapted so that they include the piezoelectric characteristic of the transducer. The updates are of small order. An example will be to add a piezoelectric coupling coefficient to a variable like the acoustic velocity, or the elastic constant or even to refine the dielectric constant. For example Hooke's law (Equation 2.59) becomes:

$$\sigma = c^E (1 + K^2) S = c^D S \quad \text{Equation 2.72}$$

Here K is the electro-mechanical coupling coefficient. The subscripts D, E, S, etc, denote that the property is measured under a constant or zero value of the variable represented by the subscript. The c^D , or c^E is the stiffened elastic constant, or the elastic constant when the displacement D, or the applied electric field are null or constant. K^2 is the piezoelectric coupling coefficient defined by Equation 2.73.

$$K^2 = \frac{e^2}{c^E \epsilon^S} \quad \text{Equation 2.73}$$

The acoustic velocity in a piezoelectric medium becomes:

$$V_{a,p} = V_a (1 + K^2)^{1/2} \quad \text{Equation 2.74}$$

The piezoelectric coupling coefficient marks the difference between a common material and a piezoelectric one. It is essential to understand how this coefficient varies to understand the

mechanical behaviour of a piezoelectric transducer when it is subjected to a perturbation such as an acoustic wave (see Chapter 7).

2.8.4 Transducers as a three port-network

2.8.4.1 introduction

In this section, a brief explanation of the origin of the equations used to model the devices presented in Chapter 7 is given. The focus of the work presented in this PhD is not based on modelling a transducer perfectly. Instead, a simple Mason model has been used to understand the basics of a piezoelectric transducer, and derive the material properties.

2.5.4.2 Mason model

The equivalent circuit definition of a piezoelectric transducer is based on the idea that the particle velocity is equivalent to the electrical current and the stress equivalent to the voltage [Mason, 1945]. The main principle of the well-known Mason model is explained in this section. However some slight upgrade of these equations was used in the model presented in this work. The reason why they are presented in appendix A, and not in this section, is because they represent a simple repetition of what is explained in this section, or their presence would have been too exhaustive and irrelevant to understand the simple use of the Mason model used in Chapter 7.

Figure 2.36 a) represents the most simple resonator, consisting of a piezoelectric disk with top and bottom electrodes. (The final model used in this work is not very different from this representation, just a single layer of SiO_2 is added under the bottom electrode). This kind transducer is often represented by a three-port network or three-port black box, which represents a simple notation of the electro-mechanical transducer behaviour. This black box, and its equivalent circuit are represented in Figure 2.36 b) and c).

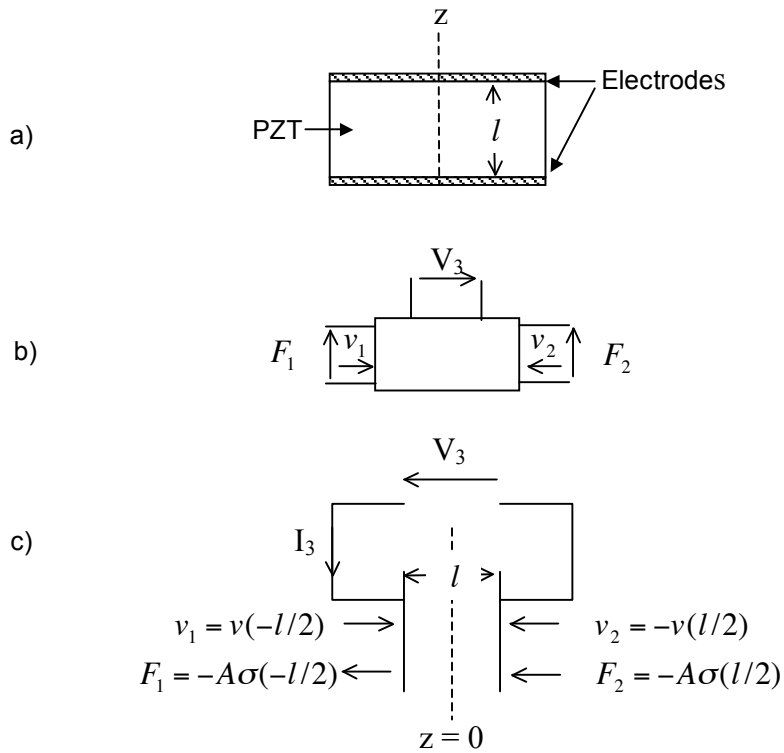


Figure 2.36: a) Schematic of piezoelectric resonator of thickness l with top and bottom electrodes, b) schematic of a three port black box, c) relation between the three-port notation and the transducer physical variables.

In Figure 2.36, F_1 , F_2 , v_1 and v_2 , represent the force and the particle velocities at the surface of each side of the transducer. The boundary conditions at the acoustic ports are given by Equations 2.75 to 2.78.

$$F_1 = -A\sigma(-l/2) \quad \text{Equation 2.75}$$

$$F_2 = -A\sigma(l/2) \quad \text{Equation 2.76}$$

$$v_1 = v(-l/2) \quad \text{Equation 2.77}$$

$$v_2 = -v(l/2) \quad \text{Equation 2.78}$$

Rausenbaum [1988], Mason [1945], and Kino [1987] present these solutions by applying the boundary conditions to the waves equations. After some algebra, the Equation 2.79 can represent the main electro-mechanical relations.

$$\begin{bmatrix} F_1 \\ F_2 \\ V_3 \end{bmatrix} = -j \begin{bmatrix} Z_c \cot \beta_{a,p} l & Z_c \operatorname{cosec} \beta_{a,p} l & \frac{h}{\omega} \\ Z_c \operatorname{cosec} \beta_{a,p} l & Z_c \cot \beta_{a,p} l & \frac{h}{\omega} \\ \frac{h}{\omega} & \frac{h}{\omega} & \frac{1}{\omega C_0} \end{bmatrix} \times \begin{bmatrix} v_1 \\ v_2 \\ I_3 \end{bmatrix} \quad \text{Equation 2.79}$$

Where C_0 is the clamped capacitance of the transducer given by Equation 2.80.

$$C_o = \frac{\epsilon^s A}{l} \quad \text{Equation 2.80}$$

The parameter h is the transmitted constant equal to e/ϵ^s , and the parameter Z_c is equal to the acoustical impedance of the transducer material times its active area A as shown by Equation 2.81.

$$Z_C = Z_{o,p} A \quad \text{Equation 2.81}$$

The electrical input impedance impedance, Z_3 , of a transducer terminated by two load impedances (Equation 2.69) Z_1 and Z_2 can be then be determined through Equation 2.71.

Z_1 , Z_2 and Z_3 can be define by Equations 2.82 to 2.84:

$$Z_1 = -\frac{F_1}{v_1} = \frac{A\sigma(-l/2)}{v(-l/2)} \quad \text{Equation 2.82}$$

$$Z_2 = -\frac{F_2}{v_2} = -\frac{A\sigma(l/2)}{v(l/2)} \quad \text{Equation 2.83}$$

And,

$$Z_3 = \frac{V_3}{I_3} = \frac{1}{j\omega_3 C_o} \left[1 + k_t^2 \frac{j(Z_1 + Z_2)Z_c \sin \beta_{a,p} l - 2Z_c^2(1 - \cos \beta_{a,p} l)}{\left[(Z_c^2 + Z_1 Z_2) \sin \beta_{a,p} l - j(Z_1 + Z_2)Z_c \cos \beta_{a,p} l \right] \beta_{a,p} l} \right] \quad \text{Equation 2.84}$$

These electrical and acoustic impedances are the basis of the Mason model. From these equations the model already defines a good model of the impedance of the transducer as a function its frequency. The coefficient k_t^2 is a variation of the electromechanical coupling coefficient defined by

Equation 2.85. It is considered, arbitrarily, as the piezoelectric coupling coefficient to be used for a transversely clamped material which the design presented in this work illustrates.

$$k_r^2 = \frac{K^2}{1 + K^2} \tag{Equation 2.85}$$

To simplify the matrix notations, Z_{ij} will be considered as the component of the 3x3 matrix of Equation 2.79, such that:

$$\begin{aligned} Z_{11} = Z_{22} &= -jZ_c \cot \beta_{a,p}l, \text{ and } Z_{33} = 1/\omega C_0 \\ Z_{12} = Z_{21} &= -jZ_c \operatorname{cosec} \beta_{a,p}l, \\ Z_{13} = Z_{31} = Z_{23} = Z_{32} &= \frac{h}{\omega}, \end{aligned} \tag{Equation 2.86}$$

Thus,

$$F_1 = Z_{11}v_1 + Z_{12}v_2 + \frac{hI_3}{j\omega} \tag{Equation 2.87}$$

$$F_2 = Z_{12}v_1 + Z_{22}v_2 + \frac{hI_3}{j\omega} \tag{Equation 2.88}$$

The forces F_1 and F_2 and their interactions are represented by the coefficients Z_{11} - Z_{12} , and Z_{12} . Mason proposed a finalised version of an equivalent circuit, which is a simple representation of the functionality of the transducer (Figure 2.37). The mechanical part, or the forces and their interactions, of the equivalent circuit is shown as a T network coaxial line. The electrical part, or the dielectric and resonator part, is represented by the electrical circuit which includes the transducer capacitance, C_0 .

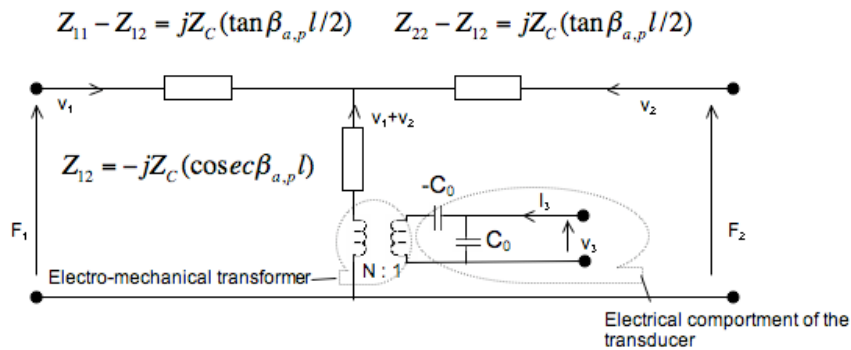


Figure 2.37: Electro-mechanical Mason equivalent circuit which model a transducer.

The piezoelectric effect is represented by the transformer characterised by the ratio, N, defined by Equation 89.

$$N = hC_0 = \frac{eC_0}{\epsilon^s} \quad \text{Equation 2.89}$$

This ratio, N, might be the most important part of the equivalent circuit, as it contains the piezoelectric constant e. It represents, simply, the amount of electrical energy converted into mechanical energy.

This model is based on theory, and a theory is always wrong, it will never reflect reality. In this description of a transducer nature, the purpose is not to disclose the real essence of the phenomena of transmitting and receiving wave with matter, but only to track down, so far as it is possible, relations between the manifold aspects of the experiment presented in Chapter 7.

2.9 Summary

This literature review mirrors the arrangement of the experimental chapters 4, 5, 6, 7. Describing the content of these chapters becomes then equivalent to describing the sections of this literature review. The sections have described the work that has been done around the world on the focused topic of each concerned chapter.

The fabrication of thick PZT films, with thicknesses of 2 micrometers up to 50 micrometers, is detailed by focussing on the techniques allowing the direct integration of the PZT film onto a silicon substrate or alumina substrate, and on detailing the patterning techniques.

While the deposition of different layers is taking place, the *in situ* stress of these layers increases or decreases. Stoney's equation was then re-derived to understand its limitations, and its advantages. This work is devoted to also understand the dielectric, piezoelectric and ferroelectric aspect of the material of interest of this project. Basic theories of these topics have been presented to understand the core of the discussions. Modelling of ultrasonic piezoelectric thickness mode transducers has been presented, focussing on high frequency transducers and on modelling the ultrasound waves received or emitted by a PZT thick film using the Mason model used in Chapter 7.

High frequency transducers have been demonstrated for approximately ten years with: the screen printing technology, the spin coating technology, the tape casting technology, the powder route. All of these technologies have been demonstrated to achieve frequencies of 20-80MHz. [Foster *et al.* 1991] [Lethiecq 1996], [Lukacs *et al.* 2000], [Snook 2001], [Brown *et al.* 2004], [Brown *et al.* 2005], , [Snook *et al.* 2006], [Gottlieb *et al.* 2006], [Pan *et al.* 2006], [Levassort, 2006]. There is no interest in reviewing all these papers demonstrating how they achieve such frequency, because the main techniques have been described during this chapter.

In order to finalise this chapter, Table 2.3 reviews the main transducer properties of the piezoelectric high frequency transducer working at 50MHz giving the state of the art of such structures.

Table 2.3: Current High frequency transducers.





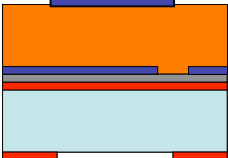
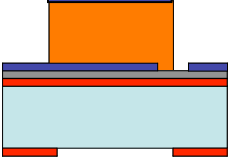
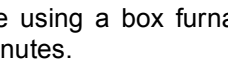
	frequency	thickness	k_t	technology	shape	substrate	diameter
Pang 2006	X	50um	X	Micro molds & spin coating PZT composite Sintered at 650°C	Patterned annular array 5 elements with 15µm kerf.	silicon	2.5mm
Pang 2006	50MHz	35um	0.32	Spin coating Sintered at 650°C	Non pattern plate	aluminum	2mm
Boamin 2003	37.5 MHz	43um	0.49	Screen printing Sintered at 1250°C	Non pattern plate	sapphire	1mm
Brown 2004	50MHz	40um	0.48	PZT bulk glued	Non pattern annular 7 elements	None	2mm
Levassort 2001	50MHz	40um	0.51	PZT.PGO/800 Screen printed	plate	PZT/alumina	8mm

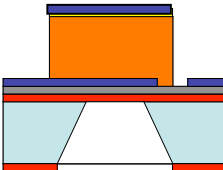
Chapter 3

Experimental procedure




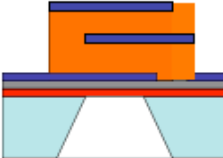
3.1 Introduction

This chapter describes the processes used to fabricate and characterise the transducer and PZT thick film material. The layout illustrates the fabrication in 9 stages of the single layer transducer. Stage 0 will be the starting wafer of silicon (blue) with both sides coated with 400nm of SiO₂ (red).

1	<p>Deposition of a 60nm ZrO₂ diffusion barrier layer by spin coating on the Si wafer (double sided coated with 400nm of SiO₂) : 3 layers spun at 3000rpm for 30 seconds. Each layer dried at 200°C and pyrolysed at 350°C. ZrO₂ layer was crystallised at 800°C for 10 minutes.</p>	
2	<p>Patterning of SiO₂ of the silicon wafer back face using photolithography (back face mask) and reactive ion etching (RIE). The etching conditions are :</p> <ul style="list-style-type: none"> - photoresist used → AZ4562 1000rpm-3min @ 90°C-45s under UV-3min of development - O₂ : 10sccm CHF₃:25sccm - Total pressure 100mTorr - Power 150, DC W bias 300 V - Time 13min (etch rate 40nm/min) <p>The patterned SiO₂ layer is used to ensure that all subsequent 'front face' structures are aligned.</p>	
3	<p>Ti/Pt (8nm/200nm) "back electrodes", or the embedded electrodes between the silicon and the PZT, are deposited using RF sputtering and patterned using lift off (back electrode mask)</p> <p>The photoresist S1818 was spun at 4000 rpm, dried for 90 seconds at 115°C, and selectively exposed under UV light for 10 seconds, and then developed in MF319 developer.</p> <p>Lift off process conducted following sputtering using acetone as solvent.</p>	
4	<p>PZT film deposited using composite sol gel technique. Thickness of PZT deposited is dependent on the resonant frequency required for each device.</p>	
5	<p>Ti/Pt (8nm/200nm) top electrodes deposited using RF sputtering and patterned using lift off (back electrode mask)</p>	
6	<p>PZT film patterned using photolithography (PZT etch mask) and wet etching.</p>	
7	<p>PZT film crystallised at 720°C for 30 minutes in air atmosphere using a box furnace. Ramp rate set to maximum, set temperature achieved within 7 minutes.</p>	

8	Si backing etched using TMAH etching or DRIE (Deep Reactive ion etching).	
9	Device poled using contact poling (30-200°C, 8 V/μm), 5 minutes. Cool to below 100°C before removing field, see chapter 3.	

The second layout summarises the fabrication of the multilayer ultrasonic transducer. Step 1 to 5 are the same as for the single layer transducer fabrication.

6	Same as step 4: PZT deposition on the embedded electrode	
7	Same as step 5: Top electrode deposition	
8	Same as step 6: PZT film patterned using photolithography (PZT etch mask) and wet etching.	
7	PZT film crystallised at 710°C for 30 minutes in air atmosphere using a box furnace. Ramp rate set to maximum, set temperature achieved within 7 minutes.	
8	Si backing etched using TMAH etching or DRIE.	
9	Device poled using contact poling (130-200°C, 8 V/μm, 5 minutes). Cool to below 100°C before removing field, see chapter 3.	

This chapter describes the experimental procedures used and developed to fabricate the capacitors and the transducers used to characterise the PZT material and to fabricate the annular array. First, the standard procedures to make PZT thick films are detailed: the preparation of the PZT sol, the composite slurry fabrication and their respective viscosity measurements. The second part describes, in detail, the film deposition and micro-fabrication

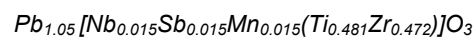
techniques. Standard poling operating procedures of the different micro size PZT devices are given, after briefly presenting different techniques of micro-structural evaluation. The last part is dedicated to briefly describe the techniques used to evaluate the film and the device properties.

3.2 PZT sol and PZT composite

3.2.1 PZT Sol

This section describes the PZT sol-gel process used throughout the project. The sol-gel syntheses were conducted in a chemistry laboratory under fan-assisted fume hoods. Some variations of the sol, such as colour due to particle sizes, and viscosity, were noticed during synthesis. They will be discussed in chapter 4.

PZT sol-gel solution general formula:



The procedure used in this project to synthesise the sol gel solution is schematically in Figure 3.1.

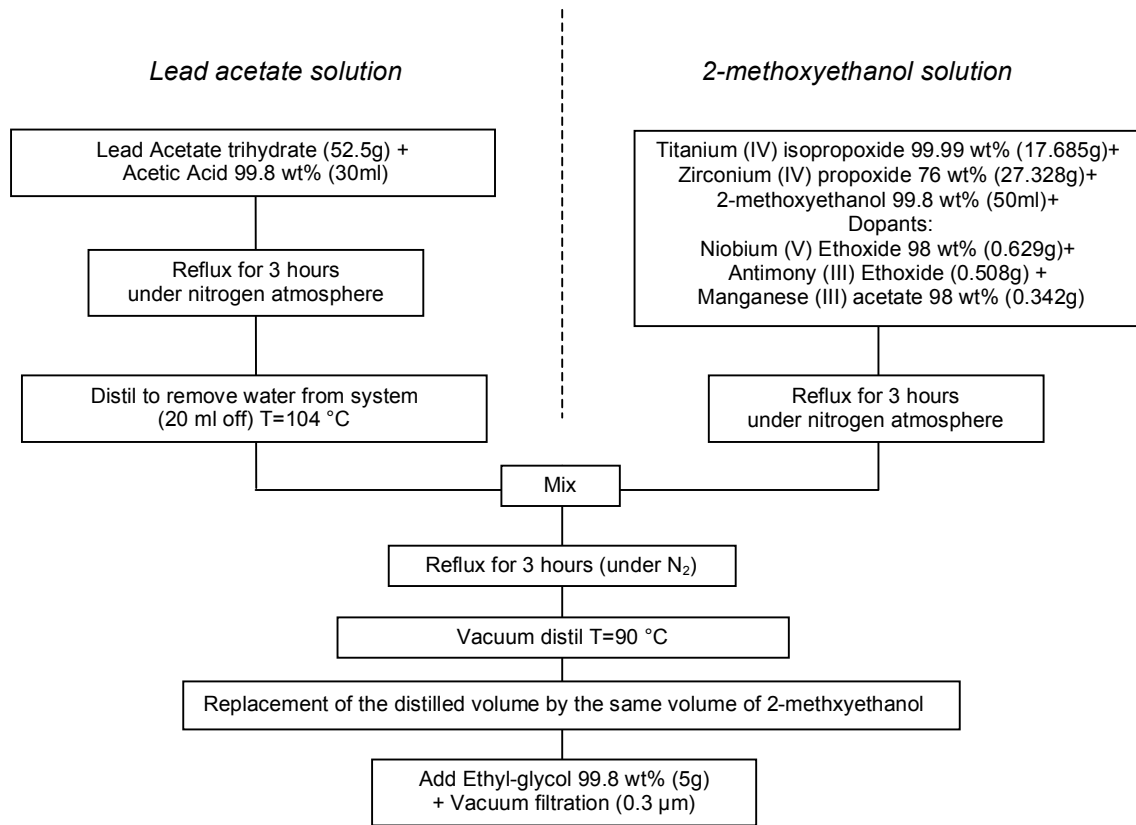


Figure 3.1: Schematic representation of the PZT sol preparation route

– Lead acetate solution

Under a fume hood, 52.5g lead acetate trihydrate was dissolved in 30ml acetic acid in a round-bottomed flask (250ml). This lead acetate solution was refluxed for 3 hours under nitrogen (Figure 3.2). Distilling off 20 ml of a water-based mixture performed the dehydration of this solution. The temperature plateaus at 100-104°C.

– 2-methoxyethanol solution

The titanium (IV) isopropoxide (17.7g), zirconium (IV) n-propoxide (27.5g), niobium (V) ethoxide (0.63g), antimony (III) ethoxide (0.51g, Inorgtech, 99.999%) and manganese (II) acetate (0.34g, Inorgtech, 99.999%) were weighed under nitrogen in a 250ml round-bottomed flask. The solvent, 2-methoxyethanol (2ME) (50ml, Aldrich, anhydrous 99.8%) was added. The solution was refluxed under nitrogen for 3 hours.

- Combination of the lead acetate solution and the 2-methoxyethanol solution

The 2-methoxyethanol (2ME) and the lead-acetate trihydrate solution were mixed together in a round-bottomed flask (250ml) and refluxed under N_2 to drive the ligand exchange (Figure 3.2).

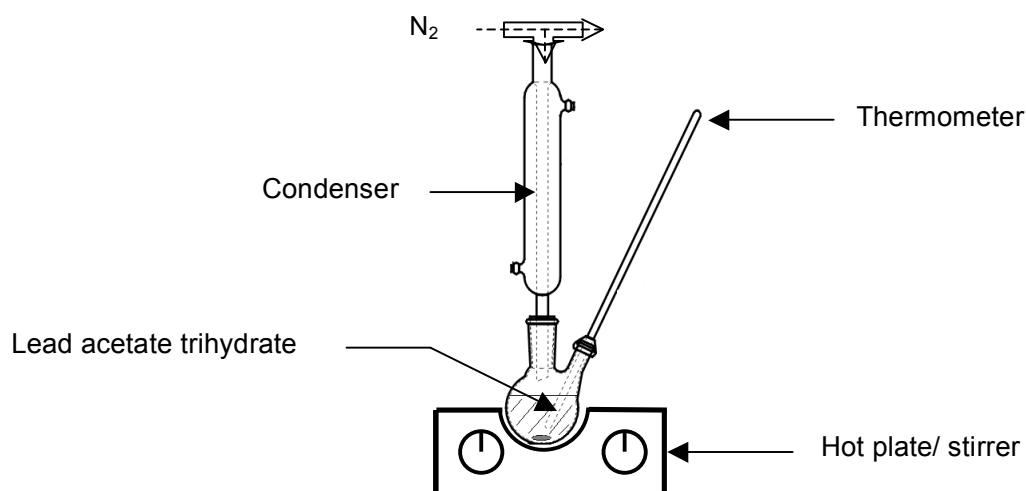


Figure 3.2: Schematic of the reflux (under nitrogen) experimental set-up

At this stage the solution was cloudy, the lead component has a lower solubility than the acetic acid. The synthesis was completed by a final vacuum distillation (Figure 3.3). The temperature first plateaus at approximately 90°C . This plateau corresponds to the boiling point of propanol used as a solvent to stabilize the zirconium propoxide. This solvent is also generated during the hydrolysis process. A second plateau is observed at $102\text{-}104^\circ\text{C}$ corresponding to the dehydration of the sol.

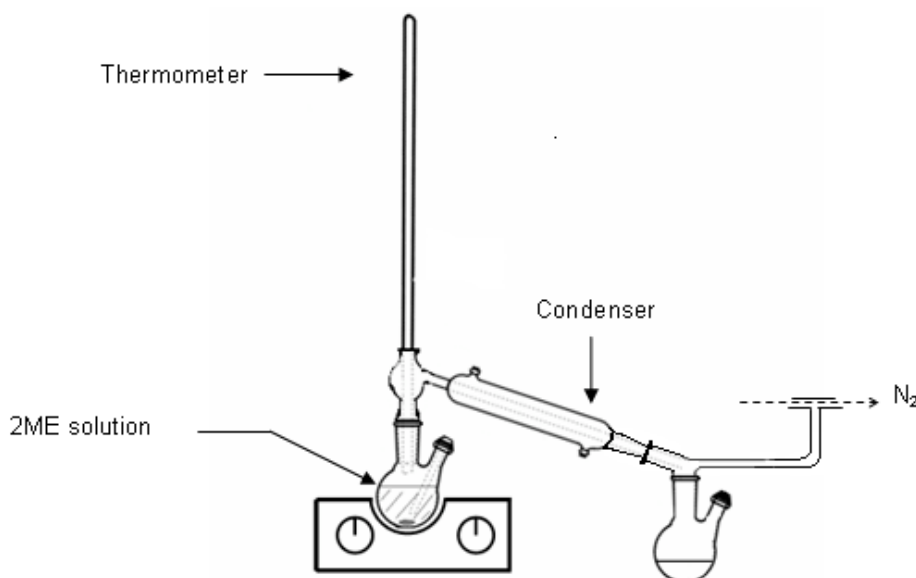


Figure 3.3: Schematic of the vacuum distillation experimental set-up

Between 50 and 70 ml of a mixture of water and by-products are removed during this distillation stage. The sol becomes yellow and clear. The amount of solution removed, during the final distillation, is replaced by the same amount of 2-methoxyethanol to attain a sol concentration of 1.1 M. The sol is vacuum-filtered sol (0.5 μ m) and stabilized by the addition of 5g of ethylene glycol (Aldrich 99.8%).

3.2.2. Composite slurry

The composite slurry, used to make thick film, is a mixture of PZT sol and powder. It is characterised by the ratio of PZT powder mass to volume of PZT sol liquid phase (see Table 3.2).

Table 3.1: Composition of the slurry used - sintering aid-assisted composite

PZT Powder (PZ 26, Ferroperm, DK)-Hard	45 g
Dispersant KR 55 (Ken React Lica 38, isopropanol isooctylalcohol)	0.9 g
PZT Sol (of similar composition than the PZT powder)	30 ml
Cu ₂ O/PbO (sintering aid)	0.3105 g/1.926 g
Zirconia balls milling media	200 g

The sintering aid Cu₂O/PbO was weighed in a 125ml flask. The weight was calculated to be equal to 4.7 wt.% of the total powder loading in the sol. The commercial PZT powder (PZ26, Ferroperm, DK) was used. The dispersant KR55 and PZ26 powder were weighed under nitrogen in the same 125 ml flask followed by the addition of sol and zirconia milling media. The slurry was then ball-mixed for 24 hours to produce a stable suspension. The slurry density obtained was 2.2 g.ml⁻¹.

3.3 Sol and composite rheology

3.3.1 Sol rheology

The sol viscosity was measured using a falling ball viscometer. A glass tube, a cap and a ball make up the falling ball viscometer. The diameter of the ball was 6.2mm, the tube was 220mm long and its internal diameter was 10.6mm. The velocity of the ball was determined by measuring the time, Δt , for the ball to cover the distance Δz , determined by the geometry of the viscometer. These measurements were repeated three times for each sol. The viscosity is given by Equation 3.1.

$$\eta = k \cdot (\rho_{\text{ball}} - \rho_{\text{liquid}}) \Delta t \quad \text{Equation 3.1}$$

Where η is the viscosity in centipoises (cP), k is a constant depending on the geometry of the viscometer (equal to 0.275), Δt is the time (in minutes) for the falling ball to cover the distance Δz , and ρ_{ball} is the density of the ball (8.02g/cm^3).

3.3.2 Composite slurry rheology

Because the viscosity of the composite was too high to be measured using the falling ball method, the viscosity was measured using a “cup and bob” configuration rheometer (Bohlin Instruments) (Figure 3.4). This technique allows the presence of a cap above the sample. This cup is used to maintain a 2ME (solvent) saturated atmosphere throughout the experiment. It limits the drying of the composite slurry during testing. A pre-shear rate of 200 s^{-1} was applied to the sample for 30s to homogenise, because the composite slurry is a suspension and not a Newtonian fluid. The suspension was rested for 1min before each measurement to ensure that the suspension shear stress was constant and known between samples. The viscosity was measured 4 times at room temperature. The average of these measurements was taken as the final viscosity. The shear stress was measured as a function of an increasing and a decreasing shear rate, thus, a loop test was obtained. The shear rate was increased from 0.5s^{-1} to 150s^{-1} and then decreased from 150s^{-1} to 0.5s^{-1} . The apparatus was connected to a computer to integrate the data.

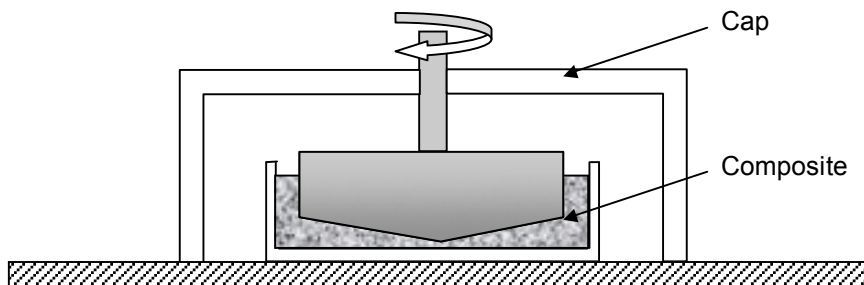


Figure 3.4: Schematic of the coaxial cylinder cup and bob configuration used to measure the composite viscosity.

3.4 Film and electrode deposition

3.4.1 Silicon wafer cleaning

Before the deposition of any layer, the silicon wafer substrates were spun at 1000rpm while a constant flow of first acetone and then isopropanol was maintained. Finally, to remove all organic components from the silicon substrate, the wafers were cleaned under an oxygen (20%)/ argon (80%) plasma (Polaron Plasma Barrel Etcher PT 7160 RF) for 10min at 1.5mbar with a power of 30W.

3.4.2 ZrO₂ diffusion barrier deposition

During the sintering process, Pb from the PZT layer diffuses into the silicon wafer, to form a lead silicate compound. To prevent this undesirable reaction, a ZrO₂ diffusion barrier is first spun on the silicon substrate. Table 3.1 gives details of the composition of the ZrO₂.

Table 3.1: Composition of the ZrO₂ diffusion barrier sol

Zirconium (IV) propoxide (75 wt% in propanol)	4.344g
Acetic acid (99.8 wt%)	3ml
Ethanol anhydride	47ml

47ml of ethanol anhydride (99.9%), known as ethanol absolute, and 3ml glacial acetic acid were measured, under nitrogen. The ethanol/acetic acid mix was then poured into a 250ml round-bottomed flask. 4.344g of zirconium (IV) propoxide was weighed under nitrogen into the round-bottomed flask. The solution was then stirred for one hour at room temperature. Three layers of this sol were spun on to the substrate to form a ZrO₂ diffusion barrier. Each layer was spun at 3000 rpm for 30 seconds, dried at 200°C and pyrolysed at 350°C for 30 seconds. The film was then sintered at 800°C for 10 min. The final thickness was 60 nm.

3.4.3 Electrode deposition

- Photoresist deposition, and patterning.

All electrodes were shaped using a photolithographic lift off process. As the photoresist chemicals are generally UV sensitive, this stage was performed in a yellow clean room to avoid any contamination before the UV exposure stage. A photoresist (S1818, Chestech UK) was spun onto the substrate at 4000 rpm for 60 seconds, and then baked at 115°C for 90 seconds. The photoresist thickness was 1.8 µm. Using a Karl Süss MLB21 mask aligner, with either an acetate sheet mask or an anti-reflective chrome mask on soda-lime glass, the photoresist was selectively exposed to UV light for 10 seconds. The electrode pattern was revealed by bathing for 60-75 seconds in the developer (MF-319).

- Ti/Pt electrodes deposition

The Ti/Pt electrode deposition was performed at room temperature using a multi-target sputtering machine (Nordiko Limited). To act as an adhesion layer between the substrate SiO₂/Si/SiO₂/ZrO₂ and the Pt, a thin titanium (8nm) layer was first deposited on top of the ZrO₂ by a RF magnetron sputtering from a titanium target (99.9%). Prior to deposition, the chamber vacuum was set to less than 10⁻⁷ torr. Argon was used as the sputter gas with a

pressure of 10 mtorr. The 300W power Ar plasma induces a Ti deposition rate of 0.3 nm/s. Without opening the chamber the Pt electrodes were deposited, on the same run, from a Pt target (99.99%). 100nm of platinum was deposited at 420V DC power at a rate of 1.7nm/s. The photoresist not exposed to UV was then removed with an ultrasound acetone bath. The metal deposited on top of this layer was removed with the photoresist revealing a patterned electrode structure.

For platinum features closer than 20 μ m to each other, a two-layer photoresist stack was used to facilitate selective removal of the deposited film. A thin layer of photoresist (LOR-2A, Chestech UK) was spun, prior to the S1818 photoresist layer, at 3000 rpm for 30 seconds, followed by a heat treatment on a hot plate at 115°C for 140 seconds. This technique is used for the fabrication of the final annular array device.

3.4.4 Thick film deposition

The substrates were fully coated with the slurry suspension and then spun at 2000 rpm for 30 seconds. The deposited film was then dried at 200°C for 60 seconds and pyrolysed at 450°C for 30 s to remove all organic components. The full film thickness was built up using multiple composite layer depositions and sol infiltrations (Figure 3.5). An infiltration step consists of spinning, on the green ceramic, a layer of a stock sol solution diluted with 2ME (20ml sol / 20ml 2 ME). Each infiltration step is followed by the same drying and pyrolysis treatments used to process the composite film, before the next infiltration step. The next composite layer was then deposited. Once the required number of infiltration layers had been completed, the whole process (composite layer(s) and infiltration sol layer(s)) can be repeated until the desired total thickness is obtained.

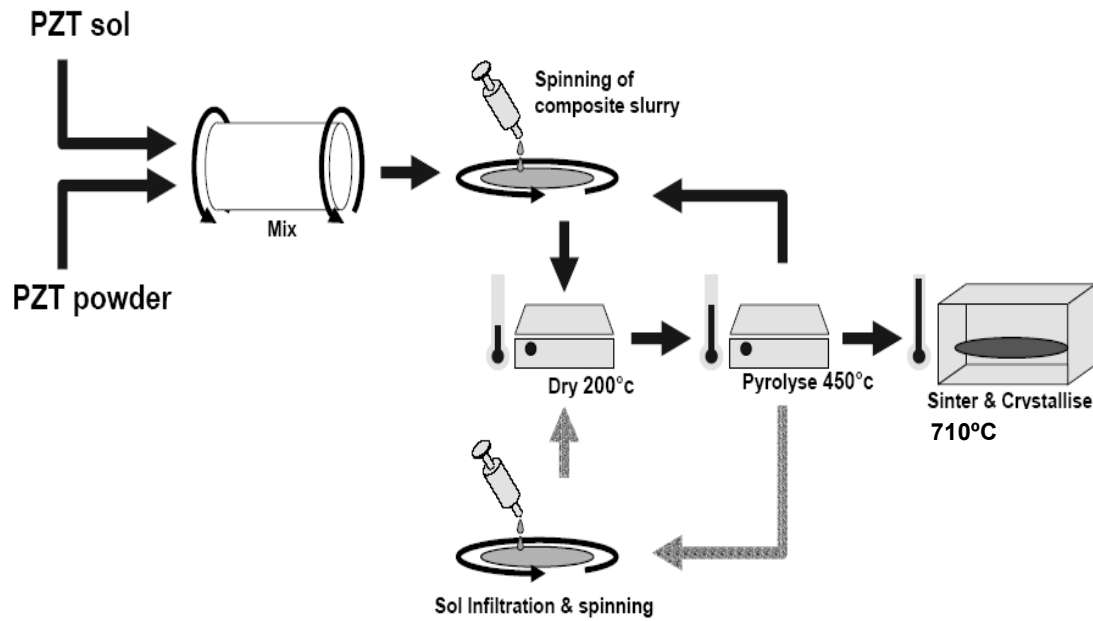


Figure 3.5: General schematic of the thick film deposition procedure using sol-gel/composite slurry including the intermediate sol infiltration stages.

To describe the film production in this way the notation is given by:

$$X[YC+ZS]$$

Y is the number of composite layers, Z the number of infiltrations per (YC) composite layers and is X the number of times the unit [YC+ZS] is repeated. Once the required number of layers was deposited, the wafer was subjected to a rapid thermal annealing process (R.T.A) or a conventional furnace thermal treatment (710°C/30min). A final cross section of the product is shown on Figure 3.6

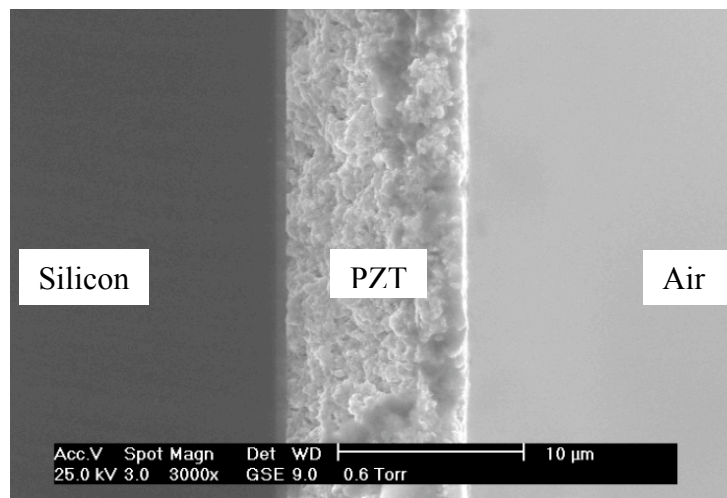


Figure 3.6: SEM micrograph of a 4[C+4S] PZT thick film cross section: 4 times [1composite layer+ 4 infiltrations sol].

3.5 Device micro-fabrication

3.5.1 Introduction

This section describes briefly the micro-fabrication techniques involved in the different etching steps used and developed to fabricate transducers presented in this work. PZT wet etching, silicon wet etching and dry etching, SiO₂ dry etching, and Pt dry etching are presented.

3.5.2 PZT wet etching

The wet etching of the PZT is carried out using a stock solution having the following proportions H₂O 95 / HCl 4.5 / HF 0.5 (vol. %). The films were wet etched at 50°C using a 50 vol. % diluted solution. Prior to wet etching, photoresist (AZ4562, Aldrich UK) was deposited by spin coating onto the PZT film at 1000rpm for 60 seconds, and then baked at 90°C for 180 seconds. The thickness photoresist achieved, using this technique, was 11-14µm. Using a Karl Süss MJB21 mask aligner, the photoresist was selectively exposed to UV light for 27s. The pattern was revealed after 90 seconds in the developer (AZ400K) diluted in water with a ratio of 1:4. Etching tests were conducted before and after final sintering of the PZT thick film to evaluate the effect of the high temperature-sintering regime on this wet etching technique. In order to understand the etching rate of this technique, the samples are soaked in the HF solution for a range of times and the resulting features characterised.

3.5.3 SiO₂ dry etching

The dry etching of the SiO₂ etch stop layer is the first stage of the device processing and conducted in order to reveal the silicon for further Si wet etching and to use the pattern for double-sided mask alignments. This step was carried out using a Reactive Ion Etching (RIE) machine (Plasmatech 80). A standard layer of S1818 photoresist was first deposited on the substrate and then selectively exposed to UV light using the mask aligner, and developed as discussed previously. The sample was etched using the conditions presented in table 3.2:

Table 3.2: RIE conditions used for silicon oxide

RIE	Oxygen (sccm)	Argon (sccm)	Trifluoromethane (CHF ₃) (sccm)	Pressure (sccm)	Power (W)	Etch rate (nm/min)
Silicon oxide	5	15	5	100	150	50

3.5.4 Silicon wet etching

The silicon etching was carried out in a solution of TMAH (Tetramethyl ammonium hydroxide, 12.5 wt. %), using silicon oxide as the etch stop layer. The experimental set up is shown in Figure 3.7. The sample was mounted, face down, on a glass plate using commercial mounting wax. The wax adhered the sample to the glass substrate and protected the PZT film from the etchant. Every 2.5 hours, the sample was removed from the etch bath and the wax sealing was re-applied. The etch bath temperature was fixed at 70°C and the etch rates was observed to be approximately 25 $\mu\text{m}/\text{h}$.

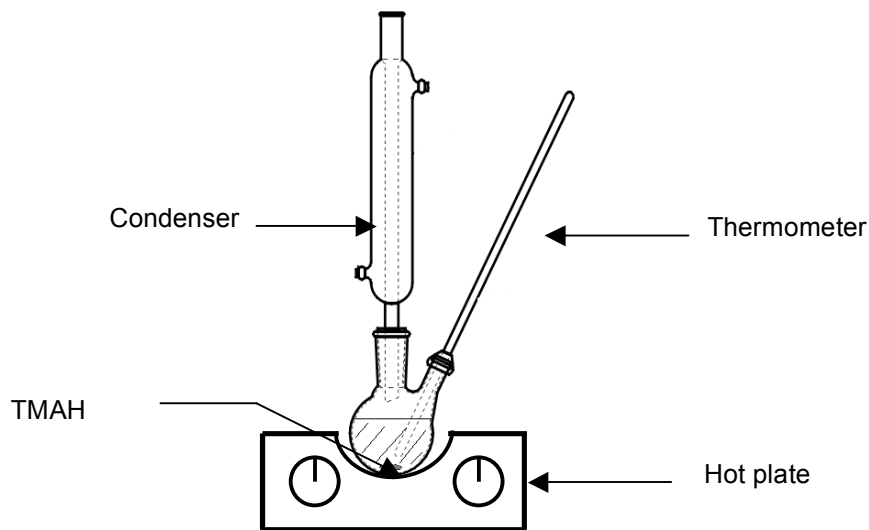


Figure 3.7: Silicon wet etching experimental set up.

The main drawback of this technology is that the mounting wax contaminates the TMAH solution, which slows down the already low etching rate. To etch faster the silicon, a dry etching process can be used: Deep Reactive Ion Etching (DRIE).

3.5.4 Silicon dry etching

In this process, etch depths of hundreds of microns can be achieved with almost vertical sidewalls. The primary technology is based on the pulsed or time-multiplexed etching process, the "Bosch process". Two different gas compositions are alternated in the reactor and each lasts for several seconds. The first gas is, C_4F_8 , which creates an inert passivation layer on the surface of the substrate. The second gas, a sulfur hexafluoride, SF_6 , constitutes a nearly isotropic plasma etch of the silicon. These etch/deposit steps are repeated many times resulting in a large number of very small isotropic etch steps taking place only at the bottom of the etched pits.

Prior to dry etching, photoresist (AZ4562, Aldrich UK) was deposited by spin coating onto the PZT film at 1000rpm for 60seconds, and then baked at 90°C for 180seconds. Two successive layers were deposited to achieve a thickness of photoresist 26-30µm. Using a Karl Süss MLB21 mask aligner, the photoresist was selectively exposed to UV light for 45s. The pattern was revealed after 180 seconds in the developer (AZ400K diluted in water with a ratio of 1:4). To protect the other side of the wafer (where the devices are) a photoresist layer (S1818) was spun onto the substrate at 4000 rpm for 60 seconds, and then baked at 90°C for 10 seconds. This thin photoresist layer allowed to glue this side of the wafer to another silicon wafer to protect the devices to be etched during the DRIE process. The wafer was then placed with the thick patterned photoresist facing up in a DRIE for the deep silicon etching process.

3.6 Microstructural evaluation

3.6.1 Introduction

This section presents the instruments used for the microstructural evaluation of the device: Scanning Electron Microscope (SEM), Scanning Field Emission Gun microscope (SFEG), and the X-ray diffraction instrument.

3.6.2 Scanning Electron Micrograph

A SEM (ABT-55 or Cambridge Stereoscan 250) was used to examine the surface finish of the films, the fracture surface and the polished cross sections. Some samples were coated with carbon to prevent charging prior to imaging in the SEM.

3.6.3 Scanning Field Emission Gun microscope (SFEG)

The Philips XL30-SFEG is a high-resolution scanning electron microscope capable of resolutions better than 2 nm, magnifications over $6 \cdot 10^5$. It has been used from voltages from 1kV up to 30 kV. At the lower potentials of the beam, it can obtain excellent topographic detail and minimum charging while at the higher potentials it can get the optimum resolution and perform efficient EDS analyses. This instrument includes an EDAX Phoenix EDS system and a TexSEM Laboratories EBSD system. The EDS (energy dispersive x- ray spectroscopy) system can be used for elemental analyses. SFEG was used to examine the PZT sol crystallization on PZ26.

3.6.4 X-Ray Diffraction

Thick PZT films and Pt films were characterized by XRD using a Siemens D-5005 diffractometer. The conditions used were a 2θ range of 10 to 90° with a step of 0.02° and a dwell time of 1 second.

3.6.5 Images analysis

The crack area density along with the film porosity was measured using the image analysis Photoshop-element. The crack area density was defined as the ratio between the area representing by the cracks and the total area. The porosity was evaluated for each layer of composite (from a cross-section) by evaluating the pore area compared to the total area.

3.6.6 The Dektak® Surface Profiler.

Assuming an initially flat substrate, depositing a thick or thin film lead the substrate to bend in either a concave or convex curvature. This curvature was measured using the Dektak Surface Profiler (Veeco). The Surface Profiler accurately measures vertical features ranging in height from ~100 micron to ~50 angstroms on a wide variety of substrate surfaces.

3.7 Poling

3.7.1 Contact poling

In order to exhibit piezoelectric properties and resonance activity, the PZT thick film must be poled. The contact poling technique was used during this project. Two probes, from a microprobe station, were connected to the bottom and the top electrode. The sample was heated to different temperatures and had different voltages applied for five minutes to determine the optimum poling conditions (chapter 6). Generally the samples were cooled under voltage.

3.7.2 Corona poling

As many devices are present on an entire wafer, corona poling was used as an alternative to standard single point poling. This technique becomes very useful for poling an annular array with many elements which have to be poled simultaneously. Corona poling offers this advantage. The voltage was applied using a single needle 4cm above the ground the copper base plate (Figure 3.8). The positive charges created at the needle tip provoke the ionisation

of the air molecules into positive species, which are responsible for the corona discharge. A PTFE (polytetrafluoroethylene) sheet shielded the copper plate areas still exposed to the electric field. The devices were poled at between 20 and 30kV for 10min at about 130°C, and cooled under voltage.

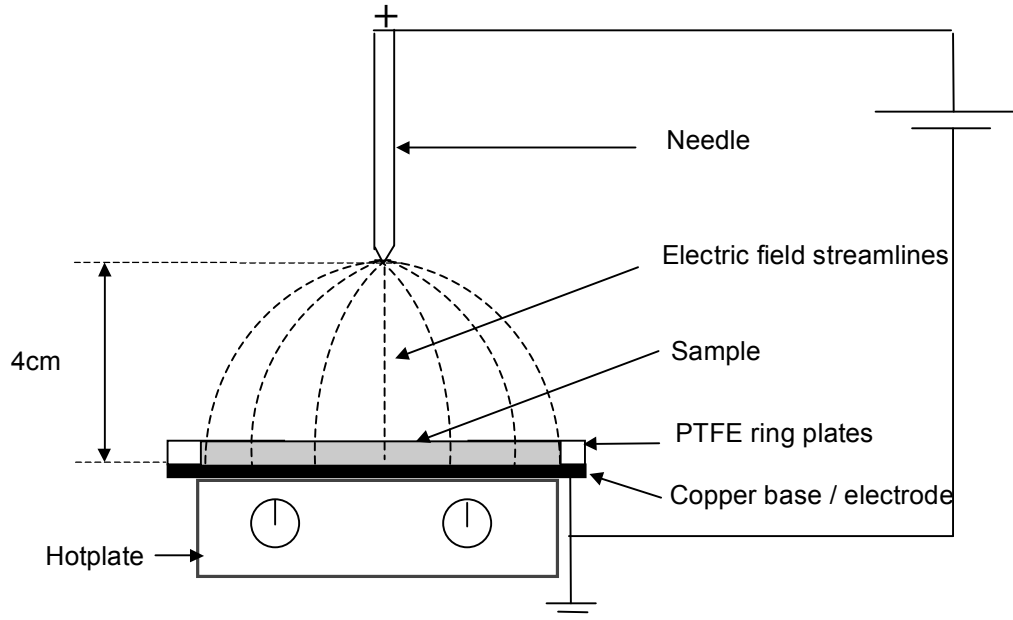


Figure 3.8: Schematic of the corona poling set up.

3.8 Measurements of device properties

3.8.1 Dielectric properties

To evaluate the capacitance and the dielectric loss at a low voltage of 0.1V and a frequency of 1kHz a Wayne Kerr 6425 Analyser was used. For each electrode, the capacitance value was taken as the average of 3 readings. The relative permittivity was then calculated using the measured capacitance, the thickness of the film and the area of the top electrode (Equation 2.1).

3.8.2 Piezoelectric Measurement

d_{33f} (the subscript f refers to the effective film value) values were measured using a Berlincourt Piezometer (Takecontrol System PM 25). This classical technique involves measuring the transverse piezoelectric value by applying a point load in the centre of the sample. This point load often damaged top electrode. An average of several measurements is a necessity (See Chapter 6.8). The e_{31f} piezoelectric coefficients were also determined using the Berlincourt Piezometer by using a method determined by Southin [2001]. The technique involves by applying a point load in the centre of the sample supported by a ring such that the

contribution of the piezoelectric coefficient e_{31} is generated. In this way, the measured piezoelectric value represents then the sum of both transverse and longitudinal piezoelectric value such that $d_{measured} = d_{33f} + e_{31f} [f(\sigma_r) + f(\sigma_t)]$ where σ_r and σ_t are the radial and tangential stress. The e_{31f} piezoelectric coefficient was calculated using this equation by measuring $d_{measured}$ for different size of ring (from 0 to 9mm).

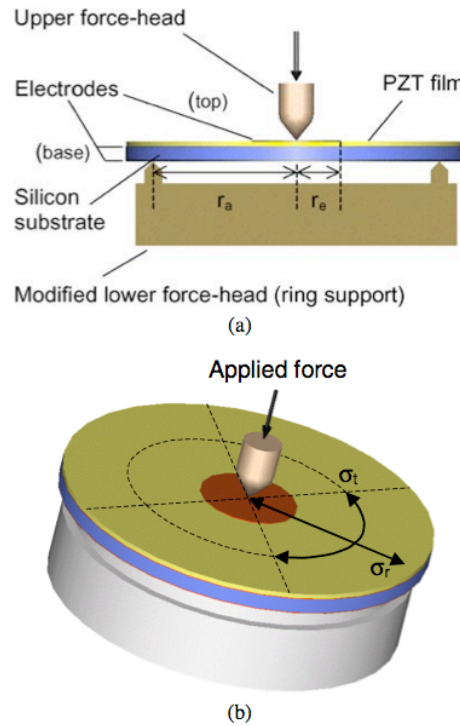


Figure 3.9: Schematic diagrams of (a) the test sample with a support ring and (b) the load geometry [Southin *et al.* 2001].

3.8.3 Resonance frequency measurement

3.8.3.1 introduction to S-parameter

Scattering parameters or S-parameters, in the same way as the admittance (Y) or the impedance (Z), describe the performance of a transducer at high frequency. They are the reflection and the transmission coefficient between the incident and the transmitted waves. S-parameters are usually measured with the device embedded between a $Z_0=50\Omega$ load (wires). If $|a_i|^2$ is power of the wave traveling towards the two-port gate (the sample), and $|b_i|^2$ is the power of the wave reflected back from the two-port gate, four S-parameters, defined by Equation 3.1, are required [Sischka, 2002].

$$\begin{pmatrix} |b_1|^2 \\ |b_2|^2 \end{pmatrix} = \begin{pmatrix} |S_{11}|^2 & |S_{12}|^2 \\ |S_{21}|^2 & |S_{11}|^2 \end{pmatrix} \cdot \begin{pmatrix} |a_1|^2 \\ |a_2|^2 \end{pmatrix} \quad \text{Equation 3.1}$$

S parameters are then:

- S_{11} : reflection coefficient of the input or power reflected from port 1
- S_{22} : reflection coefficient of the output or power reflected from port 2
- S_{21} : forward transmission gain or power transmitted from port 2 to port 1
- S_{12} : reverse transmission gain or power transmitted from port 1 to port 2

For a better insight of what represents the S parameters, considering them individually can help. Equation 3.2 and Figure 3.10 illustrates how a device tested by a network analyser can be understood through these S parameters.

$$\begin{aligned}
 S_{11} &= \frac{b_1}{a_1} = \frac{V_{\text{reflected at port 1}}}{V_{\text{toward port 1}}} \text{ if } a_2 = 0 & S_{12} &= \frac{b_1}{a_1} = \frac{V_{\text{out of port 1}}}{V_{\text{towards port 2}}} \text{ if } a_1 = 0 \\
 S_{21} &= \frac{b_2}{a_1} = \frac{V_{\text{out of port 2}}}{V_{\text{towards port 1}}} \text{ if } a_2 = 0 & S_{22} &= \frac{b_2}{a_2} = \frac{V_{\text{reflected at port 2}}}{V_{\text{towards port 2}}} \text{ if } a_1 = 0
 \end{aligned}
 \tag{Equation 3.2}$$

S parameter gives normalised amplitudes for the voltage V and the current I (Equation 3.3 and 3.4) [Sischka, 2002].

$$a_i = \frac{V_{\text{towards-twoport(sample)}}}{\sqrt{Z_o}} \tag{Equation 3.3}$$

$$b_i = \frac{V_{\text{Away-from-twoport(sample)}}}{\sqrt{Z_o}} \tag{Equation 3.4}$$

Sischka [2002] states that S_{11} and S_{21} are determined by measuring the magnitude and phase of the incident, reflected and the transmitted signals when the output is terminated in a perfect Z_o load. Anything other than a perfect load will result in a_1 or a_2 not being zero (which violates the definition for S-parameters). When the sample is connected to the network analyser a perfect termination is required. This means that a perfect contact of the different connections and a perfect impedance matching between the load, the probes and network analyser is required. Because this rarely occurs, a calibration of the Vector Network Analyser (VNA) correcting S-parameter measurements need to be performed at every run of measurements. In this work, the calibration of the A 8753D Hewlett Packard VNA (Vector Network Analyser) was carried out with an impedance standard substrate (ISS101-190) and SOLT (Short, Open, Load, Through) method. This VNA was designed to measure S-parameters from 30 kHz to 3 GHz. (Figure 3.10)

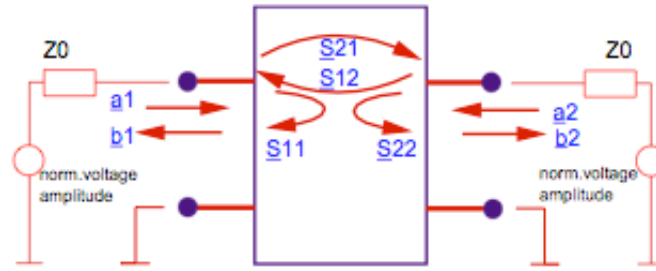


Figure 3.10: Complete representation of the S-parameter involved in a two-port network representing the sample. http://eesof.tm.agilent.com/docs/iccap2002/MDLGBOOK/1MEASUREMENTS/3VNA/3SPAR/1SparBasics_1.pdf

3.8.3.2 S_{21} Parameter

The S_{12} measurement was measured on a Summit 9000 analytical probe station connected using ACP40 (GSG200) probes. These probes are designed with a ground-signal-ground configuration. In addition to Figure 3.10, Figure 3.11 is another way to represent the S_{21} measurement via an electrical equivalent circuit.

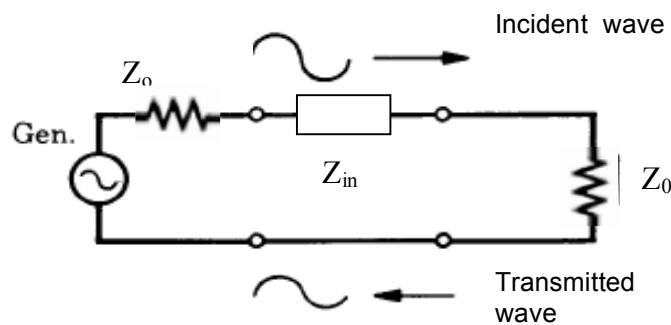


Figure 3.11: The equivalent circuit of the S_{21} measurement

The equivalent equation used to model this parameter is given by Equation 3.5 which represents this parameter directly in decibel (db). Z_0 represents the load of impedance due to the wires and Z_{in} the input impedance of the sample.

$$S_{21}(db) = 20 \log \left| \frac{2Z_0}{Z_{in} + 2Z_0} \right| \quad \text{Equation 3.5}$$

Figure 3.13 shows a typical result obtained for the S_{21} parameter.

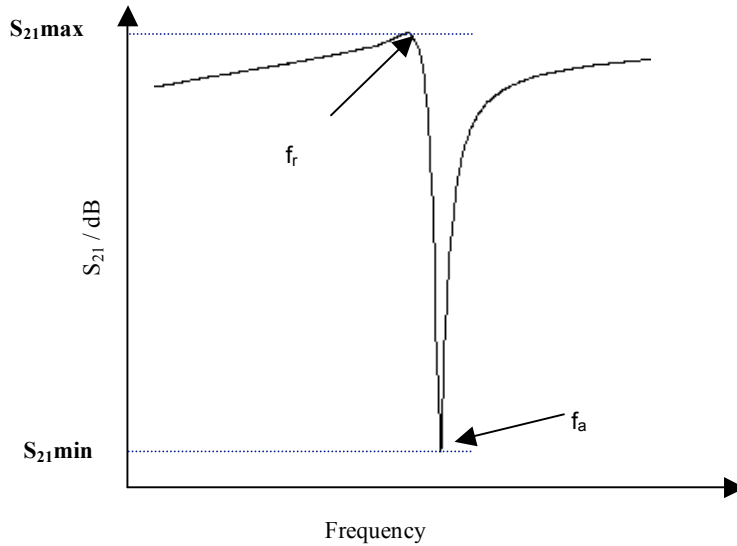


Figure 3.13: Typical result obtained for the S_{21} parameter at the frequency of resonance, (f_r). f_a represents the anti-resonant frequency.

3.8.3.3 S_{11} measurement

S_{11} is simply a coefficient illustrating the impedance ratio between the incident and reflected wave by the sample (Figure 3.11).

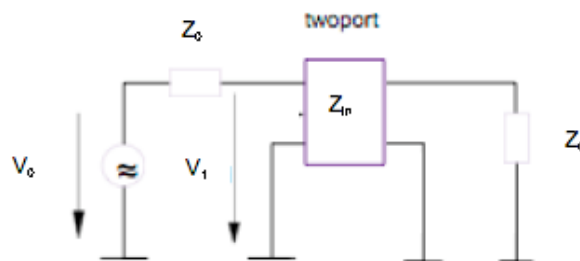


Figure 3.13: Schematic two ports representation of the S_{11} parameter.

Under the assumption that the complex component of impedance at port 1 is Z_{in} and Z_o is the wire impedance, or the system impedance, S_{11} can be represented by Equation 3.6.

$$S_{11} = \frac{Z_{in} - Z_o}{Z_{in} + Z_o} = 2 \frac{V_1}{V_0} - 1 \tag{Equation 3.6}$$

In decibel the final Equation 3.6 becomes Equation 3.7.

$$S_{11}(db) = 20 \log \left| \frac{Z_{in} - Z_o}{Z_{in} + Z_o} \right| \tag{Equation 3.7}$$

Some measurement issues explained in Chapter 7 required the measure of this parameter in an unusual way. With a simple BNC cable, the signal was connected to the bottom electrode, and the ground of the BNC cable was connected to the top electrode. A microbe probe station was designed and fabricated for the purpose (Figure 3.12).

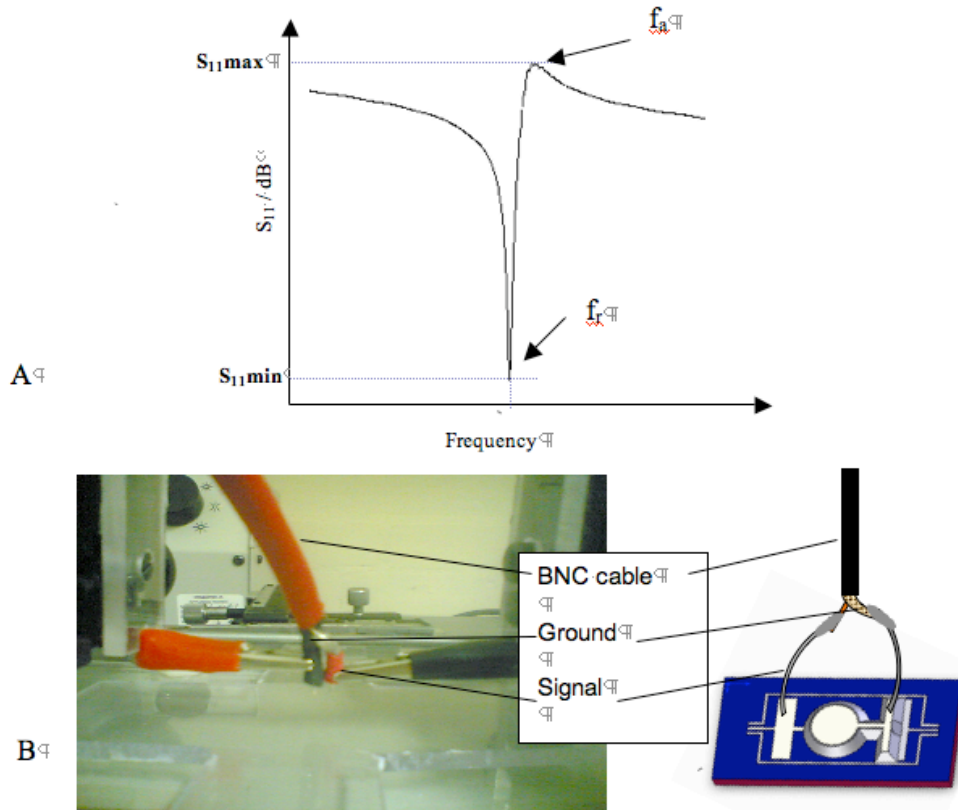


Figure 3.14: Probe station developed to measure the S_{11} parameter (B) and typical result obtain for this parameter, f_r is the resonance frequency and f_a the anti-resonance frequency (A).

Chapter 4

Material design and thick film development

4.1 Introduction

Materials are developed to serve the products realisation. Chemical composition and crystalline structure are not the only criteria used to choose a material. A third criterion was to also be considered: the microstructure of the material, or the mesoscopic organisation of the material. This parameter generates information on how to design the product and to improve the material properties. This chapter is mainly a description of the material used in this work at the mesoscopic scale for both product design and material properties.

The first section is a brief review of the composite PZT used for the thick film fabrication. The main components of this composite are presented, *i.e.* the PZT powder and sol. Information on viscosity and grain size distribution and shape are presented.

The second section explains how to improve the densification of the material with PZT sol infiltration. These infiltrations are revealed to be a key point of the fabrication process of the thick film.

The third section explains how to achieve a 35 μ m PZT thick film. Development of different adhesion on different substrates will then be studied. Once a good surface finish is achieved for such thickness, another challenge will be to shape the film into a device.

The fourth section will then describe the wet etching used in this work. The advantage and limitation of this technology will be presented in another section.

The device was then sintered and the crystallisation of the sol on the PZ26 grain occurs during that stage. The effect of the crystallisation at a nanometre scale will be presented in this short section.

The work presented in this chapter is mainly a description of this new material, the composite PZ26/PZT sol. It represents the learning stage and the discovery of how to process this material.

4.2 PZT material

4.2.1 PZT Powder

The thick PZT film is made from a mix of a PZT sol and a PZT powder (PZ26) (see section 3.2). The PZT powder is a PZ26 micro-size powder from Ferroperm. Figure 4.1 shows a SEM micrograph and a particle diameter analysis graphic of the as received PZ26 powder. Both show the size (diameter) particle distribution to be between 0.15 and 2 μ m. However, a simple analysis of Figure 4.1 shows an uneven distribution.

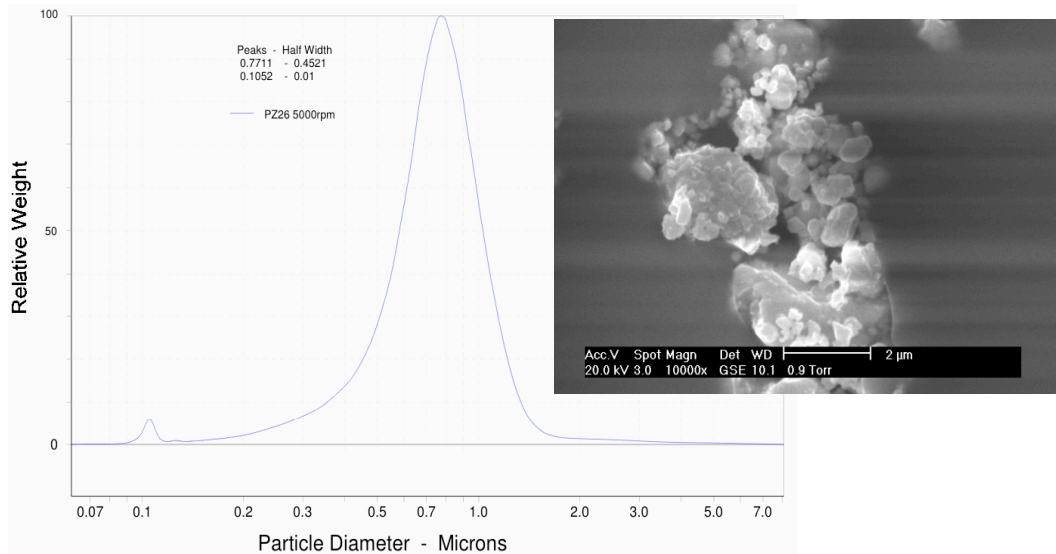


Figure 4.1: SEM micrograph and a particle diameter analysis graphic of the PZ26 powder. Mean value of particle diameter is equal to $0.74\mu\text{m}$.

The larger the particle, the heavier it will be. Hence, for an equal relative weight of particles there will be numerically more small particles than large particles. The majority of the particles are then in the submicron range in terms of diameter. This is an important consideration when the film thickness of one layer of composite is between $1.5\text{-}2.2\ \mu\text{m}$ i.e. equivalent to a maximum of 3 grains thick.

4.2.2 Sol and slurry viscosities

The sol exhibits a viscosity of $4.8\ \text{mPa}\cdot\text{s}$, measured with the falling ball viscometer, and a density of $1.3\ \text{g}\cdot\text{cm}^{-3}$. The resulting PZT slurry used in this project shows a density of $2.2\ \text{g}\cdot\text{cm}^{-3}$, and a viscosity of $0.35\ \text{Pa}\cdot\text{s}$ at $200\ \text{s}^{-1}$ shear rate value (Figure 4.2). This viscosity is constant for a higher shear rate, and corresponds to the state of viscosity of the slurry when it is spun at 2000rpm.

The composite slurry was spun, dried, and infiltrated with the infiltration sol (50% PZT sol/50% 2methoxyethanol)(see section 3.2). The PZT infiltration sol exhibited a density of $0.9\ \text{g}/\text{cm}^3$, and a viscosity of $2.3\ \text{mPa}\cdot\text{s}$.

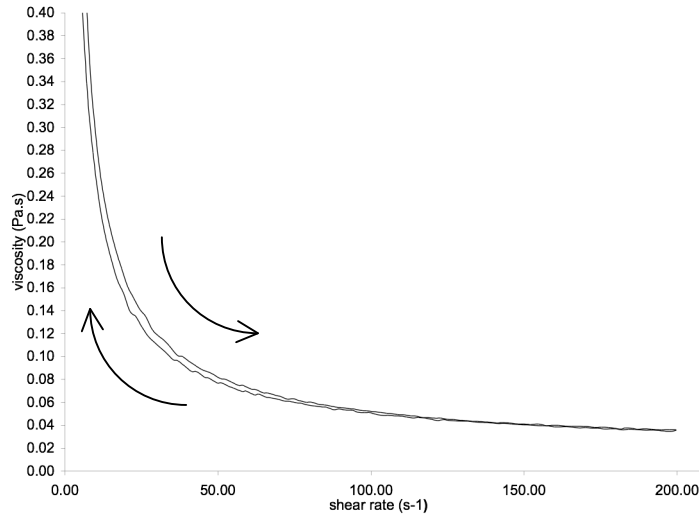


Figure 4.2: Viscosity of a 2.2 g.cm^{-3} composite as a function of the shear rate, measured with a parallel plate rheometer.

The XRD analyses, following the 710°C treatment, reveals that the film is crystallised with a perovskite structure (Figure 4.3). The XRD pattern represents the randomly oriented tetragonal phase of the perovskite PZT phase as expected.

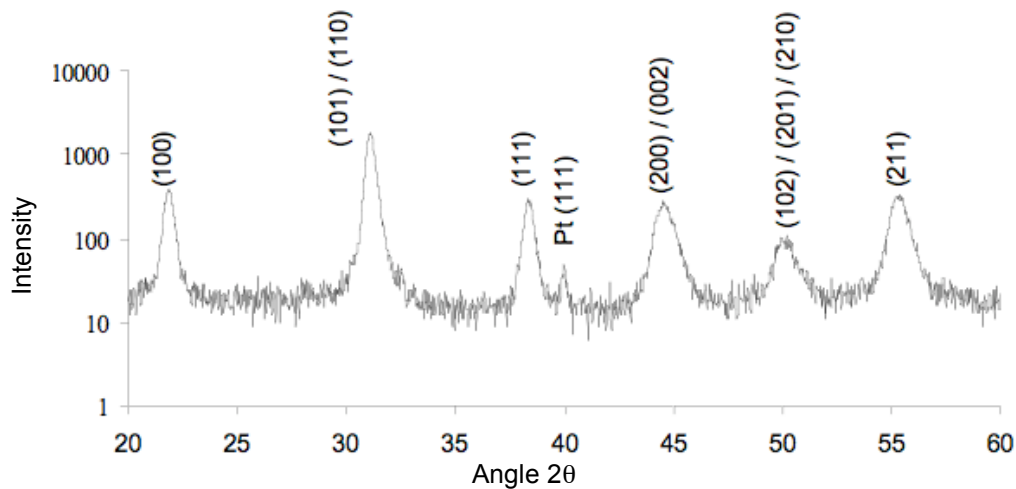
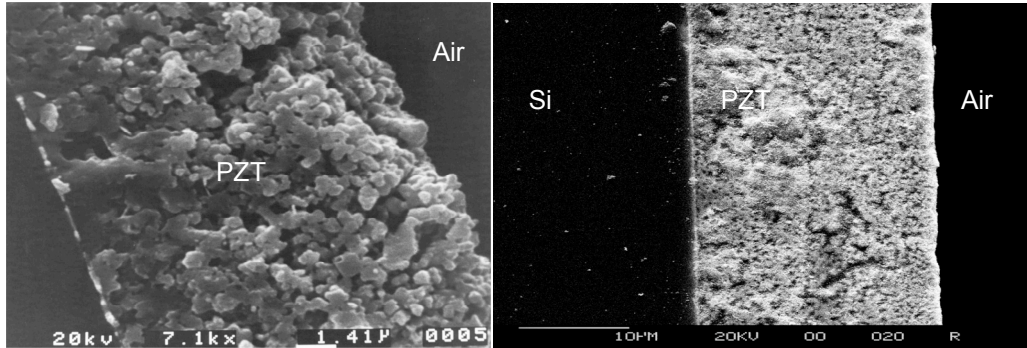


Figure 4.3 X-Ray diffraction pattern of a PZT thick film [C+4S] sintered at 710°C .

4.3 PZT Composite-Infiltration

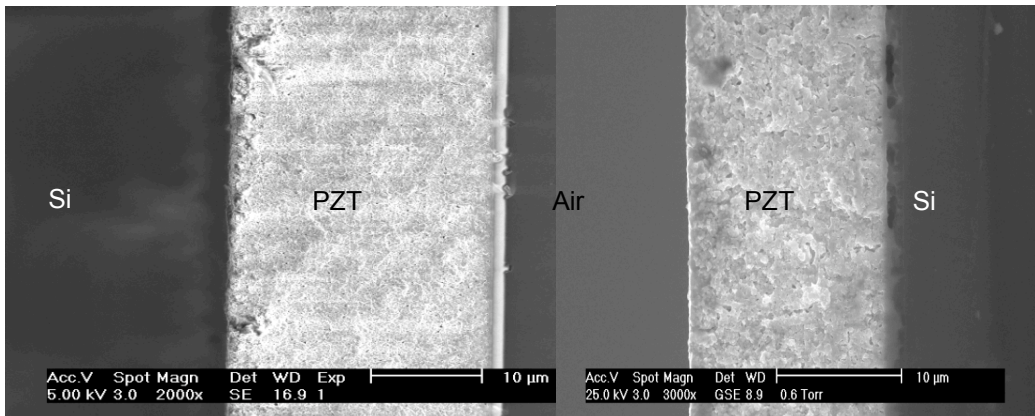
Infiltration of the composite is a crucial step of the thick film development. The infiltration process is used to improve the density of the material (section 3.4.4), and then to enhance the dielectric (section 6.2), piezoelectric (section 6.3), ferroelectric (section 6.4) and the electro-mechanical properties (chapter 7). To observe the effect of the infiltration process on

the thick film microstructure, different degrees of infiltrations are compared in this section. Figure 4.4 shows SEM images of fracture cross sections of films with different degrees of infiltrations.



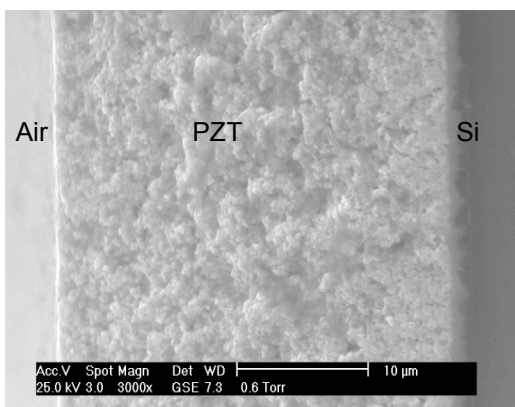
a) 0 infiltration

b) 1 infiltration



c) 2 infiltrations

d) 3 infiltrations



e) 4 infiltrations

Figure 4.4: SEM micrographs of fracture cross sections of the PZT composite film infiltrated from 0 to 4 times, images: a, b, c, d, and e respectively.

Figure 4.4 illustrates that the infiltration steps lead to a densification of the film. Analysing the pictures shows that the infiltrations densify the material gradually (Figure 4.5).

Pictures of samples with different levels of infiltration were transformed into a contrasted grey scale images, and the black areas were supposed to be porosity. It is understood that these supposed pores were compared with the original picture to verify their nature for this analysis. A pore was considered to exist if it looked like a pore in both pictures.

This analysis considers just the surface of the fracture cross-sections, not the volume. A fracture cross section is normally not random: it normally follows the path of the weakest material. However, in this case, the PZT is on a $525\mu\text{m}$ silicon substrate. When the sample is being broken, the silicon material dictates the fracture path, not the PZT. As a first approximation, the PZT fracture cross-sections are then considered to be random and that they can be used to obtain an approximation of the volume porosity where the area fraction of porosity is equal to the volume fraction. The results of this analysis are presented in Figure 4.5.

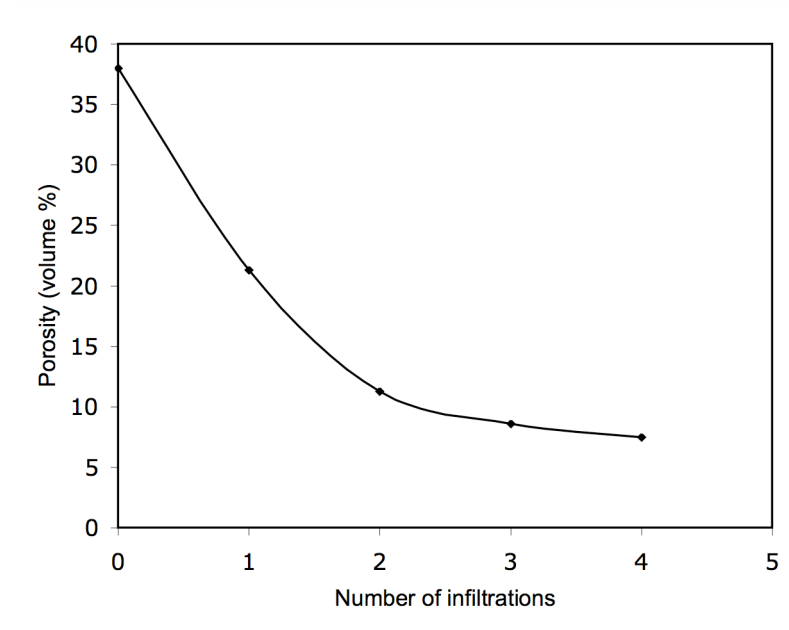


Figure 4.5: Representation of the variation of volume percent of porosity samples infiltrated from 0 to 4 times.

For each infiltration step, the same amount of infiltration sol is deposited on the surface of the film. If the pores were always opened, the sol will be received and dried at each infiltration step. Then, because the size of the pores should decrease at each infiltration, the total volume percent of porosity filled should decrease at each infiltration. Figure 4.5 shows such a non-linear variation of the material density with the number of infiltration steps. The principal source of this phenomenon should be related to the size of the pores on the surface. Actually, this size determines if the infiltration sol penetrates the material or not. Below, a certain small size of pores on the film surface, the spontaneous penetration of the infiltration sol into the

pores localised on the film surface should stop. The viscosity of the infiltration sol is known, but the work of Kornev [2000] shows some information is missing in this work in order to evaluate theoretically this minimum pore size that allows such penetration. It is necessary to know the surface tension, and the weight of each drop of infiltration sol. Only an experimental approach will be given here.

For this experimental approach, to understand at what size of pore the infiltration stops to infiltrate, Figure 4.6 illustrates the surface of the composite film with respect to the different degrees of sol infiltration of 1 layer of PZT composite. It has to be remembered that the composite and the infiltration sol were treated at 3 different temperatures: 200°C (burning of the organics and solvent evaporation), 450°C pyrolysis, 710°C sintering (see chapter 3). An infiltration was always spun unto the PZT film after the pyrolysis step. The pictures were then taken after the 450°C temperature treatment. Figure 4.7 illustrates the size of pores on the surface of the composite film as a function of the infiltration number, after the 450°C temperature treatment. The pores have an oval-like shape. An average of the maximum diameter of the porosity (Figure 4.7 plain line) and the average of the minimum diameter of the porosity (Figure 4.7 dashed line) found from the Photoshop picture analyse from the samples represented in Figure 4.6, and from 10 others samples is shown. It shows that the size of the porosity, after pyrolysis, decreased rapidly, and that the pores after the 2nd infiltration step have a constant size of ~100nm of length and a ~ 10nm of width. It seems that after this 2nd infiltration step the sol penetrated the composite via the cracks and not via the pores. This confirms the result obtained for the change in density of the film shown in Figure 4.5. If the porosity on the surface is not infiltrated after the second infiltration the density of the material will not increase as expected.

At the 2nd infiltration the size of cracks exhibit a maximum width of ~500nm, and a minimum width ~300nm. The maximum width of the cracks after the 3rd infiltration remains approximately constant, and the minimum width is reduced to 10's of nanometres. The 4th infiltration exhibits cracks with a maximum width of 10's nm and a minimum width of 10nm.

It is also observable that the length of the cracks, as well as their number seems to be reduced considerably from the 2nd infiltration steps to the 4th.

It is hard to determine with this experiment what size of pore or cracks allow the penetration of the sol into the composite. However, it can be determined that the infiltration steps seems them to fully penetrate until a certain degree of infiltration. This occurs in 2 ways:

1. Infiltration through the "natural" porosity (i.e. surface porosity different than cracks).
2. Infiltration through the cracks.

The 2nd degree of infiltration is the limit, after that the third infiltration sol does not penetrate the "natural" porosity and sol seems to cover it. However, the sol infiltration still infiltrates the composite through the cracks. Part of the cracks (minimum width part) stop to be infiltrated. The sol then covers more and more of these parts of cracks with an increase of infiltration steps from the 3rd and the 4th infiltration. The overall pictures shown in Figure 4.6 and Figure 4.7, illustrate this phenomena well.

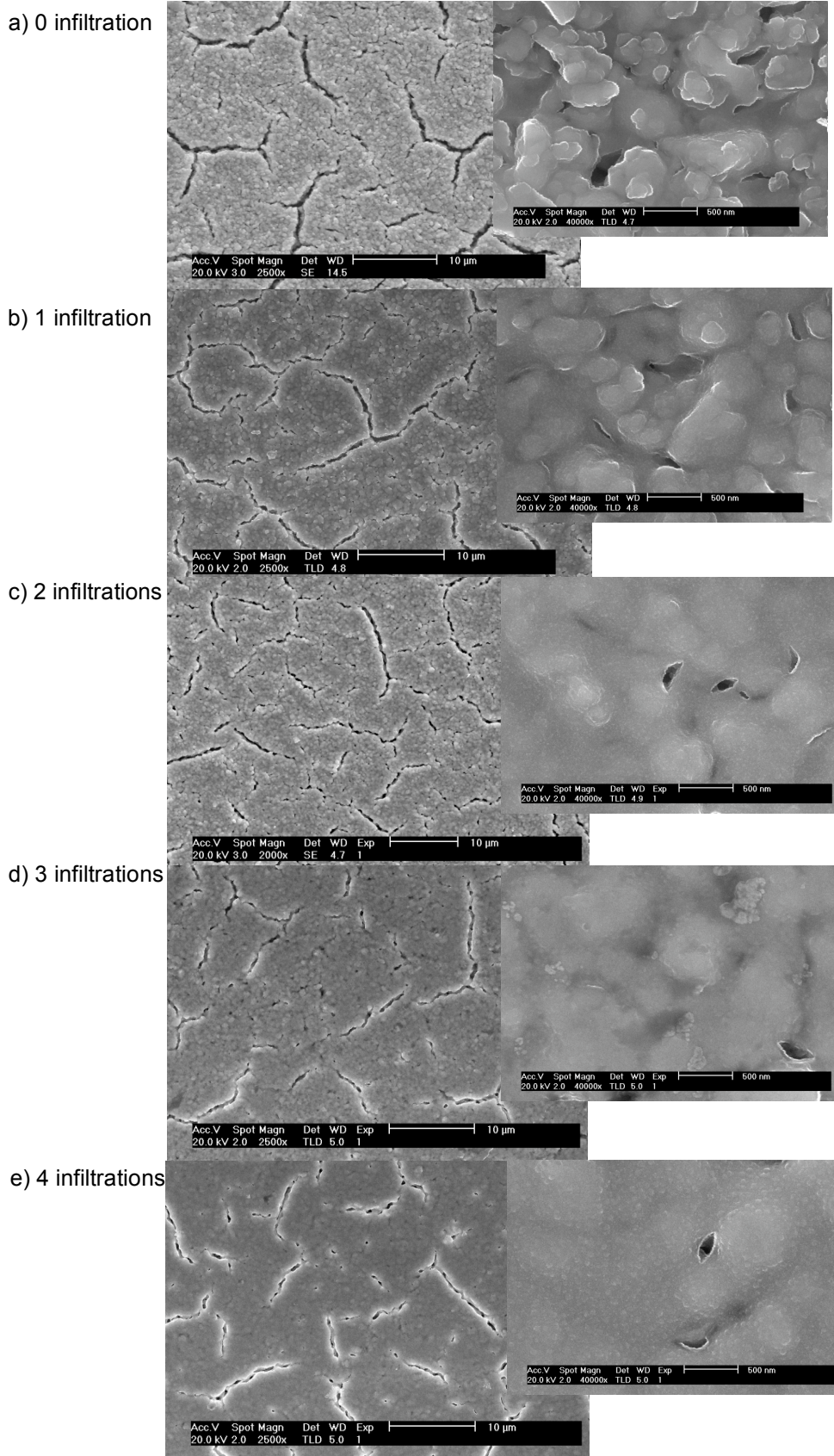


Figure 4.6: SEM micrographs of the surfaces of a single layer of PZT composite infiltrated 0 to 4 times. All the pictures were taken after the 450°C temperature treatment.

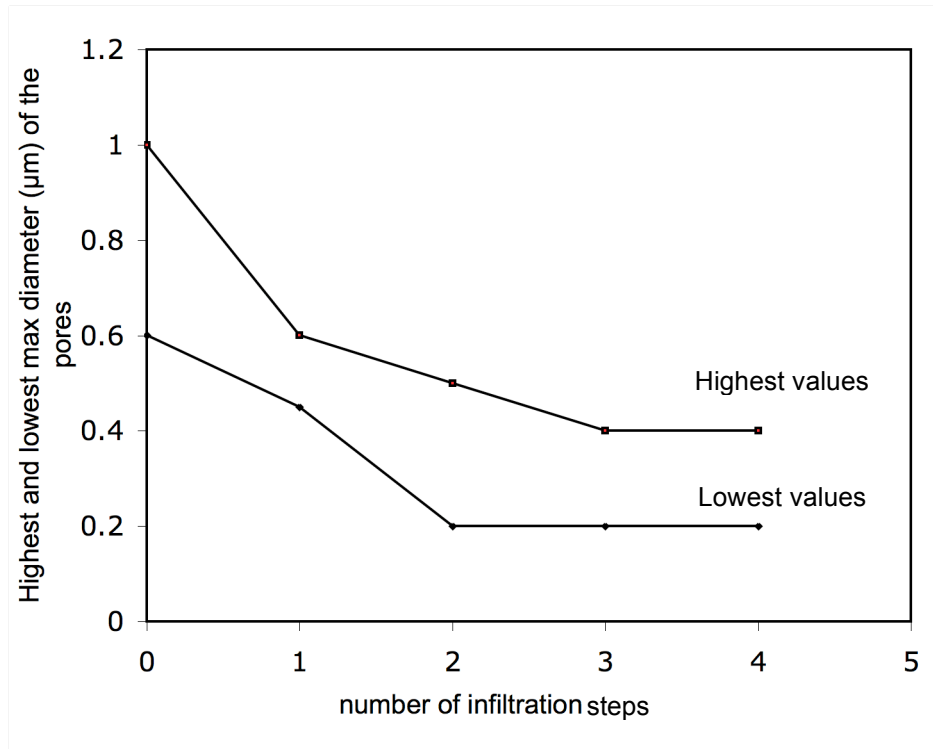


Figure 4.7: Size of pores on the surface of the composite film as a function of the infiltration degree (After the 450°C temperature treatment).

Figure 4.8 shows SEM micrograph of cross-sections of an un-sintered and sintered PZT composite film infiltrated 4 times, ($x[C+4S]$). It details how the infiltration of the cracks occurs: It reveals that an area of a denser composite is localised in the material surrounding the larger parts of the cracks. The pores around the cracks saturate like the pores of the surface and the cracks are filled with the sol until the cracks can't be infiltrated further, and are covered by the sol. This induces a non-uniformity of the density, with a zone well infiltrated and other less infiltrated zones.

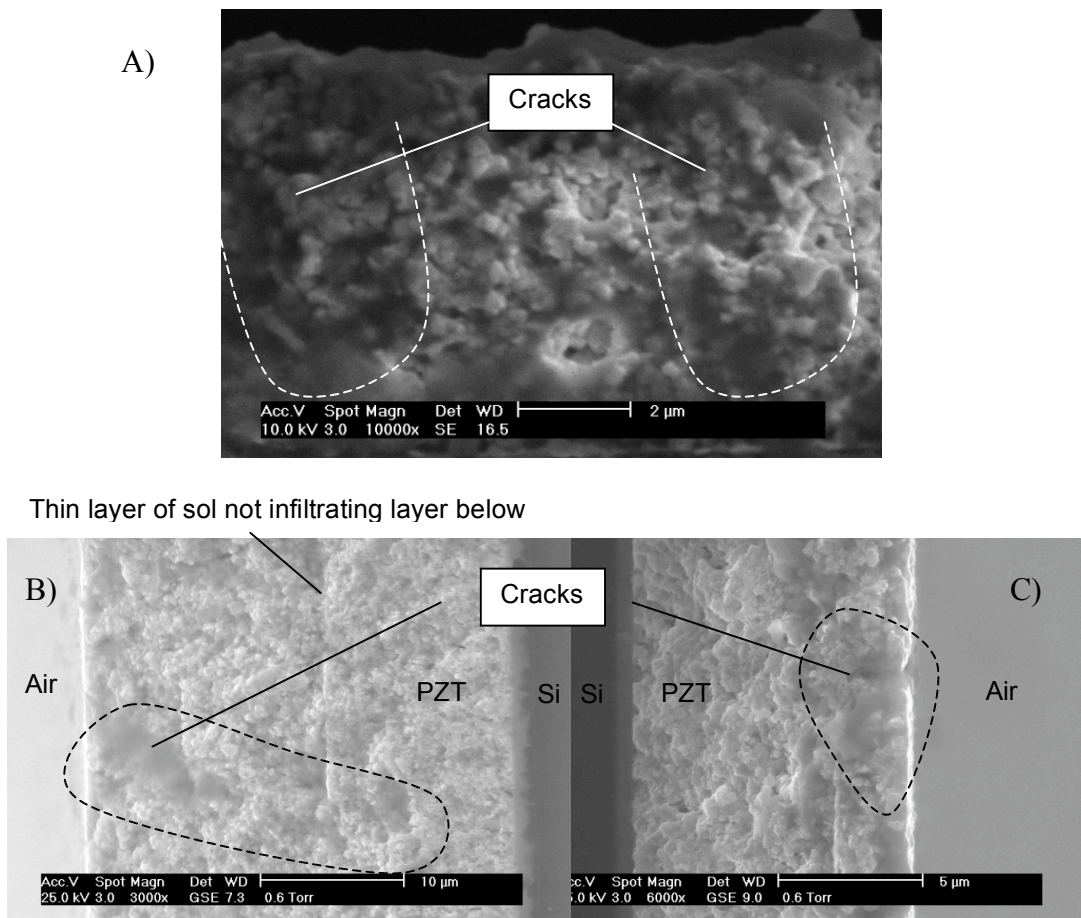


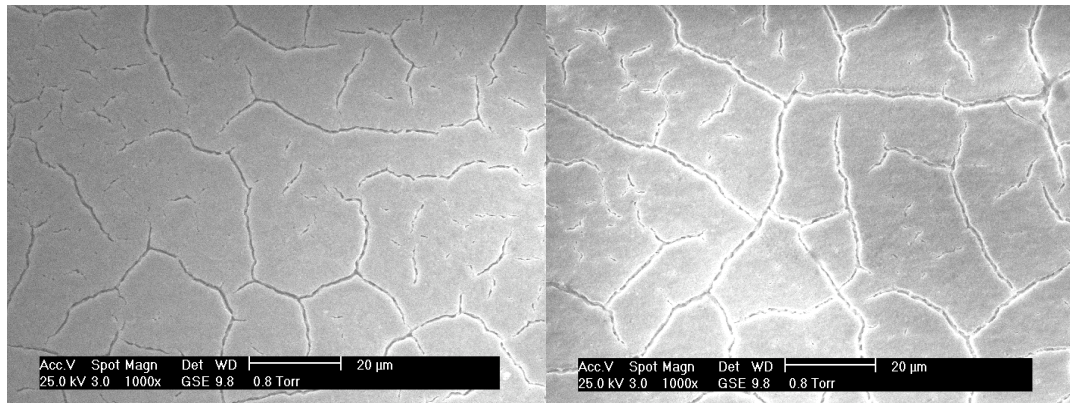
Figure 4.8: SEM micrograph of PZT composite cross sections. Showing the non-uniformity of the material density around the cracks. A) Before sintering (after 450°C). B) After sintering. C) After sintering. A dashed line highlights the aureoles of denser material.

In order to have a good transducer performance the density of the material is important. The greater the number of dipoles, the better the piezoelectric response should be. The first trials to fabricate the transducer were executed using the denser material infiltrated 4 times: x[C+4S].

4.4 PZT thick film fabrication, 35 μm the state of the art via the spin coating technique

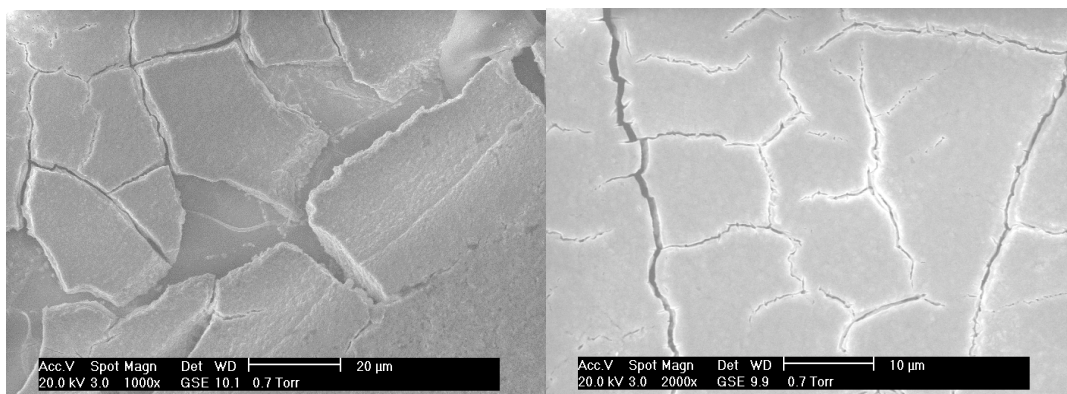
For a stack of stressed layers successively deposited on a substrate, the *in situ* shear forces of the total coating will increase with its number of layers (or total thickness). The greater the number of layers, the thicker the film, and the larger the surface cracks will be. During the deposition of the PZT composite using the spin coating technology, a delamination was observed above 10-12 layers, or above a thickness of 20-23μm. (Figure 4.9 - C). The large cracks and the delamination appear as this thickness is built up. The delamination could be solved with a better adhesion to the substrate. To do so, either the PZT or the substrate, or

both, has to be improved in term of adhesion. It has been demonstrated that in the case of the PZT spin coated on silicon, a tensile stress or shear forces were accumulated when the thickness is built up. This stress should be the origin of the cracks and delamination (Chapter 5). Since the PZT process, consisting of spinning down 4 infiltration layers per composite layer ([C+4S]), provides very good dielectric properties regarding the goal of this work (Chapter 6), it seems to be preferable, at first, not to change the PZT deposition and fabrication process. The sintering process is well known for releasing some stress because of the crystallisation stage involved [Sengupta *et al.* 1997], [Tanimoto *et al.* 1993]. The first attempt to eliminate the delamination was to change the initial sintering process. Instead of one final sintering stage at 710 °C, another sintering step process in the middle of the fabrication of the thick film should release some stress and then help to prevent the cracking and delamination of the film. The first sintering process was then performed after the 8th [C+4S] layer (16µm thick film), and the second after the 12th (24µm thick film). The contrast between Figure 4.9.C and figure 4.9.D demonstrate that the surface is effectively improved with two sintering stages and the delamination seems to have been prevented but not the cracking behaviour.



A) Surface of 4[C+4S] device.

B) Surface of 8[C+4S] device



C) Surface of 12[C+4S] device.

D) Surface of 12 [C+4S] device with 2 sintering processes: One after the 8th [C+4S], and the other after 12th layer.

Figure 4.9: SEM micrographs showing the evolution of the surface of the PZT composite thick film fabricated with the process x [C+4S] when: A) $x=4$, B) $x=8$, C) $x=12$, D) $x=12$. The composite film presented in picture D has been sintered twice: once at $x=8$ and another time at $x=12$.

Despite the prevention of the delamination, the cracks observed in the surface do not allow a continuous electrode 100nm thick to be deposited, as required in the project.

In order to retain the PZT dielectric properties found with the [C+4S] process, the choice to improve the substrate/PZT adhesion might help to grow films with the required thickness (~30µm) without delamination.

4.5. Evaluation of different substrate

The film-substrate interface depends on a specific surface energies of the film, γ_f , of the substrate, γ_s , and of the interfacial energies, γ_{sf} . The work, W_a , needed to separate the film from its substrate can be defined by Equation 4.1 [Ohring, 1992, pp 440].

$$W_a = \gamma_f + \gamma_s - \gamma_{sf} \quad \text{Equation 4.1}$$

W_a has to be positive for adhesion to occur. Chemical interactions, substrate morphology, inter-diffusional effects, interfacial impurities, etc, should also have an effect on W_a . Ohring defined 4 simple cases of adhesion represented by Figure 4.10

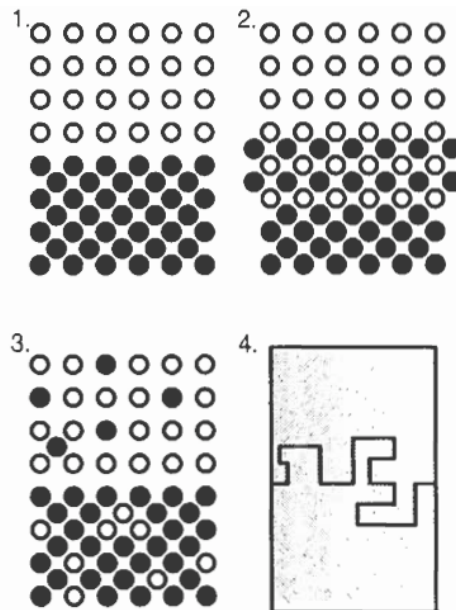


Figure 4.10: Different interfacial layers formed between film and substrate. (1) abrupt interface characterise by a sudden change from the film to the substrate, (1-5 angström), (2) compound interface, a chemical reaction between the film and the substrate form a new layer, (3) diffusion interface characterised by a gradual change in composition between substrate and the film ,(4) mechanical anchoring at interface, characterised by rough surface interfaces [Ohring, 1992].

Different substrates were tested to improve the adhesion between the substrate and the PZT composite. These different interfaces represent a mix of the first three cases described by Ohring.

- Silicon/SiO₂ (reference)
- Silicon/SiO₂/ZrO₂ (substrate used before)
- Silicon/SiO₂/ZrO₂/TiO₂
- Silicon/SiO₂/ZrO₂/PZT sol
- Alumina/PZT

The substrate used for this work is a high definition double side polished silicon. For all of these different substrates the experiment will consist of spinning a number, x , of [C+4S] layers until delamination occurred. The delamination pictures are similar to figure 4.9-c for all these experiments. This number x will be defined as the critical limit. Thus in order to have a reasonable surface quality it will be better to consider the practical limit to be $x-2$ or $x-3$. Table 4.2 summarises the results of this study.

Table 4.1: Thickness of PZT achieved until delamination occurred, x = number of infiltrate composite layer spun

Substrate	x	thickness at delamination
Si/SiO ₂	18	39 μm
Si/SiO ₂ /ZrO ₂	10 to 13	20 to 23 μm
Si/SiO ₂ /ZrO ₂ /TiO ₂	14	29 μm
Si/SiO ₂ /ZrO ₂ /PZT sol	16	37 μm
Alumina rubalit	18 (without cracks)	39 μm

- Si/SiO₂

For the Si/SiO₂ substrate, 18 composite layers were deposited, with $\sim 2.2 \mu\text{m}$ per composite layer and a final thickness of $\sim 39 \mu\text{m}$. Unfortunately this process cannot be applied for 50 MHz resonators, because of lead (Pb) diffusion into the silicon substrate during sintering (Figure 4.11) inducing a partial delamination of the PZT even for films with a thickness below $10 \mu\text{m}$.

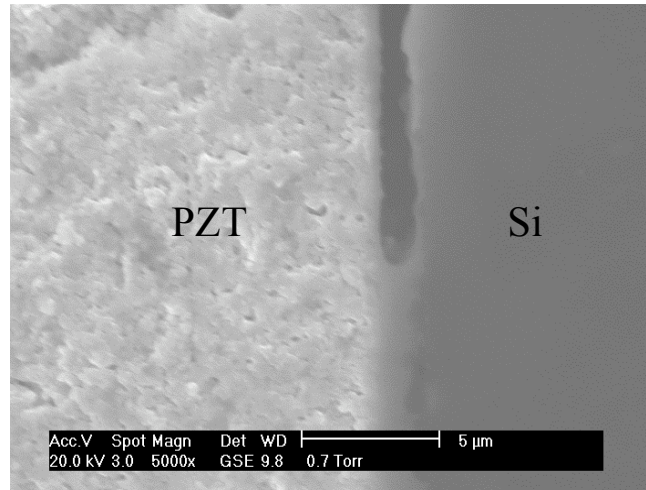


Figure 4.11: Holes produced at the Si/PZT interface due to diffusion of the Pb into the Si substrate during sintering.

– Si/SiO₂/ZrO₂

The Pb diffusion can be prevented by spinning a ZrO₂ diffusion barrier on the Si/SiO₂ substrate prior to spin the PZT layer (Section 3.4.2). It acts as a lead diffusion barrier. On top of this substrate a composite PZT layer is spun and the maximum thickness achievable before delamination with ZrO₂ present, was ~22 μm. As the interface between SiO₂/ZrO₂ is expected to be strong [Ohring, 1992 pp 443], the interface between the high surface finish of the Si/SiO₂/ZrO₂ and the PZT composite should be then the problematic interface. To confirm this assumption, an x-ray diffraction of the substrate remaining after delamination revealed that the ZrO₂ layer was still present.

– Si/SiO₂/ZrO₂/TiO₂

The ZrO₂ layer was chosen because it contains an atomic similarity with the PZT, which should help the adhesion. For the same reason, TiO₂ is also a possible interlayer to test. The connectivity between this oxide and the PZT may improve the adhesion. The interface Si/SiO₂/ZrO₂/TiO₂ with PZT allows 14 layers of composite (29μm) to be deposited before delamination.

– Si/SiO₂/ZrO₂/PZT sol

If atomic similarity, between the substrate and the film, is a valid assumption regarding their adhesion quality, a better interlayer should be a layer of a pure PZT sol. It will find a better match with the PZT composite, and a good match with the ZrO₂ layer.

The substrate, Si/SiO₂/ZrO₂/PZT sol, enabled 16 composite layers to be deposited (37μm). This confirms the assumption.

- Alumina/PZT

The 4th substrate tested is a rough substrate consisting of alumina rubalit710, which is a dense ceramic with similar grain size to the PZT composite and should have a similar roughness. The surface roughness from 20 to 80 nm was determined for both the composite and the alumina via a Dektak stylus surface profiler. The composite surface roughness measured was executed on a part of the surface without defects (cracks, comets due to spin coating). This surface definition found is surprising considering their mean grain size of $\sim 0.7\mu\text{m}$.

This interface between the PZT composite and alumina includes the 4th case of interlayer as well as the other 3 cases described by Ohring. Therefore, it shows a different result. After 18 layers of composite, no delamination or cracks were observed. This cannot be due just to the fact that there is a good adhesion existing between the two rough ceramics. This case will be treated deeper in Chapter 5 related to stress.

With all the substrates presented above, a thickness of PZT able to produce a resonance close to 75MHz in air can be reached (see Chapter 7). Some devices were fabricated using these substrates. The results are presented in Chapter 7.

Up to now, it has determined that only on alumina a good surface finish of the PZT surface. However, this substrate is well known to be hard to process, How to remove the alumina backing the sample?

Improving the PZT surface finish by adapting the PZT process, to minimise the internal stress seems still to be the easiest way.

4.6 Improvement of the ceramic surface finish

With the Si/SiO₂/ZrO₂/PZT sol substrate, 30 μm thick film deposition was achieved. However, the surface finish presents several critical cracks suggesting that if a top sputtered 100nm thick electrode was sputtered, it might be non-continuous. In order to sputter such electrodes, a layer of undiluted PZT sol was spun on the top of these cracked surfaces to cover the cracks (Figure 4.12). This sol layer does not infiltrate the cracks, and the ceramic quality remains low as a result of the cracks. The cracks considerably weaken the ceramic mechanically. However, for a 50MHz transducer application the cracks should have a more important effect than the defects or the *in-situ* porosity, as they can scatter the acoustic wave because of the different acoustic indices between air and PZT. The cracks are not large enough to creating a stationary wave. To do so the pore diameter would need to be as large as 25 μm , however, this work presents of pore with a diameter below 1 μm . (Equation 4.2) [Poynting *et al.* 1909]

$$d_{cav} = \frac{n\lambda}{4} \quad \text{Equation 4.2}$$

Where d_{cav} is the diameter of the cavity created by a pore or by the width of a crack, n is a integer, and λ is the wavelength of the acoustic wave.

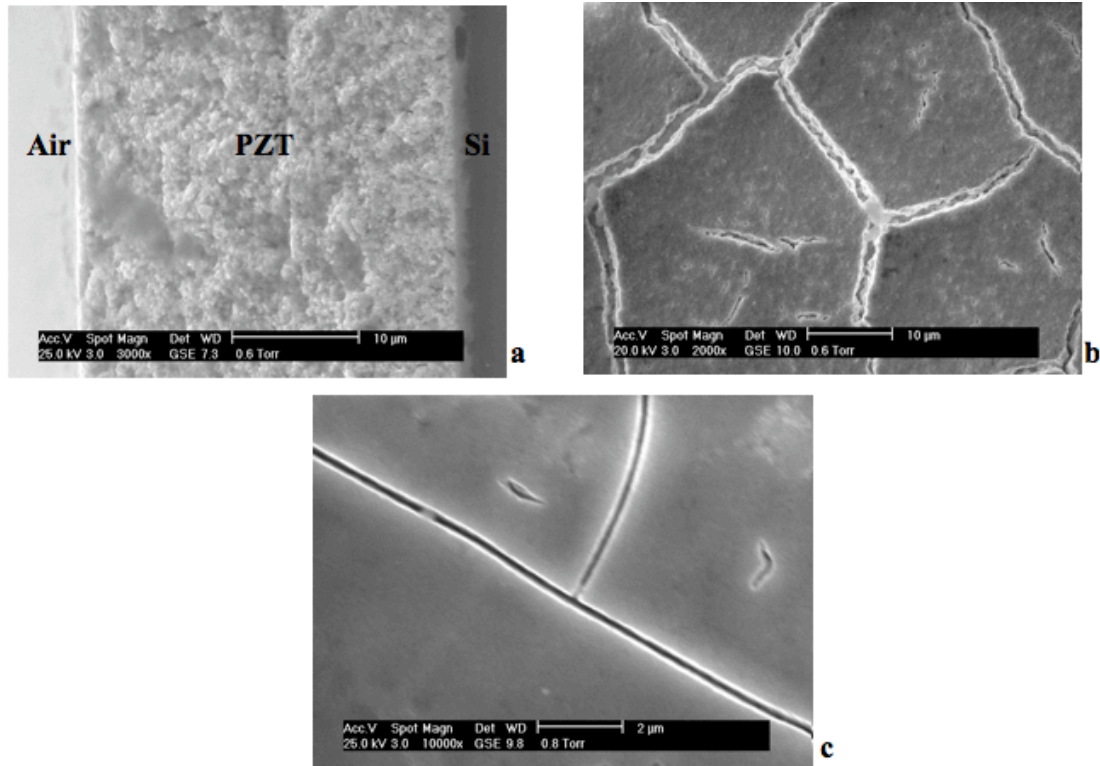


Figure 4.12: SEM micrograph of PZT thick film composed of 16[C+4S] a) cross section, b) surface, c) surface of the same film + 1 layer of pure PZT sol spun leading to a surface with non-critical crack size. Substrate used was Si/SiO₂/ ZrO₂/PZT sol.

The process consisting of 4 infiltration sol stages per composites layer, [C+4S], provides good dielectric properties regarding the industrial specification (Chapter 6). However, for any industrial application the ceramic surface finish still has to be enhanced. Doing so by changing the thick film fabrication process might affect the film dielectric properties.

As explained in the preceding section, the cross section analysis reveals that for this process residual infiltration sol remained at surface of each composite layer (Figure 4.13).

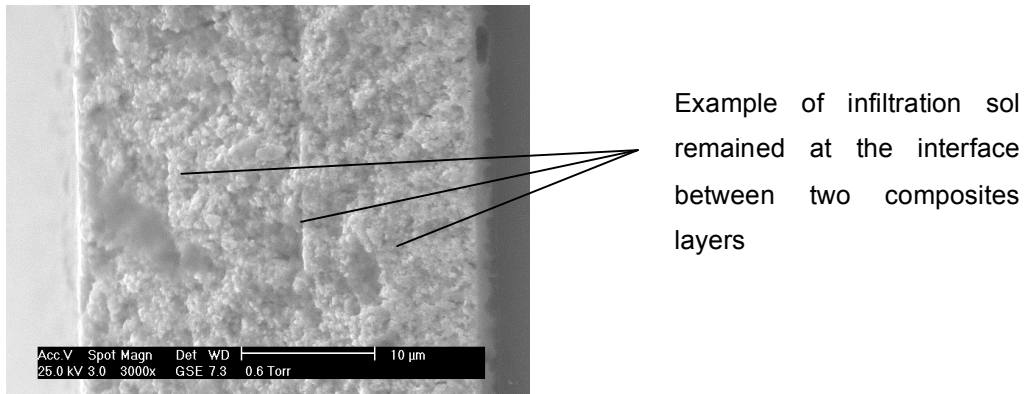


Figure 4.13: SEM micrograph of a cross section of PZT thick film composed by 16[C+4S], highlighting the boundary between composite layers caused by the infiltration.

This effect is even more observable during the wet etching process (see section 4.8). The work presented by Ong [2005] on undiluted PZT sol, presents pictures of cross sections of thin films similar to the interfacial PZT sol layer presented in here. These cross sections can be compared with the cross section of PZT composite to demonstrate that the composite is less dense than a PZT sol. This difference of density should induce a considerable amount of tensile stress due to its solidification on a non-oriented substrate, which might lead the composite film to crack and delaminate. A full study on stress is presented in Chapter 5.

Section 4.3 showed that with 2 infiltration steps instead of 4, the interlayer sol should disappear. Therefore, the process was changed to layering two composite layers, and infiltrating 4 times as a repeatable unit, [2C+4S].

Three wafers were processed, $x[2C+4S]$ with $x=5, 6,$ and $7,$ and their surface finish and cross section were compared with the [C+4S] process. Figures 4.14 and 4.15 illustrate the evolution of the surface of these samples and their cross sections. They show the surface finish achieved with the $x[2C+4S]$ when the thickness increases. These figures reveal that the stress assumptions about the interfacial infiltration sol remaining appear to be verified:

- The infiltration sol remaining between two composite layers observable in Figure 4.14, is not observable with the new process (Figure 4.15).
- The cracking situation is improved significantly even for a thick layer of $28\mu\text{m}$, where the surface finish remains better than for a $10\mu\text{m}$ thick film fabricated with the [C+4S] process. This confirms a reduction in internal forces between the two techniques. (Figure 4.14)
- [2C+4S] films are slightly more porous than for the [C+4S] films, as they are less infiltrated. (Figure 4.14 and Figure 4.15)

Experimentally, the cracks appeared during the drying stage at 200°C , especially with the [C+4S] process when the infiltration sol did not totally infiltrate the PZT. By reducing the number of infiltration, the interfacial PZT layer is eliminated as well as the added shear forces

which accompany it. If the internal forces decrease the crack formation is slower, and the surface finish can then be improved.

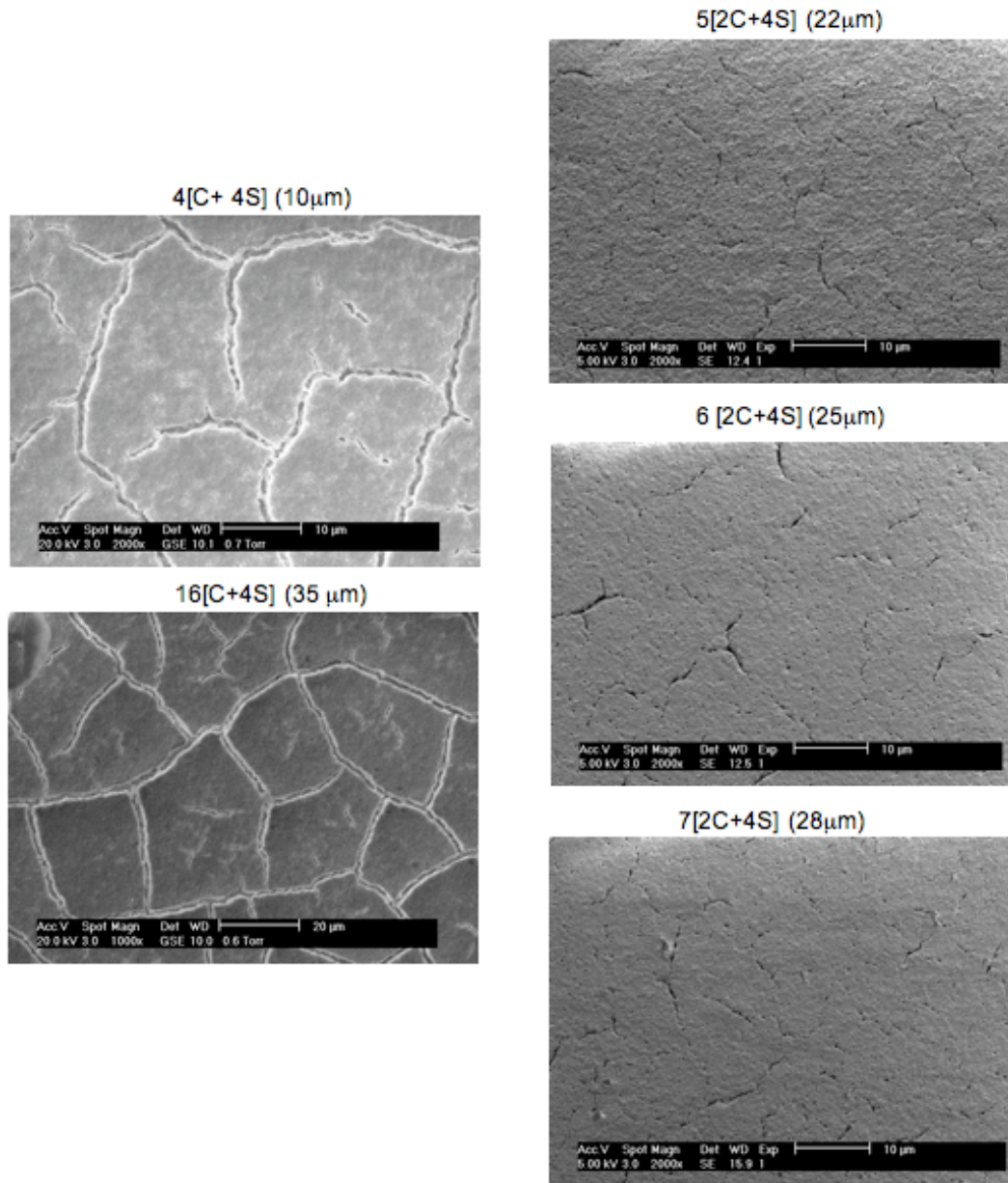


Figure 4.14: SEM micrographs showing the surface finish of the new process $x[2C+4S]$ compared to the surface states of the process $x[C+4S]$.

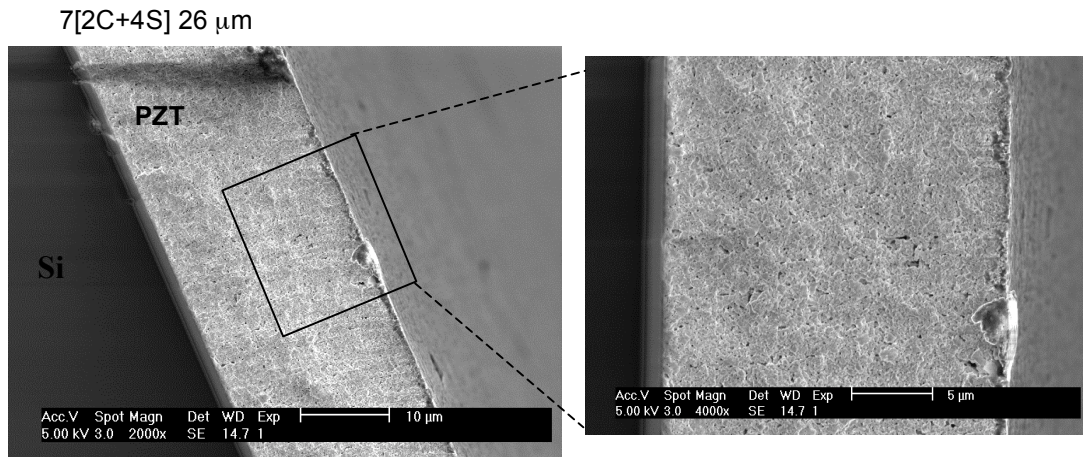


Figure 4.15: SEM micrographs of the PZT thick film cross section of a 7[2C+4S] process. The residual infiltration layers are not observable.

The thick film quality is improved radically with the second process. However, the porosity is reduced between these two processes, the relative permittivity is reduced from 700 to 600-630. In Chapters 6 and 7, films based on [2C+5S] and [2C+6S] processes are presented as a trade off between the two surface finishes and the dielectric and ferroelectric properties. In both of them the residual infiltration layers reappear gradually with the cracks on their surface. Once 35 μm of an un-cracked surface finish is achieved the film needs to be crystallized prior to a dielectric characterization. The crystallization will have an effect on the micro and nanostructure of the film. A study of these physical transformations can generate major information toward the future development of this thick film technology. The next section will then be dedicated to the nano and micro-scale transformation occurring during the sintering stage at 710°C.

4.7 Microstructure of sintered films

A study of the microstructure will help to understand the material behaviour through the final sintering treatment. In the section above, it has been reported that the cracks appear during the drying stage at 200°C. It has also been suggested that the shear forces added by the infiltration sol provoke the composite slurry to crack gradually with increasing number of infiltration step. This was found to be due to a residual infiltration sol remaining at the surface of each composite layer. The detailed mechanism of addition of stress by this interlayer is still unknown.

An EDX analysis performed on 5 samples [C+zS] with z=0,1,2,3,4, reveals that 9wt% of the oxygen disappears during the sintering process (Table 4.2).

Table 4.2: EDX composition analyses of 50 μ m of the PZT composite film surfaces infiltrated 4 times (samples [C+zS] with z=0,1,2,3, exhibit similar analysis).

Element	Weight% Before 710°C	Weight% after 710°C	Weight% Theoretical	Formula verification
O K	18.08	16.46	14.74	3
Ti K	7.59	7.98	7.06	0.49
Zr L	13.09	14.01	14.57	0.51
Pb M	61.24	61.56	63.63	1
Totals	100.00	100.00	100.00	4

Figure 4.16 represents a TGA analysis performed on a dry 2ME based PZT sol, reported by Leclerc, [1999]. This TGA analysis shows that between 450°C and 710°C the loss of mass is minimal (less than 4%) (Figure 4.16). The loss of mass observed in both cases is certainly due to residual organics burned out during the sintering process. The theoretical and the experimental value of oxygen seem to confirm that the sample is constantly exposed to the atmospheric air. The rest of the analysis fits a theoretical PZT composition.

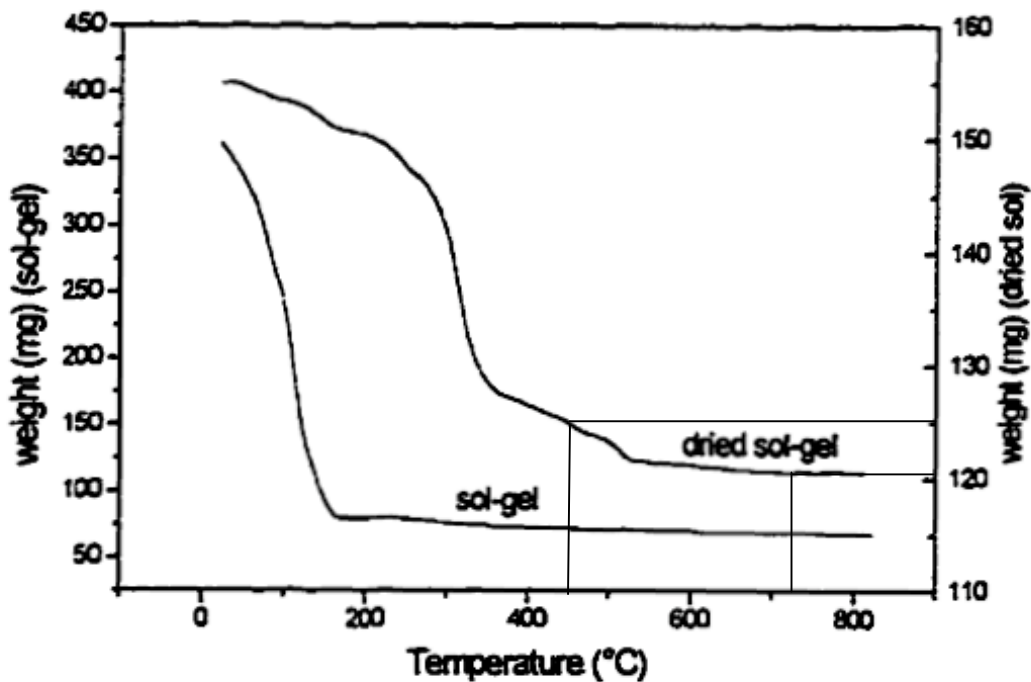


Figure 4.16: Thermogravimetric analysis (TGA) of a PZT sol / 2ME based: dried and not dried. [Leclerc, 1999]

Figure 4.6 shows that during the 3rd and 4th infiltration steps, the cracks are infiltrated less and less, and are covered by the thin residual layer of sol. A sample composed of 1[C+4S] was crystallised at 710°C and SEM micrograph pictures were taken before and after sintering

(Figure 4.17). After sintering, the surface topography appears rougher than before sintering (Figure 4.17). An “opening” of the cracks and pores seems to be observed.

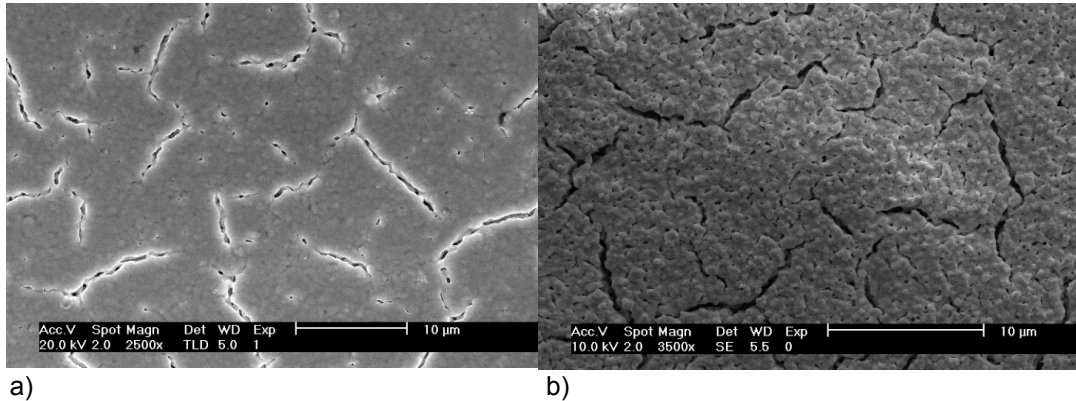


Figure 4.17: SEM micrograph of the surface of a PZT composite layer infiltrated 4 times (1[C+4S]). a) before sintering (after 450°C) and b) after sintering (after 710°C)

At 710°C, the crystallisation steps organising the atomic structure of the green ceramic explain the reduction of volume of the composite and of the residual layer observed in Figure 4.17. This phase transformation, or loss of volume, opens some pores and cracks. A loss of volume of films deposited on a rigid substrate would be accompanied by an increase of internal stress. However, Chapter 5 demonstrates that this crystallisation process releases a great deal of the internal stress. Two processes are involved during the sintering of the composite material:

- The amorphous PZT is crystallising on the PZT powder grains, acting like cement between grains.
- Interfacial atomic diffusions assisted by high temperature (and the internal stress of the film), leads to the grain centres approaching each other.

The chosen approach of atoms on the crystallisation seed (PZT crystal grain) should cost the minimum amount of energy. This approach dictates the reorganisation of atoms from an amorphous phase to a crystalline phase, and results in an apparent decrease of volume (with a constant mass). Then, a crystallisation process results in decreasing the energy of the system, and this energy liberated from this process is shown by the observed decrease of in-situ stress.

To do so, the PZT grains have a tendency to eliminate the interfacial energy of their grain boundaries, and the PZT gel grows either in a planar way or in a columnar way, Figure 4.18. Both result in a reduction of volume and stress.

An SEM micrograph of the sintered film, focussed on 1 of the grain of the material, reveals that the infiltration sol crystallises mainly in a columnar way (Figure 4.19). The diameter of each column is between 1-10 nanometers.

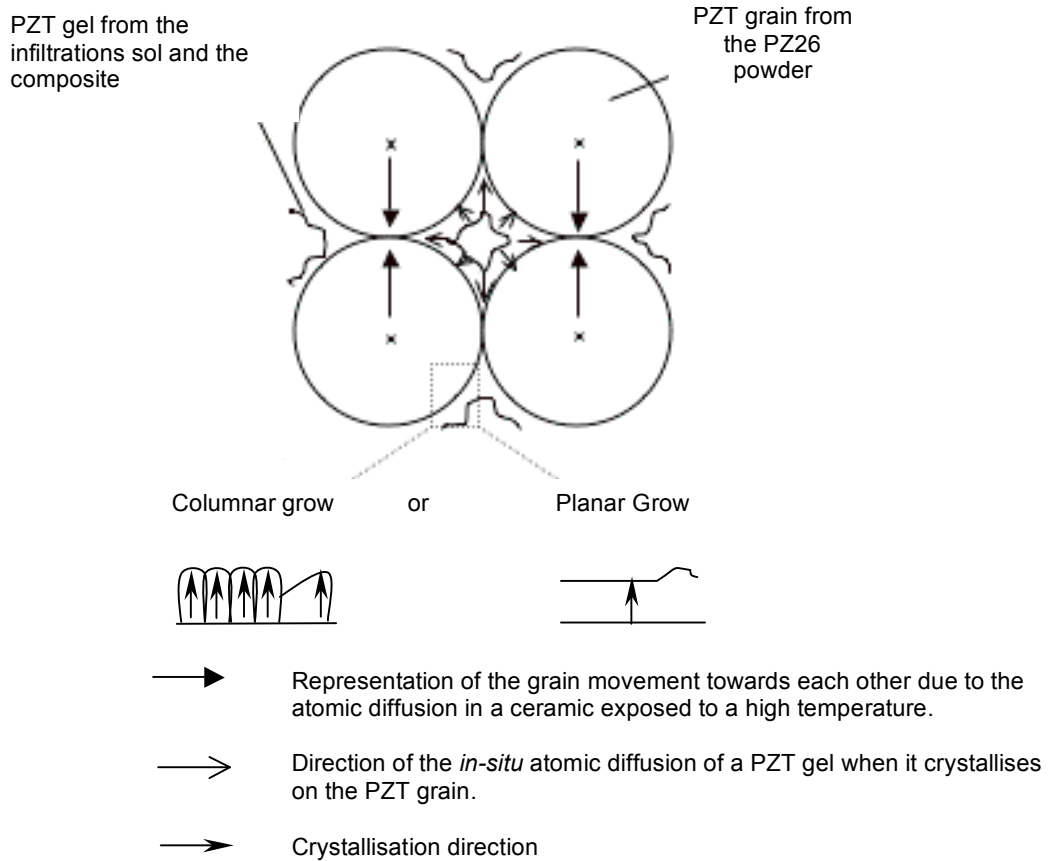


Figure 4.18: Illustration of processes involved during the sintering process of the PZT composite.

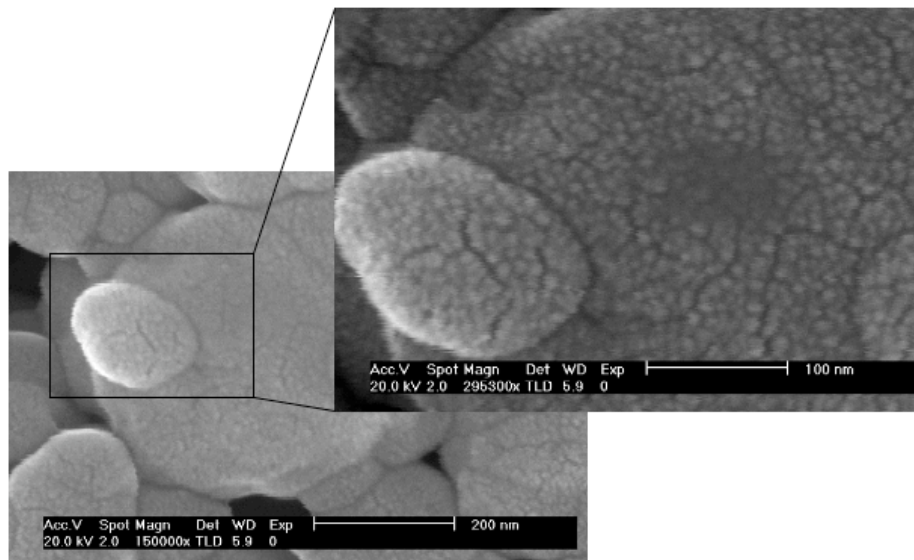


Figure 4.19: SEM micrograph of the carbon-coated surface of the PZT composite 1[C+4S], at 200nm and 100 nm magnitude of resolution, showing the columnar crystallisation of the PZT sol on PZT grain.

To summarize, in the amorphous phase of the dry PZT sol on the PZT grain, or before the sintering process, the sol covered the cracks and the pores. The sintering process is accompanied by a loss of volume due the crystallization, which exposes the pores and cracks. In order to use this effect to improve the density and the electromechanical properties of the transducer, an intermediate 600°C furnace temperature stage should be added to the present process. This temperature is lower than the melting temperature 695°C of the sintering aid, which avoid a full densification, while opening the porosity. The exposed porosity should improve the efficiency of the infiltration steps.

The 35µm thick film fabrication is now understood. However, the fabrication of a patterned transducer requires more than just knowledge of the thick film fabrication as the device has to be actually shaped physically.

4.8 PZT wet etching

4.8.1 PbClF Residue

The solution used to etch the green ceramic was a HF/HCl aqueous solution with the following composition [HF (0.5%), HCl (4.5%), H₂O (95%)]. The solution was held at 60°C during the procedure. When the PZT was etched a white layer was left on the surface of the PZT. An XRD study on wet etching thin films of PZT (2ME based) conduct by Zheng [2003] indicated that the product was PbClF.

Several tests were performed to find the adequate etching conditions for removing the PbClF residue.

The first trial was to use the procedure presented by Zheng [2003], which consisted of dipping the sample for 1 minute every 3 minutes in a HNO₃ solution (50wt% in water). The results are shown in Figure 4.20.

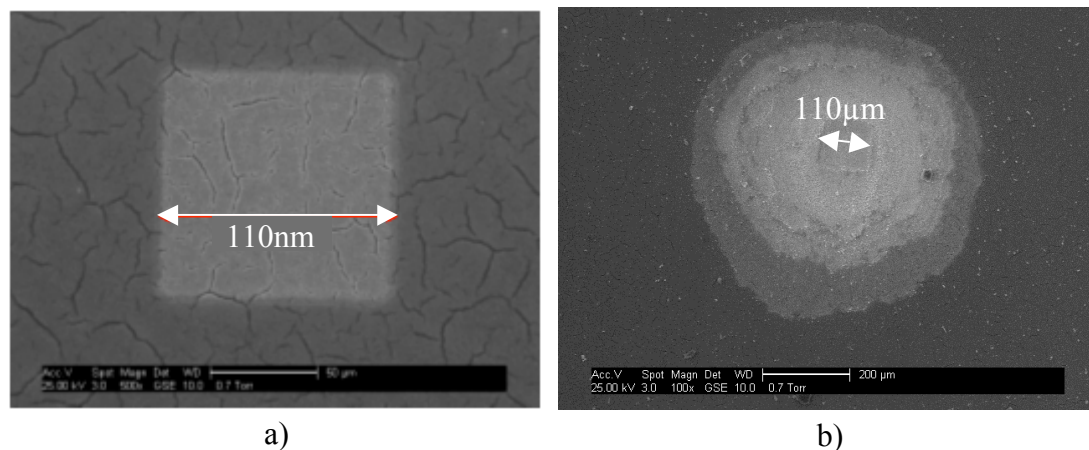


Figure 4.20: a) SEM micrograph of a 110 µm hole in the photoresist. b) Resulting hole in a 35 µm thick PZT film using the HNO₃ process.

In this work, for all etched PZT thick film, the PbCIF couldn't be removed completely that way. Zheng [2003] presents that the nitric acid reacts with the PbCIF and then removes it away from the thin film. However it seems that for thicker film the PbCIF layer is, the more alternated baths of HF and citric acid are needed. The photoresist (S1818 spun at 4000rpm and dried at 115°C (dark grey)) seemed to be removed by the HNO₃ process where the undercuts occurred. This enlarges the hole considerably from 100µm to more than 500 µm (Figure 4.20 a, and b).

The second trial was to use an ultrasonic water bath every two minutes to remove the PbCIF white residue. The typical Figure 4.21 shows that the photoresist was even more removed by the ultrasonic agitation.

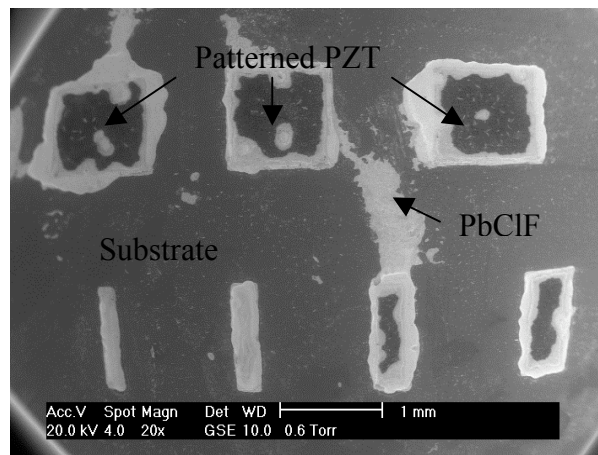


Figure 4.21: SEM micrograph of a 21 µm PZT thick film patterned, the device definition illustrates the photoresist delamination due to the ultrasonic agitation every two minutes in order to remove the PbCIF residue.

The third attempt was to remove this residue by cleaning the sample in water in an ultrasonic water bath for 15 minutes, at the end of the etching process, and not every 2 minutes as Zheng suggested. As explained above, Zheng dealt with dense thin films, his undercut wasn't critical as 90 seconds was enough to etch his structure. Here, thick porous films are being etched and the undercut is a real issue, because of the time required to etch 30 µm thick films, and because of the films porosity. Removing this PbCIF residue at the end of the etching process avoids a deep delamination of the photoresist. This process gave the best result obtainable with a isotropic wet etching process giving an etch slope ~0.8 (Figure 4.22).

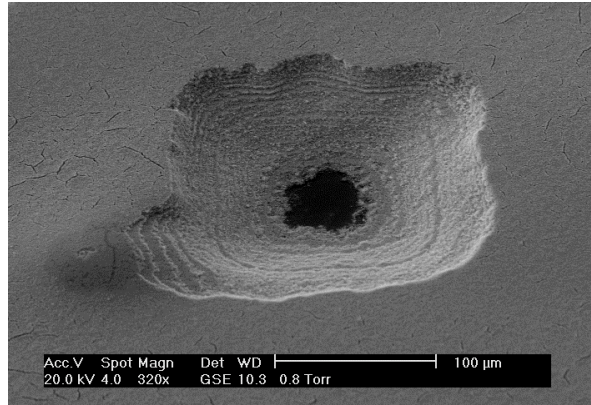


Figure 4.22: SEM micrograph of a 150 μm hole PZT in a 35 μm thick PZT film resulting with a mask of 110 μm .

The first trials were conducted to determine the etching conditions for the PZT thick film. These experiments were only executed on samples fabricated through the first process x[C+4S]. A second set of experiments were run afterwards to characterize the etching rate and quality of the second process, x[2C+4S]. Because of the residual layer of sol between each layer of composite the results showed different etching rate between the processes [C+4S] and [2C+4S].

4.8.2 Etching of PZT thick film ([C+4S])

4.8.2.1 Using with the photoresist S1818

Table 4.3 reveals that the thicker the films are, the lower the etching rate is. The PbClF residue constitutes a barrier, which slows the etching process [Dauchy *et al.* 2005].

Table 4.3: [C+4S] PZT thick film etch rate by wet etching, (HF (0.5%), H₂O (95%), HCl (4.5%))

	Time	PZT thickness	etch rate
[C+4S]	7min	21 μm	3 $\mu\text{m}/\text{min}$
14[C+4S]	12min	30 μm	2.5 $\mu\text{m}/\text{min}$
16[C+4S]	15min	35 μm	2.3 $\mu\text{m}/\text{min}$

The edge resolution, as well as the etching slope, observed in all of the present pictures seems to be dependent on the thickness and the uniformity of the spun photoresist and the immersion time in the HF solution.

Two thicknesses of photoresist, 1.6 and 4 μm , have been tested. The thicker the resist, the harder the photoresist, and the longer the photoresist can stay in the HF solution without being removed. Therefore, the thicker the photoresist is, the smaller the undercut. Figure 4.23 represents the typical gap between two devices achievable by this wet etching technique. A kerf of ~50-60 μm between surfaces and a gap of 10 μm between features on the silicon is

shown for a 21 μm thick PZT film. The cross, shown in Figure 4.24, reveals the possibility of patterning a 10 μm wide bar of 21 μm thick PZT film. These results are the optimum results achievable with a wet etching technique considering the thickness and the isotropy of the film, with an etching slope of ~ 0.8 .

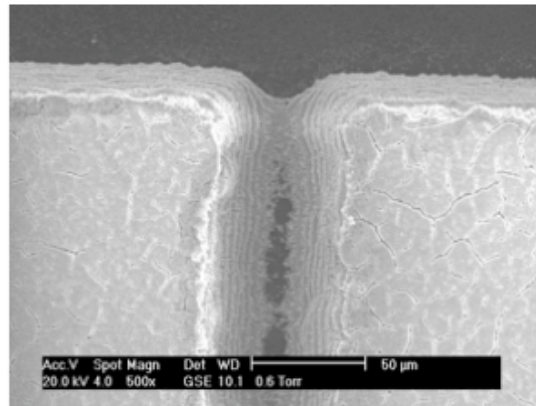


Figure 4.23: SEM micrograph of a 21 μm PZT thick film, patterned with features of 10 μm , spun at 2000rpm/30s.

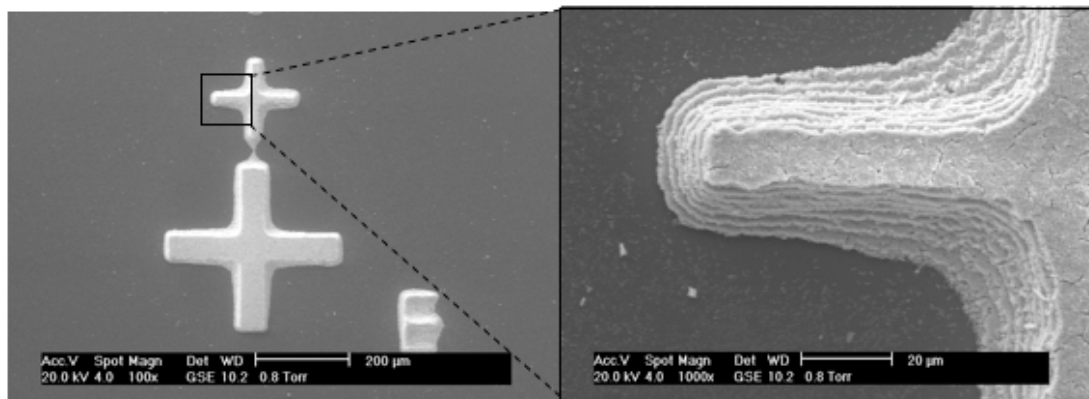


Figure 4.24: SEM micrograph of a 21 μm thick PZT film, patterned to a 10 μm wide device.

4.8.2.2 AZ4562 photoresist etch mask

Similar wet etching results were found by using a thicker photoresist, AZ4562. The advantage of this photoresist is that it can be spun in one step at 1000rpm and baked at 90°C, thus given a thickness of 12 μm . This thickness requires an UV light exposure time of 45 seconds using the Karl Süss MJB21 mask aligner and 3-4 min in AZ351B developer diluted in water. (proportion 4 (H₂O)/1 (351b)).

4.8.2.3 Etching process of [2C+4S] PZT thick film

The same wet etching process was tested on [2C+4S] thick film, using the photoresist AZ4562. The results are summarized in Table 4.4.

Table 4.4: Etching rate of x[2C+4S] PZT thick film.

	Time	thickness	etch rate
5[2C+4S]	5.30min	22 μm	4.2 $\mu\text{m}/\text{min}$
6[2C+4S] +4S	6.15min	22 μm	3.6 $\mu\text{m}/\text{min}$
7[2C+4S]	6.50min	26 μm	4 $\mu\text{m}/\text{min}$

When compared to Table 4.3 (etching rate of [C+4S] process), Table 4.4 demonstrates etching [2C+4S] film is faster. This result seems reasonable considering that during the [C+4S] process the PZT composite was infiltrated twice much.

The “stepped pyramidal” etching shape observable in the process (Figure 4.25) still observable in the process x[2C+5S] (Figure 4.26), not longer observable in the process x[2C+4S] (Figure 4.25). Because the thin PZT residual inter-layer sol layer is denser, it acts like a very thin protection layer against the etching solution. (Figure 4.25 12[C+4S], Figure 4.26). Thus it slows etching rate. Since this layer is not present in the second process [2C+4S], the HF/HCl aqueous solution can have a more uniform surface of reaction with the PZT. The edge resolution is therefore better. Both the porosity and the interfacial sol layer are responsible for these differences, unfortunately as these two variables change together after the 2nd infiltration, it is impossible to determine which has the major effect.

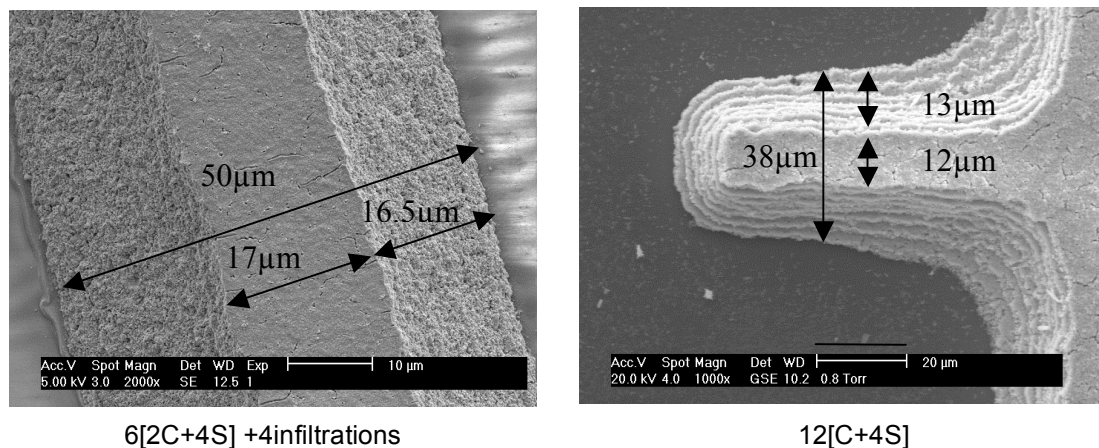


Figure 4.25: SEM micrograph of PZT thick: Comparison between the etching definition of the two process, [2C+4S] (22 μm thick) and [C+4S] (21 μm thick).

4.9 Summary on the device fabrication

PZT films up to 35 μm thick were fabricated, using a composite sol gel route combining a PZT powder and a PZT sol gel. The maximum temperature for the process was 710°C. This study yields to set up experimental conditions in which a crack free surface finish of a 28 μm thick film revealed the adaptability of the spin coating technique to fabricate such thick films on silicon.

The wet etching technology revealed the possibility of a great adaptability to pattern and shape innovative devices such as bars 10 μm wide of 21 μm PZT thick film. These results open the way to a wide range of new industrial applications requiring small features and/or multilayer PZT thick film with embedded electrodes. Figure 4.26 represent a laser scan of an etching slope of a sample produced with the process [2C+5S]. The etching slope shown in this figure illustrates the undercut characterising an isotropic wet etching process. It shows as well irregularities of the etching due to the non-uniform density of the composite, and that the PZT sol interlayer starts to appear at this degree of infiltration (2C+5S).

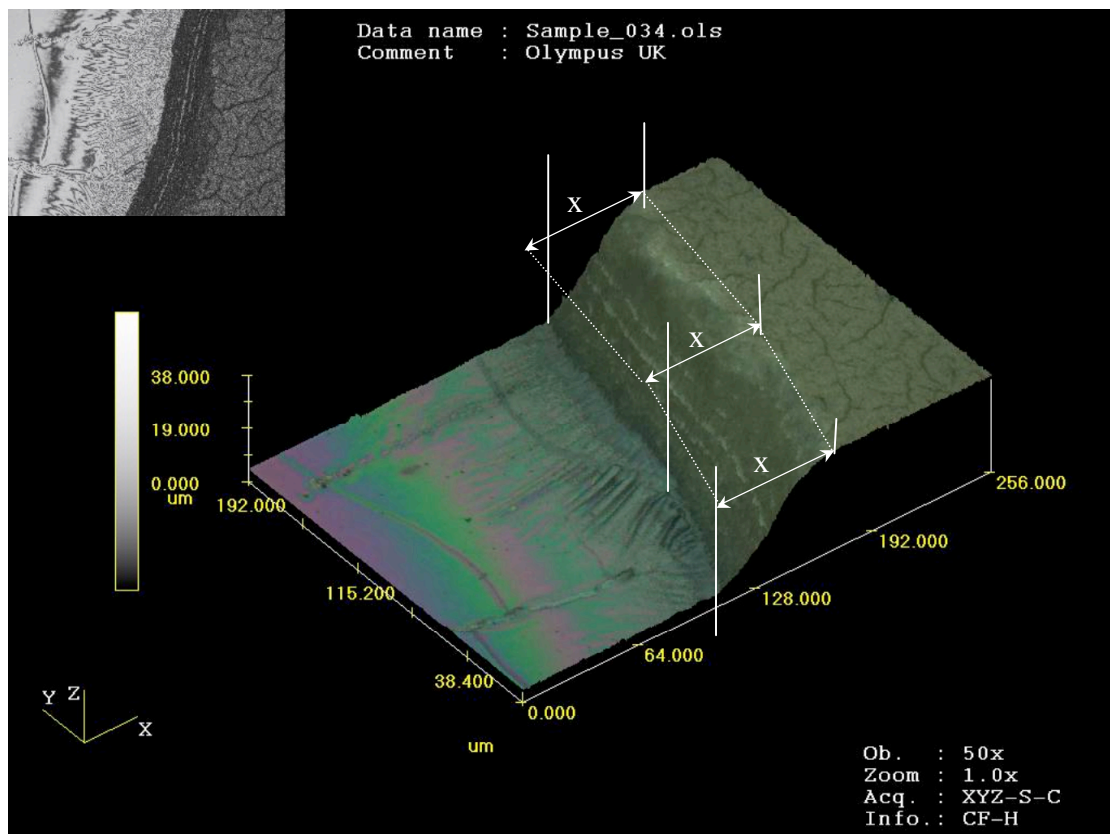


Figure 4.26: Laser scan of the (2C+5S) PZT composite showing: undercut characterising an isotropic wet etching, irregularities of the etching due to the non-uniform density of the composite, and that the PZT sol interlayer starts to appear at this degree of infiltration (2C+5S).

The interlayer sol appears at the same time as the surface crack. As the interlayer is made of pure sol its density is higher than the composite, this difference of density may cause an increase of *in-situ* film stress inducing these cracks formations.

A proper study on the stress behaviour during the film fabrication is presented in the next chapter to understand this phenomenon. With Stoney's Equation, studies of the in-situ film stress development as a function of the film thickness and density were performed. It should help to demonstrate that the internal forces increase considerably with the film thickness and density. After that study, a proper insight of how to control the quality of the ceramic will be gained. The two final chapters will then be dedicated to the characterisation of the dielectric and impedance properties of the material.

Chapter 5

PZT thick film stress development

5.1 Introduction

The previous chapter has addressed the processing problems encountered during the PZT thick film of 40 μ m fabrication. It opened a discussion on the cracking behavior by a qualitative characterization of pictures. This chapter makes precise the stress issues by a detailed study of the stress development throughout the process via a wafer-curvature measurement method. The origin and nature of these internal residual stresses are the source of many defects of films deposited on substrate.

Residual stresses are, of course, not restricted to composite film/ substrate structures, but also occur in homogeneous materials under special circumstances. We will see that a state of non-uniform plastic deformation is observed in our case. This deformation seems to occur mainly during thermal processing. This residual stress distribution will be presented as locked into the thick film. This makes the phenomena of our system very close to the situation described by Stoney [1905].

In the first sections, the stress calculation from the experimental curvature is explained, and, the spin coating technique is discussed as well as its influence on the measured wafer curvature. Once the measurement is understood, the influence on the film in-situ stress due to the temperature processes at 200°C, 450°C, and 710°C, will be presented. The wafer curvature as a function of the number of infiltrations will be demonstrated to increase the curvature and the internal stress. The choice of the number of infiltrations will be demonstrated to be the major concern in the thick film fabrication process with this composite material. It will be demonstrate that the thickness of the film does not increase the internal stress of the film, however, the curvature of the wafer will be increase. This indicates that the free energy of the film is increased with an increase of thickness. It will be demonstrated that using a certain number of infiltration steps should be associated with a thickness maximum before some critical cracks appears. In order to demonstrate that the stress of the spun thick film is fully dependent of its substrate match, the example of the same film spun on an alumina substrate will be finally presented. This last section demonstrates that the future of this technology might move away from the silicon as a substrate choice.

5.2. Stress calculation from the curvature of the wafer

When a thin or thick film is deposited onto a substrate it interactes with the substrate via forces applied at their interface. This is due to a different thermo-mechanical behavior of the substrate and film material. These forces generally bend the substrate and result in curvature of the wafer. This curvature was measured with a "Dektak stylus" surface profiler, which allows the radius of curvature of the wafer to be calculated, using either Equation 2.37 or 2.38 from Chapter 2.

$$R = (1 - f(x)^2)^{3/2} / f(x)'' \quad \text{Equation 2.37}$$

$$R' = \frac{L^2}{8z} \quad \text{Equation 2.38}$$

Equation 2.37 considers the whole measurement: $f(x)$ is a polynomial, which approximates the measurement. Its choice will be discussed later. For Equation 2.38 L is the scan length, and z is the deflection of the wafer.

Equation 2.37 and 2.38 represent two ways to approximate the curvature of the wafer. In addition to the approximation already made by Stoney, the curvature needs to be approximated by a polynomial $f(x)$, or a deflection z . This new approximation is then transferred to the stress calculation through Stoney equation (Equation 2.45 from Chapter 2).

$$\sigma_{11} = \frac{1}{6} \frac{Y}{(1-\nu)} \left(\frac{1}{R_{after}} - \frac{1}{R_{before}} \right) \frac{l_s^2}{l_f} \quad \text{Equation 2.45}$$

The stress calculation based on the radius of the curvature of the wafer is explained in the literature review (Section 2.2.5). Section 2.2.5 shows that this theory is based on approximations like: a constant curvature of the wafer; a perfect anisotropy of the substrate, assumption on thermal expansion on each layers; and the main approximation, only the substrate mechanical properties are considered. This part of the literature review demonstrates that any stress calculations are just approximations. Generally, this stress model can be considered to be useful to compare experiences between them, and a good quantification of stress can be made in just rare simple cases. This section presents then the inexactitudes of this stress model, and demonstrates that the stress quantities, presented here, have to be considered as a tool for comparison between samples, and not as the exact *in-situ* stress amount of the system.

5.3. Stress due to the platinum layer and validation of Stoney's equation

This section presents the stress calculation obtained from the curvature caused by a thin platinum layer (100nm thick) on a 4 inches multilayered substrate: SiO₂ (400nm)/Si (525 μ m)/SiO₂ (400nm)/ZrO₂ (40nm) (Figure 5-1). Because this substrate is mainly constituted of silicon, the analysis will be simplified by considering it as a pure silicon substrate.

Figure 5.1 shows that the Pt/Si system exhibits a compressive stress in the Pt layer. This compressive stress is a well-known phenomenon when the platinum is sputtered. The conditions of the sputtering plasma generally dictate if the system Pt/Si exhibits a compressive or a tensile stress or no stress [Ohring, 1992]. Here, the plasma conditions induce a compressive stress. The resulting curvature shown in Figure 5.1, needs to be approximated in order to calculate the radius of curvature in 2 ways (Equations 2.37 and 2.38):

- 1) A polynomial function $f(x)$ at the 2nd degree is used to approximate the measured curvature of the wafer (red lines, Figure 5.1-B). The polynomial approximation fits with the measured data. The radius of curvature, as a function of position, is calculated based on that polynomial function using Equation 2.37. The stress was then calculated through the Stoney's Equation (Equation 2.45) and the mean value of the curvature across the wafer.
- 2) The maximum deflection (green line in Figure 5.1-A) of the bent wafer was used to calculate the curvature. The radius of curvature is calculated based on that deflection using equation 2.38, and then the stress can be calculated using Stoney's equation.

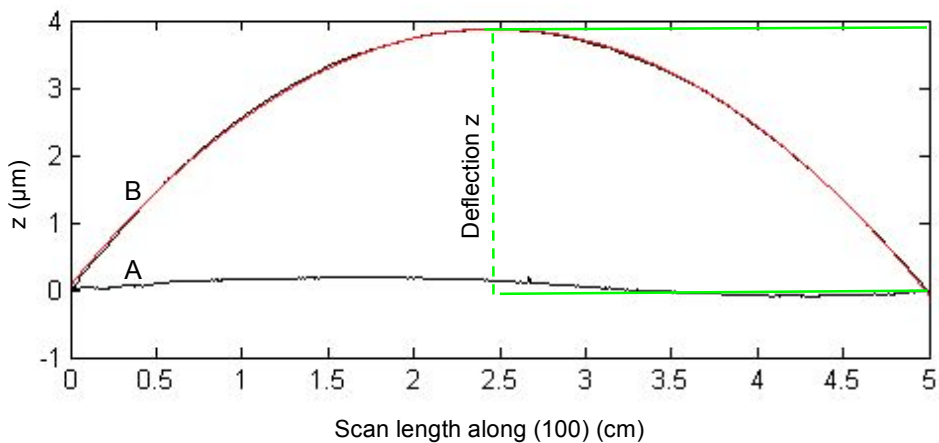


Figure 5.1: Surface profile in the direction [100] of: A) The substrate SiO_2 (400nm)/Si (525)/ SiO_2 (400nm)/ ZrO_2 (40nm). B) The same substrate A coated with a 100nm thick Pt layer showing the presence of compressive stress. The curvature is approximated in two ways: 1st) The polynomial function $f(x)$, used to calculate the stress, is represented by the red lines which fits well with the measured data. 2nd) The maximum deflection z , used also to calculate the stress, is represented by the green lines.

In this case, prior to the platinum layer deposition, the substrate is considered to have an infinite radius of curvature (Figure 5.1-A). The observed curvature in figure 5.1-B is then considered to be due to the 100nm thick platinum layer sputtered on this substrate.

Table 5.1 displays the results of the stress calculation obtained for this Pt coated wafer. For the calculation, the Young's modulus (130 GPa in direction (010) and (100)) and the Poisson ratio (0.28) of the silicon were considered only [Wortman *et al.* 1965].

The stress results for both the polynomial and deflection approximation of the curvature, are in the same order of magnitude as the result obtained for a similar work by Ong [2005].

Table 5.1 Calculated stress of a 100nm thick Pt layer on the substrate: SiO₂ (400nm)/Si (525)/SiO₂ (400nm)/ZrO₂ (40nm).

100nm of Pt on SiO ₂ (400nm)/Si (525)/SiO ₂ (400nm)/ZrO ₂ (40nm)	Curvature calculated (m)	Stress calculated (MPa)
Measurement approximated with the 2 nd order polynomial function (red lines)	+87.2	+937
Measurement approximated with the wafer deflection approximation (green lines)	+82.2	+993

The curvature of the silicon wafer coated with 100nm of platinum is symmetric from the centre toward the edge of the wafer in the direction [100]. This curvature symmetry reflects the symmetry of silicon crystal space group $Fd\bar{3}m$: the particular symmetry A_2 axes running through the direction [001] are responsible of this symmetry (Figure 5.2).

The measurements of the curvature in the direction [010] (dashed line, figure 5.1) coincides perfectly with the curvature measurement executed in direction [100] represented by the plain line. This phenomenon is confirmed by Figure 5.4 representing the tensile stress due to thick film of PZT spun on top of this Pt coated substrate scanned in the same 2 directions. Both directions are perpendicular to each other, which mean that the mechanical properties of the silicon follow the symmetry of an axe A_4 . The mechanical forces inducing the curvature face the same resistance from wafer in direction [100] and in direction [010]:

The symmetries of the unit cell simplify considerably the stiffness tensorial matrices and reveal that $s_{11}=s_{22}$, meaning the mechanical properties in the direction [100] and [010] are equal. The Young's modulus values follow then the symmetry of a A_4 placed in the [001] direction (figure 5.2-B.a), even if this axes doesn't appear in the unit cell symmetries figure 5.2-A.

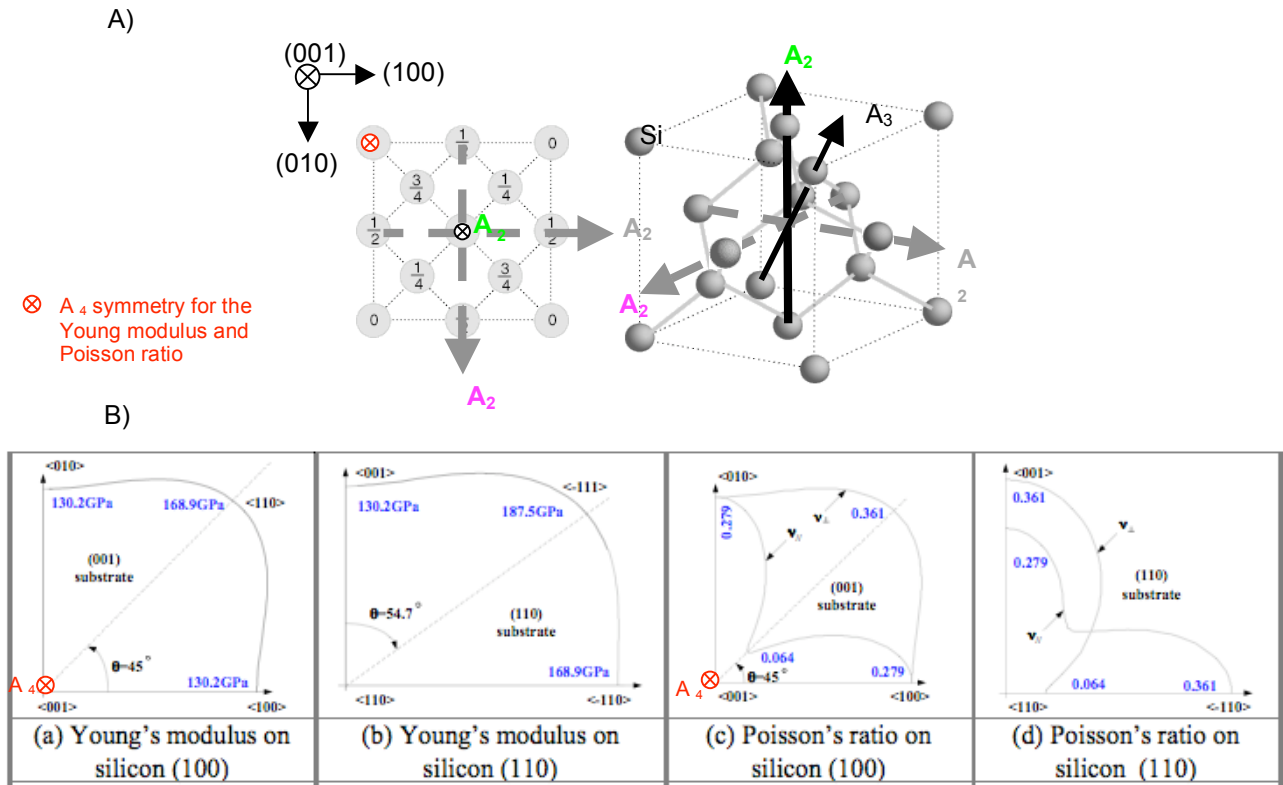


Figure 5.2: A) Axes of symmetry present in the silicon unit cell, (diamond structure). B) Young's modulus and Poisson ratio of silicon in different crystal orientations. www.mtl.mit.edu/researchgroups/mems-salon/sriram_Si-111-better.pdf

The measurements of the curvature were also executed in the directions [110] and [-110]. They generate the same curvature of the wafer as the ones observed for the direction [100] and [010], however the simply stiffness matrices generate a different value for s_{12} than for s_{11} . This means that the Young modulus and the Poisson ratio should be different and should generate a different calculated stress. But, the stress observed in direction [110] is approximately the same as the one observed in direction [100] (Figure 5.3).

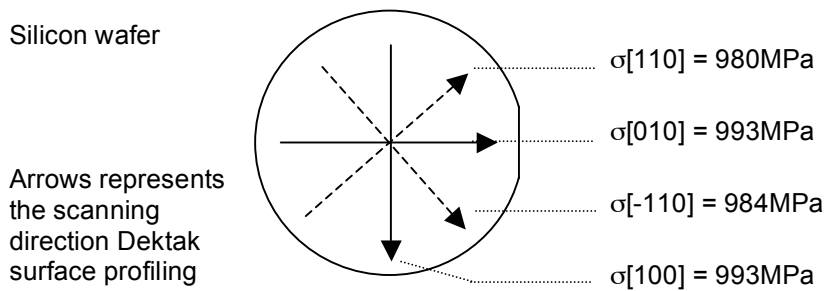


Figure 5.3: Stress induced by a 100nm thick platinum layer on 525 μm silicon. Four directions of curvature measurement were probed: [110] & [-110], and, [100] & [010].

The Poisson ratio, ν , and Young's modulus, Y , used for the calculation of the stress were respectively, 170GPa and 0.064. Therefore, the ratio $Y/(1-\nu)$ used in Stoney equation stay constant in both case [110] and [100]. Then, the stress value of the system remains identical in the four directions, [110] & [-110], and, [100] & [010], of the wafer profiled.

Stoney's equation applied for plates, (Equation 2.45), is based on the biaxial Young's modulus, $Y/(1-\nu)$. The Poisson ratio is used to include the deformation perpendicular to the scanned direction. For this reason, this biaxial Young's modulus and then the Stoney equation, is usable for only isotropic material. Of course, considering the silicon as an isotropic material seems unreasonable, but the stress results, presented in Figure 5.3, illustrate this isotropy in four different directions. This phenomenon validates, at least for these directions, the use of the biaxial Stoney equation as a first approximation.

For such a thin layer of Pt sputter on silicon, a considerable stress (~ 990 MPa) was calculated. The next section shows that for a PZT thick film a lesser stress is applied to the substrate. However, the next section presents also that the calculation is affected considerably by the stress measurement, due to the thickness variation of the film, and the spin coating technology. Once again, it demonstrates that the quantitative aspect of this stress analysis cannot be the target if this chapter.

5.4. Stress measurement of a PZT thick film on a Pt coated silicon substrate

The use of the spin coating technique involves the phase transformation from liquid to solid on a rigid substrate. This phase transformation generates shrinkage of the spun material, which induces shear forces applied at the interface between the spun film and the substrate. This shrinkage is then the principal source of tensile stress present in this system, and is the main source of the crack formation and the delamination of the film. The adhesion forces must be higher than these shear forces, if not, the film delaminates.

A number of possible defects such as comets, striations, chuck effects, arise with the use of the spin coating technique. They are generally localized on the PZT surface and affect the curvature measurement by roughening locally the surface of the PZT, which generates some artificial increases or decreases of the curvature. In this case, two main defects are observed when spinning the thick film of the composite material: comets and a thickness variation across the wafer:

- The thickness was discovered to vary considerably when spinning the composite slurry on a substrate (Section 6.4.2.3). Close to the wafer centre, the spinning doesn't spread the composite on the substrate, the material turns on itself. A "hill" of material is then observed around the rotation axes. This phenomenon induces a "hill" of material located at the centre of the wafer. The thicker the film, the larger and higher

the “hill”. Figure 6-13 illustrates this phenomenon, and, Figure 5.5 represents how the curvature measurement is affected in the centre by this “hill”.

- Figure 5.4 represents a description of the other main defect, the comets, and its effect on the curvature measurement. This defect happens when any perturbation impedes with the normal flow of the solution on the spinning wafer. The main perturbations are generally: a relatively large particle, a non-uniformity spin velocity and/or a non-uniform environment temperature.

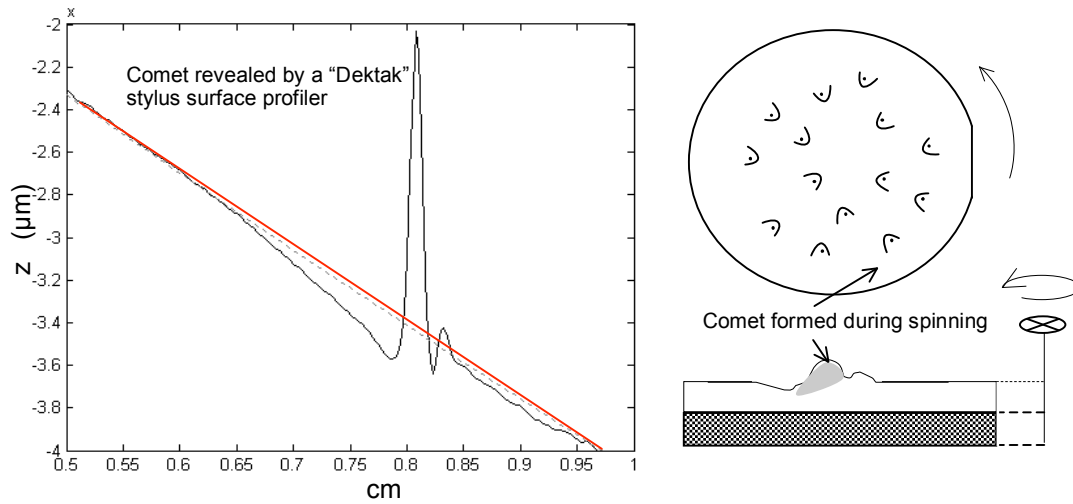


Figure 5.4: Example of surface profile with the “Dektak” stylus profiler, when the profiled surface contains a comet.

In the case of Equation 5-1, these defects affect locally the calculated radius curvature, and don't disturb the overall fitting of polynomial function of the 2nd degree (red line). Comets can then be tolerated in this approximation.

However, the increasing thickness causes the “hill” of PZT at the centre to affect the polynomial fitting of the measurement. A slight offset of the polynomial (red line) in comparison with the measurement (black line) is observable in Figure 5.5.

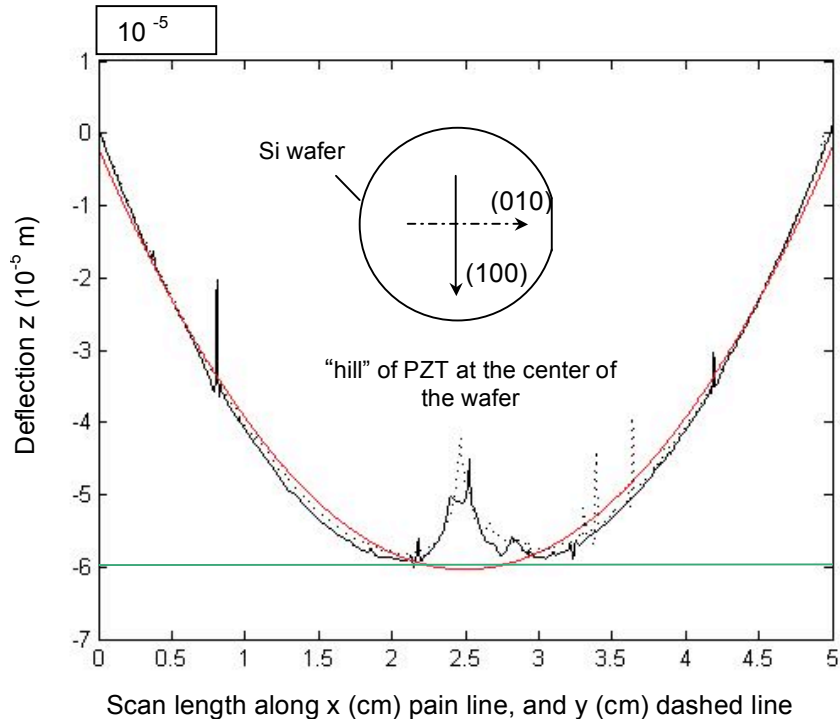


Figure 5.5: Surface profile in the direction (100) (plain line) and (010) (dashed line), obtained for a 27 μ m PZT thick film fabricated with the [2C+6S] process. For the stress calculation, the measurement was approximated in 2 ways: The red lines representing an approximation of the measurement, along the (100) plan, by a polynomial function $f(x)$ at the 2nd degree, and the green line representing the maximum deflection of the wafer.

The observed offset of the fitting function $f(x)$ (in red) will be here neglected. As said before, this chapter doesn't aim to find an exact value of stress. The goal of this chapter is to find a tool to observe the trends of the *in-situ* stress of a sample subjected to different processing conditions. The order of magnitude of the stress of the 27 μ m thick PZT film used for such comparison, will then be approximate by this function $f(x)$ and by the wafer deflection. (Table 5.2)

Table 5.2: Calculated stress of in a 27 μ m thick PZT layer on the substrate: Pt(100nm) /ZrO₂ (40nm)/ SiO₂ (400nm)/Si (525)/SiO₂ (400nm).

27 μ m thick PZT on Pt/ZrO ₂ /SiO ₂ /Si /SiO ₂	Curvature measured (m)	Stress calculated (MPa)
Measurement approximated with the 2nd degree polynomial function (red lines)	-19.7	-19.0
Measurement approximated with the wafer deflection approximation (green lines)	-4.34	-60.7

The difference in calculated curvature is considerable between the polynomial approximation to the deflection approximation, ($\sim 15\text{m}$ of difference). To a lesser degree the same phenomena is observable in the simpler system of 100nm platinum layer on a silicon wafer (4m of difference (Table 5.1)).

In the first case, the measured wafer curvature is approximated by a polynomial function. The radius of curvature is calculated on each point of that function, and then averaged. The whole measurement is taken into account. The hoop forces which are dependent on the quantity of matter present on the hoop are also taken into account, and this hoop stress, has a tendency to flatten the wafer curvature (Figures 5-6 A): The bigger the wafer circumference, the more material is present (Figures 5-6 B) and the harder it is to bend the wafer resulting in a bigger the radius of curvature. Then this hoop stress is not constant throughout but increases from the wafer centre toward the edge as does the radius of curvature. Through the Stoney equation, equation 2.45, these phenomena tend to decrease the stress calculated. The stress of 19MPa obtained for the 27 μm layer of PZT composite on a silicon substrate, is likely to be much lower than the actual stress that actually exist in the film (Table 5.2).

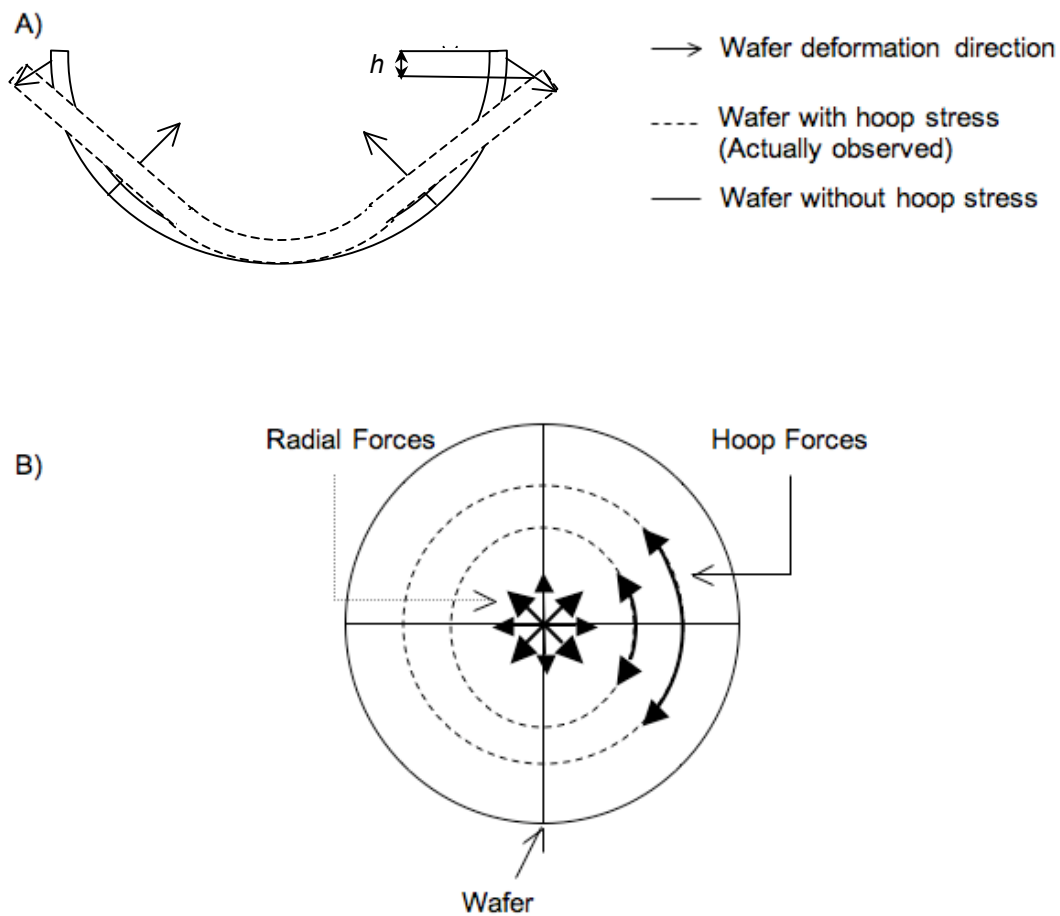


Figure 5.6: Hoop stress: A) effect on curvature, B) hoop stress increases from the centre toward the edge of the wafer.

In the second case, the used deflection to determine stress is a more radical approach, and it can be assumed that the deflection should be less affected by the hoop stress than the polynomial approximation. If this is so, the hoop stress will decrease the observed deflection value by an amount h (Figure 5.6-A) which will decrease the value of *in-situ* stress of the film calculated with the Stoney equation. The real value of stress, assuming all the approximations made here, should be greater than the stress value found with the polynomial approximation and the deflection of the wafer route.

Summary of this section:

This chapter considers some radical approximations, which are implied in the Stoney's equation, except for the first one:

- As seen in Chapter 6, the thickness of the film will be considered as non-constant in a circle of 1 cm radius for the 2-15 μ m thick film and 1.5 cm radius for all films thicker than 15 μ m.
- The films will be considered: infinite, uniformly stressed and without defects. An example of defects is comets due to the condition of spinning affected the data (Figure 5-1).
- The substrates will be considered to be silicon.
- The silicon will be considered as an isotropic material.
- The hoop stress is not taken into account.

The *in-situ* stress calculations presented in this chapter have to be considered as a tool for comparison between experiments. It is impossible to identify accurately the exact forces or stresses present in these PZT thick films using just a wafer curvature measurements, it has to be considered as a rough approximation. Both, the polynomial and wafer deflection approach for the curvature calculation generate errors. This 2 approximations have a different meaning: as said above, the Stoney approach induces errors in the stress value due to the fact that it doesn't take into account the hoop stress. It also has been said above that the deflection approximation, is less affected by the hoop stress than the polynomial approximation, and should increase the value of the in-situ film radial stress calculate through Stoney.

Because of the thickness of the film, the hoop stress is too important to be neglected. The deflection approximation was then chosen as a first approximation throughout this chapter.

5.5 Effect of drying and pyrolysing of PZT thick film on *in-situ* stress

It has been observed that the cracking behavior began during the drying and pyrolysing stages. Figure 5-7 represents the stress variation in composite layers between two temperatures 200°C and 450°C. 2 PZT thicknesses were considered:

- 1 PZT composite layer (~2 μ m).
- 2 PZT composite layers (~4 μ m).

The surface of the structure Si/Pt was profiled after several temperature treatments. The substrate was heated and cooled and these surface-profiling measurements weren't affected. This substrate will be considered unchanged by the temperature treatment.

For both thicknesses, the drying process at 200°C induces a tensile stress and the 450°C pyrolysing process releases some stress (Table 5.3).

- The drying process is conducted at 200°C. At this temperature the solvent is removed and the solidification of the sol occurs. The shrinkage of the film induces an *in-situ* tensile stress in the composite layer, and a shear stress at the interface between the film and its substrate.
- The pyrolysing process at 450°C burned the organic components remaining in the sol, and began the sol crystallization on the PZT powder particles. Both of these processes could relax the *in-situ* stress through creep mechanisms, micro-cracking or generation.

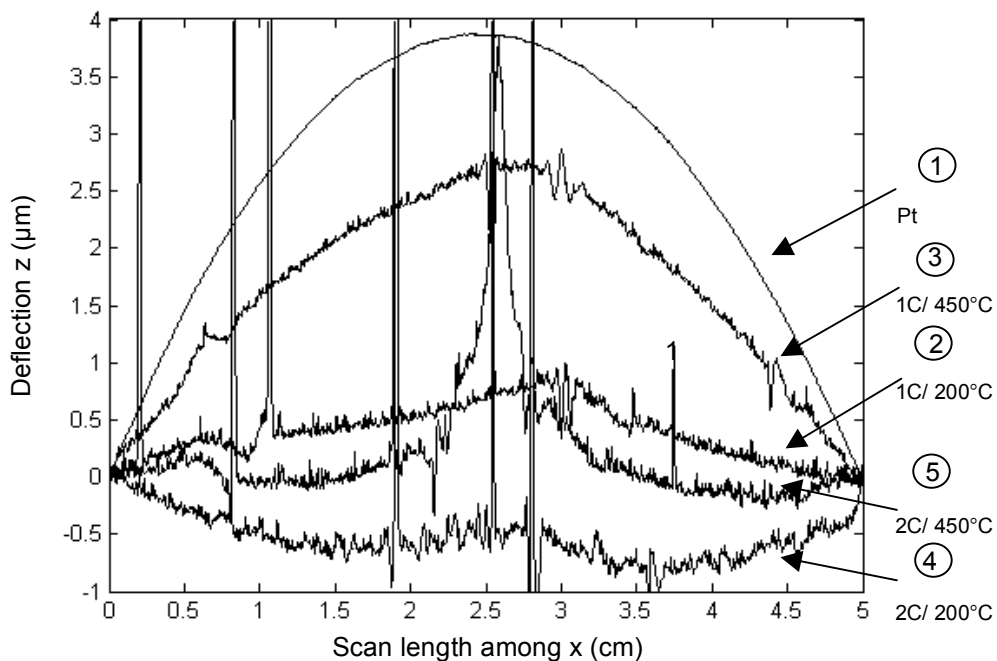


Figure 5.7: Surface profiling of the system $x\text{C}/\text{Pt}/\text{SiO}_2/\text{Si}/\text{SiO}_2$: $x=1,2$ and is the number of composite layers, C. Both layers were profiled at 20°C after a temperature treatment of 200°C and, after a further temperature treatment of 450°C. (Circle numbers show the succession of the deposition and temperature treatment)

Table 5.3 Stress calculation of the system $x\text{C}/\text{Pt}/\text{SiO}_2/\text{Si}/\text{SiO}_2$: $x=1, 2$ and is the number of composite layers, C . Both layers were profiled at 20°C , after a temperature treatment of 200°C and, after a further temperature treatment of 450°C .

Comp. layer	Temperature	deflection (μm)	R_{PZT} . of curvature	Stress (MPa)
1C (~2.5 μm)	200°C	+0.5	+625	+34
1C (~2.5 μm)	450°C	+2.5	+114	+10.8
2C (~5 μm)	200°C	-1	-313	-37.5
2C (~5 μm)	450°C	-0.25	-1560	-20.5

The stress relaxation is 23.2MPa between 200°C and 450°C for the 1st composite layer, and 17MPa for the 2nd composite layer:

- For the first composite layer, the deflection is measured, then the curvature is calculated. The radius was then corrected for the platinum radius curvature according to the Stoney's equation correcting coefficient, $(1/R_{\text{PZT}/1\text{C}} - 1/R_{\text{Pt}})$.
- For the second layer the calculation cannot be done as if the 2 composites layers were deposited together. Here, the discussion is on the relaxation of the 2nd composite layer. Considering just the addition of the second layer; the substrate becomes 1C/Pt/Si. Its thickness will be formed by the 525 μm of silicon, and by the thickness of the added composite layer, 2.5 μm . Considering the Stoney's radius curvature coefficient $(1/R_{\text{PZT}/2\text{C}} - 1/R_{\text{PZT}/1\text{C}})$, a stress of 37.5MPa is calculated for the 2nd composite layer treated at 200°C and a stress of 20.5MPa for this system treated at 450°C .

The stress relaxation for the second composite layer between the 2 temperatures is 17MPa, which considering the approximation, can be considered equivalent to the relaxation of ~23MPa found for the 1st layer. The main issue with this calculation is that the substrate curvature is considered for the system 1C/Pt/Si, but just Young modulus and the Poisson ratio of the silicon are considered for the stress calculation. As the comparison of thicknesses is 1C(2.5 μm)/Pt(100nm)/silicon(525 μm), the approximation seems reasonable. However, when the number of composite layers layer increases, the approximation becomes arguable, as the Young's modulus and the Poisson ratio of the composite are unknown, and this analyse can be done just for the first layers.

The last temperature treatment that the sample is subject to, is the final sintering process at 710°C . The curvatures of a 27 μm PZT thick film after the 450°C thermal treatment and after the thermal sintering process at 710°C were measured to approximate the stress relaxation occurring between these 2 temperatures (Figure 5.7):

At high temperature, (710°C), the PZT crystallized through atomic diffusion. This atomic rearrangement minimizes the energy of the system and then should release some stress.

In this case the whole film thickness releases the stress. The stress calculation was therefore done with a radius of curvature coefficient equal to $(1/R_{\text{PZT, total-thickness}} - 1/R_{\text{Pt}})$. The sintering process is then demonstrated to release 17.5MPa of stress. This explains why sintering the PZT during the fabrication process can help to reduce the stress, and can help to increase the final film thickness. (Chapter 4.4)

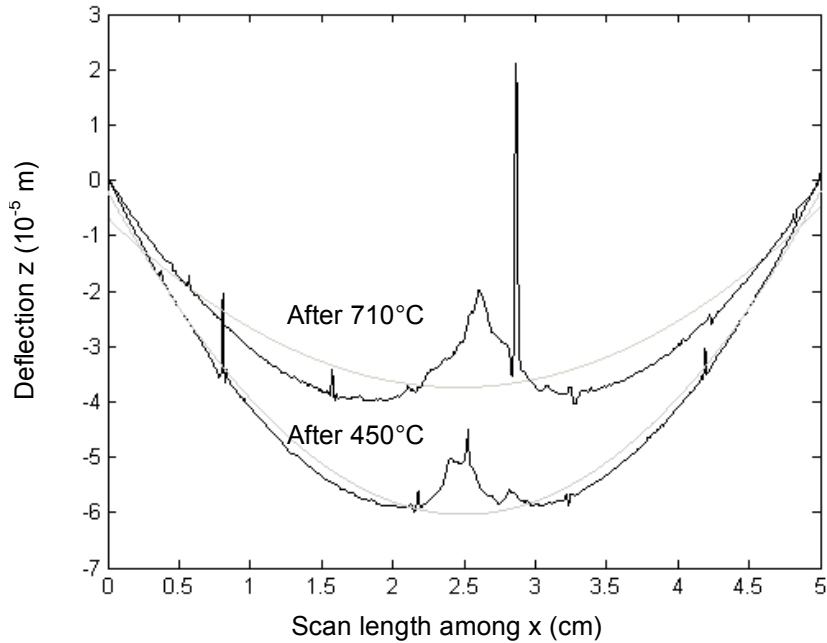


Figure 5.8: Surface profile of the system 6[2C+6S]/Pt/SiO₂/Si/SiO₂: The surface of this system was profiled at 20°C, after a temperature treatment of 450°C and, after a temperature treatment of 710°C.

Now that the effect of the different temperature treatments on the *in-situ* stress of our system is understood, temperature treatments like the sintering process can be used as a tool for reducing the stress in a system.

After the drying stage the stress is considerable (30MPa), and the PZT film stiffness is low because it has not crystallized yet. The experiment demonstrated that the cracks start to form mainly during this stage after a certain number of infiltrations. A study of the evolution of stress during the infiltration process needs to be done to understand the crack formation, and so to control their formation.

5.6. Stress added via the PZT sol infiltration steps

The sol infiltration is used to fill the pores of the composite layer. This densification process raises another stress due to the solidification of the infiltration sol inside the pores. Figure 5.9 and 5.10 represent the increase of stress with respect of the number of infiltrations.

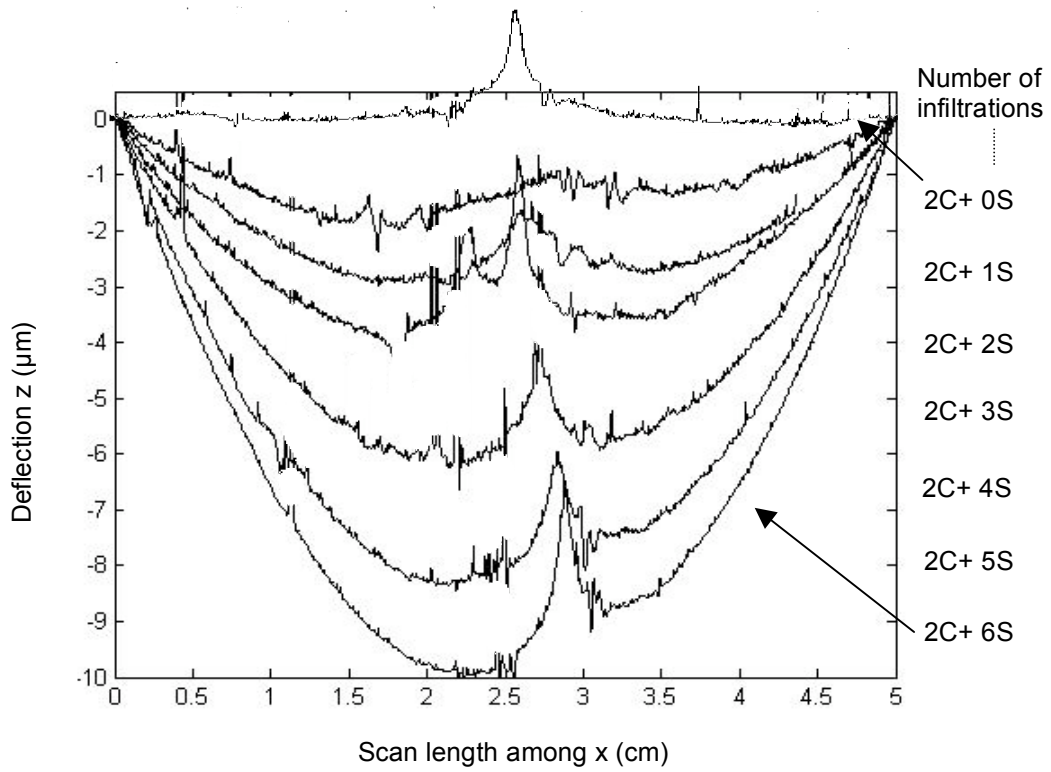


Figure 5.9: Surface profiles of system $[2C+xS]/Pt/SiO_2/Si/SiO_2$: where x is the number of infiltrations. The curvature of the system increases but the thickness is considered constant throughout the infiltration steps, and equal to $5\mu m$.

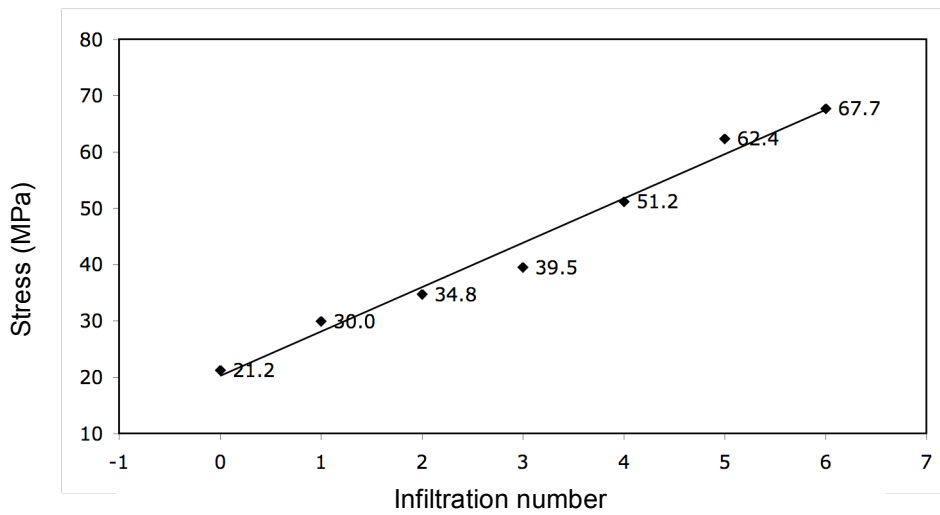


Figure 5.10: Stress calculated from the deflection of the surface profiles of system $[2C+xS]/Pt/SiO_2/Si/SiO_2$: where x is the number of infiltration steps (Figure 5.10).

The infiltration number dictates the curvature of the wafer: the more the number of infiltrations the more the curvature, and then, the greater the stress (Figure 5.10).

Because of all the approximations done, the increase of stress with regard to the number of infiltration steps will be considered linear. With reference of Chapter 4:

- The 1st infiltration penetrates well into the material, the shrinkage, induced by the drying and the pyrolysing stage, increases the in-situ stress by ~10MPa (from 21.7MPa to 30MPa). The infiltration sol dried inside the porosity induces the tensile stress.
- From the 2nd to the 3rd infiltration, the infiltration steps have less effect on the film *in-situ* stress: the penetration of the pores by the infiltration sol is less effective in term of percentage of filling of the porosity, and the surface porosity is less and less open.
- The 4th infiltration step is characterized in Chapter 4 by its surface porosity which starts to be closed. The 4th infiltration concentrates the sol on the film surface and increases the in-situ stress considerably by another 10MPa. The infiltration penetrated the film and closed the surface porosity.
- The 5th and 6th infiltrations mainly stay on the film's surface and do not infiltrate. Two layers of dense pure PZT sol remain on the surface. The stress increases by another 10MPa (Figure 5.10).

Chapters 6 and 7 will present a study on how the number of infiltration steps improves the properties of the device: Dielectric, and piezoelectric properties increase while the number of infiltration steps increases. The best sample will have the smallest amount of stress and the highest piezoelectric properties.

For the 30 μ m thick film devices, Chapter 4 reveals that the 4th and 5th infiltration steps represent the highest infiltration steps before the appearance of cracks that can become critical. The devices infiltrated 6 times start to form these cracks, and the 7th and 8th stage infiltrated films are mainly cracked at this thickness in a way that some device can still be analyzed but are not usable industrially (more than 70% of the devices present on one wafer are not usable).

This study reveals that the in-situ stress of the film evolved linearly with the number of infiltration steps, and that devices infiltrated 4 times could be the better trade off between the surface finish (Chapter 4) and the stress situation of the film. The devices infiltrated 5th or 6th times see a considerable increase of stress and a formation of an interlayer sol, as observed in Chapter 4.

A trade off between this stress situation, which degrades the surface finish by crack formation, and the properties of the sample has to be made for an industrial application. The 1st critical cracks seem to appear at the 6th infiltration for this kind of thickness (~30 μ m). The next section examines the evolution the stress with an increase in the thickness of a [2C+6S] film. This study was stopped when the first critical cracks appeared.

5.7 Effect of PZT film thickness on *in situ* stress

A major contribution to the *in-situ* stress seems to arise from the infiltration step process. However, the stress should also be thickness-dependent. The more material, the greater the force applied at the interface between the PZT film and the silicon wafer. Figure 5.11 illustrates that the deflection of the wafer increases linearly from 9 to 59 μm with an increase of thickness.

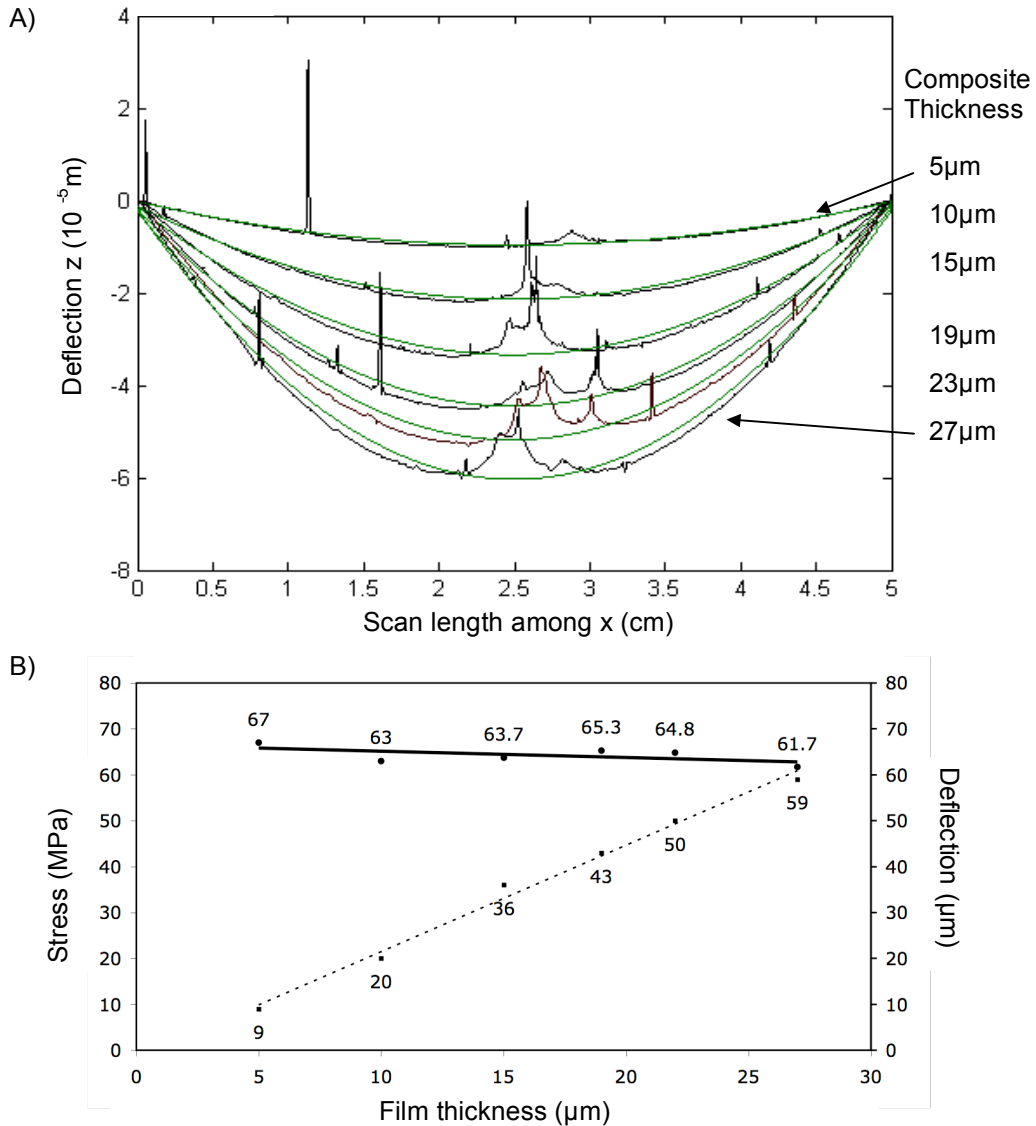


Figure 5.11: A) Surfaces profile of system $x[2\text{C}+6\text{S}]/\text{Pt}/\text{ZrO}/\text{SiO}_2/\text{Si}/\text{SiO}_2$: where x is the number of $[2\text{C}+6\text{S}]$ units. B) Stress calculation from the Stoney's equation and the wafer curvature: The deflection of the system increases with an increase in the thickness.

The deflection of the wafer relates to the tensile force in the film. These forces increase by a factor of six between films of thicknesses of 5 μm and 30 μm . In the Stoney's equation, the

calculated stress is proportional of the deflection, and inversely proportional to the film thickness. Therefore, the stress value remains constant.

The experiment was stopped when the first critical cracks appear. When the thickness reached $30\mu\text{m}$, the first cracks appear close to the edge of the wafer and in the centre (Figure 5.12).

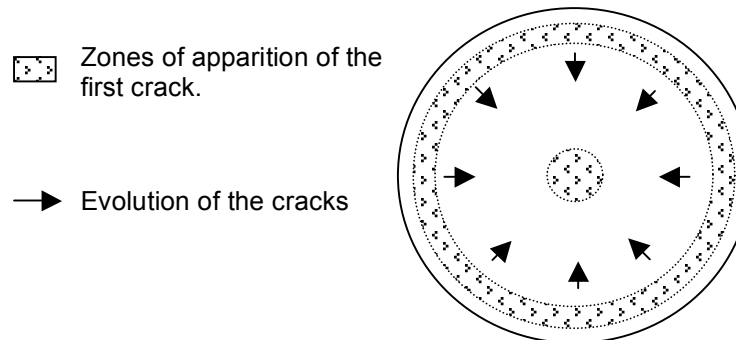


Figure 5.12: Illustration of the location of the first cracks when a $30\mu\text{m}$ thick PZT composite thick film is spun on a silicon substrate coated with 100nm of Pt (process [2C+6S]).

The cracks are first localized on the external hoop, and they evolve from the edge of the wafer towards the centre of the wafer. At $30\mu\text{m}$ of film thickness, the cracks are not localized yet in the area of the wafer where the devices are supposed to be developed (mid radius). However this thickness can consider as the limit for a [2C+6S] process.

It is not surprising that, for processes involving less infiltration steps, the maximum thickness achieved increases before the appearance of critical cracks. Then for a [2C+4S] process the deflection of $60\mu\text{m}$ inducing cracks is achieved for a film of $35\mu\text{m}$. However, the [C+4S] process achieved this deflection for a thickness of film equal to $21\mu\text{m}$.

It seems then reasonable to think that the hoop stress is first responsible for the crack formation. This hoop stress is purely dependent on the amount of material present on the circumference. The central cracks are mainly thickness stress related, and are due to the unspun amount of material accumulated in the centre of the wafer, due to the use of the spin coating technology.

The silicon substrate is used in MEMS technology because it is well known material that is relatively easy to shape. However, a lot of devices cannot be produced on silicon wafer because of the stress development situation. The next section demonstrates that silicon is not the best match for the composite PZT thick film technology. However, an alumina substrate allows the deposition of more than $40\mu\text{m}$ of PZT composite thick film without the appearance

of critical cracks. It demonstrates then that for a future development of this technology a full study on the choice of the substrate needs to be done.

5.8 PZT thickness effect on the *In-situ* stress on alumina different substrates

This section, represents the first test of spinning a thick film of the PZT composite onto alumina. The bending behaviour of the alumina wafer with 30 μ m thick film of the PZT composite films illustrate the development of a compressive stress, while the stress of such thick film on silicon has tensile character (Figure 13.A and B).

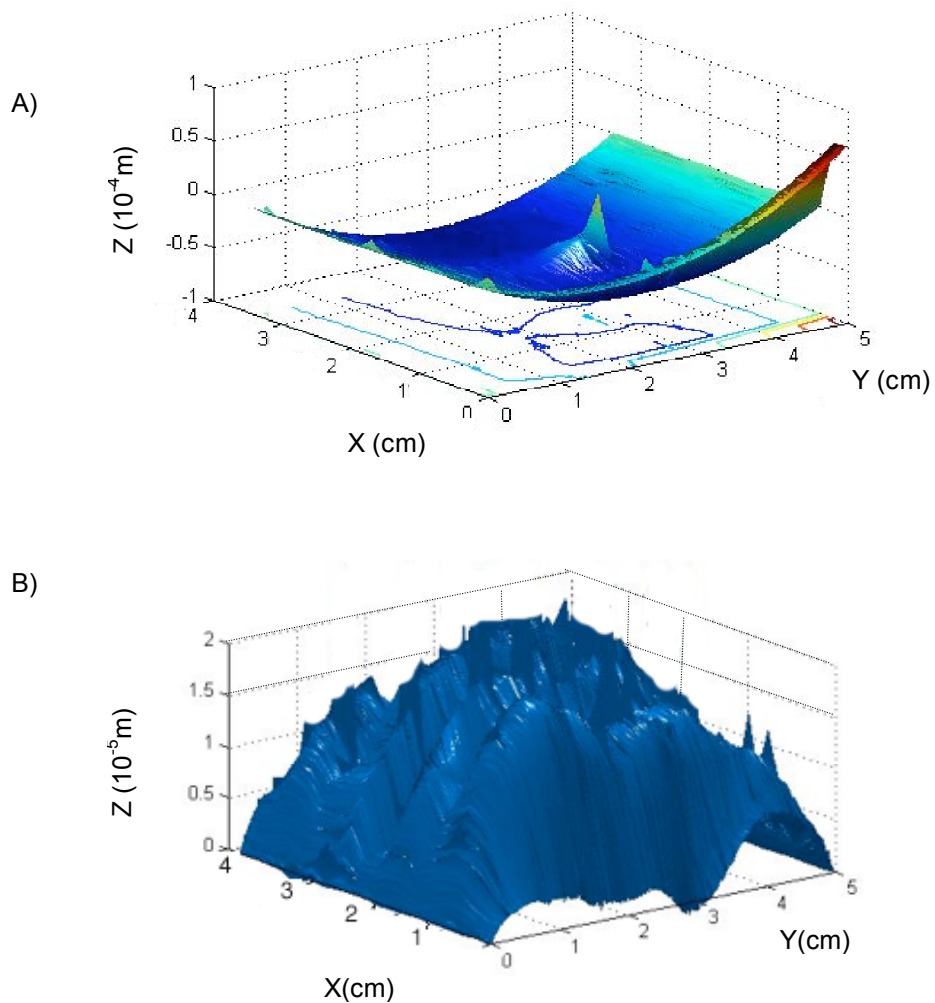


Figure 5.13: Surface profile of: A) a 27 μ m PZT composite thick film on a silicon substrate. (7[2C+6S]/Pt/ZrO/SiO₂/Si/SiO₂), B) a 30 μ m PZT composite thick film on an alumina substrate. ([2C+6S]/Pt/AL₂O₃).

The deflection of the system, PZT thick film on a alumina wafer, remains approximately constant with an increase of thickness, and the stress decreases from ~35MPa to ~15MPa (Figure 5.14.c) and d)). On a silicon wafer, such a thick film induces a considerable deflection, which induces the stress to be approximately constant around 65MPa.

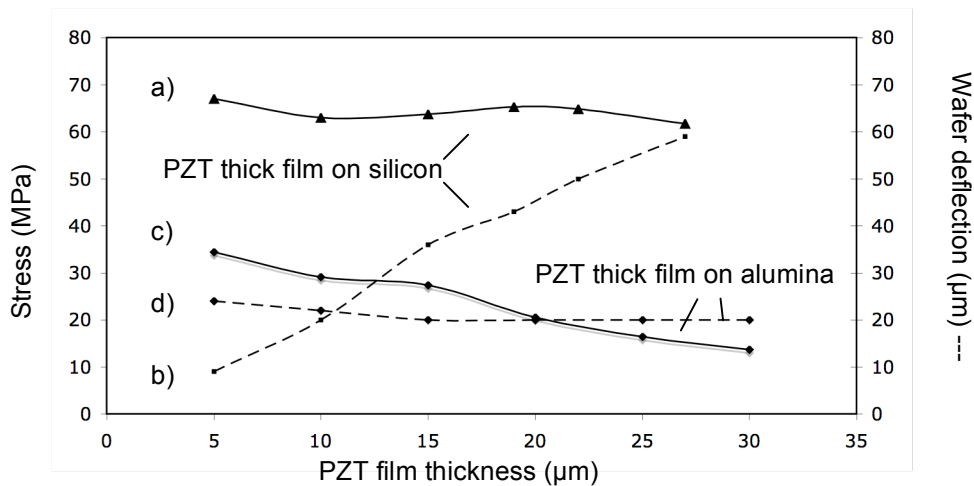


Figure 5.14: Stress calculated from the wafer deflection for different thicknesses of PZT composite on alumina and on silicon: a) stress value developed by a increase of PZT thickness on silicon, b) deflection of the silicon wafer, c) stress value developed by a increase of PZT thickness on alumina, b) deflection of the alumina wafer.

For the thick film deposited on silicon, when the wafer deflection increases above 60µm, cracks begin to appear. On an alumina substrate, an increase of the PZT thickness does not increase the wafer deflection, which remains approximately constant. Then, the increase of the shear forces observed at the interface PZT/silicon are no longer observed on alumina, and, on average, the stress of thick film on alumina is calculated to be approximately half of the stress developed on alumina. At this stage the PZT gel has not been converted to crystalline oxide ceramic. Considering this, two explanations can be given for this phenomenon:

The thermal expansion coefficient is 3 times higher for alumina than Silicon [Orhing, 1992]. For the case of silicon substrates, heating the coated wafer results in relatively small curvature of the wafer and small-scale creep relaxation prior to pyrolysis. On cooling, the low thermal expansion coefficient of silicon with regard to PZT causes the PZT stress to become tensile and cracks are generated.

- 1) For the case of Al_2O_3 substrates the coated wafer exhibits large positive curvature indicating tensile stresses in the PZT/Sol-gel film. This tensile stress can be accommodated through creep relaxation of the organic sol-gel phase prior to full

pyrolysis. On cooling, the high thermal expansion coefficient of alumina places the PZT under compression preventing cracking.

- 2) The thermal conductivity of the alumina is 5.2 times lower than that of silicon [Orhing, 1992]. The PZT composite gel molecules, therefore, have more time to reorient themselves when converting to a solid state, inducing less in situ stress in the PZT composite green ceramic.

The thermal match between alumina and the green PZT opens a wide range of possibilities for multilayer technology using the spin coating as a deposition technique.

5.9 Summary

The Stoney's equation has been validated to be usable as a comparison tool between different processes. This validation allowed the understanding of how temperature treatment relaxes some of the *in-situ* film stress through creep mechanisms, micro-cracking, or pore generations. It also helped to understand the stress dependency of the infiltration degree of the composite film, the substrate and the film thickness. With the preceding qualitative Chapter 4 and this chapter on stress situation reveal that the process involving 6 infiltrations represents the maximum possible infiltration for the fabrication of film as thick as 30 μ m. In the trade off between the surface finish and the film properties, just the surface finish has been studied. The next chapter will then focus on a study of the dielectric and the ferroelectric properties with regard the effect of the number of infiltrations and the thickness of the film.

Chapter 6

Dielectric, piezoelectric and ferroelectric properties of PZT thick films

6.1 Introduction

A transducer's performance is defined by its electromechanical behaviour. The electromechanical behaviour of a piezoelectric material is itself defined through the polarisability, which is itself controlled by the charge displacement ability, or the electrical permittivity.

Understanding the relative permittivity of a material is one of the main targets when a new material is to be used for a transducer, or capacitor application. In order to give an insight into this new material behaviour the changes in permittivity with different processes inducing more or less porosity are presented here. The permittivity will be analytically modelled as a function of the porosity level, and compared to experimental results. For this section, a simple test structure (Figure 6.1) was used.

As transducer development tends to smaller elements, the permittivity of different size of elements was analyzed, as well as the dielectric loss.

The transducer studied is piezoelectric and ferroelectric, thus once the permittivity was understood, the piezoelectric coefficient (d_{33}) as function of different degrees of porosity is also presented. This study led to an optimisation of the poling process through the measurement of the piezoelectric coefficient.

As a transducer is driven with an applied electric field, it is indispensable to present the polarisation of the material as a function of the applied electric field as given by the hysteresis loop. This last section presents an introduction to the importance of the choice of a fabrication process regarding the polarisation behaviour in particular the different behaviour of the same material arising from the use of different substrates.

6.2 Experimental set up

Using the test structure shown in Figure 6.1, two processing routes are compared in Figure 6.2. This first experiment shows the behaviour of three wafers coated with 4[C+4S] film from three slurries processed with the same route. The data presented here represents an average of 27 devices per wafer.

The first wafer was exposed to a rapid thermal annealing (RTA) process ($710^{\circ}\text{C}/200^{\circ}\text{C}\cdot\text{s}^{-1}/30\text{min}$) designed to develop the perovskite structure (Figure 6.2.B). The 2nd and 3rd wafers were exposed to a thermal treatment in a large chamber furnace where the temperature was set at 690°C and 710°C respectively (Figure 6.2.C, and Figure 6.2.A). The heating rate of this furnace was $3^{\circ}\text{C}/\text{min}$.

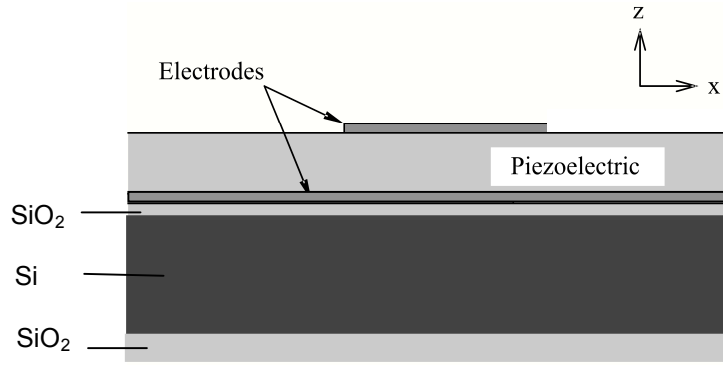


Figure 6.1: Test structure use for the relative permittivity, d_{33} , and e_{31} measurements.

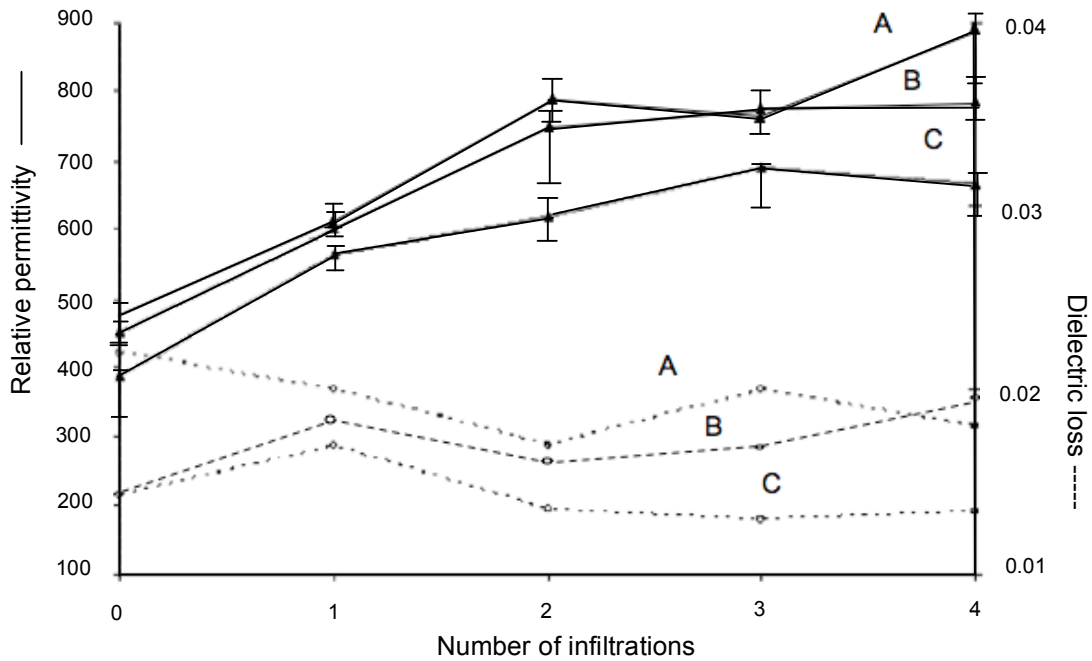


Figure 6.2: Relative permittivity and dielectric loss of the [C+4S] PZT composite thick film crystallised with a furnace at 690°C (C) and 710°C (A) (wafer temperature), and an RTA at 710°C (B).

The general behaviour of the dielectric constant with the sol infiltration can be observed in Figure 6.2. The more sol infiltrations, the more the relative permittivity values, until a saturation value at the third/fourth infiltration is reached. As the first infiltration has a better access to the porosity than the second, etc, the rate of change of relative permittivity decreases with increasing infiltration.

The sol infiltrations and the sintering aid fill in the film porosity, defining a densification process. The added sol will directly crystallise on each grain, which will act like a seed, and

then fill in the porosity. The sintering aid will melt during the sintering process and add a liquid phase which will improve this densification process. This densification process will naturally increase the dielectric constant because of:

- The increase of the amount of material: replacing air by a dielectric [Cho *et al.* 1995]
- The porosity represents more than just air. It can be considered as an impurity, represents an obstacle for the electric field and for dipole displacement. [Cho *et al.* 1995]

6.3 Effect of the sintering temperature

The main difference between the samples is the final sintering temperature used (experiment C and B) and the sintering temperature-heating rate (experiment A and B). From Figure 6.2, some general trends of the relative permittivity can be observed. The dielectric loss and the relative permittivity are lower for material sintered at 690°C compared to that sintered at 710°C. The relative permittivity and dielectric loss of samples sintered in the RTA at 710°C are lower than the one passed in a furnace at 710°C.

- i. Crystallisation temperature.

The experiments illustrated by Figure 6.2 represent the results obtained for three different samples from different composite slurries. The observed trend could have been just due to random differences between the three composite slurries. To confirm this experiment, two parts of the same sample (D) were crystallised in the same furnace at two different temperatures: 710°C and 690°C (Table 6.1). It was confirmed that crystallising at 710°C resulted in a higher relative permittivity.

Figure 6.3 illustrates the sintering process increasing the material density. The grain radius r and neck radius n are dependent on the temperature through the equation 6.1 [Ohring 1992].

$$\frac{n^5}{r^2} = \frac{A_L}{T} t \text{ and } \frac{n^7}{r^3} = \frac{A_S}{T} t \quad \text{equation 6.1}$$

Where r is the grain radius, A_L and A_S are two linear constants depending respectively on the lattice atomic diffusion and the surface atomic diffusion, and t is the time.

Equation 6.1 shows that a high crystallization temperature increases the grain size while reducing the radius of neck. Thereby, the atomic diffusion on the grain surface and lattice during the crystallisation reduces the porosity. Replacing air with a dielectric material will increase the dielectric permittivity. Also when the atomic diffusion is increased the sintering

process help the *in situ* migration of defects in each grain. This can remove some defects which improve the effective charge displacement and the relative permittivity.

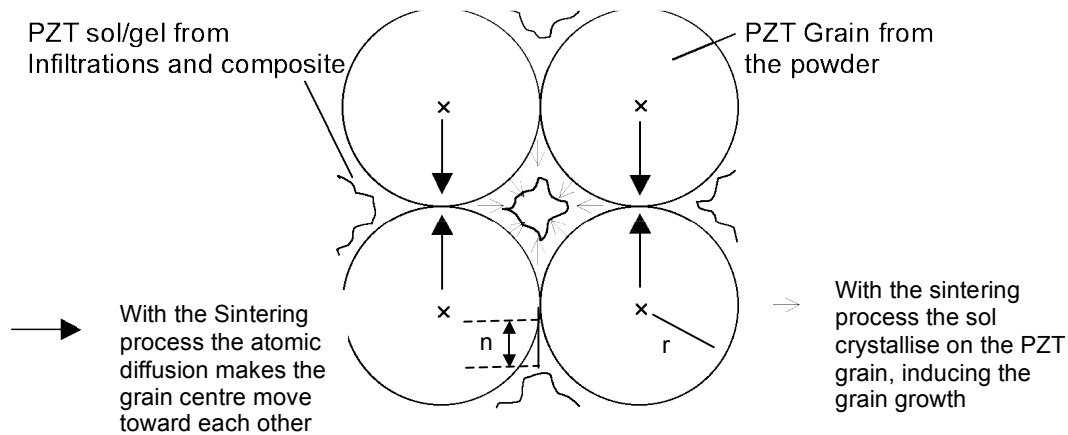


Figure 6.3: Schematic of 2 atomic diffusion processes taking place during the sintering process.

The most important effect here is that the sintering aid (CuO_2) has a melting point of 688°C . The liquid phases are well known to accelerate the surface atomic diffusion during a sintering [Ohring, 1992]. At 690°C the sintering aid might not be fully melted, which should reduce dramatically the atomic diffusion, and hence the densification process.

In this case, both a pure temperature effect and the suppression of the liquid phase during the sintering will affect the density of the sample sintered at 690°C .

ii. The furnace-heating rate

In order to confirm the trends observed in Figure 6.2, where the heating rate seemed to influence the permittivity. Two parts of another samples (E) were sintered at the same temperature but at two different heating rates: in a furnace at $3^\circ\text{C}/\text{min}$ and in a RTA at $200^\circ\text{C}/\text{min}$. In Table 6.1, the sample sintered in the RTA exhibited a lower relative permittivity which confirms the trend observed in Figure 6.2.

The heating rate is not a variable that should influence the sintering process. However, the sintering time is. The difference observed between these samples is due to the difference of the sintering time. All the samples were sintered for 30 minutes. However, the sample sintered in the furnace remained for approximately 7 minutes more at a temperature above 688°C than the sample sintered with the RTA due to the slower heating and cooling rates.

The dielectric loss of the sample sintered in the RTA is higher than that of the sample sintered in the furnace in Table 4, but the reverse trend is observed in Figure 6.2 for samples with less

than 4 infiltration treatments. This dielectric loss effect will be discussed later in this discussion (section 6.6)

Table 6.1: Confirmation of the trend observed in figure 6.2: influence of the temperature and heating-rate on samples prepared with the [C+4S] process.

Sample	Heating conditions	Relative permittivity	loss
Furnace (sample D)	690°C@3 °C/min	600	0.01
Furnace (sample D)	710°C@3 °C/min	808	0.01
Furnace (sample E)	710°C@3 °C/min	800	0.01
RTA (sample E)	710°C@300 °C/min	760	0.02

6.4 Modelling of porosity effect on relative permittivity

The level of porosity within a material will directly influence the relative permittivity through the James Clerk Maxwell equation (Equation 6.1):

$$\epsilon_{Composite} = \epsilon_{PZT} \cdot \left\{ 1 + \frac{3V_p (\epsilon_{porosity} - \epsilon_{PZT})}{\epsilon_{porosity} + 2\epsilon_{PZT} - V_p (\epsilon_{porosity} - \epsilon_{PZT})} \right\} \quad \text{Equation 6.2}$$

Here V_p is the volume fraction of porosity. This formula was developed in order to characterise mixtures of dielectrics. In this case, a mixture of air (porosity) and PZT [Moulson *et al.* 1990].

This equation assumes that the pores are spherical in shape. While this is not true for this material, it does provide a useful starting point to analyse the effect of porosity on the relative permittivity. A very good text book on the effect of the porosity on permittivity enters in detail in that discussion. [Rice, 1962]

Many experiments carried out for this PhD revealed a very inconsistent behaviour of the relative permittivity. Sometimes, two sample batches showed a difference of 10 to 15% in their values. Equation 6.1 is not used to predict exactly the dielectric constant values. Instead, the main goal is to gain an insight into how the relative permittivity of the material changes in relation to its porosity.

The reality is that the relative permittivity of our material is an unknown variable. As stated above, through different experiments a very inconsistent series of values were found for the same process. The James Clerk Maxwell approximation represents a trial to understand the fluctuation of this relative permittivity in the most effective way.

In Equation 6.2 the relative permittivity of a dense composite (ϵ_{PZT}) is required to predict the relative permittivity of the porous composite. This dense composite doesn't exist. However, since it was established in Chapter 4 that the porosity of the material after the second infiltration is roughly 10%. The experimental relative permittivity of these materials was set as the lowest $\epsilon_{PZT} = 700$ and 850 for the highest, to correspond to 10vol% of porosity. Thus these highest and lowest relative permittivity values generate two different curves described by Equation 6.2. A 3rd curve represents the case of unpoled bulk PZ26 established as reference. Its full density relative permittivity is 1200. Figure 6.4 shows that the PZ26 bulk relative permittivity is far above the highest values achieved with the composite system.

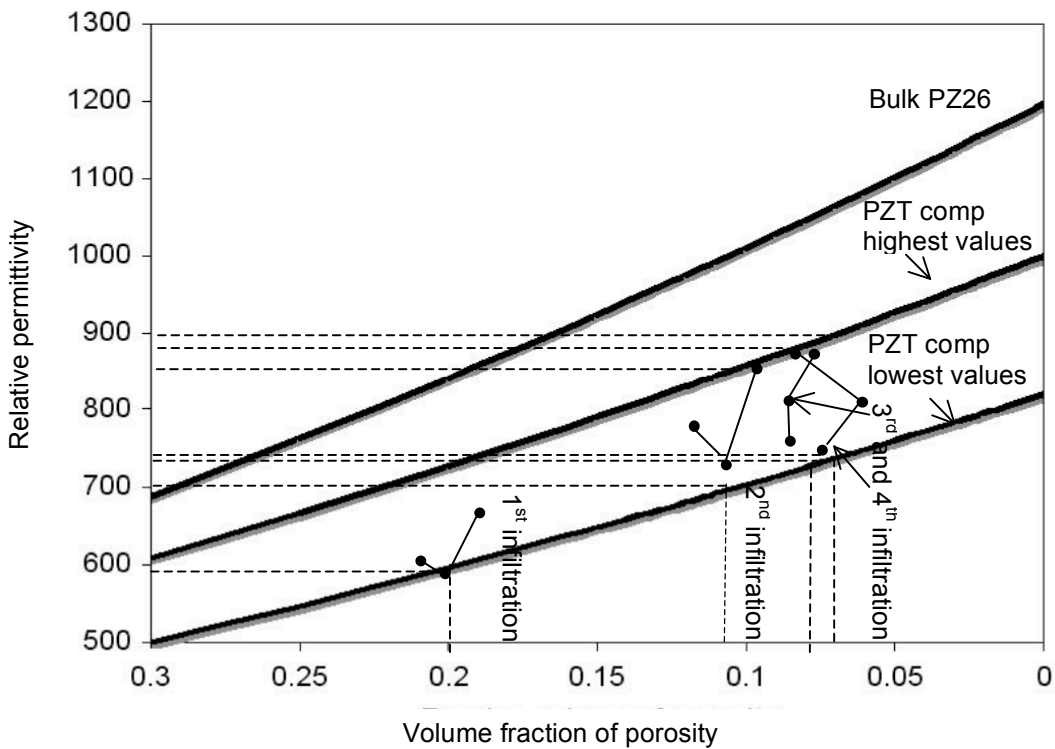


Figure 6.4: Illustration of the PZT composite relative permittivity as function of its porosity using the James Clerk Maxwell equation. The two lowest lines represent the equation 6.2. The highest line represents the same equation applied to an unpoled bulk ceramic. The model is then compared to some experimental data.

Figure 6.4 shows that the lower the volume percentage of porosity the higher the relative permittivity. Also, the bulk PZ26 relative permittivity is higher than the composite one. The main explanation of this difference is based on the sintering temperature process. The raw material used to make this bulk ceramic is grains of PZT powder sintered at a high temperature of 1300°C, which is far higher than the unpressed-710°C process used for the composite system.

The temperature remains the principal explanatory factor, but to that it has to be considered that the PZT composite has a much more complex structure than the bulk PZ26. The fabrication of bulk PZ26 involves just one phase, the PZT powder. However, the PZT composite is processed using 2 different phases, the PZT powder and a sol-gel solution. Figure 6.3 represents a schematic of this composite PZT powder- sol-gel. To the complexity of a powder ceramic is added the complexity of a sol-gel solution as seen in literature [Livage, 1992]. The PZT sol is a second phase, adding interfaces in the system that can have a different composition. This composite system includes many interfaces, which add surface effects to the system such as surface tension and un-complete dipoles. The less dipole, the less charge displacement, the less energy can be stored in the system. This can also explain partly the difference of relative permittivity between the two systems compared in Figure 6.4.

This model includes many incorrect aspects, but this approximation allows the understanding of how the relative permittivity evolves as a function of the level of porosity. The model needs to be confirmed by experimental data. Some typical data are included in Figure 6.4 to validate the model.

The relative permittivity of all the samples was measured to be consistent with the proposed model. The samples infiltrated 1 and 2 times are distinctly different in terms of the relative permittivity. The model and the experiments show that between the 1st and the 2nd infiltration the relative permittivity increases by a value of 100. The samples infiltrate 3 and 4 times cannot be considered to have different values of relative permittivity. Their porosity can even be considered approximately the same. This illustrates that the first infiltration has a better access to the porosity than the second, which has a better access than the third infiltration etc... However always the same amount of infiltration is added, the preceding chapters show that after the second infiltration some sol remains at the surface of each composite layer infiltrated. Any infiltration remaining at the surface of each composite layer slows even more the infiltration process. Figure 6.4 illustrates also that the powder/sol ratio has an influence on the relative permittivity. When spinning the 3rd and 4th infiltration less infiltration remains into or on the film than for the 1st and 2nd infiltration step. They therefore influence the relative permittivity less.

Figure 6.4 illustrates that the dielectric constant cannot be predicted with precision when a sample is being processed. However, for a given infiltration level this model will be capable of predicting a range of values of relative permittivity. Based on this short analysis, an approach to the PZT composite relative permittivity is possible.

The thickness of the different film was then patterned by different degrees of infiltration. The surface finish and relative permittivity was then studied through Chapters 4, 5, and the beginning of this Chapter 6. To fabricate an array transducer, single elements composing this array need to be studied. In general the possibility to have even smaller elements in a transducer is important for the development of this research as the more elements that are involved in a transducer the more pixels the final image can include. A study on their size

effect needs then to be led. As the goal of this work is to fabricate an annular array, a first study on the influence of cylindrical electrode sizes on the relative permittivity and the dielectric loss will be conducted.

6.5 Cylinder device: relative permittivity of free standing elements

6.5.1 Cylinder device design

Figure 6.5 shows a general view of the chromium mask set used for all of the experiments. The masks are fully presented in Appendix B. Different sizes of electrodes were designed to facilitate the measurement of the dielectric and the impedance properties. A typical structure is illustrated in figure 6.6.

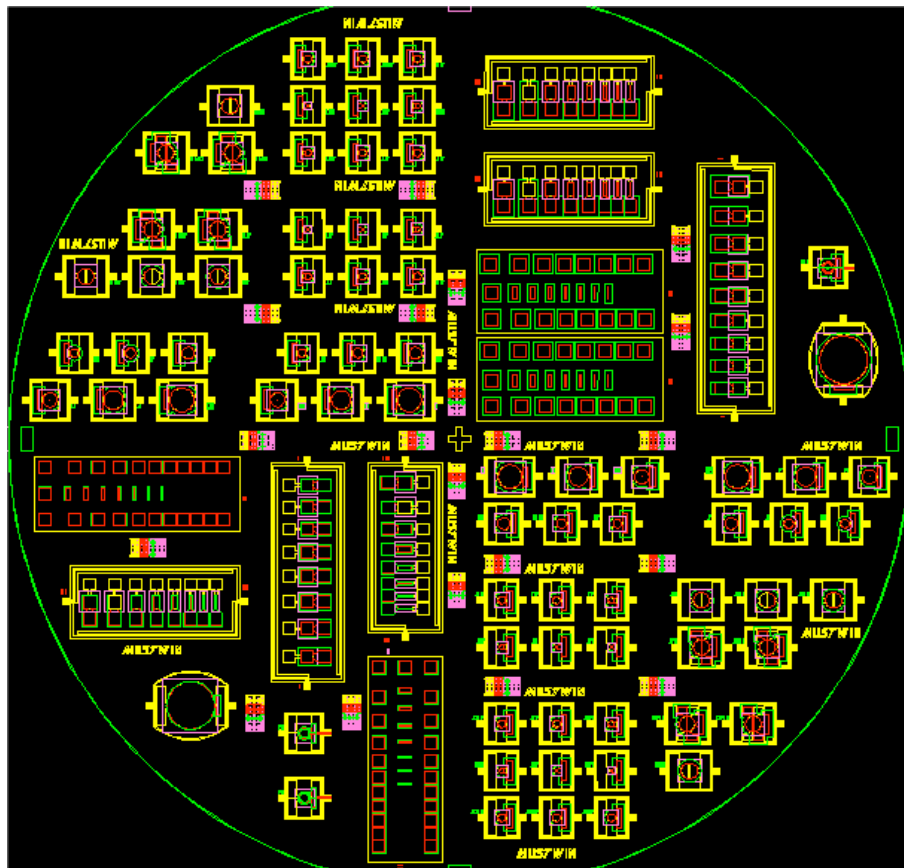


Figure 6.5: AutoCAD drawing of the chromium masks used to process the cylinder device and to characterise the PZT composite material.

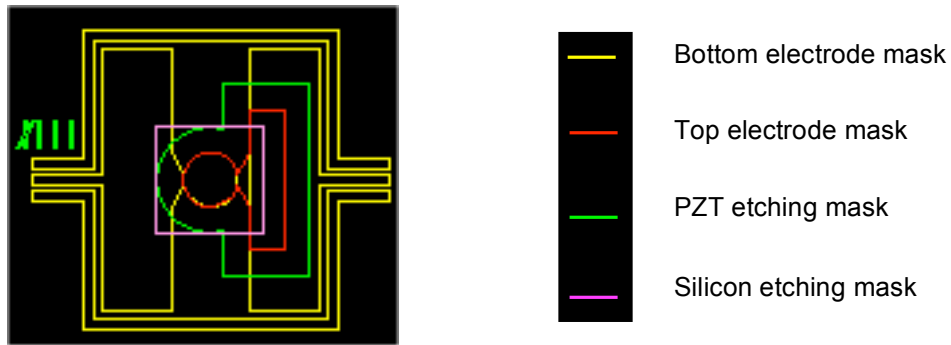


Figure 6.6: Chromium mask design for the cylinder device presented in Figure 6.7.

The electrode sizes ranged between $50\mu\text{m}$ and 2mm radii for the active area. The rectangular pad was added to the bottom electrode to measure S_{11} with single probes and to measure the capacitance of the devices. (Appendix B)

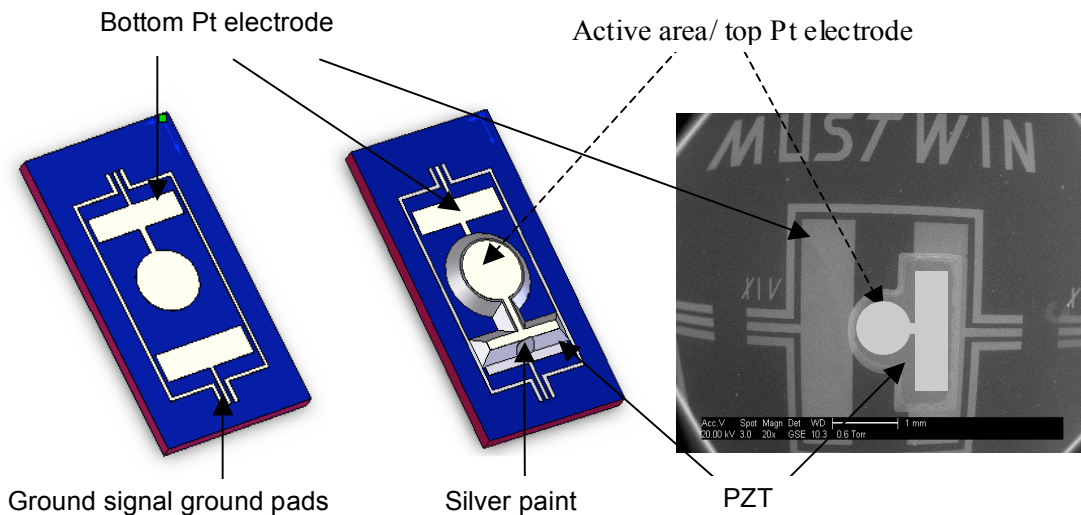


Figure 6.7: Schematic of a typical device made with masks. The top electrode on the SEM micrograph has been added for clarity.

The ground-signal-ground pads shown in Figure 6.7 were designed to measure the S_{21} parameter (Section 3.8).

6.5.2 Capacitance and relative permittivity

6.5.2.1 Effect of electrode size on capacitance

The dielectric characterisation of the PZT is an important step in understanding the transducer (chapter 2 literature review).

The experimental capacitance should increase with the electrode size proportionally to the square of the radius. Using Equation 2.3, Figure 6.8 illustrates the theoretical capacitance

calculated using a relative permittivity of 630. The experimental figures show a deviation from the predicted capacitance behaviour for different devices having an electrode radii below to 0.5mm. Of course, this behaviour is mirrored by the relative permittivity. The extreme values found for this relative permittivity cannot describe any real material.

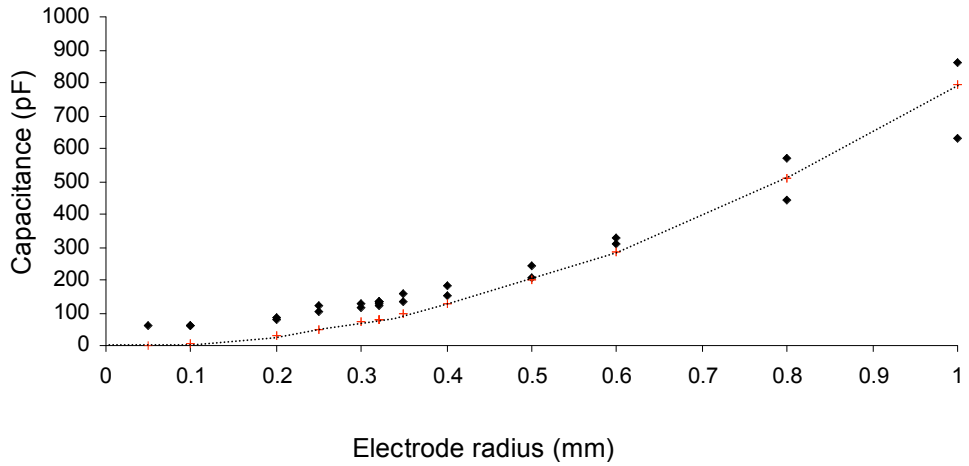


Figure 6.8: Capacitance function of the electrode size. On a 24 μ m sample fabricated with the 6[2C+4S] process. [* = experimental data, + = theoretical capacitance calculate with an $\epsilon_r=630$]

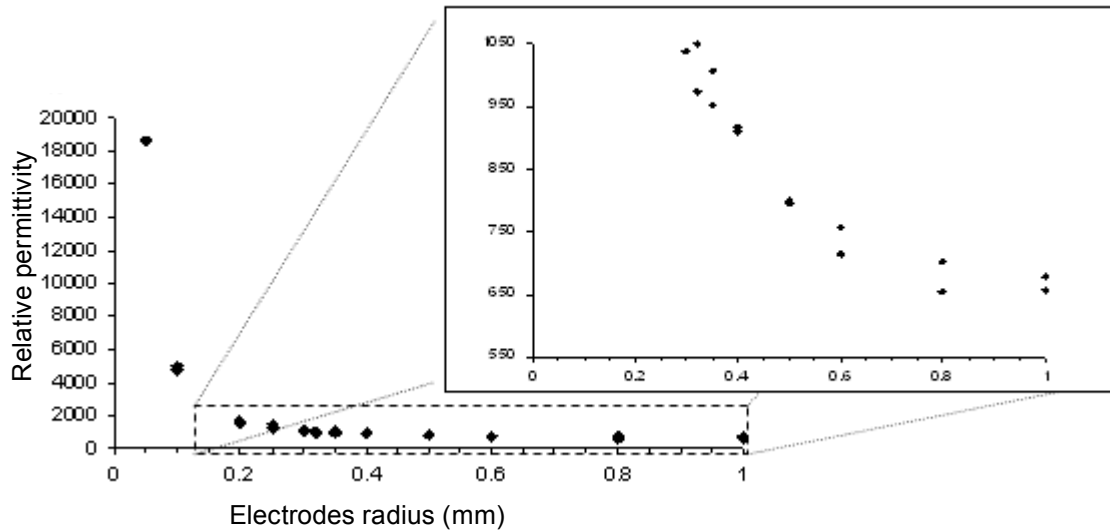


Figure 6.9: Raw relative permittivity calculated for different electrode sizes. (samples fabricated with 6[2C+4S])

The relative permittivity values seem reasonable for electrodes larger than 0.4mm. For smaller electrode sizes the relative permittivity increases exponentially as the electrode size decreases (Figure 6.9).

These phenomena cannot be explained by the fringe effect alone. The relative permittivity of the bulk PZ26 is 1200. If we compare this value to the extreme value found in Figure 6.9, 20000, for the smallest electrode. The extra capacitance must arise from the electrode design.

However, the fringe effect should also be important in this case, considering the PZT thickness. The smallest electrode has a 50 μm radius, which for a 29 μm thick device should exhibit a significant fringe effect.

6.5.2.2 Stray capacitance

The extra-capacitance found is due primarily to the electrode design. These electrodes are sputtered onto a Si/SiO₂ wafer. The oxide layer is designed to be the protective layer for the silicon etching process [see Section 4.5]. However it is also a low permittivity medium. The relative permittivity of SiO₂ is 3.9 [Houssa *et. al*, 2001]. The silicon acts like a floating electrode and so generates an extra capacitance every time the SiO₂ thickness of 400nm is embedded between the silicon and a platinum electrode. (Figure 6.10)

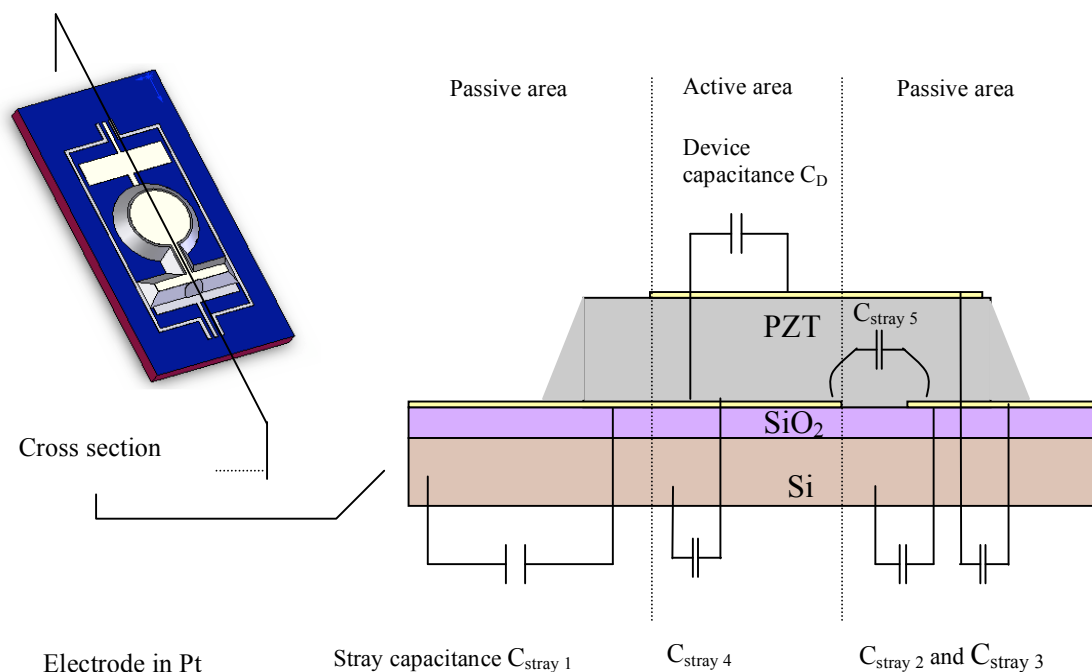


Figure 6.10: Extra-capacitance possible in this design.

The extra capacitance problem was divided into 2 parts: the active parts, or transducer parts, and the passive parts, or pad connection parts.

An equivalent electrical circuit was drawn as a visual aid (Figure 6.11).

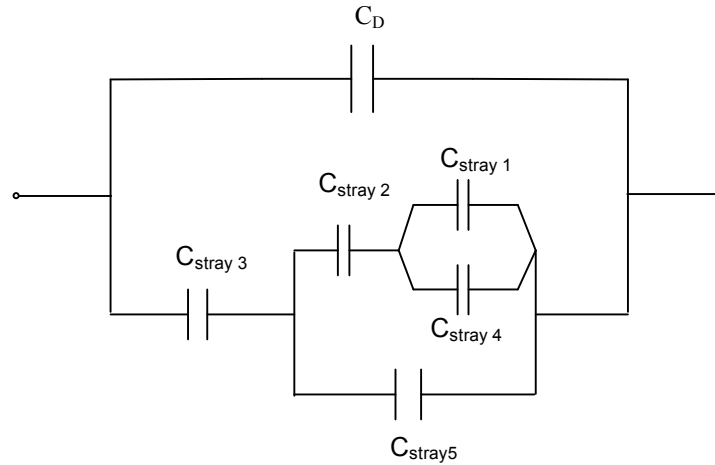


Figure 6.11: Electrical circuit for determining the effect of stray capacitance.

The extra-capacitance can be derived for each separate case:

$$C_{stray1} = \frac{\epsilon_r(SiO_2)\epsilon_0 A_{stray1}}{l_{SiO_2}} \quad \text{Equation 6.3}$$

$$C_{stray2} = \frac{\epsilon_r(SiO_2)\epsilon_0 A_{stray2}}{l_{SiO_2}} \quad \text{Equation 6.4}$$

$$C_{stray3} = \frac{\epsilon_r(PZT)\epsilon_0 A_{stray3}}{l_{PZT}} \quad \text{Equation 6.5}$$

$$C_{stray4} = \frac{\epsilon_r(SiO_2)\epsilon_0 A_{stray4}}{l_{SiO_2}} \quad \text{Equation 6.6}$$

The stray capacitance C_{stray5} is harder to derive. The geometry of the two electrodes involved in this stray capacitance makes the derivation non-trivial. As a first approximation we will consider it negligible. Its value should be very low as the gap between the two electrodes is very large $\sim 300\mu\text{m}$ in relation to all other gaps. Equation 6.7 of the stray capacitance, when C_{stray5} is included, illustrates it can be ignored.

$$\frac{1}{C_{stray}} = \frac{1}{C_{stray3}} + \frac{1}{\frac{1}{\frac{1}{C_{stray2}} + \frac{1}{C_{stray4} + C_{stray1}}} + C_{stray5}} \quad \text{Equation 6.7}$$

The different areas are defined:

$$A_{stray1} = A_{Pad \text{ for the bottom electrode}} + A_{Ground \text{ Signal Ground central pad}}$$

$$A_{stray1} = 3 * 0.8 + 0.120 * 0.8 \quad \text{Equation 6.8}$$

$$A_{stray1} = 2.448 \text{ mm}^2$$

$$A_{stray2} (Pt \text{ connection pad for the top electrode}) = A_{stray1} \quad \text{Equation 6.9}$$

$$A_{stray3} = A_{PZT \text{ connection pad}}$$

$$A_{stray3} = 1.5 * 0.4 \quad \text{Equation 6.10}$$

$$A_{stray3} = 0.6 \text{ mm}^2$$

$$A_{stray4} = A_{electrode} = \pi(\text{radius})^2 \quad \text{Equation 6.11}$$

The total stray capacitance, without C_{stray5} , is:

$$\frac{1}{C_{stray}} = \frac{1}{C_{stray2}} + \frac{1}{C_{stray3}} + \frac{1}{C_{stray4} + C_{stray1}} \quad \text{Equation 6.12}$$

A finite element model, made with the software FEMlab, indicates that the theoretical stray capacitance should be 60pF (with the theoretical PZT relative permittivity of 630, see Figure 6.7). By cutting the top electrode and measuring the capacitance in the same way, (This was executed for the biggest and the smallest electrode) an experimental stray capacitance was found to be around 50pF. It is only 10 picofarads below that predicted by the FE model, but it is of comparable magnitude to the capacitance of the smallest electrodes ($\leq 100\text{nm}$). In the future, the experiments have to be more precise, as the top electrodes were disconnected with a cutter. A more accurate experiment can be made by etching selectively the top electrode using RIE (Reactive Ion Etching) while the rest of the wafer is protected by a thick patterned photoresist like A4562.

In order to correct the measured capacitance the experimental stray capacitance was subtracted ($C_s=50\text{pF}$) and the relative permittivity recalculated.

Figure 6.12 shows that the corrected relative permittivity is relatively constant for the electrode radii larger than $100\mu\text{m}$. The experiment consisting of removing the active part of the top electrode should give an idea of what the experimental stray capacitance is, with an error closer to the picofarad. It will then be possible to have an idea of the real difference between the values of $C_{stray \text{ theoretical}}$ and $C_{stray \text{ exp}}$.

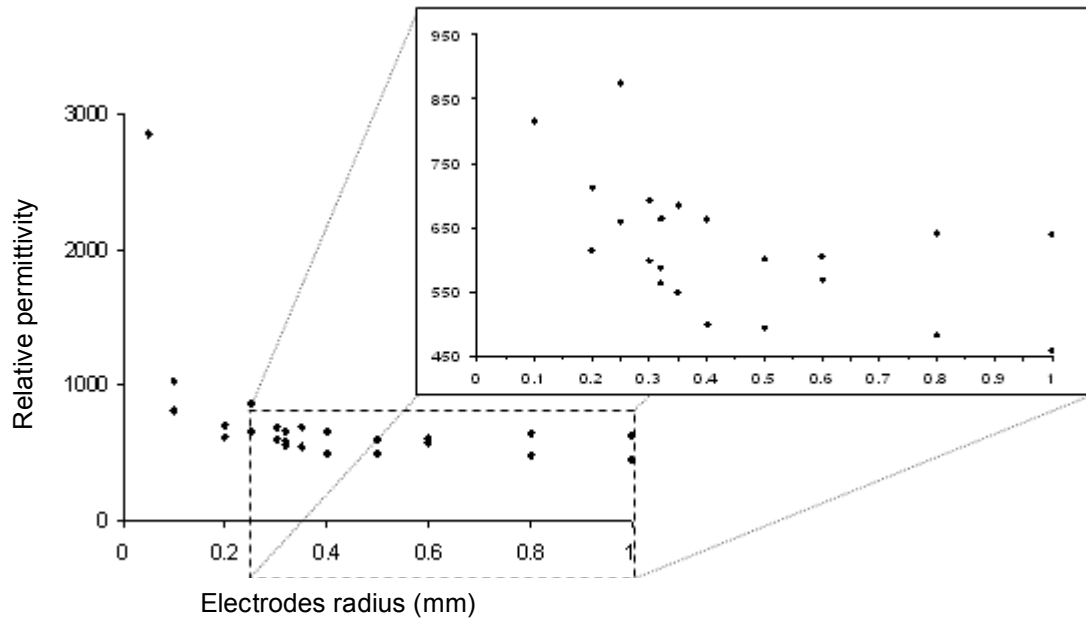


Figure 6.12: Relative permittivity corrected assuming a stray capacitance of 50pF.

Figures 6.12 and 6.9 reveal, as well, that for some electrodes the results are different for the same electrode size. It has also been noticed that all these samples were located closer to the wafer centre.

6.5.2.3 Thickness variation due to the spin coating technique for thick film

The work presented by Duval [2003], was done using 7 μm thick film while the thickness of the PZT thick films in this work is at least three times that thickness. Figure 6.13 shows that the PZT film thickness varies significantly within 3cm from the centre of the wafer affected zone. This is due to the spin coating technique used. This is enormous compared to Dr Duval's work that shows that the spin coating influence on the film thickness never exceeded 0.7 cm.

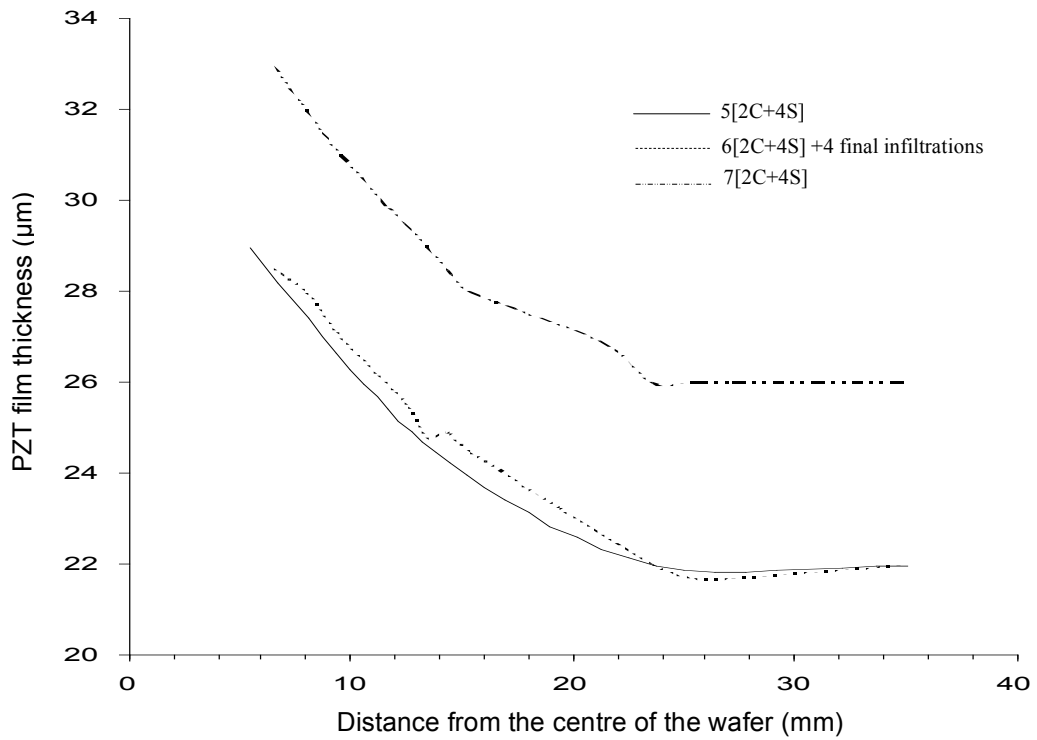


Figure 6.13: PZT film thickness variation as a function of the distance from the spin coating centre. The thickness is in μm , the distance in mm.

As a visual aid, figure 6.14 demonstrates how far this effect can influence the thickness across a 4 inch wafer.

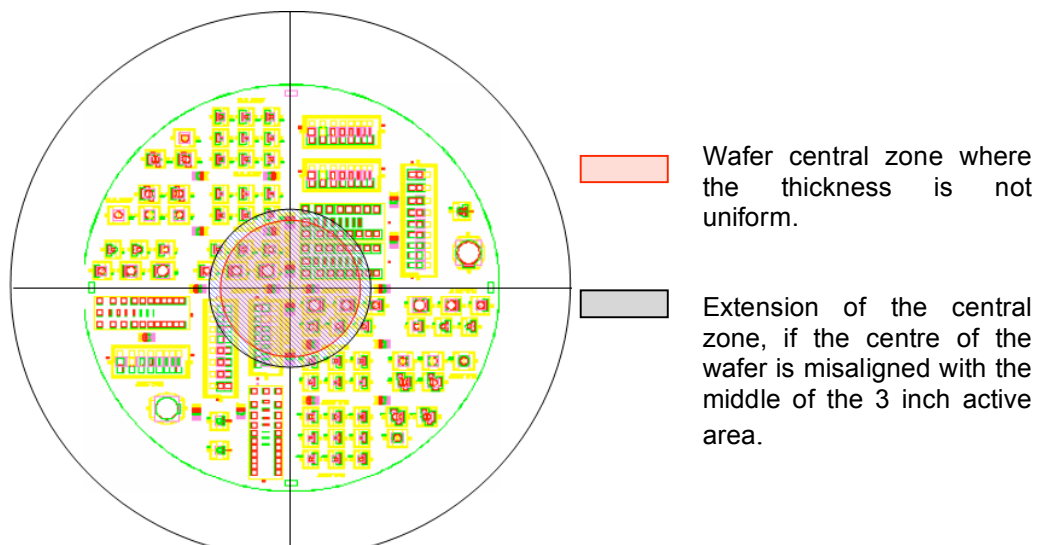


Figure 6.14: Zones where the thickness is influenced by the spin coating effect for a PZT thick film deposition.

This thickness variation across that the use of the spin coating technique induce, will have to be taken into consideration for the relative permittivity measurement. The next section presents the thickness corrected result of the relative permittivity.

6.5.2.4 Thickness correction of the relative permittivity

Once corrected for the spin coating thickness effect, even the electrodes of 100 μm radius have a relative permittivity under 1000, which is closer to the expected value of about 700. The difference between two samples of the same size also became much smaller. However the 50 μm radius device still exhibits a value of 2800 for the relative permittivity, and once again the fringe effect cannot multiply the value by a factor of 4. (Figure 6.15 and 6.16: more than 15 samples were tested). A more accurate experiment will be to measure the extra-capacitance with the active area of the electrode etched with the RIE.

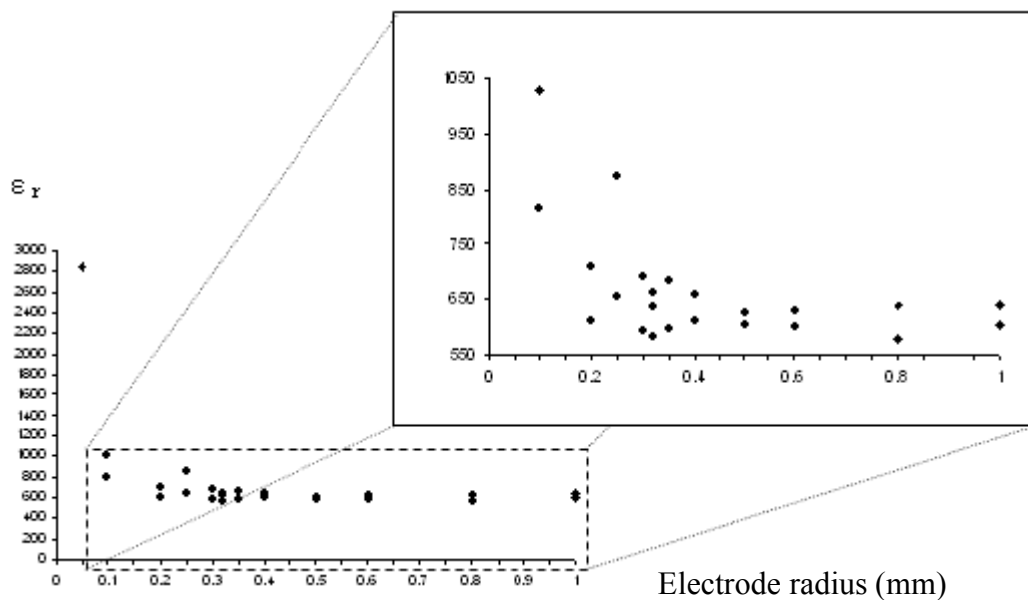


Figure 6.15: Relative permittivity corrected for the stray capacitance and the thickness variation. 6[2C+4S] sample.

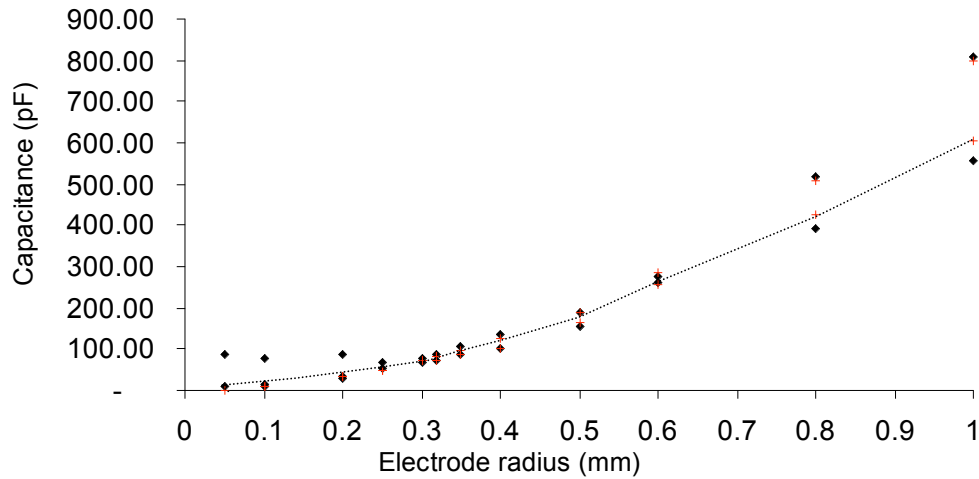


Figure 6.16: Theoretical capacitance calculated with $\epsilon_r(\text{PZT})=630$ (dashed lines) versus the thickness corrected capacitance (black square), 6[2C+4S] sample.

Figures 6.15 and 6.16 reveal that the corrections begin to be reasonable, theory and experimental results are closer in value.

To further enhance this accuracy, the thickness will have to be physically measured for each sample. The stray capacitance will have to be understood with greater accuracy in order to observe the experimental fringe effect and then to take this effect into consideration in the theoretical values.

Another chromium masks needs to be set up to design the top electrodes with the smallest pads possible. However, an alternative solution to avoid any extra capacitance from the substrate will be to use a high-resistivity substrate. Alumina (Rubalit 710) has been chosen for this experiment, its ohmic resistivity is $10^{14} \Omega \cdot \text{cm}^2$ which is far more than silicon that of (1-100 $\Omega \cdot \text{cm}$).

6.6 Capacitance on an alumina substrate and fringing fields

Substituting the silicon substrate for a higher electric resistive substrate such as alumina improved the understanding of the composite material. As said above, an alumina substrate (Rubalit 710) has been chosen for this experiment, its ohmic resistivity is $10^{14} \Omega \cdot \text{cm}^2$ which is far more than silicon one ($1-100 \Omega \cdot \text{cm}$). The extra-capacitance due to the Si/SiO₂ substrate will then disappear, and only the stray capacitance due to the fringing fields will remain. This substrate substitution should reveal if for small features ($50 \mu\text{m}$) of thick films ($30 \mu\text{m}$) the fringing fields generate an important stray capacitance or not (Figure 6.17).

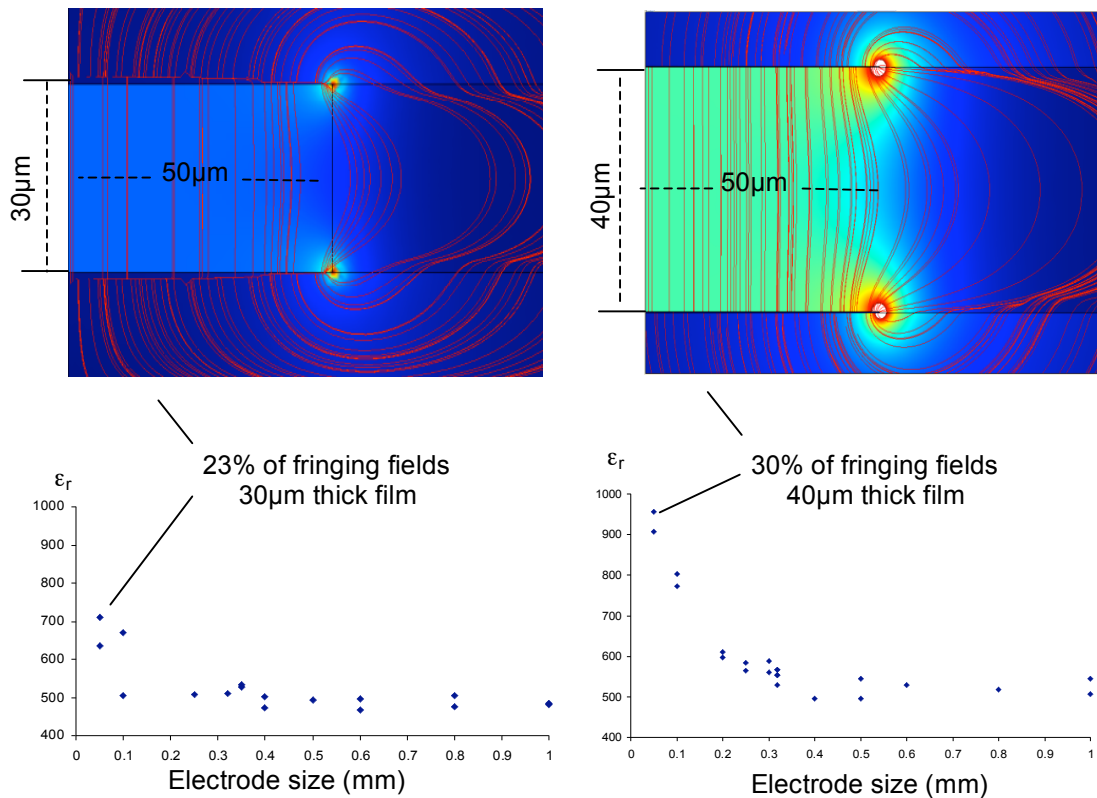


Figure 6.17: Relative permittivity of thick film fabricated with the [2C+4S] process on alumina substrate. Two film thickness are represented here $30 \mu\text{m}$ and $40 \mu\text{m}$.

The relative permittivity's values are less scattered than that observed for the same film system on silicon substrate. The stray capacitance observed on silicon is no longer presents. Figure 6.17 reveals also that the relative permittivity still varies with the electrode size smaller 0.3mm . The only explanation for this variation is that the fringing fields add a capacitance for small features.

A finite element model realised with the software FEMlab helped in understanding this fringing field effect. For the cylindrical features of $50 \mu\text{m}$ electrode radius and $30 \mu\text{m}$ thick film, the fringing field increases the capacitance by 23% above the value expected for a perfect capacitor (without fringing field) with the same geometry. and by 30% for cylindrical features

of 50 μm electrode radius and 40 μm thick. Both experiment and the finite element analysis agree with these results. This demonstrates that the curvature of the relative permittivity as a function of the electrode size is due to the fringing fields.

Another important result is that the average relative permittivities for bigger radii features is between 500-600 (above 200 μm radius). This result is based on several wafers. Also Figure 6.17 represents the lowest range of relative permittivity found for thick films fabricated with the [2C+4S] process on alumina.

This relative permittivity result seems a bit low compared to samples with the same structure presented in figure 6.14 for device on silicon. They exhibited an average relative permittivity between 600-700. This average agrees with the model presented in Figure 6.4.

The only difference between the sample presented in figure 6.17 and 6.14, is their substrate. The stress condition of thick films is demonstrated to be radically different on silicon than on alumina. On alumina the film is subjected to a compressive stress, on silicon the film is subject to a tensile stress. The compressive stress reduces the charge displacement and so the relative permittivity. On silicon the tensile stress doesn't compress the film and doesn't affect the charge displacement.

6.7 Dielectric loss

A high dielectric loss is undesirable in almost all applications. It lowers the quality of the resonant circuit, which is especially undesirable for transducer applications. It results in the generation of heat and, therefore, to raising the temperature of a capacitor. The dissipation factor is generally taken as an indication of the quality of a particular type of capacitor. Thus a value of 0.1 might be acceptable for an aluminium electrolytic value, and 0.02 for a high permittivity (high K) capacitor. In our case, the high K material, like the PZT composite, exhibits a dissipation factor range between 0.01 and 0.02.

The PZT composite exhibits a very low dissipation factor, as shown in Figure 6.18. It can be considered that the dissipation factor is free from a frequency dependence, since the higher value is 0.012 at 80kHz and the lower is 0.005 at 10 kHz. The observed behaviour of the loss above 10 kHz is linear with a slight increase with the frequency. This might reflect the time dependence on the charge movement: the higher the frequency, the less time the charge has to move, which might increase the loss.

However, at very low frequencies the loss slightly increases for all the samples. Herbert explains that for the region below 10 kilohertz, the slower the frequency, the more time is available for the displacement of defects, such as vacant oxygen sites or interface defects [Herbert *et al.* 1987]. This might increase the dissipation factor as well as the capacitance. With a DC field applied, the migration of defects may cause an accumulation of donor traps near the electrodes with a corresponding accumulation of compensatory space charges. This develops an internal electric field, which is opposed to the applied field.

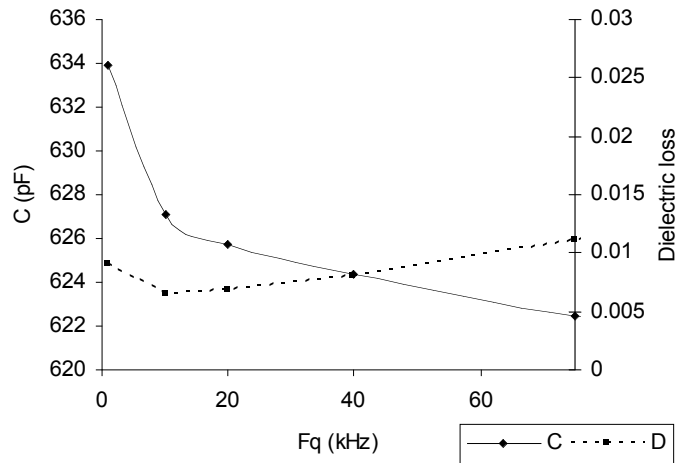


Figure 6.18: Capacitance and dielectric loss frequency dependence of 6[2C+4S] (24µm thick), electrodes radius of 350µm.

Pores are an important source of loss because surfaces of the ceramics contain a high concentration of defects. These are due to the interface between the solid crystal structure and the gas phase. If the external atmosphere has access to pores, they can absorb atmospheric moisture that will result in a higher dielectric loss. This phenomenon occurs in our case during hot and humid summers, with the result of a higher loss compared with results obtained in winter. Figure 6.19 shows results obtained during the winter, where the dielectrics measured are mainly below 0.01. During the summer the majority of the dielectric losses measured are ≥ 0.02 . In the summer, it is also practically impossible to pole the PZT, because of a current leakage that shorts the devices. This current leakage is thought to be due to the absorbed surface moisture.

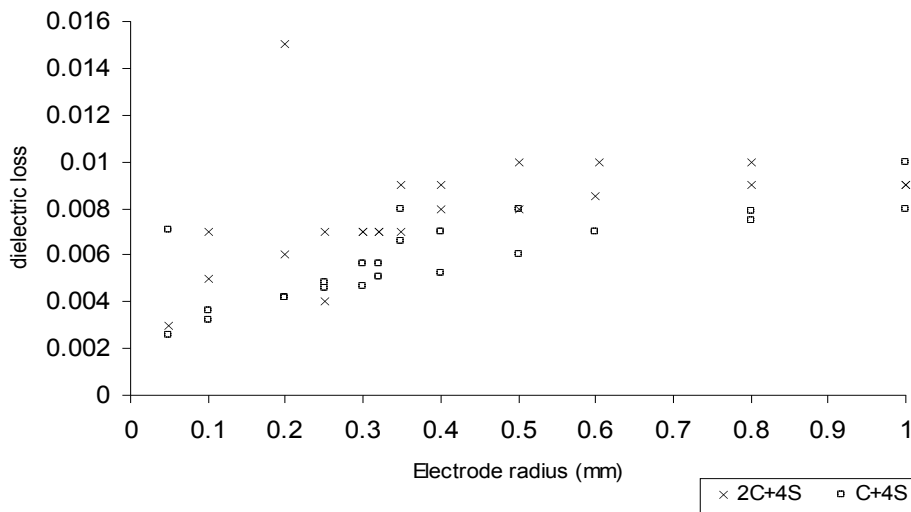


Figure 6.19: PZT thick film dielectric loss dependence on electrode radius, measure at 1kHz, during the winter.

The dielectric loss is thus strongly dependent on ceramic defects. These defects in the ceramic come from different sources, doping, crystallisation of spun coating, composite sol gel, *etc.* However, these defects aren't scattered uniformly in the ceramic, therefore the smaller the electrode, the smaller can be the dielectric scatter loss. This should be reflected by a different behaviour for the two processes [C+4S] and [2C+4S]. Figure 6.19 shows that there is a slight difference in the dielectric loss behaviour as a function of the electrode size. The range of results obtained increases when the electrode size decreases. This is due to the probability that the electrode will cover an area of the film which contains more or less defects.

6.8 PZT composite piezoelectric coefficient results for the test structure

If a stress is applied to a piezoelectric crystal, such as PZT, it develops an electric moment whose magnitude is proportional to the applied stress, and *vice versa*. Equations 6.13 and 6.14 describe the dependence of the electromechanical coupling on the piezoelectric constants e_{ijk} and d_{ijk} for the thickness mode of excitation. It describes as well the importance of these constants in the transducer application.

e_{33} and e_{31} are dependent on d_{33} and on each other (Equation 2.31 and 2.32) [Moulson, 1998]. This chapter presents values of d_{33} obtainable from the Berlincourt piezoelectric measurement of the composite.

As stated in Section 2.3.2, all values presented here should be considered as effective because they describe the piezoelectric constant of a polycrystalline ceramic film and not a single crystal. Figure 6.20 compares the piezoelectric coefficient measured for [C+xS] samples with x ranged from 1 to 4. For each degree of infiltration 2 different temperatures of sintering were tested 690°C and 710°C.

It was observed that:

1. For both temperatures the piezoelectric coefficient increases with the number of infiltration stages.
2. The deviation range decreases with the number of infiltration stages.
3. The samples sintered at 690°C exhibit a very low value of $d_{33}=50\text{pC/N}$, but the samples sintered at 710°C achieved the mean value of 76pC/N .

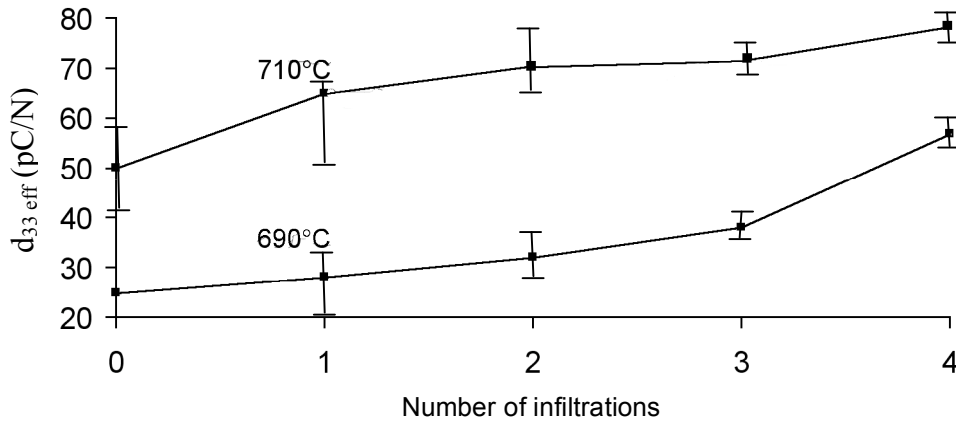


Figure 6.20: Piezoelectric coefficient $d_{33,eff}$, of a $10\mu\text{m}$ 4[C+4S] PZT composite film poled at $130^\circ\text{C}/5\text{min}$ and cooled under voltage. 2 samples were sintered at 2 different temperatures (690°C and 710°C).

As seen in section 6.3 increasing the furnace temperature to 710°C increased the measured relative permittivity. Figure 6.20 shows that it also increases the piezoelectric coefficients, which is consistent with Equation 6.13:

$$e_{33} = h_{33} \varepsilon_{33}^S \quad \text{Equation 6.13}$$

Figure 6.2 and Equation 6.1 illustrate the process of sintering. They describe that higher the temperature, higher material density. Plus, when the porosity is infiltrated, or the air of pores is replaced by a piezoelectric material the density increase. Both phenomena make the overall piezoelectric constant should increase. As explained in section 6.3, the temperature effect is enhanced by the addition of a CuO-PbO sintering aid. The phase diagram shows that this added sintering aid has a melting point of 688°C . At 690°C this sintering aid might not be completely melted. The liquid phase formed by the sintering aid should increase the atomic diffusion, and so increase the density [Corker, *et al.* 2002]. Then, Figure 6.20 reveals that when the sintering aid is active (melted) the piezoelectric coefficient increases considerably by $\sim 100\%$. The samples sintered at a lower temperature increase their values by 50% when infiltrated, while the ones sintered at higher temperature see their values increase by 30%. They both increase their original value by approximately 25-30 pC/N due to a pure 2ME sol-gel process (the infiltration steps) crystallises under a lower temperature, around 600°C [Zhang, *et al* 2003]. This confirms that the sintering aid acts directly on the grain boundary to enhance the density and then d_{33} .

The deviation range of the d_{33} measurement observed in Figure 6.20 illustrates that the Berlincourt measurements are less scattered with an increased number of infiltration steps. The less infiltration sol, the less stiff the material. Then the more the load induced by the Berlincourt measurement, the more the structure can be deformed. The deformation of the

structure will decrease the actual piezoelectric value. This illustrates how carefully this data needs to be treated. Laser displacement measurements of the piezoelectric constant should be conducted and compared with these results.

Table 6.2 summarises the measurements obtained during this work for the 4[C+4S] structure.

Table 6.2: Piezoelectric properties and dielectric constant of a PZT composite thick film 4[C+4S] process sintered for 30 minutes.

4[C+4S] on silicon	Relative permittivity	loss	d_{33} ($\mu\text{C}\cdot\text{N}^{-1}$)	ϵ_{31} ($\text{C}\cdot\text{m}^{-2}$)
Furnace (690°C@3°C/min)	600	0.01	50	x
Furnace (710°C@3°C/min)	772	0.01	73	4.82
RTA (710°C@200°C/min)	730	0.02	74	4.71

These values are much lower than the d_{33} of the bulk PZ26 ($\sim 330\text{pC/N}$) [Ferroperm catalogue], and a pure PZT sol (150pC/N) [Corckovic *et al.* 2006]. The thin films presented by Corkovic are denser, and exhibit preferred orientation of the grains so no direct comparison is possible. The bulk PZ26 measurements of d_{33} are conducted on a 5mm thick bulk compact structure with 5mm diameter fully coated by the bottom and top electrodes (non-clamped structure). Clamping a structure should decrease the piezo-coefficient efficient [Southin *et al.* 2001]. Then using the characteristics of the bulk material is unlikely to generate a good reference of comparison. Plus, due to the different processing conditions, the resultant microstructures obtained result in different mechanical properties.

The samples tested here are $10\mu\text{m}$ thick, and poled at 130°C under $10\text{V}/\mu\text{m}$ for 5 minutes. They were then cooled down over 5 minutes under the same voltage. This poling process was standard, until the thickness of the film increased. The samples needed to be poled at higher voltage. For $35\mu\text{m}$ thick film the sample were exposed to 350V over 5min at 130°C . Most of the samples did not survive the poling process.

6.9 Piezoelectric coefficient versus poling temperature / Poling

$35\mu\text{m}$ thick films need a high voltage to pole. Application of these high voltages often causes the top electrodes to become damaged. The effect of different poling conditions for PZT thick film ceramics is summarised by Figure 6.21. It shows the results obtained for $d_{33\text{eff}}$ for samples poled at different temperatures and at different fields for 5 minutes. Samples were either cooled once the voltage had been removed or cooled under the applied voltage.

Three key points are observed:

1. As the field increases the d_{33} value increases for a given poling temperature.
2. As the temperature increases the d_{33} value increases for a given poling field.
3. If the samples are cooled down under field, the d_{33} values increase for given poling temperature and field.

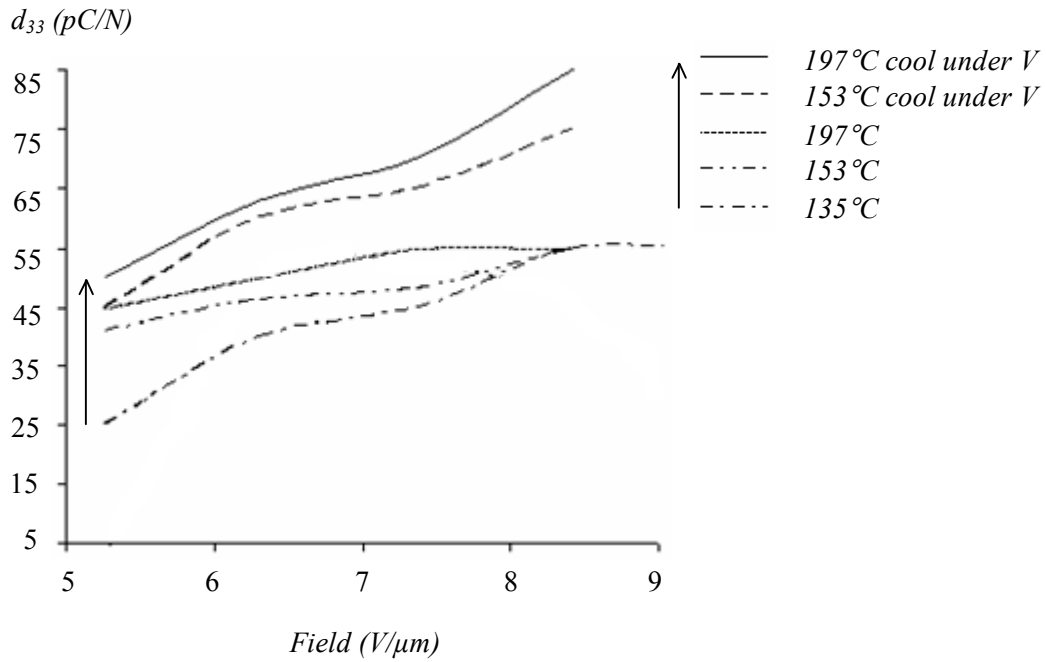


Figure 6.21: Measured $d_{33, \text{eff}}$ as a function of temperature, applied field, and cooling conditions (from (2C+4S) samples).

The highest $d_{33, \text{eff}}$ value (85 pC/N) was obtained for samples poled under $8.5 \text{ V}/\mu\text{m}$ at 197°C for 5 minutes and allowed to cool down under voltage until the temperature dropped below 80°C . This value is comparable to those obtained in previous work for thinner films. The observed behaviour can be explained by considering dipole reorientation which affects the piezoelectric coefficient. High temperature makes the dipole reorientation easier and high fields provide more energy to reorientate the dipole, hence the observed temperature and field effects. The need to cool down under voltage is due to the *in situ* stress which has a tendency to switch back the dipole orientation to a position which needs a lower energy. This phenomenon is enhanced by the non-oriented microstructure of this composite, as many of the dipoles require little movement to switch back to their positions dictated by the *in-situ* stress. That is the reason for the need to maintain the field until the samples are cool as the stress alone cannot fully reorientate the dipoles easily.

6.10 Ferroelectric properties

6.10.1 Presentation of the PZT composite thick film hysteresis loop

For the same material at different thicknesses, i.e. bulk, thick or thin films, the polarisation switching behaviour differs. As the thickness decreases the E_c increases, P_r decreases, and the hysteresis curve is tilted. Until now the origins of these differences are not clear

[Damjanovic, 1998]. It seems reasonable to think that fabrication process should play an important role in these differences.

The hysteresis loop will be used to understand the basic behaviour of the PZT composite thick film. An hysteresis loop of a thick film fabricated with the [C+4S] process will be presented. The effect of different maximum magnitude electric fields on the dipole switching behaviour will be presented. This experiment will be compared to results obtained for two [2C+4S] thick films on two different substrates, one on silicon and the other one on alumina, in order to see the effect of stress on the hysteresis loop of the composite.

6.10.2 Hysteresis loop of the 8 μm thick film of 4[C+4S]

The PZT PZ26 bulk ceramic, presented in the Ferroperm catalogue, has a coercive electric field (E_c) of $2.5 \text{ V}/\mu\text{m}$, and a remanent polarisation (P_R) of $35 \mu\text{C}/\text{cm}^2$, for a full saturation of the dipole switching (E_{sat}) at $10 \text{ V}/\mu\text{m}$. Here, a PZT composite thick film of PZ26 powder (from Ferroperm)/ PZT sol-gel with a thickness of $8 \mu\text{m}$, presents a coercive electric field of $27 \text{ V}/\mu\text{m}$ and a remanent polarisation of $23 \mu\text{C}/\text{m}^2$ when the process of dipole switching seems complete, at $55 \text{ V}/\mu\text{m}$ (Figure 6.22)

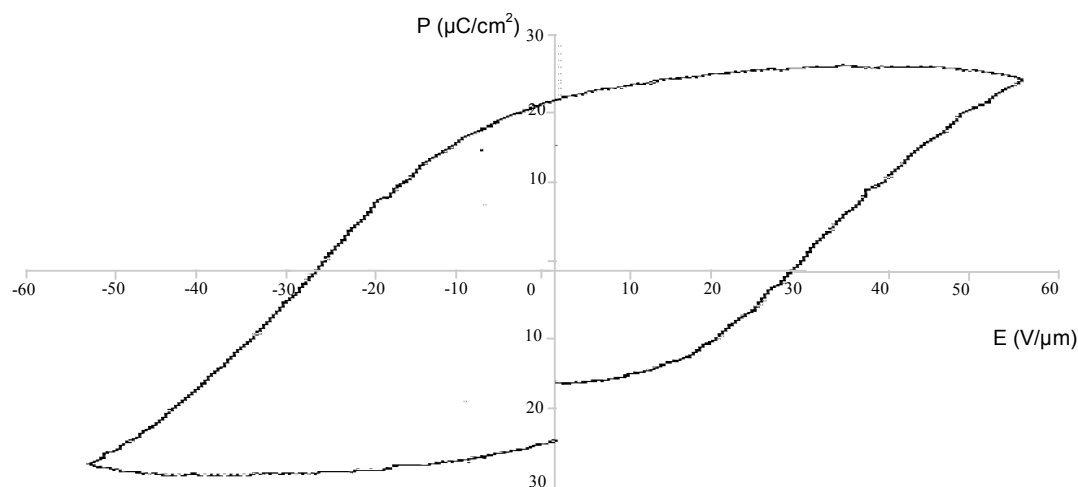


Figure 6.22: Hysteresis loop of PZT composite thick film ($8 \mu\text{m}$ thick).

Even if the microstructure of the bulk PZ26 is different to the composite one, a comparison of the two processes is used as a starting point of the discussion. The PZ26 has a higher stiffness, a higher relative permittivity, a lower in-situ stress, and a higher piezoelectric constant than the composite system. The results described above should not be surprising.

Three main characteristics differentiate the bulk structure from the thick composite structure: the thicknesses, the added sol, and the sintering temperature.

According to the analysis review by Tagantsev, the model of a depletion on the coercive field inducing domain wall switching nearby the top and bottom electrodes is one of the most probable explanations for the problem of the thickness dependence of the coercive electric field. (Section 2.4.3). However, this thickness dependence is valid for films thinner than 1 μ m. For thicker films the electric fields due to this depletion screening the applied electric field are constant (Equation 2.34). However, Equation 2.34 is proportional of the concentration, N, of free charges which should be much higher in a composite than the PZ26.

The composite thick PZT film which contains a certain number of different kinds of interfaces between PZT grain and PZT sol, plus the porosity, the number of cracks, and spin coating defects such as comets. These defects increase the mobility of free charge as well as their concentration (N). If these defects increase the screening fields due to this depletion energy barrier due to the contact metal-ferroelectric material, they also pin the in-situ domain wall motion (section 2.4.3). These phenomena should considerably reduce the spontaneous polarisation of the material and so the coercive field and the remanent polarisation.

The sol adds a lot of interfaces into the system, especially at the grain boundaries. Each interface adds defect pinning domains wall motion and trapping free charges [Lee *et al.* 2002] (section 2.4.3).

To summarise, three main phenomena occur to screen the applied electric field:

1. Contact metal-ferroelectric material screening field is enhanced by surface defects.
2. The grain *in-situ* defects pin the domain wall motion, which reduce the polarisability of the film. Furthermore a high sintering temperature has a tendency to reduce the number of lattice defects such as dislocation, and atomic vacancies, also “pinning” the domain walls by trapping charges. This increases considerably the ferroelectric properties of the bulk ceramic compared to the PZT composite.
3. Grain boundary interfaces are more complex in the PZT composite due to the presence of the added sol. This complexity adds defects into the structure that traps charges, and increases the “pinning” effect of the domain wall motion phenomenon.

This phenomenon can be added to the explanation given in section 6.3 on having an higher relative permittivity for the bulk PZ26 (1100) than for the [C+4S] composite (720) at 10vol% of porosity (Figure 6.3).

In the case of the composite, a high screening electric field should be expected. The depletion model due to the contact electrode-ferroelectric material should be constant with the thickness. However, the screening due to the pinning of the domain wall motion and charge trapping should be thickness dependent, as the thicker the film, the higher the defects concentration.

Another effect that influences the hysteresis loop shape of such a polycrystalline composite sol-gel ceramic is the original orientation of domains, or the spontaneous polarisation before

the electric field applied. As said in Chapter 2, for such a ceramic the total spontaneous polarisation should be null, each single crystal composing the ceramic is randomly oriented.

6.10.3 Effect of stress on the hysteresis loop

This section presents the effect of an increasing maximum intensity of the applied electric field on samples fabricated on two different substrates.

The first series of hysteresis loops, as a function of an increasing electric field, were obtained from several samples from the same silicon wafer coated with [2C+4S] thick film (Figure 6.23)

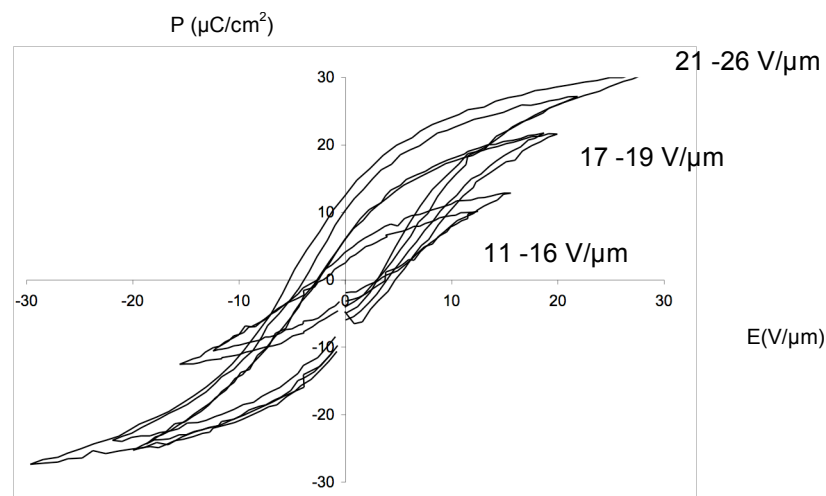


Figure 6.23: Hysteresis loops of the composite [2C+4S] on silicon substrate, illustrating the influence of tensile stress during fabrication process by applying different maximum electric field during the hysteresis loop experiment, from 11 to 26V/μm in 1 μm increments.

Three groups of the hysteresis loops are observed:

- 1) Group 1: the maximum of the electric field intensity ranges between 11-16V/μm
- 2) Group 2: the maximum of the electric field intensity ranges between 17-19V/μm
- 3) Group 3: the maximum of the electric field intensity ranges between 21-26V/μm.
(20V/μm is missing)

If during the fabrication process the sample is subjected to stress, an overall spontaneous polarisation should be observable. Chapter 5 demonstrated that the technology used to fabricate such ceramics (a spin coated composite slurry, dried and sintered) adds a certain amount of stress at the interface between the substrate and the film, which is transmitted to both the substrate and its coating. The fabrication of a PZT composite thick film on the silicon substrate exhibited a high tensile stress. The tensile stress appeared during the very early stage of the fabrication process, during the spin coating, and during the 2nd stage of fabrication, the drying process at 200°C. This stress is still present after the final sintering process (chapter 5).

A tensile stress is a stress directed in a plane parallel to the silicon substrate, and oriented towards the outside of the silicone wafer. Tensile stress tends to contract the film. This contraction applies a stress influencing the dipoles orientation in each grain of the ceramic and in the crystallising PZT sol during the sintering process. Such stress should be favourable to the formation of domains orientated parallel to the silicon substrate. They will be randomly oriented but directed parallel to the film plane, or 90° to the applied electric field. Figure 6.23 illustrates the behaviour of the hysteresis loop of the composite PZT thick film [2C+4S] when the maximum applied electric field varies. Therefore, the three groupings of hysteresis loops, represented by their lower and maximum electric field, are as result of.

- 1) The group where the maximum intensity of the electric field ranging between 11-16V/ μm switches the easiest dipoles (having an angle below 90° domains, here the angle relates to the electric field direction).
- 2) The group where the maximum of the electric intensity is ranged between 17-19V/ μm representing the dipoles having a direction of 90° with the electric field (their formation were influenced by the tensile stress). A jump of the remanent and spontaneous polarisation represents a large amount of dipole (90°) switching all at the same time.
- 3) The group 21-26V/ μm . (20V/ μm is missing) representing the rest of the dipoles which are harder to switch.

The hysteresis loop is less tilted when the maximum of the electric field is increasing. However, the coercive electric field remains approximately constant. Considering the non-trivial physics associated with this hysteresis loop, a simple assumption will be made on that topic. As stated above, the coercive field is influenced by the overall free charge mobility (close of the electrodes and in the film). A tensile stress should facilitate the charge mobility and also the dipole mobility in the thickness direction. This means that the saturation is rapidly achieved in the first group of hysteresis loops (11-16V/ μm), because it orientates all the free charges. This should explain why the first group is less tilted than the others, which only switch the dipole.

On alumina the situation is different, Chapter 5 demonstrates a development of a compressive stress. According to the logic followed with the tensile stress, a compressive stress, induced during sintering should be favourable for the development of domains directed in a thickness direction as the material is compressed. Of course, the spontaneous polarisation will still be randomly oriented. Compared to the electric field direction, these domains should be oriented with the electric field or at 180° . These compressed domain walls would be expected to have difficulty switching. Figure 6.24 represents the same experiment as the one for the silicon substrate with the same material, but different substrate and different stress state. No groups of switching are observed here between 7-20 V/ μm . The

remnant polarisation, the coercive electric field increase together, and leave the tilt of the hysteresis loop unchanged (when $E_{\max} > 7$).

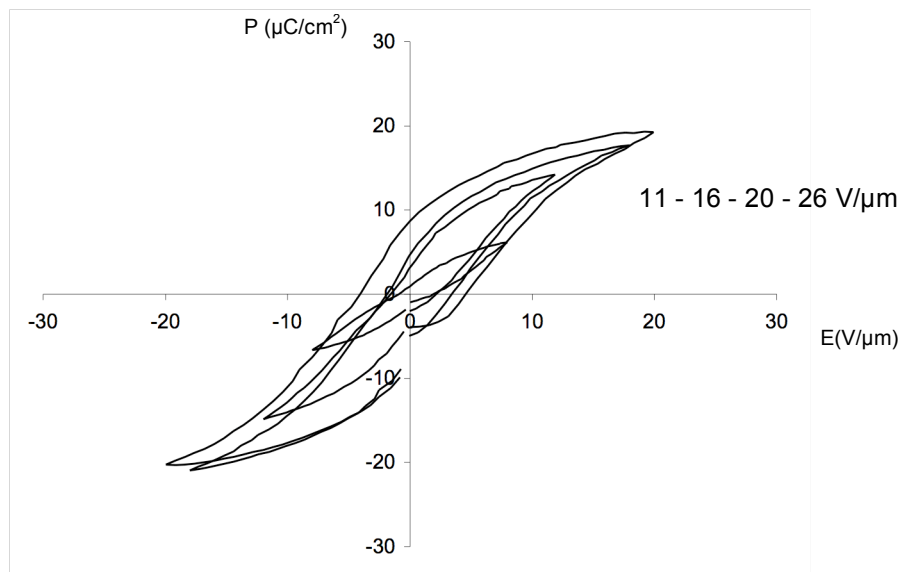


Figure 6.24: Hysteresis loops of the composite [2C+4S] on alumina substrate, illustrating the influence of a compressive stress during the fabrication process, by applying different maximum electric fields during the hysteresis loop experiment

Figure 6.25 shows that the PZT composite subjected to compressive stress (alumina substrate) is less tilted in comparison with the thick film under a tensile stress (silicon substrate). The reason has already been discussed, when the thick film is under a tensile stress the remanent polarisation increases with maximum of the applied electric field, but the coercive electric field remains approximately constant.

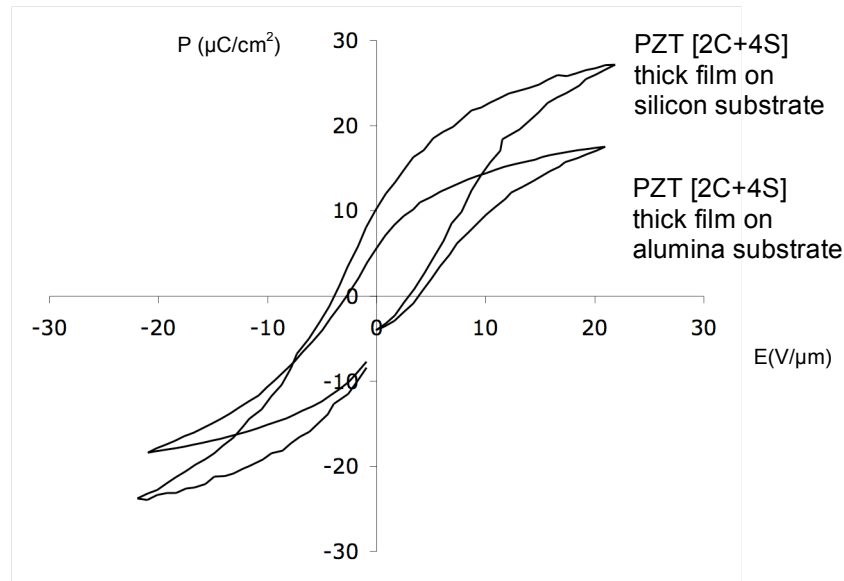


Figure 6.25: Hysteresis loop of the PZT composite film [2C+4S] on alumina substrate and on silicon substrate. It shows the compressed shape of the hysteresis loop when the film is subjected to a compressive stress, on alumina.

6.11 Summary

The dielectric properties of PZT films, used to fabricate the single element transducer presented in the next Chapter, has been analysed and modelled in this chapter. The relative permittivity of the PZT composite increases with the number of infiltrations until a saturation is observed around the 3rd and 4th infiltration at 700-800. Fringing fields have been analysed through a finite element model by using the software FEMlab. It has been found that for small features ($\sim 50\mu\text{m}$ radius) they are responsible for the increase of the relative permittivity by 30%. This effect will have to be carefully considered for the analysis of the annular array, which includes annular of $20\mu\text{m}$ width. The piezoelectric coefficient has been also found to increase with infiltration until saturation at 75-85pC/N.

A study on ferroelectric properties revealed that the stress developed during the fabrication process influences the dipole direction. On silicon tensile stress, most of the dipoles seem directed along a plane parallel to the substrate plan. On alumina a compressive stress seems to direct most of the dipole in a plane perpendicular to the substrate plan. These differences in orientation affect the shape of the hysteresis loop.

Now that the evolution of dielectric, piezoelectric and ferroelectric properties with the fabrications processes are understood, single TmpMUT elements can be fabricated and analysed in regards to their acoustic behaviour with different number of infiltrations and size of element.

Chapter 7

TmpMUT:

Thickness mode piezoelectric micro-machined ultrasonic transducer

7.1 Introduction to high frequency transducer

The aim of this project was to answer the industrial demands for a high frequency ultrasonic transducer, for medial imaging applications. The characteristics specified for the transducer are summarised in the Table 7.1.

Table 7.1: Characteristics specified for the annular array ultrasonic transducers for the material

Device (figure 3.1)	
Resonant frequency	50MHz
Max Diameter	2-4mm
Number of annular rings	3-10
Workable through water	√
Electromechanical coupling coefficient	> 0.4
Bandwidth	> 60%

Why annular arrays? "First, an annular array maintains an almost uniform lateral resolution, and thus achieves a better depth of field compared to the single-element transducer. Second, whereas dynamic focusing can be applied only in the lateral direction in linear arrays, and the beam in the elevation direction has only one focal point determined by the lens. The annular array transducer has ability for dynamic focusing in both these lateral directions. An annular array consists of a small central disc with several concentric annuli. This arrangement allows a focus to be produced at any desired depth along the beam axis by introducing delays in the electrical signal paths to each element starting at the outside and moving toward the centre. Third, compared to linear and phased arrays, annular arrays have larger elements for the same resolution, and thus less elements are needed for imaging, which, in turn, requires less electronics and less cost. Obviously, the disadvantage of an annular array imaging system is that it has to be driven by a motor or actuator to perform the scan". [Hu *et al.* 2006]

Piezoelectric ultrasonic transducers currently used work at frequencies between 1 and 20 MHz, and the PZT layer (piezoelectric material) thickness is often >800µm. One of the aims of the MUSTWIN project is to extend the maximum frequency by 40MHz. [Stuart *et al.* 2000] [Levassort *et al.* 2001] [IMASONIC][Pan *et al.* 2006].

As an annular array is a complex structure, simpler structures such as cylindrical devices, were first fabricated. Their main uses were to understand how to measure the mechanical behaviour of the material, and to have a first approximation of how to vary the frequency, k_t^2 , and Q with the thickness and the density of the film. To do so, a set of chromium masks was fabricated (their AutoCAD drawings are presented in the appendix B). The same base design that used for analysing the dielectric properties (Chapter 6) was used to fabricate these cylindrical devices. One mask was added in order to pattern the SiO₂ to allow the removal of

the silicon from the back of the device (section 3.1), to allow characterisation of the resonance behaviour.

This chapter deals with the characterisation of high frequency transducers. 5 main parts explain how the S parameters (Section 3.8.3) of the device were used to analyze the mechanical behaviour of the device.

1. The first part of this chapter, results obtained for the S_{21} parameters are presented. It is explained why some measurement issues encountered during this work obliged us to use S_{11} parameter in addition of the S_{21} parameter.
2. The second parts presents the S_{11} parameter of a thick film infiltrated 4 times, [C+4S]. The technique used to measure S_{11} is explained in Chapter 3.
3. The S_{11} parameter was compared to the theoretical results obtained via a MASON model written in MATCAD.
4. The model was then adapted to better describe the thick film material, by accounting for the porosity observed, the dielectric loss, and the acoustical loss.
5. Once this measurement and their model are set up, the thickness mode of vibration was demonstrated to work with the thick technology by presenting different resonating frequencies due to different PZT film thicknesses. Results obtained for different levels of material porosity will be presented in the fifth part. A brief discussion about the size and shape of electrodes will be open for the future work chapter, and the understanding of the annular array electrodes.

7.2. Thickness mode of excitation

Equation 7.1 predicts that with an increasing film thickness the resonant frequency, f_r , should decrease.

$$k_t^2 = \frac{f_a^2 - f_r^2}{f_a^2} \rightarrow f_r = \sqrt{\left(\frac{1}{2l_t} \sqrt{\frac{c_{33}^D}{\rho_{PZT}}}\right)^2 (1 - k_t^2)} \quad \text{Equation 7.1}$$

Where f_a is the anti-resonant frequency, C_{PZT} the acoustic velocity in the PZT material ($\sim 4500 \text{ m}\cdot\text{s}^{-1}$), l_t the total thickness of the device, c_{33}^D is the material stiffness at zero or constant displacement ($= 15.8 \cdot 10^{10} \text{ N/m}^2$), ρ_{PZT} the density of PZT ($= 7700 \text{ Kg}\cdot\text{m}^{-3}$), and k_t the electromechanical coupling coefficient.

The values of the material parameter presented above are experimental values reported for bulk PZ26 (powder used in our composite) by the company Ferroperm. Figure 7.1 shows the predicted variation in resonant frequency as the thickness of PZT increases. The resonant frequency is not dependent of the electrode area. As it is not area dependent, shape or size of the electrode should not influence the resonant frequency. However, it is understood that

this rule should have a limitation. For example, very wide or narrow electrodes may be influenced by stress. However, the main limitation will be for PZT films with high thicknesses, as the electrodes have to be able to support the minimum voltage to pole and drive the transducer. This equation should contain a term that takes into account its limits conditions. When l_t tends to 0 the limits will be the mechanical response of the material when the resonant frequency tends to infinite.

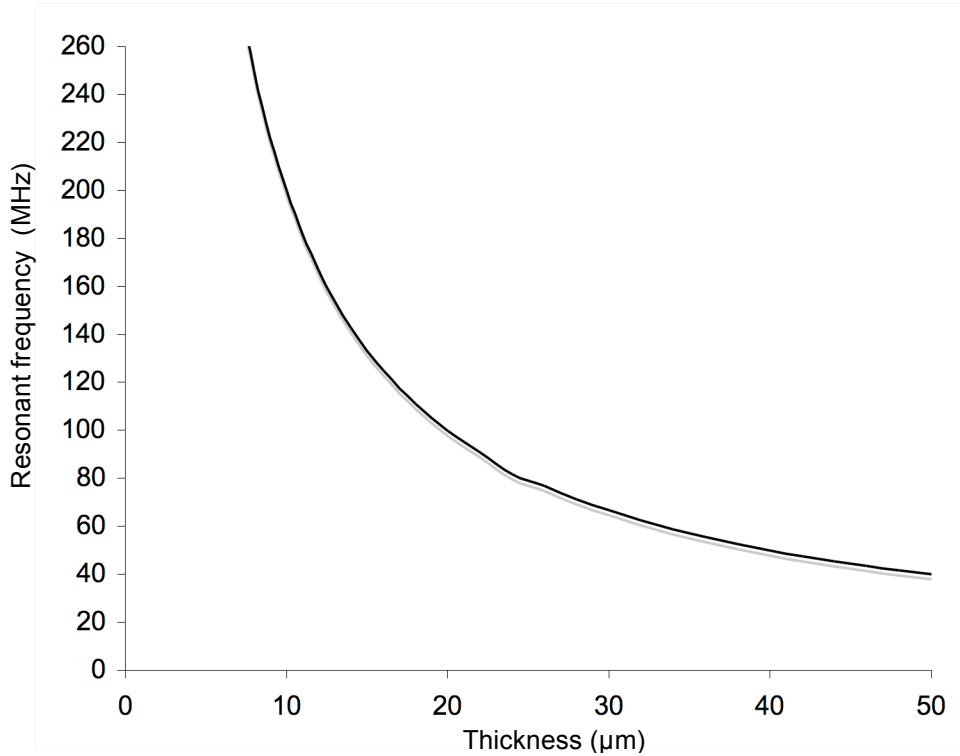


Figure 7.1: Calculated variation in resonant frequency as a function of thickness as predicted by Equation 7.1 (PZ26 bulk parameters).

According to Figure 7.1, a 40μm thick film will resonate at 50MHz, which is consistent with the work conducted on PZ26 thick film by Wolny [2001].

7.3 S_{21} parameters results

The first task was to develop a technique to conduct the impedance measurements. The first trials were oriented toward the S_{21} parameter measurement (Section 3.8.2). The S_{21} parameter is the transmitted impedance between the top and the bottom electrode given by Equation 7.2 representative of the forward transmission gain, or power transmitted, from port 1 to port 2.

$$S_{12}(db) = 20 \log \left(\frac{100}{Z_{in}(\Omega) + 100} \right) \quad \text{Equation 7.2}$$

Where Z_{in} is the input impedance.

This measurement approach induces conditions due to the probe design and the network analyzer used. The main one is that all the electrodes have to be designed having an impedance of 50 Ohms. The design chosen for the measurement was the ground-signal-ground design. The middle electrode is the one transmitting and receiving the signal. The side electrodes connect the grounds of the 2 probes. The ground electrodes were designed with an impedance of 50 Ohms. However, this electrode design generated additional parasitic capacitances. These added capacitors added a background signal which reduced the measured signal down to -30db (Figure 7.2 (red lines)).

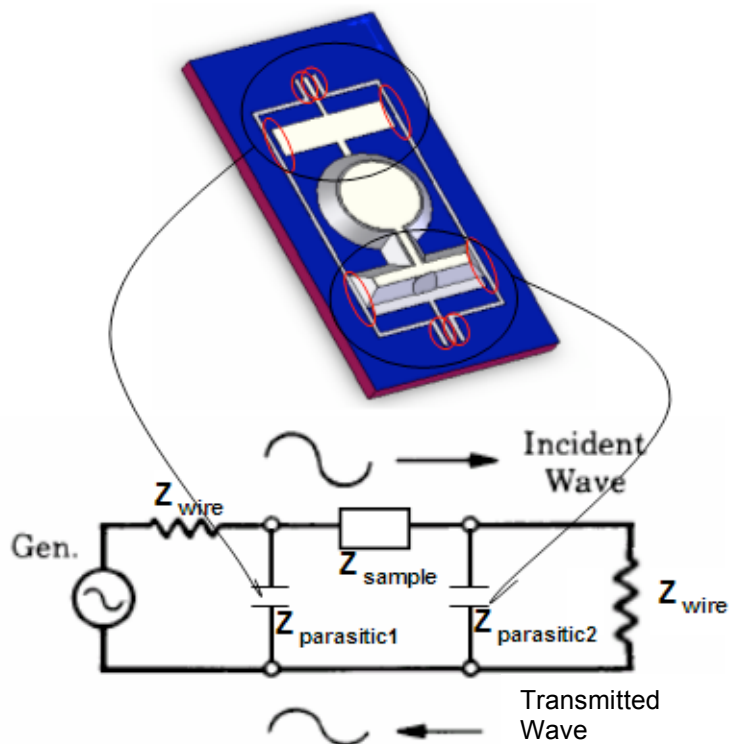


Figure 7.2: Illustration of the measured device design: red lines reveals the location of parasitic capacitances added by the ground signal ground pads, which reduced the measured signal. In the equivalent circuit of the S_{21} parameter measurement, the parasitic impedance $Z_{\text{parasitic 1}}$ and $Z_{\text{parasitic 2}}$ represent this parasitic capacitance.

Figure 7.2 illustrates the measured device design. It represents the location of the parasitic capacitors added by the electrode design. This parasitic impedance generates a background signal, which masks the device response (Figure 7.3). Despite a weak measured signal, comparison of the 2 measured S_{21} parameters from poled and unpoled devices, demonstrates that a poled 22 μm thick film device resonates at 77MHz. This frequency does not correspond to the theoretical frequency calculated for the PZ26 bulk ceramic as shown in Figure 7.1 which predicted that a 22 μm thick PZ26 film should resonate at 96MHz. Analyses of this preliminary low magnitude signal indicated that the reason for this lower resonant

frequency could be because the composite PZT material exhibited a lower c_{33}^D/ρ_{PZT} ratio than the PZ26 bulk (Equation 7.1). In this Equation 7.1, to explain the lower frequency with the electro-mechanical coupling coefficient, k_t^2 would need to increase, but the next section demonstrate that the composite has a tendency to have a lower k_t^2 . However, to validate this hypothesis confirmation using a higher quality signal is needed.

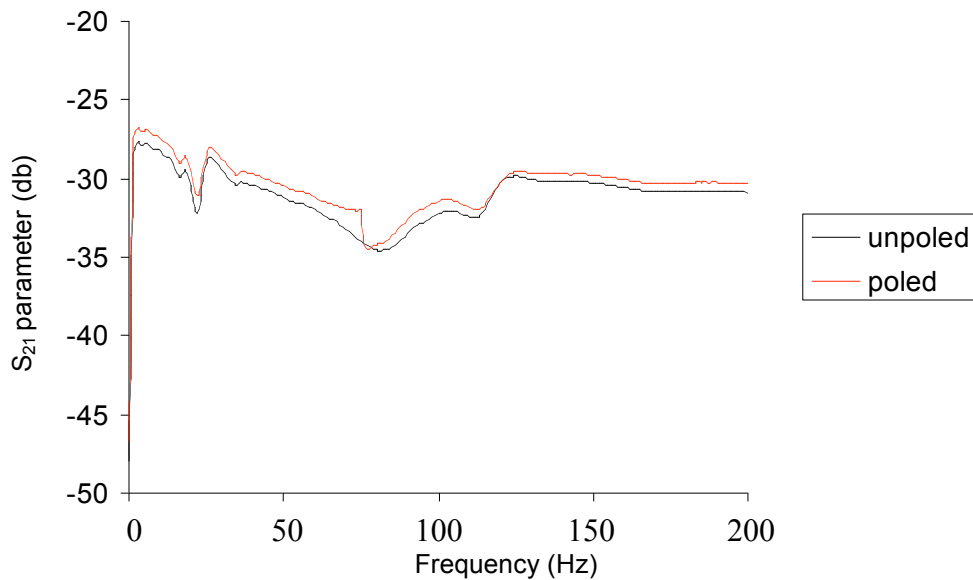


Figure 7.3: S_{21} characteristic of a 22 μm thick [C+4S] PZT film after and before poling. When poled, it resonates at 77MHz.

7.4 S_{11} parameter results

The noisy S_{21} transmitted signal was due to the ground-signal-ground probe design. The reflected parameters S_{11} and S_{22} were found to be as lossy as the S_{12} . To overcome this issue, a non-conventional method was used to measure S_{11} (section 3.2.8). The signal probe (the centre of a BNC cable) was connected to the bottom electrode and the ground probe (the other part of the BNC cable) was connected directly to the top electrode.

Using this connection technique, the resonant frequency was confirmed to be ~77MHz for a 22 μ m thick film. This signal, shown in Figure 7.5, is in agreement with that measured using the S_{21} parameter ground-signal-ground techniques (Figure 7.3). A probe station was specially designed and fabricated to measure this parameter in a reliable way.

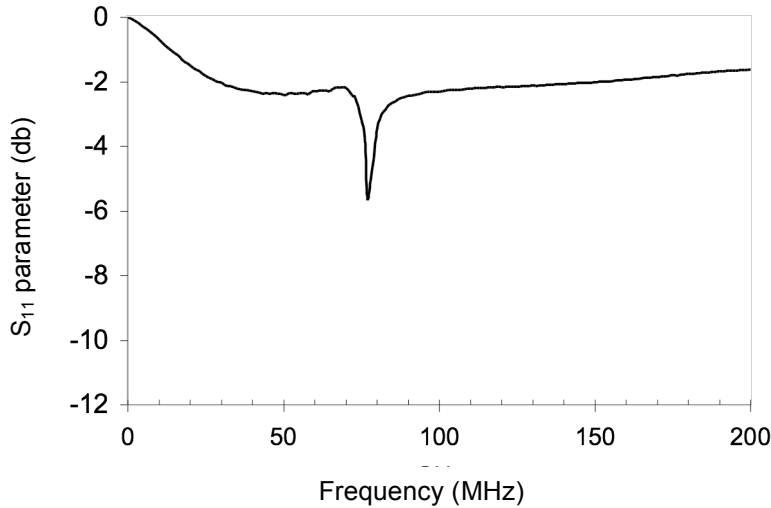


Figure 7.5: S_{11} parameter of 600 μ m radius electrode of a 22 μ m thick PZT [C+4S] device with the backing silicon etched.

The S_{11} parameter shows the resonance frequency at ~77MHz and anti-resonance at ~90MHz. The resultant electro-mechanical coupling coefficient k_t was calculated using Equation 7.3 and found to be equal to 0.42.

$$k_t = \sqrt{\frac{\pi f_r}{2 f_a} \cot\left(\frac{\pi f_r}{2 f_a}\right)} \quad \text{Equation 7.3}$$

Where f_r and f_a are the resonant and anti-resonant frequencies respectively. The quality factor is calculated using Equation 7.4 and found to be equal to 11.

$$Q = \frac{f_a}{\Delta f} \quad \text{Equation 7.4}$$

The parameters, Q and k_t , can be considered as figures of merit for the device. These values fulfil the industrial demands set by the MUSTWIN partner IMASONIC.

To gain a better understanding of the difference between the behaviour of the bulk PZT and the composite film PZT a MASON model analysis was conducted.

7.5 Modelling the resonant frequency

7.5.1 Impedance

The main principle of the Mason model is explained in section 2.3.2. Equation 2.76 describes a loaded transducer. A first approximation is to simplify this equation by considering the input impedance of an unload transducer (i.e. a simple PZT layer, in air). Z_1 and Z_2 in Equation 2.76 are then considered to be null, and lead to Equation 7.5.

$$Z_{3,unload} = \frac{V_3}{I_3} = \frac{1}{j\omega_3 C_o} \left[1 - k_t^2 \frac{\tan(\beta_{a,p} l/2)}{\beta_{a,p} l/2} \right] \quad \text{Equation 7.5}$$

The values for bulk PZT material constants were used in this model (Table 7.2) as a first approximation.

Table 7.2: Bulk (PZ26) material constant parameters input in the Mason model [Ferroperm catalogue] (the thickness of the PZT film was measured by a stylus dektak surface profiler)

k_t	Thickness l (μm)	Permittivity ϵ^σ	Density (10^3 kg/m^3)	Stiffness (10^{11}N/m^2)	Attenuation coefficient (Np/m)
0.47	22 ± 0.05	1300	7.7	15.8	4000

This model predicts an interesting behaviour in comparison to the S_{11} experimental result. The resonant frequency predicted by the Mason model, for a $22\mu\text{m}$ thick unloaded PZT transducer in air, is 103MHz. This is 26MHz higher than the experimental resonance frequency observed at 77MHz for a $22\mu\text{m}$ thick devices (Figure 7.7). Figure 7.7 shows a comparison of the predicted and observed variation of S_{11} as a function of frequency. Figure 7.6 compared the prediction of the resonant frequency obtained using Equation 7.1 with experimental data obtained for different PZT thicknesses demonstrating 19MHz difference of frequency. The Mason model includes a full set of electro-mechanical variables. The difference of results between a simple equation such as Equation 7.1 and a comprehensive model such as the Mason model is considered acceptable.

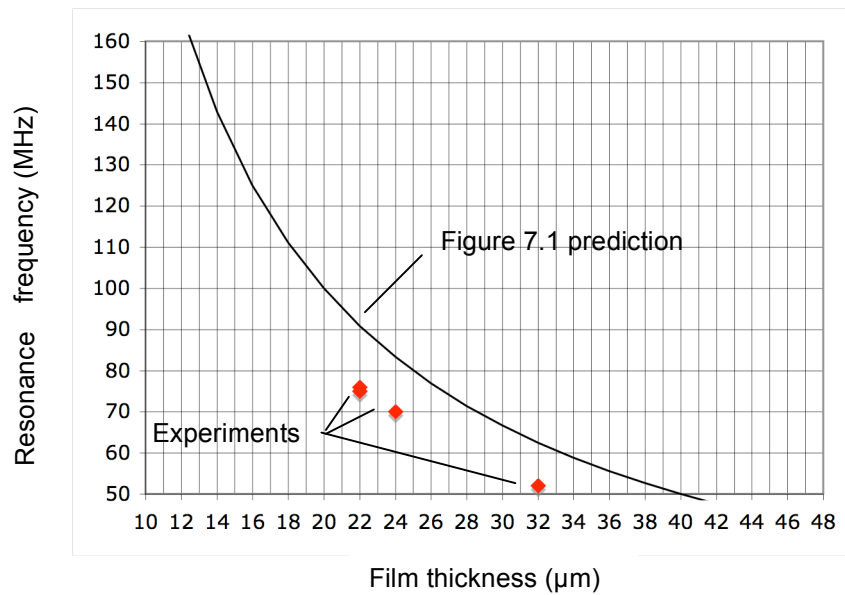


Figure 7.6: Variation in resonant frequency as a function of thickness as predicted by equation 7.1 (with PZ26 bulk parameters), in comparison to experimental data obtained for the PZ26 powder/ PZT sol-gel composite thick film (x[C+4S]).

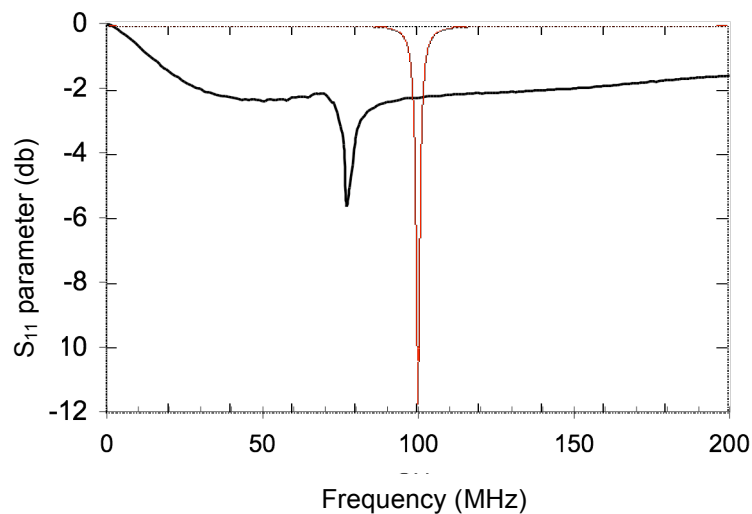


Figure 7.7: red line: Mason model of a simple layer of 22μm PZT transducer fabricated with PZ26 bulk. Black line: experimental data from the same transducer via the [C+4S] composite route.

This difference of resonance frequency between experiment and theory can have different sources considering that the model does not include:

- The load imposed by the Pt electrodes, silicon oxide and the ZrO_2 backing the device.
- The difference of behaviour between bulk PZ26 ceramic and the PZT composite (PZ26 powder and PZT sol). It includes a very different porosity, dielectric

constant, density, stiffness and then the electromechanical coupling factor.

This data mainly analyzed in preceding chapters, will be included in the Mason model presented here, in order to correct this frequency difference.

7.5.2 Influence of the load (SiO₂, Pt, ZrO₂)

a) Influence of the backing on the resonant frequency predicted by Equation 7.1

Figure 7.6 illustrates resonant frequency predicted by Equation 7.1 and shows a 22±0.1 μm thick film to resonate at 96±1MHz. To account for additional layers, a first approximation consists of taking into account the different added thicknesses. This approximation considers that the PZT film activates the whole thickness, but just the just acoustic velocity of the PZT film is taking into account. This backing influence of the transducer should mainly be due to the SiO₂ (400nm) and the Pt electrodes (100 nm per electrode). The ZrO₂ is too thin to have a noticeable influence (~40nm). The thickness becomes, in this modified case, 22.6±0.1μm and reduces the resonant frequency by just 3 MHz (Equation 7.6) [Rosenbaum 1988]:

$$f_r = \sqrt{\frac{C_{PZT}}{2(t_{SiO_2} + t_{PZT} + t_{Pt} + t_{ZrO_2})}} [1 - k_t^2] \approx 93 \pm 1 \text{ MHz} \quad \text{Equation 7.6}$$

b) Influence of the backing on the resonant frequency predicted by the Mason model

When the SiO₂ and the Pt layers are included in the Mason model, the resonance frequency is confirmed to be reduced by 3±1MHz. With the additional load the resonant frequency is found to be 100±1MHz. In this case the Mason model includes the acoustic and electrical properties of the added layers (Equation 7.7 and 7.8): To include the top and bottom electrode and the SiO₂ layer, Equation 2.76 was used, and can be represented by Equation 7.7.

$$Z_{3,load} = \frac{V_3}{I_3} = \frac{1}{j\omega_3 C_o} \left[1 - k_t^2 \frac{\tan(\beta_{a,p} l/2)}{\beta_{a,p} l/2} Z_{a,L} \right] \quad \text{Equation 7.7}$$

Where $Z_{a,L}$ is the acoustic impedance of the load, top electrode/bottom electrode/SiO₂ given by Equation 7.8.

$$Z_{a,L} = \frac{(Z_{a,Pt} + Z_{a,Pt/SiO_2})Z_{a,PZT} \cos\left(\frac{\beta_{a,p} l}{2}\right) + jZ_{a,PZT}^2 \sin(\beta_{a,p} l)}{(Z_{a,Pt} + Z_{a,Pt/SiO_2})Z_{a,PZT} \cos \beta_{a,p} l + j(Z_{a,PZT}^2 + Z_{a,Pt} Z_{a,Pt/SiO_2}) \sin(\beta_{a,p} l)} \quad \text{Equation 7.8}$$

Where $Z_{a,pt}$ and $Z_{a,pt/SiO_2}$ are the acoustic impedances of the front load (top platinum electrode), and the back load (bottom platinum electrode and SiO_2). Their equations are presented in appendix B. This analytical analysis proves that the load of the thin Pt electrodes and SiO_2 are not responsible for the difference in resonance frequency of 26MHz. Instead only 3 ± 1 MHz can be accounted for due to the added loads.

7.5.3 Influence of the porosity on Equation 7.1 and on the Mason model

Another possibility, to explain this difference in resonant frequency, consists of combining the porosity analysis realised in Chapters 4 and 6, with the Mason model and Equation 7.1. Here, the density, the stiffness, and the relative permittivity will be considered to change with the porosity. In the Mason model, these changes will affect the large majority of the modeled variables, including the electromechanical coupling coefficient, and acoustic velocity.

a) Influence of the porosity on the resonant frequency predicted by Equation 7.1

In Equation 7.1 just the effect of porosity on density and the stiffness needs to be modelled.

The variation of the density of a material with a spherical porosity can be considered linear. This variation is given by Equation 7.9 [Rice, 1998].

$$\rho = \rho_o(1 - P) \quad \text{Equation 7.9}$$

Where ρ_o is the bulk density of the considered material, and P its volume percentage of porosity. For a thick film infiltrated 4 times, [C+4S], Chapter 6 reports a porosity ranged between 5 vol.% and 8 vol.%. If the bulk density of PZ26 is chosen for ρ_o (7700 kg.m^{-3}), then the density ranges between 7084 and 7315 kg.m^{-3} .

The change in the level of porosity will also influence the stiffness of the PZT composite. The Equation 7.10 presented by Rice [1998] is used to predict the mechanical behaviour of materials presenting spheroidal porosity. Once again, the porosity is considered here to be spherical as a first approximation.

$$Y = Y_o(1 - \sqrt{3}P^{2/3}) \quad \text{Equation 7.10}$$

Here Y_o is the Young's modulus of the bulk PZ26. For the purpose of this analysis, the Young's modulus and the stiffness will be considered to vary in the same manner with a variation of porosity. This approximation can be justified by considering the definition of the

Young's modulus as the inverse of the compliance (Equation 2.32). Here, equation 7.10 becomes Equation 7.11:

$$c_{33}^D = c_{33bulk}^D (1 - \sqrt{3}P^{2/3}) \quad \text{Equation 7.11}$$

Then $c_{33}^D(P = 5vol\%) = 1.2 \cdot 10^{11} N/m^2$ and $c_{33}^D(P = 8vol\%) = 1.07 \cdot 10^{11} N/m^2$.

Section 7.5.3.b demonstrates that k_t is constant with the porosity. Using Equation 7.1, Equations 7.9 and 7.11, a first approximation of the influence of porosity on the frequency predicts the resonant frequency to be 81 and 85 MHz for films containing 8 and 5vol.% of porosity respectively. These values correspond to a model of a 22 μm thick film PZ26 with 5-8vol.% of porosity. This modelled film is far from the real structure of the composite PZT thick film tested here. The real composite film contains the PZT sol-gel, sintering aid, plus defects such as comets and cracks. These variables are not included in this model, and should further a decrease of the stiffness. The cracks and other defects lower the mechanical stiffness of the material, and the sintering aid and the sol add another phase disturbing the mechanical behaviour.

Even if these variable are not included in this model, it seems that the resonant frequency is considerably influence by the PZT stiffness. The porosity and the added sol lower the stiffness and so lower the resonant frequency.

This model only takes into account, the thickness, the density, and the stiffness of the PZT film. The effect of porosity on the resonant frequency needs to be confirmed by a more comprehensive model, such as the Mason model, which includes a full set of electro-mechanical variables.

b) Influence of the porosity on the resonant frequency predicted by the Mason model

The density and the stiffness as function of the porosity will be modelled in the same way in the Mason model as in the previous section. The model result will be compared with the same sample infiltrated 4 times, exhibiting a porosity of 8% and measured to have a dielectric constant of 830 when poled. However, the initial relative permittivity input in the Mason model was equal to the predicted value for the bulk PZ26 with 8% of porosity, i.e. 1150 (Equation 6.2). The relative permittivity and the electromechanical coupling coefficient used in this model vary with the porosity.

The bulk PZ26 relative permittivity as function of the porosity is given by Equation 6.2. In Chapter 6, a range of relative permittivity was considered per degree of infiltration.

In Chapter 6, the process x[C+4S] has been analysed to have a relative permittivity ranging between 730 and 900 (or ~830 and 1000 for poled PZT), and porosity ranged between 5 and 8 vol.%. However, in order to be consistent with this analyse, the model will use predicted values of relative permittivity as calculated using Equation 6.2.

Affected by the piezoelectric constant, the relative permittivity and the stiffness, the electromechanical coupling coefficient should also be affected by an added porosity. This effect is represented by Equation 7.12.

$$k_t = \sqrt{\frac{e_{33}^2}{c_{33}^D \epsilon_{33}^S}} = \sqrt{1 - \frac{c_{33}^E}{c_{33}^D}} \quad \text{Equation 7.12}$$

Dunn [1993] derived k_t as function of the porosity and found that e_{33}^2 should vary approximately as the product $c_{33}^D \cdot \epsilon_{33}^S$ does with different amounts of porosity. He confirmed his theory with experiments demonstrating a constant k_t with an increase of porosity. In his model and experiment, Dunn used different shape of porosity. The tested materials were bulk PZT-5A and PZT-5H ceramic. Banno [1987] reported an increase of 0.2 of k_t , with an increase of 10vol.% of porosity in a PLZT sample. These 2 models are based on the full set of ferroelectric matrices for the same materials.

The full set of mechanical, dielectric and piezoelectric constants of these 2 materials are known, which is not the case for the new PZT composite presented in this work.

For the trend analysis of an unknown PZT-PMN material Bast [1989] used the electrostatic moduli of the PZT-5H ceramic modelled by Dunn which has a similar composition. This trend shows an approximately constant k_t with a variation of porosity.

The bulk ceramic PZT-5A is reported to be close enough to the PZ26 bulk ceramic in term of electromechanical properties [Ferroperm catalogue]. Therefore, the e_{33} of the PZ26 ceramic will be supposed to vary in the same way as the e_{33} of the ceramic PZT-5A with a variation of porosity. The model done by Dunn [1993] can then be used, and the equivalent values of e_{33} found for the PZ26 ceramic, containing different volume percentage of porosity, are presented in Table 7.3.

Equation 7.12 and Table 7.3 reveals, with the imprecision due to the lack of an exact model of e_{33} , that the electromechanical coupling coefficient should remain constant with changes in the porosity.

Table 7.3 represents the values input in this Mason model in order to model k_t as function of the porosity. Table 7.4 summarise all the values input into the Mason model up to now, and compare them with the measured variable of the sample tested in this section.

Table 7.3: e_{33} (C/m^2) values of PZ26, considered to vary like the PZT-5A ceramic with an increase of porosity, revealing a constant k_t with an increase of porosity

	e_{33} (PZT-A5) [Dunn, et.al. 1987]	C_{33}^D (10^{11}) N/m ²	ϵ_{33}^S	e_{33} (PZ26)	Modeled k_t (PZ26)
bulk	15.8	1.58	700	14.7	0.47
P=5 vol.%	14.9	1.21	665	13.8	0.48
P=8 vol.%	14.3	1.07	619	13.2	0.50
P=10 vol.%	13.3	0.99	600	12.2	0.48

Table 7.4: Dielectric and mechanical properties of PZ26, PZ26 (with 8% of porosity) that are input in the Mason model. The measured constants characterising the composite PZ26 powder/PZT sol-gel infiltrated 4 times, are also presented.

	PZ26	PZ26 P=8%	Composite [C+4S] P=8%
ρ (kg/m ³)	7700	7084	7084
ϵ_{33}^{σ}	1300	1150	830
ϵ_{33}^s	700	619	x
c_{33}^D (10 ¹¹) N/m ²	1.58	1.07	x
c_{33}^E (10 ¹¹) N/m ²	1.23	0.83	x
e_{33} C/m ²	14.7	13.2	x
k_t	4.7	4.7*	4.2

(*as k_t is considered constant, the value from the catalogue Ferroperm is considered, and not the derivate one from Table 7.3)

Figure 7.8 represents the change in predicted resonant behaviour when the influence of the porosity on the resonant frequency is corrected. In this Figure, a 22 μ m PZ26 thick porous film with 8% of porosity is modelled, and compared with the experimental results from a 22 μ m Composite PZ26/PZT sol-gel 10[C+4S] with 8% Porosity.

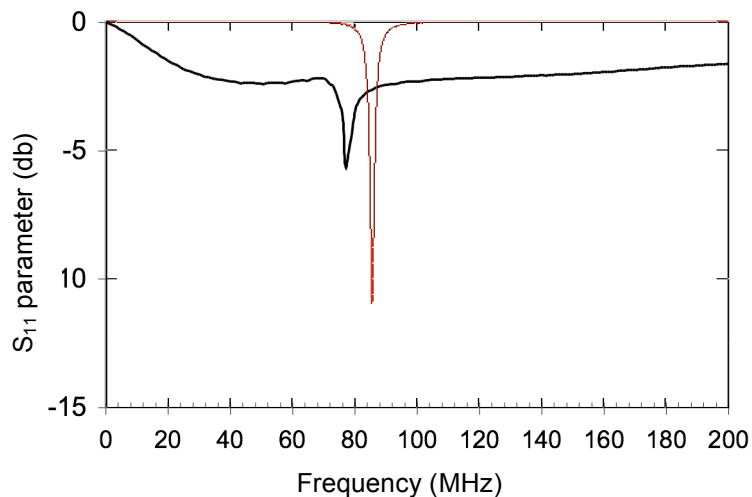


Figure 7.8: The red line represents the Mason model prediction for a loaded transducer Pt/PZ26(P=8%, $l=22\mu\text{m}$)/Pt/SiO₂. The black line represents the experimental result for a 10 [C+4S] thick film with 8vol.% of porosity ($22\pm 0.1\mu\text{m}$ thick).

The resonance frequency is predicted to be at $85\pm 1\text{MHz}$ for a thick film, with 8% of porosity. The experimental resonant frequency is at 77MHz.

The Mason model is much more comprehensive than the simple Equation 7.1. From now on, Just the Mason Model will be considered in this Chapter.

7.5.4 Discussion and precision of this observed difference between a porous PZ26 and the composite [C+4S] films.

Figure 7.7 represents result obtained from the modelled Pt(100nm)/ PZ26(P=8%,l=22 μ m)/ Pt(100nm) transducer. This transducer was modelled to resonate at 103MHz. When the backing and the top electrode were added to this Mason model, the Pt(100nm)/SiO₂(400nm) /PZ26(l=22 μ m)/Pt(100nm)transducer was modelled to resonate at 100MHz. To this modelled loaded transducer was added 8% of porosity. The modelled Pt(100nm)/SiO₂(400nm) /PZ26(P=8%,l=22 μ m)/Pt(100nm) transducer was then predicted to resonate at 85MHz with a precision of 1MHz due to the accuracy of the thickness measurement.

The real transducer exhibits a resonant frequency at 77MHz. 18MHz of the 26MHz difference in resonant frequency is understood. Only 3 \pm 1MHz are due to the backing increasing the thickness, and 15MHz are due to the porosity, mainly because it lowers the stiffness of the material. Approximately 8 \pm 1MHz still has to be explained.

In Section 6.2 the PZ26 bulk relative permittivity value at different levels of infiltration was compared with that of the composite PZ26/PZT sol-gel film at different levels of infiltration. It was observed that the relative permittivity of the PZ26 system was higher than the relative permittivity of the composite films by at least 100 (Figure 6.2). If the relative permittivity of the porous PZ26 system is that different compared to the composite one, it can be assumed that other constants can also be very different.

These possible variations of the relative permittivity and other constant, can find their origins in the main difference between the PZT composite tested and the porous PZ26 modelled, the presence of the second phase such as the PZT sol-gel.

In case of the PZ26 powder route the sintering temperature is generally higher (1200°C). This allows the sintering process to act directly on each grain by increasing the neck size formed between each grain (Figure 6.3). The composite sintering route occurs at a lower temperature (710°C). It might start to activate the same process, however the main sintering process between grains is mainly due to the PZT gel crystallisation. The sol crystallises on each grain and acts like a glue.

The sol cannot have exactly the same structure as the PZ26 because of different fabrication processes. Then it can be considered as a second phase, and the mechanical strength between grains goes through this PZT gel crystallised phase. This adhesion process will obviously be weaker than, a sintering process involving two grains that interpenetrated each other as in PZ26 powder sintered at 1200°C.

As this added sol is the only difference between the two routes, the remaining 8 \pm 1MHz difference between the model resonant frequency and experimental one, should be

explained by the presence of the sol. As its presence reduces the stiffness, it lowers the resonant frequency (Equation 7.1).

Figure 7.9 reveals, if $C_{33}^D(\text{PZ26 } P=8\%)=1.07 \cdot 10^{11} \text{ N/m}^2$ needs to be reduced in the model by 0.2 N/m^2 to fit the observed resonant frequency of the composite PZT thick film. The input stiffness is then equal to $C_{33}^D(\text{PZT composite } P=8\%)=0.87 \text{ N/m}^2$ and 0.2 N/m^2 should mainly represent the stiffness influence of the PZT sol-gel on a porous PZ26 thick film, plus the approximations made.

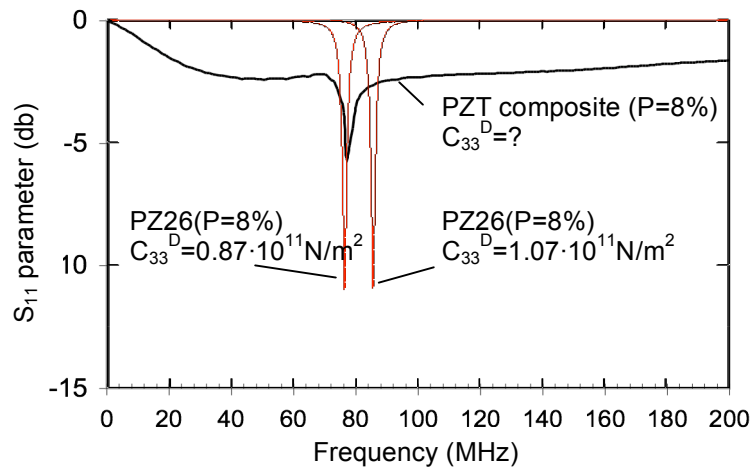


Figure 7.9: Illustration of the change needed on the stiffness to explain the difference of the resonant frequency between the Mason model of a PZ26 system and the composite system experimental result. Reducing the stiffness of PZ26($P=8\%$) by $0.2 \cdot 10^{11} \text{ N/m}^2$, shifts the model resonance toward the experimental resonance.

7.5.5 Effect of the relative permittivity on the Mason model

Figure 7.10 represents the modelled resonance frequency when ϵ^{σ} (PZ26 ($P=8\%$)) equal to 1150 is replaced by the measured relative permittivity of 830. This relative permittivity ϵ^{σ} is then reduced by the considerable amount of 320. This decrease represents also the effect of the PZT sol-gel on the porous PZ26 modelled. A change of relative permittivity does not change the frequency of the resonance only alters the magnitude of the A change of stiffness shifts the resonant frequency but leaves the magnitude of the S parameter untouched.

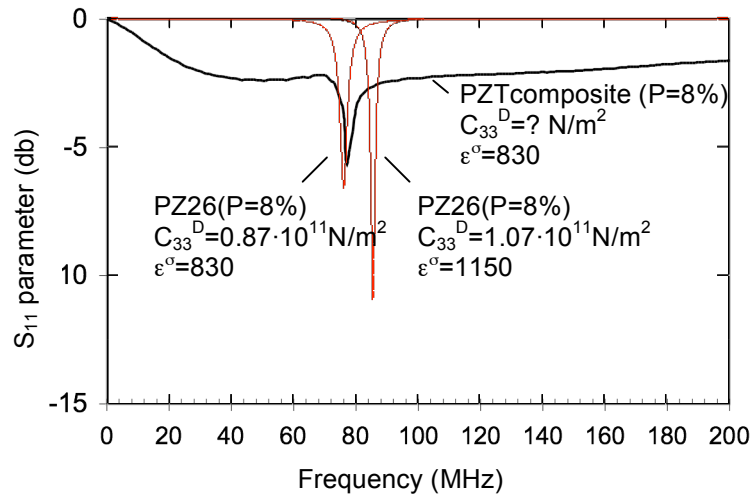


Figure 7.10: Variation of the magnitude of the modelled resonant frequency peak for a 22 μm thick 10[C+4S] sample, when ϵ^σ (PZ26(P=8vol.%)) is reduced from 1150 to 830 (A difference of stiffness does not change the magnitude of the peak resonance) (Figure 7.9).

The peak of the modelled PZ26(P=8%, $C_{33}^D=0.87 \cdot 10^{11} \text{ N/m}^2$, $\epsilon^\sigma=830$) has a 6db lower intensity than the PZ26(P=8%, $C_{33}^D=0.87 \cdot 10^{11} \text{ N/m}^2$, $\epsilon^\sigma=1150$) one. This means considering the definition of the S_{11} parameter in Chapter 3, that when the material has a smaller relative permittivity the signal is reflected less by the device. Having a lower relative permittivity, the capacitor is considered to store less charge, which allows a quicker transmission, with less energy lost in storage.

The k_t of the 10[C+4S] sample was measured to be 0.42 representing a drop of 0.05 compared to the k_t value of the bulk PZ26 equal to 0.47. With ϵ^σ , C_{33}^D predicted from the model and the measured k_t , the piezoelectric coefficient e_{33} of the composite can be calculated to be equal to 10.5 C/m² (Equation 7.12). The precision of the measurement of k_t can't be considered to be accurate. Between different samples of the same composition a k_t range between 0.42 and 0.46 was observed. The piezoelectric constant e_{33} of the composite infiltrated 4 times is then between 10.5 and 11.5 C/m².

7.5.6 Dielectric Loss in the Mason model

The Mason model doesn't yet include the dielectric loss due to the electrode and the PZT. The dielectric loss of all the samples tested has been measured to be between 0.01 and 0.02 at 1kHz. It can be modelled, very simply by adding a resistor to the equivalent circuit [Rosenbaum, 1987].

R_{PZT} (Ω) in parallel with C_0 represents the dielectric loss due to the PZT layer and the loss due the Pt electrode (Figure 7.11). For the sample represented in Figure 7.11, these loss terms, δ , were measured together to be 0.01. In this model, as a first approximation, the added resistance will be considered to be constant with an increase of frequency and equal to the loss term, $\epsilon_r(\text{PZT})\tan\delta$ [Moulson *et.al.* 1990] [Rosenbaum, 1987]. R_{PZT} will then be considered to be 8.3Ω , when $\epsilon_r = 830$.

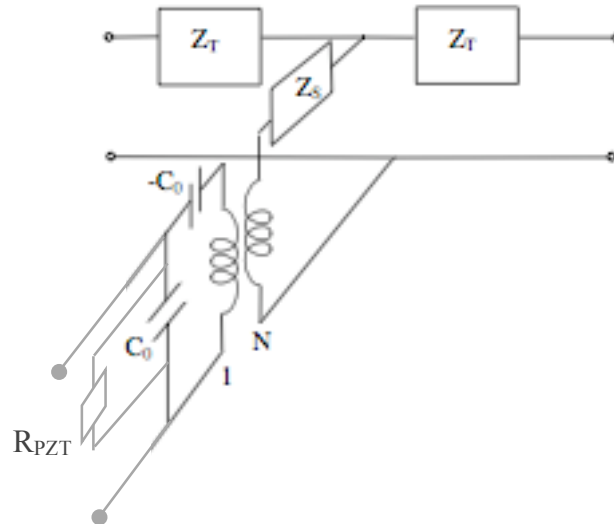


Figure 7.11: Modification of the Mason equivalent circuit presented in Figure 2.30. This figure represents the final Mason equivalent circuit considered in this model.

Figure 7.12 shows results obtained when the dielectric loss due to the electrode and the PZT film was input into this modified Mason model.

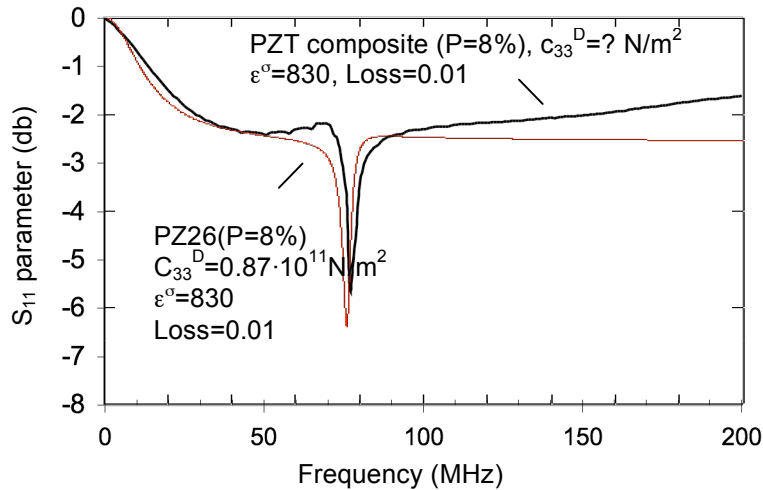


Figure 7.12: Comparison of the modelled S_{11} of PZ26 with 8% of porosity, a stiffness equal 0.87, a relative permittivity equal to 830, and a loss of 0.01 and The measured S_{11} of PZT composite PZ26/sol-gel, 10[C+4S], with 8% of porosity, an unknown stiffness, a relative permittivity equal to 830, and a loss of 0.01.

The device tested in this section is thickness mode activated. Now, that the Mason model is set up, the next section will focus on the study on the thickness mode activation.

The predicted variable, the stiffness of 0.87, and measured variables, the relative permittivity of 830 and the loss of 0.01, will now be considered constant throughout the next comparison between the Mason model and experimental data.

7.6 The thickness mode of excitation

7.6.1 Thickness effect on the thickness mode of excitation

For both the Mason model and the experiment, all parameters of the transducer are kept constant apart from the PZT thickness, which was fixed at 3 different values 7, 22, and 32 μm .

The Mason model predicts that, for an increasing thickness, the S_{11} signal will:

- 1) Show a reduction in resonant frequency with an increasing thickness.
- 2) Decrease in magnitude of the S parameter.
- 3) Show an approximately constant k_t
 - a 32 μm thick films exhibit a k_t of 0.43 \pm 3
 - a 22 μm thick films exhibit a k_t of 0.44 \pm 2
 - a 7 μm thick films exhibit a k_t of 0.47

Experimental data, shown in Figure 7.13.B follows the same trend, and the k_t values are approximately constant at 4.7.

In Figure 7.13 the 32 μm thick film exhibits an apparent higher loss, however, the measured loss at 1kHz is 0.007. This result represents the limits of this model. The losses theory is complex, and cannot be justified by a simple loss factor input in this analytical model [Gurevich *et al.* 1991]. To the loss theory the measurement instrument defect has to be added. The connection of the cables needed for the s-parameter determination are very sensitive, a simple movement of these cables generates also a virtual loss.

Figure 7.13.A and B provide illustrate the resonant frequency decreasing with an increasing film thickness. The harmonic H1 of the 52MHz resonant frequency generated by 32 μm thick film is observable in both figure 7.13.A and 7.12.B at 158MHz. The second and third harmonics, H2 and H3 of this signal, are predicted in Figure 7.13 A to be at 264MHz and 364MHz. These are harmonics of the fundamental resonance at $f_r=52(2n-1)\text{MHz}$, when n is successively equal 1, 2, and 3.

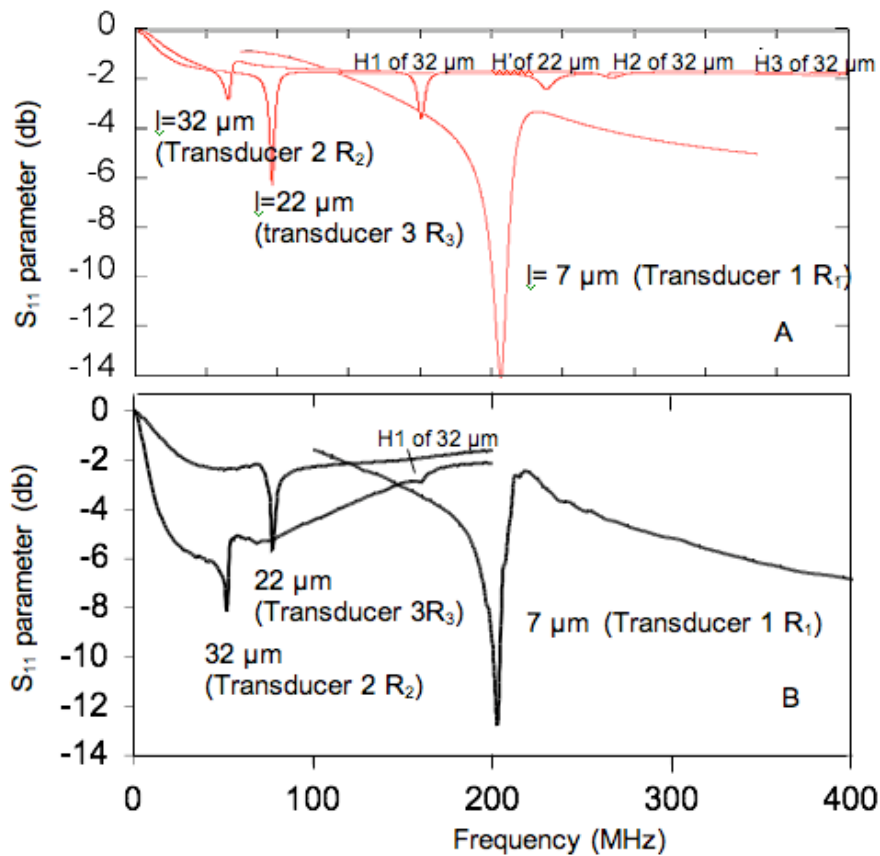


Figure 7.13: S_{11} parameters as a function of frequency for Mason model (A) and experimental data (B). For both A and B, the material considered is the PZT composite PZ26 / PZT sol-gel infiltrated 4 times [C+4S]. 3 different thicknesses of PZT are tested: 7, 22, 32 μm .

A loss in magnitude of the S_{11} parameter peak is observed when the thickness of the film increases, meaning that more energy is transmitted to port 2 (acoustical port) and less signal

intensity is reflected from the port 1. In order to understand this phenomenon, PZ26 transducers with different thicknesses have been modelled with and without load, porosity and loss. All of these models prove that this increase of transmission power with an increase of thickness is only due to the addition of material when the thickness increases. This result generates a good introduction to the next section, which discusses the effect of the ratio of electrode surface area to PZT thickness on the transducer.

7.6.2 Electrode area /PZT thickness ratio effect on the resonant frequency peak magnitude

As stated in the introduction of this chapter, this section on electrode area is a simple opening to a deeper discussion on what factors influence the magnitude of the S_{11} parameter at the resonant frequency.

In the previous section, it has been demonstrated that the difference of magnitude of the resonant frequency peak is due to the amount of material constituting the transducer, or to the impedance of the device. Then, transducer of different thicknesses, l , with different electrode square radius, r^2 , should exhibit similar variation of the resonant frequency magnitude of the S_{11} parameter with the ratio R equal to r^2/l .

7.6.2.1 First approach of the variation of the ratio electrode radius/ thickness.

A model of the 3 transducers (A, B, C), with the 3 different radius² to thickness ratios (R_A , R_B and R_C) and with the same film thickness fixed at $32\mu\text{m}$, was constructed. Table 7.5 compares the magnitude of the resonant frequency peak of these modelled transducers with the magnitude of the resonant frequency peak of the experimental transducers (1, 2, 3) characterised by the same radius² to thickness ratios (Figure 7.13).

Table 7.5: 3 transducers, (A, B, and C) modelled with three different ratios of r^2/l (electrode radius r and PZT thickness l).

	<i>Mason</i>	<i>Figure 7.13</i>
	transducer A	transducer 1
l (μm)	32	7
r (μm)	147	69
r^2/l	$R_A=680$	$R_1=680$
f_r magnitude (db)	-12.5	-14
Impedance (Ω)	239.7	50.4
	transducer B	transducer 2
l (μm)	32	32
r (μm)	600	600
r^2/l	$R_B=11250$	$R_2=11250$
f_r magnitude (db)	-4.5	-4.5
Impedance (Ω)	14.3	14.3
	transducer C	transducer 3
l (μm)	32	22
r (μm)	722.5	600
r^2/l	$R_C=16313$	$R_3=16363$
f_r magnitude (db)	-8	-6
Impedance (Ω)	9.9	6.77

Table 7.5 demonstrates that when the ratio, r^2/l , is constant between modelled transducer and experimental transducer, the magnitude of the resonant frequency peak is constant.

Table 7.5 validates, by experimental data, the Mason model of the resonant frequency peak magnitude.

This validation allows the use of this model for predicting the variation of this magnitude with the transducer's electrode radius.

Three transducers D, E, F had been modelled with three different electrodes sizes (Figure 7.14). Transducer D is set with a ~ 50 ohms impedance load to match the Network analyser and wire impedance. The model shows the further that the impedance of the device is from this impedance of 50 ohms the more the signal of the resonant frequency is reflected, and then the greater is the magnitude of the S_{11} peak.

The difference of shape of the general signal between the transducer D, E, F, illustrates a pure electrical effect of the increasing capacitance. The higher the capacitance, the quicker the saturation is achieved.

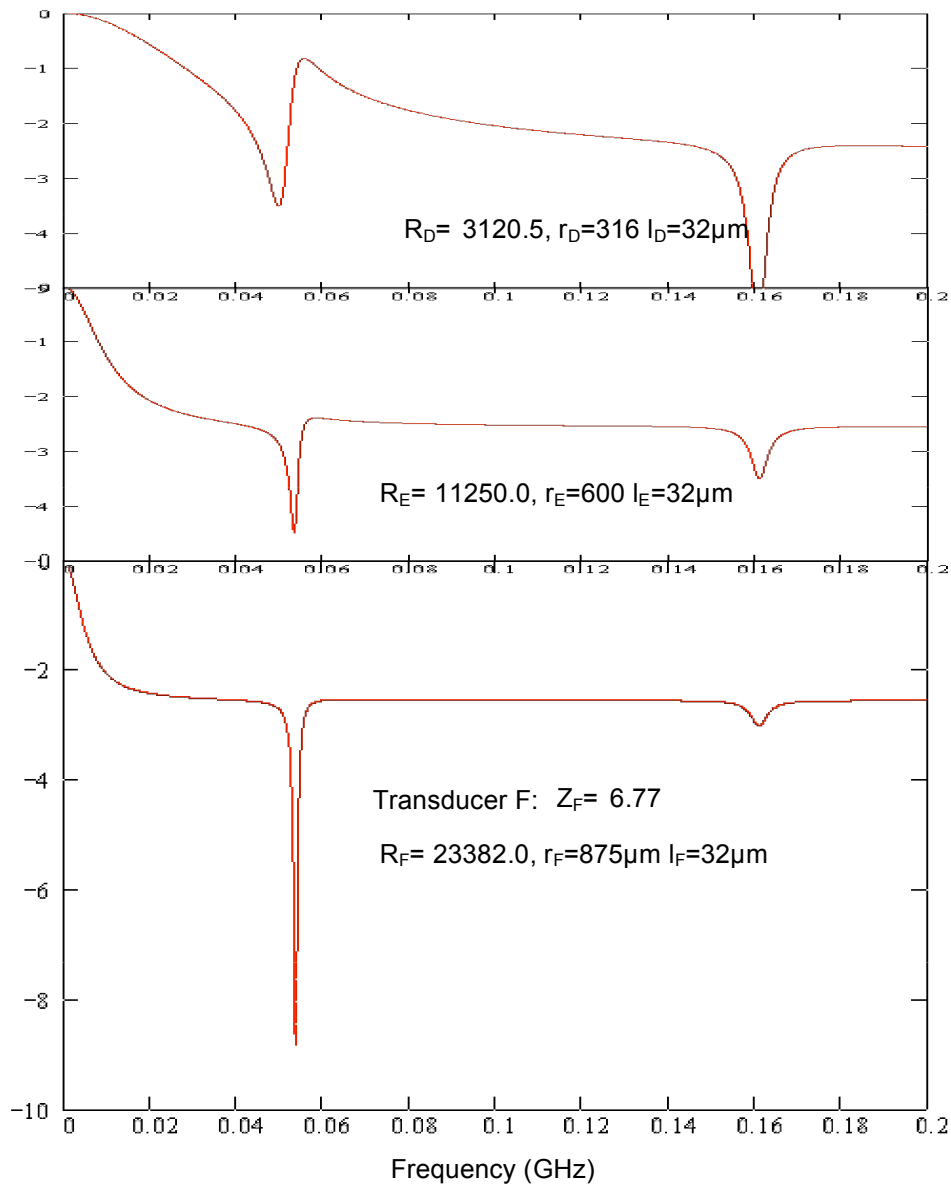


Figure 7.14: Model of 3 PZT composite ($P=8\%$) transducers with 3 different ratios (of electrode radius to film thickness, (r^2/l)). The transducer A, characterised by the ratio R_1 , is $32\mu\text{m}$ thick. It can be compared with the transducer 1 in Figure 7.13. The transducer B, characterised by the ratio R_3 , is the model presented in figure 7.13 (transducer 2). It is used as reference. The transducer C is characterised by the ratio R_3 and is $32\mu\text{m}$ thick, it can be compared with the transducer 3 Figure 7.13.

It has been demonstrated, that an increase in film thickness decreases the resonant frequency, and that the ratio r^2/l affects the background shape of the signal and the resonance peak magnitude.

However, up to now, none of the different electrode sizes and/or film thicknesses were found to affect the electromechanical coupling coefficient.

7.6 Effect of infiltration steps on the electromechanical behaviour of the transducer

All the devices presented in this section have electrode radii of $316\mu\text{m}$ radius.

Chapter 4 explained that transducers fabricated using the [C+4S] process contain large cracks. In order to reduce the cracking behaviour, the number of infiltrations was decreased with the effect of decreasing the density of the film.

A first measurement of a [2C+4S] transducer is presented and analyzed in this section in order to first characterise the electromechanical behaviour of this process (Figure 7.15 and 7.16). Then, in the next section, different degrees of infiltration will be compared, and modelled through the Mason model.

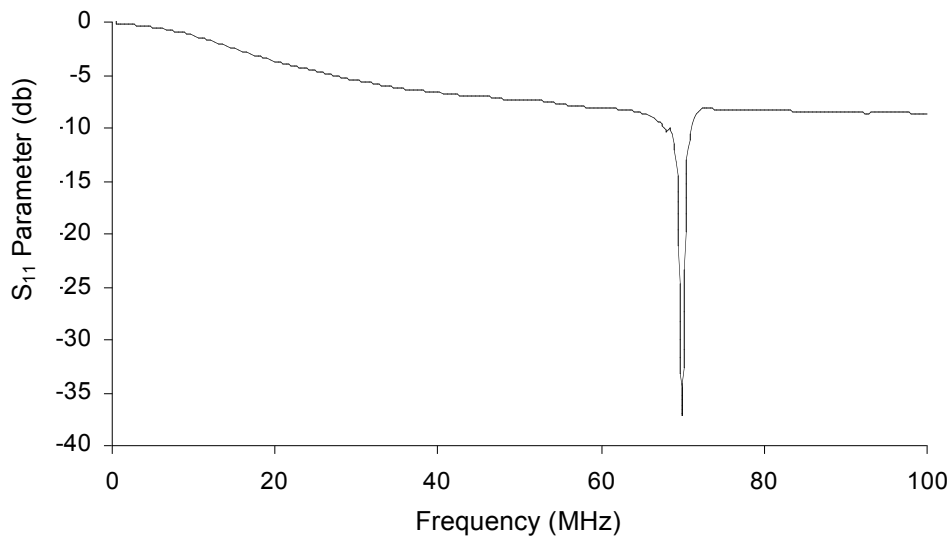


Figure 7.15: S_{11} parameter of a $24\ \mu\text{m}$ thick transducer fabricated with the [2C+4S] process (electrodes radius is $320\mu\text{m}$).

This $24\mu\text{m}$ thick [2C+4S] transducer exhibits a resonant frequency at 70MHz . An increase of infiltration seems to increase the k_t . The k_t measured for the [C+4S] process is 0.42 , and the k_t measured for the [2C+4S] process is 0.2 (Figure 7.15).

This measurement was confirmed by another instrument from the industrial partner IMASONIC. The measurement is presented in Figure 7.18, and confirms the drop of k_t between the two processes.

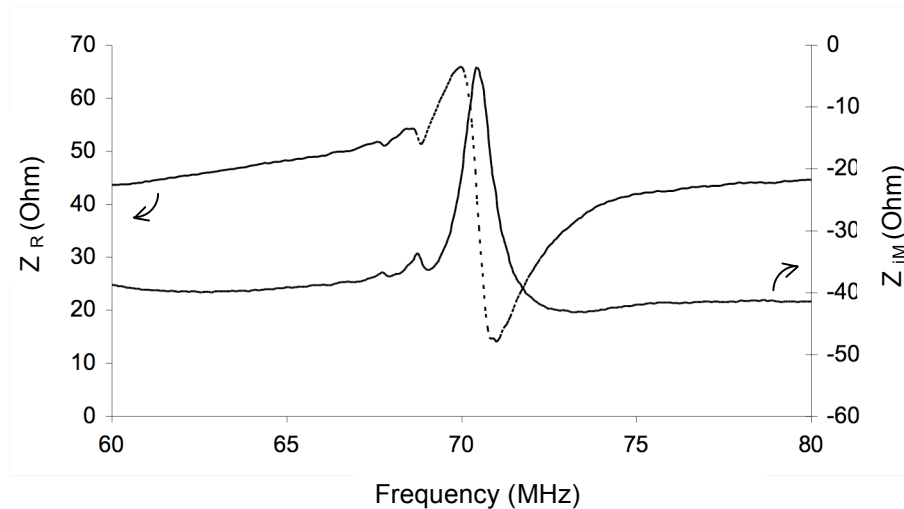


Figure 7.16: Real impedance and real admittance of the 24 μm thick transducer fabricated with the [2C+4S] process (electrode radius is 320 μm).

k_t represents the piezoelectric efficiency of a piezoelectric ceramic. More specifically, it represents the efficiency of converting electrical energy (applied across the electrodes of a piezoelectric ceramic) into mechanical energy.

From the [C+4S] process and the [2C+4S] process only the number of infiltrations per composite layer changes. In Chapter 4, it was shown that the infiltration affects the degree of porosity, and in Section 7.5, it was demonstrated that the degree of porosity does not affect this electromechanical coupling coefficient.

All the transducers used in this section contain Pt electrodes of 316 μm radius. Three transducers were used:

- A 30 μm thick PZT transducer fabricated with the [2C+6S] process with a measured porosity 9.6 vol.%.
- A 24 μm thick PZT transducer fabricated with the [2C+4S] process with a measured porosity of 11.8 vol.%.
- A 22 μm thick PZT transducer fabricated with the [C+4S] process with measured porosity of 8 vol.%.

The number of infiltration stages is not a variable of the Mason model developed in this chapter. However an approach to model the infiltration via the porosity was developed in sections 7.5 and 7.6. It shows the relative permittivity, stiffness, and the piezoelectric constant should all decrease with an increase of porosity (section 7.5).

The decrease of stiffness from the [C+4S] process to [2C+6S] and [2C+4S] should shift the resonant frequency, however as for this section, transducers of the exact same thicknesses were not available this shift cannot be observed.

The relative permittivity measured and modelled decreases from 730 for the [C+4S] process to 660 for the [2C+6S] process and 630 for the [2C+4S] process. This decrease should increase the peak magnitude of the resonant frequency, because the lower the relative permittivity, the less energy the capacitor stores, the more the transducer mode is active, and the less signal is reflected from the transducer (figure 7.10 section 7.5). This trend is observed in figure 7.17 B

Decreasing of the piezoelectric constant only should decrease the k_t but because the density and the stiffness also decrease, this electromechanical coupling coefficient might remain constant (section 7.5). The previous section shows that an increase of infiltration, which should decrease the porosity, is accompanied by an increase of k_t . Figure 7.17 B, confirmed this trend:

- The transducer fabricated with the [C+4S] process exhibits a k_t of ~ 0.43 .
- The transducer fabricated with the [2C+6S] process exhibits a k_t of ~ 0.47 .
- The transducer fabricated with the [2C+5S] process exhibits a k_t of ~ 0.30 . (not represented in figure 7.17)
- The transducer fabricated with the [2C+4S] process exhibits a k_t of ~ 0.21 .

Because, the S_{11} parameter represents the reflected power from the device, an increase of the electro-mechanical coupling coefficient should decrease the S_{11} resonant frequency peak magnitude. This is observed in Figure 7.17.

However the reason that k_t decreases with an increase of porosity is still unknown. In this work, k_t becomes the constant used to characterise the number of infiltration steps. The number of infiltration steps was found to change the porosity level, in Chapter 6. However, it is known from Section 7.5 that k_t does not vary with a variation of density. Hence, the only difference between the processes presented here and the PZT composite model presented in Section 7.5, is the level of infiltration the composite film.

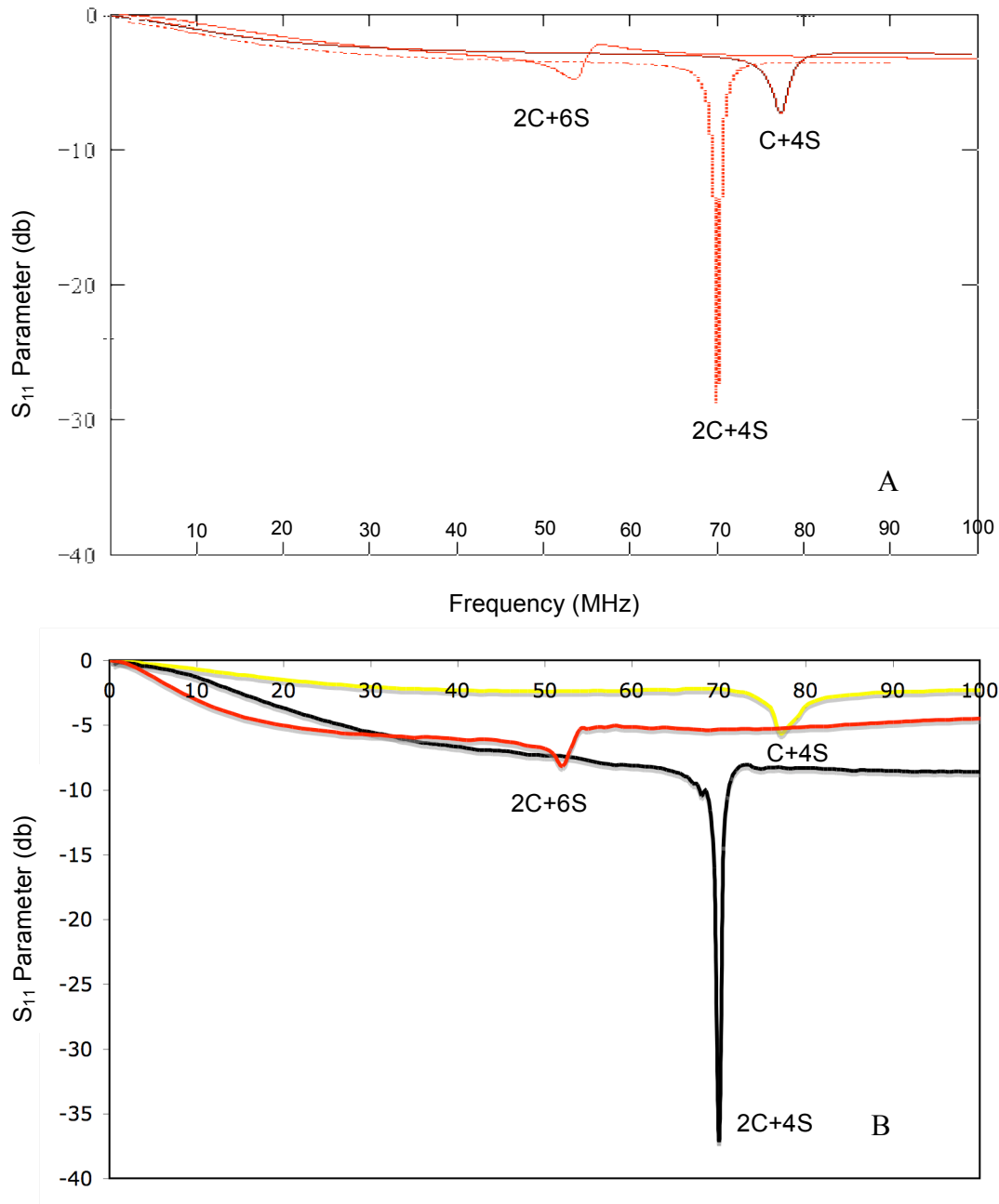


Figure 7.17. Analytical model (A) and experimental data (B) of the S_{11} parameter for three different process 2C+4S, 2C+6S, and C+4S.

In section 7.5, Figure 7.9 represents the reduction of stiffness due to the effect of the sol that soften the mechanical behaviour of the composite. It shows that this reduction is $\sim 0.2 \text{ N/m}^2$ for the [C+4S] thick film compared to a PZ26(P=8vol.%) model. This shift allowed the calculation of the piezoelectric constant of the PZT composite [C+4S] to be equal to 10.46 C/m^2 .

The same shift of stiffness needed to fit the model of PZ26(P=8vol.%) transducer with the resonant frequency of many [2C+4S] transducers was found to be induce ($\sim 0.15 \text{ N/m}^2$).

The fewer infiltration steps that are executed the closer the PZT composite behaviour is to the PZ26 behaviour. The ratio of the PZT composite volume to the volume of infiltration sol has an effect on the stiffness, which is different than the effect that have the porosity has on the stiffness.

Assuming that e_{33} is constant, using Equation 7.12, this decrease of shift of stiffness between the [C+4S] and [2C+4S] is calculated to reduce the k_t by a maximum of just 0.05, which is not enough to explain fully the difference of k_t observed between the two processes. As the permittivity was measured, the only constant left to explain this drop of k_t is the piezoelectric constant. To fit the coupling coefficient measured to 0.2 for transducer fabricated with the [2C+4S] process, the piezoelectric constant needs to be reduced to the value of $6.5C/m^2$.

In addition, with the process [2C+5S], the pure sol inter-layer begins to be observed (Chapter 6). A multilayer model needs to be developed to examine the effect of the piezoelectric interlayer on the k_t of the system. This represents the limits of this work where only trends can be observed. Table 7.6 summarises the results obtain for the electro-mechanical coupling coefficient.

Table 7.6 Summary of results obtained for the electro-mechanical coupling coefficient

Thickness l (μm)	k_t [2C+4S]	k_t [2C+5S]	k_t [2C+6S]	k_t [C+4S]
7				0.47
22				0.44
24	0.21	0.30		
31			0.47	
32				0.43

7.7 Summary

A model based a Mason theory [1945] explained by Kino [1987] has been set up to understand the behaviour of the TmpMUT resonating at $\sim 50\text{MHz}$ fabricated during this work. With this model compared to experimental data, it has been demonstrated than an increase in film thickness decreases the resonant frequency, that the ratio r/l affects the background shape of the signal, and that a deeper analyses of the resonant frequency magnitude needs to be done to understand how the ratio r/l affects it. It has also been demonstrated that none of the different electrode sizes and/or film thicknesses were found to affect the electromechanical coupling coefficient in this chapter. The eletro-mechanical coupling coefficient was demonstrated to increase when y increase in the composite [xC+yS]: A decrease of 50% of infiltration sol induces, a decrease of $\sim 10\%$ of the relative permittivity value, a decrease of $\sim 25\%$ of the stiffness. These effects are negligible on the electromechanical coupling coefficient, which seems to be more affected by a decrease of

40% of the piezoelectric coefficient, e_{33} , from 10.46 to 6.5C/m², induce by this decrease 50% of infiltration steps.

A demonstration of single layer structures was given to present the efficiency of this technology to fabricated tmpMUT structures. The wet etching technology revealed the possibility of a great adaptability to pattern and shape innovative devices such as film patterned in thickness. These results lead the way to open a wide range of new industrial applications requiring small features, such as multilayer PZT thick films with embedded electrodes (presented in the future work section), or annular array. A prototype of an annular array is presented to illustrate one of many of the possibilities offered by this technology.

Chapter 8

**Prototype presentation:
Annular array**

8.1 Introduction

This chapter 8 and the Chapter 9, present three of many design possibilities for the application of the technology developed during this work. 50MHz PZT tmpMUT 2mm wide annular array transducer design was a command from the industrial partner IMASONIC. These prototypes were fabricated at Cranfield and tested at IMASONIC. This section is a summary of all the technologies, and analysis done as part of this work and presents 27 to 30 μ m thick patterned PZT films shaped into an annular transducer arrays.

A first section will present the design of the array commonly agreed with IMASONIC, and then the 2 prototypes. A second part presents the dielectric behaviour of such capacitor structures, and a third section will presents the acoustic responses, including the pulse echo acoustic response of the prototype working under water.

The purpose of this chapter is to purely demonstrate the successful integration of all the technologies developed in this thesis to produce functionary TmpMUT annular array transducers. A full analysis of the these transducers is beyond the scope of this thesis.

8.2 Annular array prototypes

In Chapter 7, it has been demonstrated that the thickness mode resonant frequency is independent of electrode size. Once its mechanical behaviour is known, only the thickness of film dictates its resonance frequency. This technology allows the possibility to include any shape of electrode in the design of such transducer.

Acoustic waves have similar behaviour as electromagnetic waves. They can be transmitted, refracted, diffracted, interfered, amplified, and focussed. For superficial skin or eye medical imaging, a short focal length of the transducer is a key point to control. High frequency (50MHz) acoustic waves, helped with a transducer designed to act like an acoustical lenses, are the solution to help the acoustic waves emitted by the array to shorten the focal length. An array of transducer shaped in rings allows the acoustic focal point to be varied dynamically by changing the phase of operation of each ring transducer (Figure 8.1).

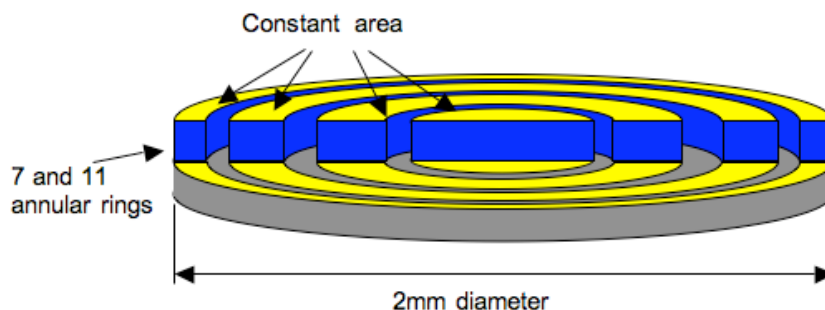


Figure 8.1: Schematic illustration of an array of transducers shape in rings. (cross section of the rings of PZT is represented in blue, the yellow represents the bottom and top electrodes and the grey the 100nm thick silicon oxide membrane and acoustic backing)

Two designs were commonly agreed with IMASONIC: one with 7 rings and another one with 11 rings. The first one was designed to be an unclamped annular array transducer with 7 rings, with a space etched in the PZT material between each annular ring. The second designed was not etched between the rings (Figure 8.3).

Taking into account technological constraints for the inter-element spacing in the annular array, the number of elements was determined in order to get elements with the same area and an overall diameter close to 2 mm.

Attention was paid to keep the element width larger than $15\ \mu\text{m}$ (smallest width of the external element : $30\ \mu\text{m}$ in both configuration). Because of the use of the wet etching technology, inter-element spacing constraints were $90\ \mu\text{m}$ minimum for etched PZT array (physical separation of the rings) and $20\ \mu\text{m}$ minimum for the electrode patterning only (Chapter 4).

The electrode area was chosen in order to get the electrical impedance of the element (with electrodes, backing and matching layer, estimated in water) as close as possible to 50 Ohms at 50MHz.

A series of Pt lines were designed to access to each annular bottom electrode. These connection lines require that 8° of the transducer will not be activated. IMASONIC had modelled the beam waves emitted by the annular array and had demonstrated that the dead area had a negligible effect on the acoustic beam at different distances from the transducer (Figure 8.2).

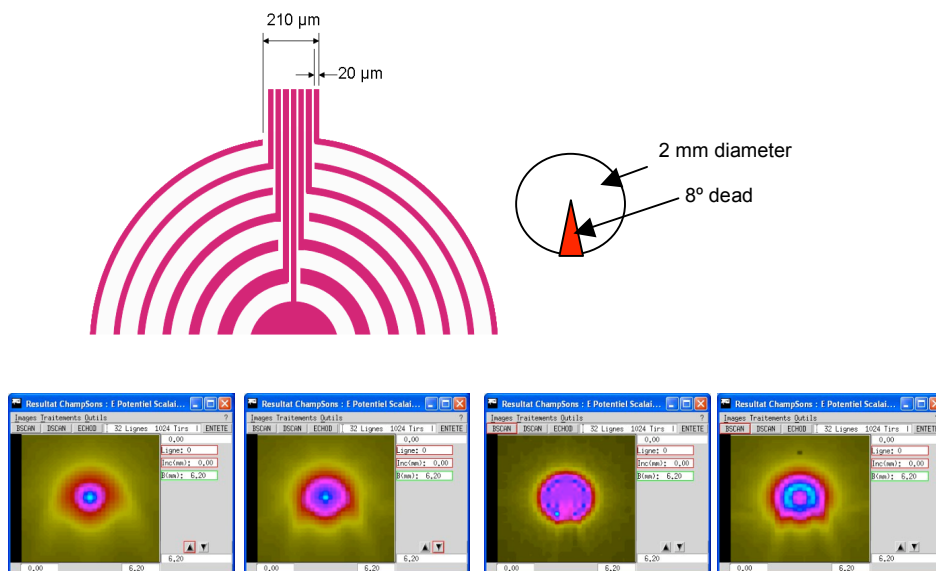



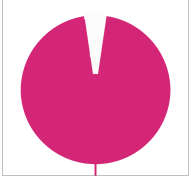


Figure 8.2: Schematic illustration of the transducer dead area induces by the connection lines. IMASONIC modelled the beam of waves emitted by the annular array demonstrating that the dead area effect on the beam at different distance from the transducer can be neglected (respectively 5, 10, 15, and 20mm, from left to right)

Beam forming performance models demonstrated the capability of focusing in transmission from 5 mm up to 20 mm for both configurations. Lateral resolution at focus is estimated for different focusing distances ($< 150\mu\text{m}$ up to 10 mm). Simulations showed that the sensitivity of the array seems to be the most critical point. Rather high insertion losses are predicted. For the etched PZT configuration, a further loss of sensitivity is expected due to the loss of active area (large inter-element spacing) and thus the capability of the array to focus energy. The final dimensions and design of each annular are presented in Table 8.1.

Table 8.1: Measurements and design of each annular

Annular array etched				K _{eff}	Area				
Electrode	Internal diameter (μm)	External diameter (μm)							
centre	0	520	90μm	$2.1 \cdot 10^{-11} \text{m}^2$	Bottom electrodes		Pattern top electrode		
2	700	872							
3	1052	1174							
4	1354	1450							
5	1630	1711							
6	1891	1961							
7	2141	2203							
Annular array un-etched					20μm	Bottom electrodes		Full top electrodes	
centre	0	520							
2	560	764							
3	804	958							
4	998	1125							
5	1165	1276							
6	1316	1415							
7	1455	1545							
8	1585	1668							
9	1708	1786							
10	1826	1898							
11	1938	2007							

Annular arrays had been processed with $[2C+xS]$ thick films, with x ranging between 4 and 6. The connections lines of the bottom and top electrodes of the prototype were prepared for a flip-chip packaging (Figure 8.4).

Both un-etched and etched design prototypes were processed, but only the un-etched prototypes were tested. Their dielectric and acoustic properties are presented in the next sections.

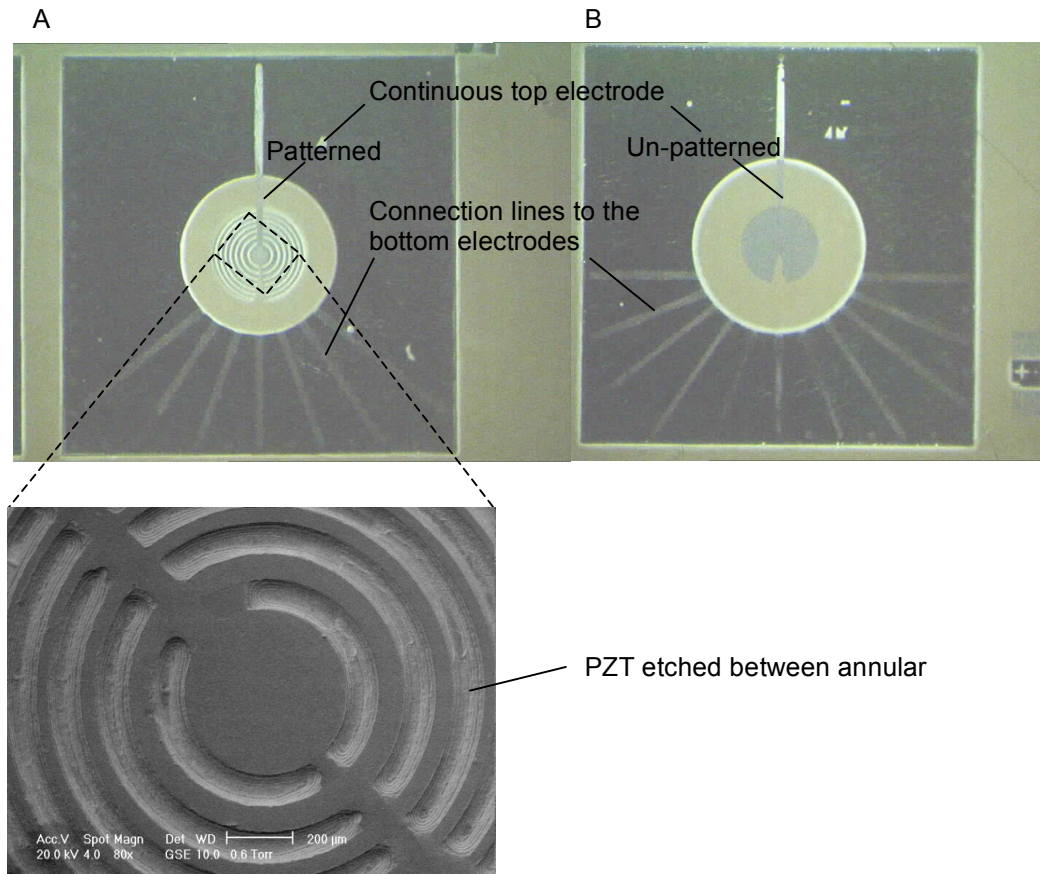


Figure 8.4: A) Annular arrays with the PZT etched between annular rings, B) Un-etch annular array with a full un-patterned top electrode. The connections lines of the bottom and top electrodes of the prototype were prepared for a flip-chip packaging design.

8.3 Dielectric properties of the annular array

Chapter 6 demonstrated that the dielectric properties of small transducer element can not be measured accurately on a silicon substrate. On silicon, the capacitance of the external ring measured on the non-etched [2C+4S] prototype is approximately constant around 110pF. The theoretical capacitance of such capacitor is calculated to be 39pF.

A similar prototype made on an alumina substrate exhibits values of capacitance consistent with theoretical values obtained with the finite element FEMlab software. The electrode area is constant but their width decrease from the central to the external electrode. Due to an increase of fringing fields, the value of the measured and modelled capacitance is predicted to increase from the central annular to the external annular (Table 8.2). On the etched prototype, the constant value of ~39pF is observed on each ring, representing that each capacitor are free from fringing fields.

Table 8.2: Fringing fields increase the measured capacitance from the central electrode to the external annular electrode. The prototype tested is a 30 μ m thick [2C+4S] annular array on alumina.

Electrodes	Thickness (μ m)	Capacitance (pF) Experiment	Relative Permittivity	Capacitance (pF) Finite element	% of error
centre	30	35	559	41	15
2	30	29	463	55	47
3	30	49	783	53	8
4	30	50	798	56	11
5	30	55	878	57	4
6	30	56	894	58	3
7	30	58	926	60	3
8	30	60	958	63	5
9	30	61	974	63	3
10	30	70	1120	64	-9
11	30	63	1010	64	2

A comparison between the acoustic properties of the two prototype designs should highlight the influence of the fringing fields on the resonant frequency peak. However, as the etched prototype is still under investigation, only the un-etched prototype acoustic behaviour, measured by the industrial partner IMASONIC, will be presented in the next section.

8.4 Acoustic behaviour of the tmpMUT annular array

The amplitude and phase of the complex impedance of a [2C+5S] annular array prototype is presented in Figure 8.5. However the processes [2C+4S] and [2C+6S] were also tested.

The results are consistent with the analyses of the single elements presented in Chapter 7. The electromechanical coupling coefficient are measured from the central element. The obtained value were ~ 0.25 to ~ 0.35 and 0.45 respectively for the [2C+4S], [2C+5S] and [2C+6S] processes.

The 11 rings of the devices were shown to resonate at a parallel resonance frequency of approximately 60MHz (measured in air). The resonant behaviour of the concentric rings gradually changes depending on their position in the structure. The central rings exhibit a single resonance at about 60MHz. As the position of the rings becomes more peripheral additional resonances are observed (Figure 8.5) corresponding to lateral modes. The quality of the resonance lowers (less amplitude for the main resonance is observed) when the width of the ring decreases due to appearance of these parasitic modes.

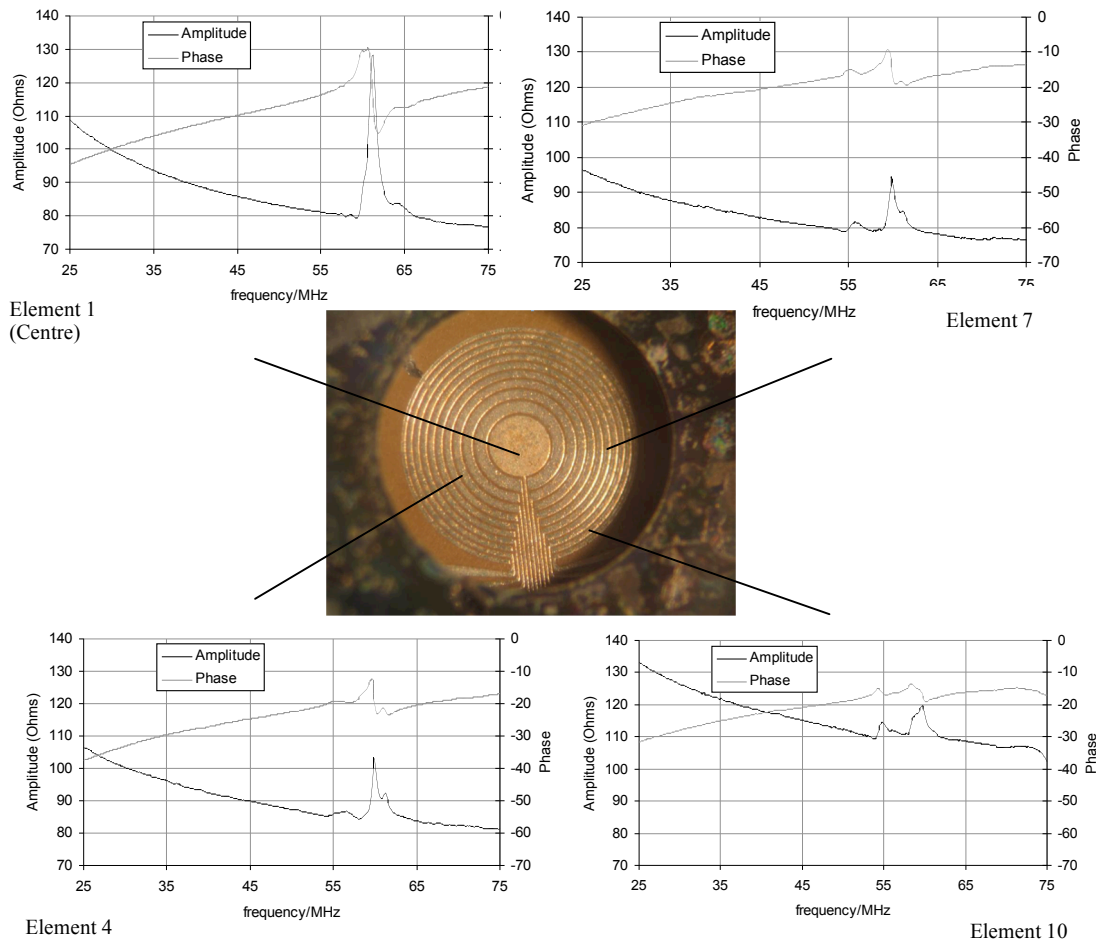


Figure 8.5: The amplitude and phase of the complex impedance of a [2C+5S] annular array prototype elements 1 (center), 4, 7, are presented. It shows the evolution of resonance behaviour across the device (the optical micrograph picture represented the back electrode observable when the backing Si is removed).

Pulse-echo responses were observed in water for the 2C+5S based device showing that the Tm-pMUT devices are able to operate in water. To do so, parylene was deposited on the front face, acting as an acoustic matching layer but also as a protective layer for operation in water.

For this test, the centre element was excited by a negative pulse of 20V peak amplitude and 4ns width at -6dB (JSR-DPR500 pulse generator). The recorded waveform, reflected on the centre element from a plane target at 15 mm, exhibits a -6dB centre frequency of 53 MHz and 47% -6dB bandwidth which is comparable to that achieved for the bulk PZT device reported by Brown [2004]. These figures are comparable with 1D simulation results predicting a -6dB centre frequency of 55 MHz and 40% -6dB bandwidth (Figure 8.6). Bandwidth values are quite low compared to usual imaging transducers performances due to the fact that no backing was added to damp the resonance of the transducer. Backing influence will be evaluated in as part of a future project.

The [2C+6S] prototype pulse echo is still under analyses. Its electromechanical coupling coefficient is 0.47 compared to 0,35 for the [2c+5S] transducer. This increase should improve the amplitude of the signal and might increase the bandwidth.

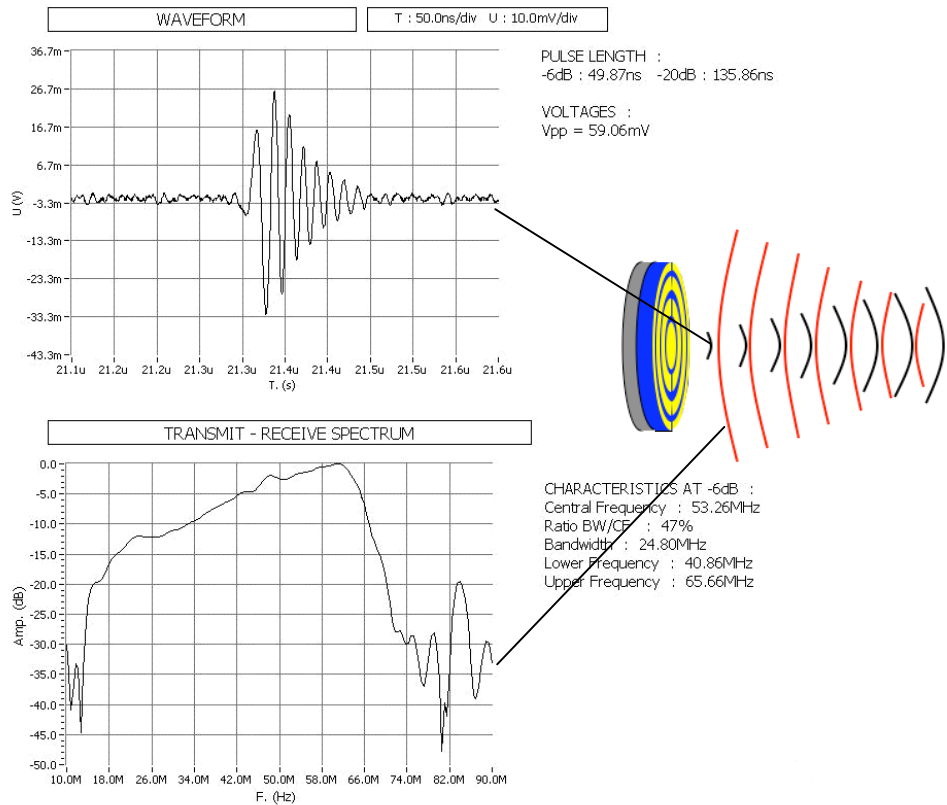


Figure 8.6: Pulse-echo responses observed for the 2C+5S based device showing that the TmpMUT devices are able to operate in water.

8.5 Summary

2 designs of TmpMUTs annular array prototype had been realised. The first prototype was designed with 11 rings transducers, the second with 7 rings transducers. They have been realised using a low temperature composite sol gel thick film processing route in combination with silicon micromachining techniques. The results obtain for k_t are consistent with results obtained in Chapter 7 for single element transducers fabricated using the [2C+4S] [2C+5S] [2C+6S] processes. The electromechanical coupling coefficients of annular arrays were confirmed to be ~ 0.25 , 0.35 and 0.45 respectively. The devices have been shown to resonate at approximately 60MHz in air and 50 MHz in water.

Chapter 9

**Conclusion
And Future work**

9.1 Introduction

The future work includes presentation of potentially useful technologies for the next generation transducers. This has been undertaken to understand which direction this research could take to improve the design of high frequency transducers fabricated with the spin coating technology. Results of two interesting structures discovered during this work will be presented and discussed. In this chapter preliminary work on possible future directions of study will be presented before presenting the main conclusion relating to the thesis as a whole.

9.2 Next generation of high frequency transducers

9.2.1 PZT [2C+6S] thick films on alumina substrates

The first structure presented in this chapter, is a single element of PZT composite on an alumina substrate. On alumina the situation is very different from that found for silicon. Without etching under the active area, the single element behavior on a 500 μm thick alumina substrate is shown in Figure 9.1 B) and C). As the substrate is not removed below the resonant device, the total thickness of the device is equal to both the PZT thickness (35-42 μm) and the substrate thickness (500 μm). This kind of structure is well known as a high-overtone bulk acoustic resonator HBAR [Zhang et al. 2005].

For such structure, the resonant frequency can be calculated, as first approximation, by using Equation 7.6, considering that the majority of the device thickness to be due to the substrate. The resonant frequency was calculated to be approximately equal to 13 MHz.

This first approximation seems to fit the fundamental resonant frequency measured, corresponding to the first peak in Figure 9.A and B, (16 and 18 MHz respectively). The other peaks correspond to resonant harmonics. The two thicknesses of PZT composite examined (27 and 42 μm) demonstrate a fundamental resonant frequency very close to 13 MHz. On the silicon substrate device, no signal can be observed when the silicon is not etched. This indicates that the PZT/Silicon bilayer system is lossy. Rosenbaum explained this phenomenon using a model which showed a non-linearity in the relationship between the FOM factor (Figure Of Merit $\propto k_t^2 \cdot Q$) and the ratio of the substrate /film thickness. He demonstrates that when this factor decreases the system get lossy. The Q factor at 1GHz of alumina is around $240 \cdot 10^3$, while on silicon this factor is $3 \cdot 10^3$. It is now well known that for such structure film on non-etched substrate that Alumina is one of the best substrate, with YAG, LiTaO₃, LiNbO₃ because of their high Q coefficient [Rosenbaum 1988].

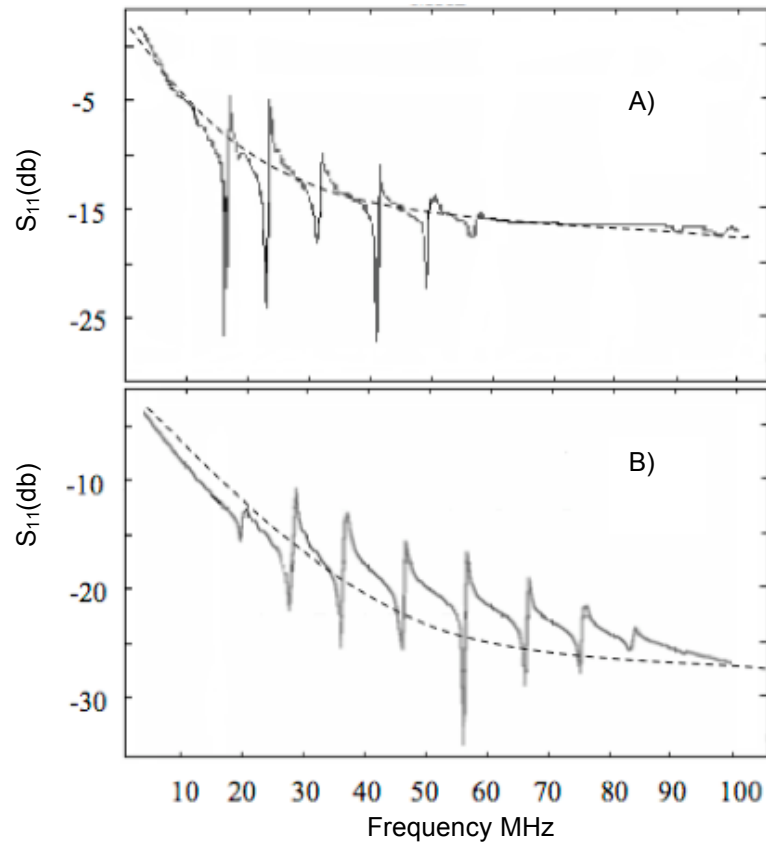


Figure 9.1: S_{11} parameters as function of the frequency, for: A) 42 μm PZT thick film on 500 μm thick alumina substrate, B) 27 μm PZT thick film on 500 μm thick alumina substrate.

The electro-coupling coefficient of HBAR is dependent on the thickness of the substrate: the thicker the substrate the smaller k_t [Pao *et al.* 2005] [Zhang *et al.* 2005]. The k_t found in this case (Figure 9.1.A and B) is 0.23 and the HBAR was fabricated with the PZT [2C+5S] process, which normally exhibits a k_t of 0.35. An analytical model developed by Pao [2002] demonstrated the drop of the electromechanical coupling coefficient is purely due to the Q of the substrate. It demonstrated that the drop of k_t is normally higher (>50%) for good HBAR structures. The spacing between the resonances observed could be increased by the use of thinner alumina substrate to achieve a single mode of vibration [Pao *et al.* 2005]. This opens the possibility of working with a substrate, which does not need to be totally removed for a transducer application. It will be an enormous reduction in fabrication time by eliminating the difficulty removing the backing material removal. The better substrate for such structure will of course be a PZT substrate. The conditions of thickness and density of this PZT substrate are presented in the work of [Levassort *et al.* 2001]. However, such substrate is not easy to use for a future 50MHz multilayer using this technology: the PZT substrate cannot survive all the thermal treatments needed to grow such thickness structure due to its poor shock resistance.

9.2.2 Multilayer piezoelectric structure

9.2.2.1 Advantage of a multilayer

The possibility of making a multi-layer film structure for the thickness mode excitation is also of technological interest (Figure 9.2). The thickness mode and multilayer structure gives several advantages when dealing with such arrays of small active elements:

- The good properties achieved by the one layer transducer (a relative permittivity around 750, and a d_{33} around 80pC/N) are retained.
- The drive voltages (100 μ m PZT layer need \approx 100V as driving voltages) are reduced
- The element capacitance is increased leading to better electrical matching for small elements.
- The vibration amplitude is increased for a given drive voltage.
- Control of bandwidth of individual layers through control of density or thickness.

9.2.2.2 Electrical characterization

The multilayer structure was characterised electrically with measurement made using the top and bottom electrodes. The permittivity, the piezoelectric constant e_{31} and piezoelectric coefficient d_{33} were found to be of 750, 3.9C/m² and 77.8pC/N respectively. Both top layer and bottom layer also exhibited the same permittivity of 750, meaning that the middle electrode remains intact during processing.

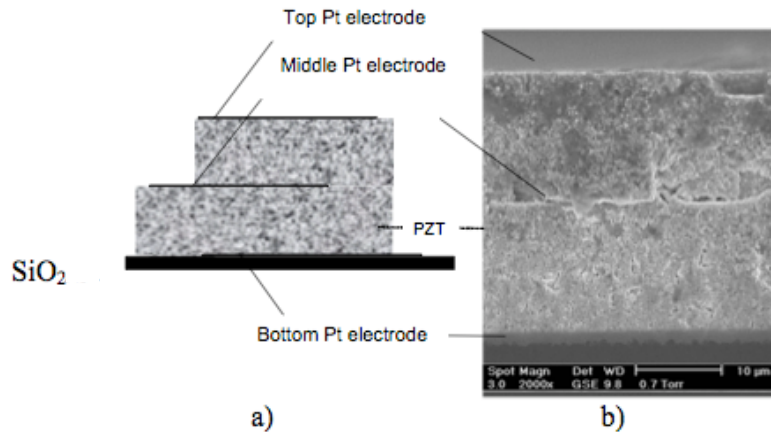


Figure 9.2: a) Schematic and b) SEM photomicrograph of the multilayer structure with embedded electrode

Two ways of poling this multilayer transducer were considered: the anti-parallel poling and the parallel poling (figure 9.3). In both cases the impedance of the multilayer transducer was measured by connecting the top and the bottom electrode with a silver paste.

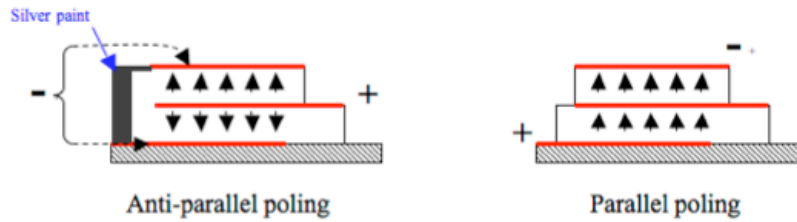


Figure 9.3: the anti-parallel poling and the parallel poling.

Since the technology is new, this section presents results obtained from 60 devices analyzed from a single wafer, which survived the fabrication process. More devices from several different wafers are needed to confirm the results obtain here. A multilayer Mason model needs to

be developed as well. However since at least thirty devices from the same sample generate similar results, this section represents a good representation of preliminary work of a 50 MHz bi-layer PZT transducer. The first results presented will be the separate measurements of resonant frequency of the top and the bottom layer. Then, results from samples poled with the parallel technique (Figure 9.3) are presented. Then, Anti-parallel poled sample were poled at 100 V for 32 μ m sample instead of 200V for monolayer structure, and presented in a second section.

The wafer presented here was processed using the [2C+6S] process. However this section, because of a lack of a model, generates just a simple presentation of a bi-layer device. Assumptions are made to explain unexpected resonant frequency, but a deeper analyze would need to be done to confirm these assumptions, and understand their origins. Such work is beyond the scope of the current work. Fukuda [2006] presents similar works and confirmed the results obtain in this chapter, however deep analyses still need to be done.

9.2.2.2 Bi-layer transducer: Single layer resonance

Figure 9.5 represents the S_{11} parameter result obtain of a bi-layer transducer poled with the parallel technique (figure 9.3), then poled in the exact same way as a mono-layer cylindrical transducer presented in Chapter 6. For the S_{11} measurement of the top layer, the ground tip was in contact with the middle electrode and the signal tip with the top electrode. Similarly, the S_{11} measurement of the bottom layer, the ground tip was in contact with the bottom electrode and the signal tip was in contact with the middle electrode. Both the top and bottom resonate at 55MHz. (Figure 9.5).

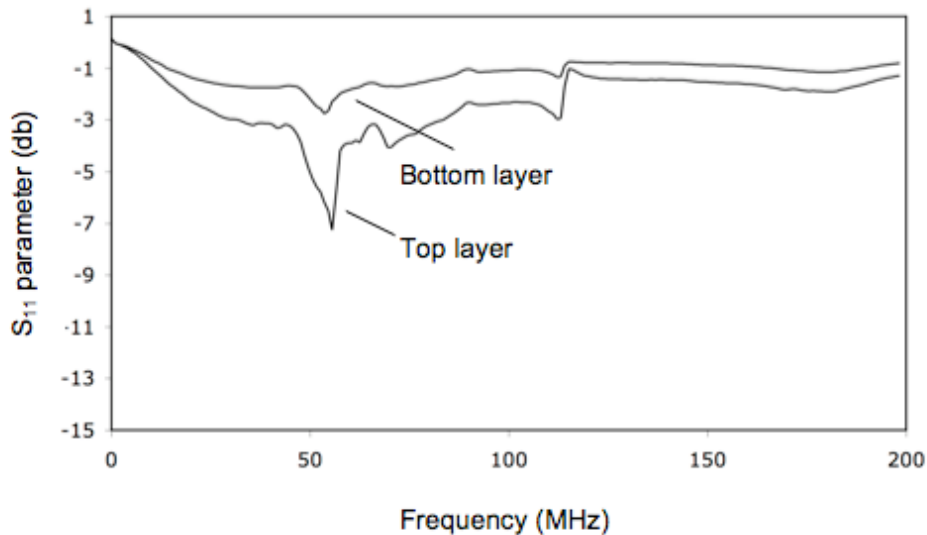


Figure 9.4: Bi-layer structure transducer of a 30 μm thick PZT film fabricated with the process [2C+6S], the top layer is a 10 μm thick PZT film and the bottom layer is a 20 μm thick PZT film.

The top layer represented in Figure 9.4 is a typical case of HBAR structure, or thickness extensional resonator where the total thickness is $\sim 30\mu\text{m}$. The top layer is a PZT thick film 10 μm and the bottom layer a PZT thick film of 20 μm (or the substrate) plus 100nm of SiO_2 . As in the case of the work presented in the precedent section, the whole thickness is activated by the top layer vibration, at 55MHz for the fundamental resonance and 110MHz for the first harmonic. The bottom layer generates the same situation but over this PZT layer there is 10 μm of thickness of the top layer, and under this PZT bottom PZT layer there is 100nm of SiO_2 , which doesn't seem to stop the resonance.

9.2.2.3 Bi-layer transducer poled in parallel

Figure 9.6 represents the measurement of the S_{11} parameter, where the top and bottom electrodes are connected of the same bi-layer structured transducer as the one presented in the above section. The ground tip was in contact with the middle electrode, and the signal tip was connected with the top and bottom electrode.

This transducer generated a resonant frequency corresponding to the thickness mode at 55MHz, with k_t equal to 0.59. This enlargement is due to another resonant frequency observed at 70MHz, which overlaps the total thickness mode frequency. Another resonant frequency is observed at 155MHz. If the bottom and top layers were free to resonate on their own these layers could have generated resonant frequencies at 80MHz and 165MHz respectively. Both are 10MHz above the observed resonance. As the two layers of the transducer are poled in a parallel way, the two layers are activated with an opposition of phase when the device is driven using the middle electrode and the connected bottom/top electrodes. The middle electrode was expected to generate a displacement but not the top and bottom electrode, and the signal was then expected to be confined in the film. However,

in Figure 9.5 it seems that all the layers generate an observable signal. This surprising results is observable in all the samples poled that way. A multilayer model and another batch of samples need to be produced to confirm the theory that when a bi-structured transducer is poled in a parallel way 3 resonant frequencies are observable, which might corresponds to the total thickness, and the 2 separate thickness of each layer.

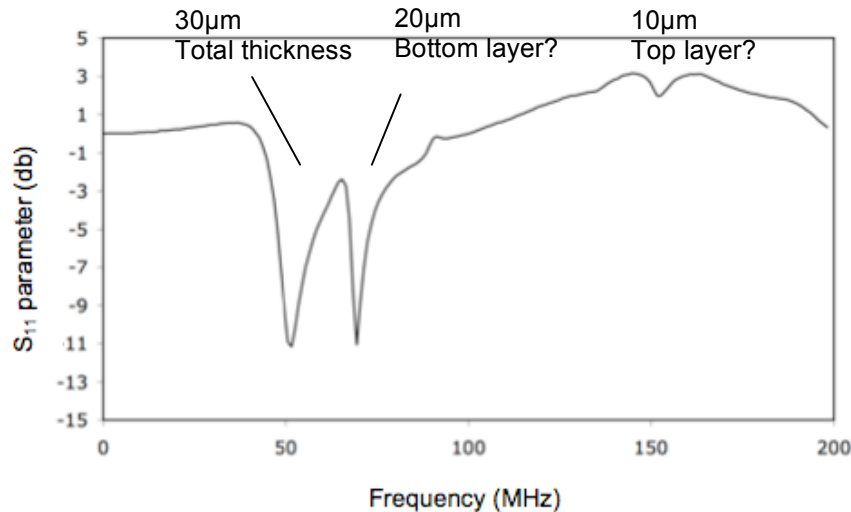


Figure 9.5. Bi-layer structures transducer of a 30 μm thick PZT film fabricated with the process [2C+6S]: the top layer is a 10 μm thick PZT film and the bottom layer is a 20 μm thick PZT film. The system poled with the parallel technique, and the measurement was taken with the bottom electrode and the top electrode connected with silver paint.

9.2.2.3 Bi-layer transducer poled in anti-parallel

Figure 9.6 shows the resonance result obtained from samples poled with the anti-parallel technique explain in Figure 9.3. These samples were poled with half the voltage. This means that because the two layers have different thicknesses, (10 μm for the top layer and 20 μm for the bottom), the two layers are poled differently. These devices represent one possible future development for the high frequency transducer. The S_{11} parameter showed the resonant frequency to be as expected at 55MHz for such thickness. As the layers are both expected to be activated in phase, this fundamental thickness mode frequency, and its first resonance, are observed. The electromechanical coupling coefficient is equal to 0.44, which correspond to the value expected for a transducer fabricated with the process [2C+6S].

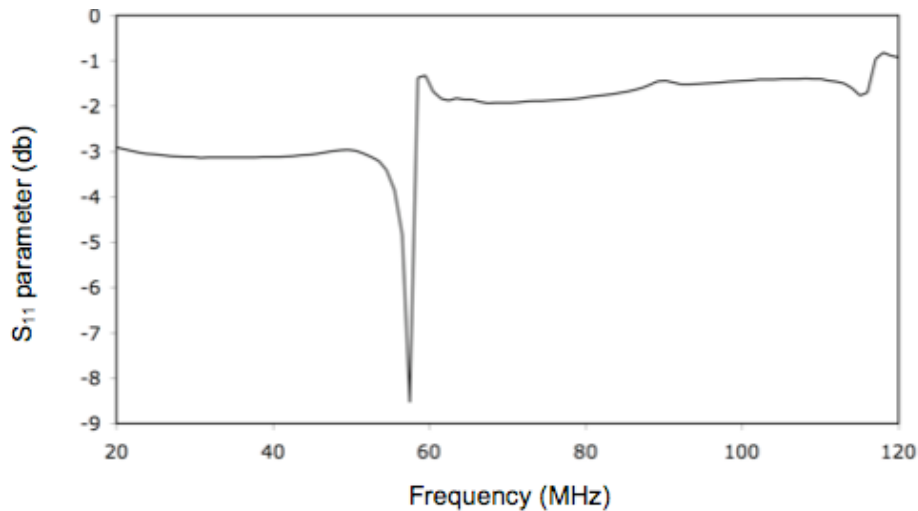


Figure 9.6. Bi-layer structure transducer of a 30 μ m thick PZT film fabricated with the process [2C+6S]: the top layer is a 10 μ m thick PZT film and the bottom layer is a 20 μ m thick PZT film. The system poled with the parallel technique, and the measurement was taken with the bottom electrode and the top electrode connected with silver paint.

9.3 General conclusion

This study had five linked aims. They were to provide:

- A new fabrication technique to deposit patterned 30 μ m thick films (Chapter 4).
- To understand the stress development in order to be able to control the cracking behaviour of the films (Chapter 5)
- To characterise the dielectric, piezoelectric, and ferroelectric properties of the films produced (Chapter 6).
- To characterise and model the acoustic properties of a single element high frequency transducer operating at frequencies ranging from 50 to 200MHz (Chapter 7).
- To fabricate and characterise a pattern high frequency annular array working at 50MHz (Chapter8)
- To present the first results of the fabrication and characterisation of the next generation of high frequency transducers: Single elements of PZT on alumina substrate, and multilayer transducer with embedded electrodes (Chapter 9).

9.3.1 A new fabrication technique

PZT films up to 35 μ m thick were fabricated, using a composite sol gel route combining a PZT powder and a PZT sol gel. The maximum temperature for the process was 710°C. A demonstration of single layer and multilayer structures were manufactured to show the

flexibility of this technology. This study yields to set up experimental conditions in which a crack free surface finish of a 28 μm thick film revealed the adaptability of the spin coating technique to fabricate such thick films on silicon.

The wet etching technology revealed the possibility of a great adaptability to pattern and shape innovative devices such as bars 10 μm wide of 21 μm PZT thick film. These results open the way to a wide range of new industrial applications requiring small features and/or multilayer PZT thick film with embedded electrodes.

9.3.2 stress development

The Stoney's equation has been validated to be usable as a comparison tool between different processes. This validation allowed the understanding of how temperature treatment relaxes some of the in-situ film stress through creep mechanisms, micro-cracking, or pore generations. It also helped to understand the stress dependency of the infiltration degree of the composite film, the substrate and the film thickness. With the preceding qualitative Chapter 4 and this chapter on stress situation reveal that the process involving 6 infiltrations represents the maximum possible infiltration for the fabrication of film as thick as 30 μm .

9.3.3 Dielectric, piezoelectric, and ferroelectric properties of thick film

The dielectric properties of PZT films have been analysed and modelled. The relative permittivity of the PZT composite increases with the number of infiltrations until saturation is observed around the 3rd and 4th infiltration at 700-800. Fringing fields have been analysed through a finite element model by using the software FEMlab. It has been found that for small features (~50 μm radius) they are responsible for the increase of the relative permittivity by 30%. This effect will have to be carefully considered for the analysis of the annular array, which includes annular of 20 μm width. The piezoelectric coefficient has been also found to increase with infiltration until saturation at 75-85pC/N.

A study on ferroelectric properties revealed that the stress developed during the fabrication process influences the dipole direction. On silicon tensile stress, most of the dipoles seem directed along a plane parallel to the substrate plan. On alumina a compressive stress seems to direct most of the dipole in a plane perpendicular to the substrate plan. These differences in orientation were found to affect the shape of the hysteresis loop.

9.3.4 Characterise and model the acoustic properties of a single element

A model based a Mason theory [1945] explain by Kino [1987] has been set up to understand the behaviour of the TmpMUT resonating at ~50MHz fabricated during this work. With this model compared to experimental data, it has been demonstrated than an increase in film thickness decreases the resonant frequency, that the ratio r/l affects the background shape of

the signal, and that a deeper analyses of the resonant frequency intensity needs to be done to understand how the ratio r/l affects it. It has also been demonstrated that none of the different electrode sizes and/or film thicknesses were found to affect the electromechanical coupling coefficient in this chapter. The eletro-mechanical coupling coefficient was demonstrated to increase when y increase in the composite $[xC+yS]$:

A decrease of 50% of infiltration sol induces, a decrease of $\sim 10\%$ of the relative permittivity value, a decrease of $\sim 25\%$ of the stiffness. These effects are negligible on the electromechanical coupling coefficient, which seems to be more affected by a decrease of 40% of the piezoelectric coefficient, e_{33} , from 10.46 to $6.5C/m^2$, induce by this decrease 50% of infiltration steps.

A demonstration of single layer structures was given to present the efficiency of this technology to fabricated tmpMUT structures. The wet etching technology revealed the possibility of a great adaptability to pattern and shape innovative devices such as film patterned in thickness.

9.3.5 High frequency annular array working at 50MHz

Two designs of TmpMUTs annular array prototype had been realised. The first prototype was designed with 11 rings transducers, the second with 7 rings transducers. They have been realised using a low temperature composite sol gel thick film processing route in combination with silicon micromachining techniques. The results obtain for k_t are consistent with results obtained in Chapter 7 for single element transducers fabricated using the $[2C+4S]$ $[2C+5S]$ $[2C+6S]$ processes. The electromechanical coupling coefficients of annular arrays were confirmed to be ~ 0.25 , 0.35 and 0.45 respectively. The devices have been shown to resonate at approximately 60MHz in air and 50 MHz in water.

9.3.6 Next generation of transducer

A demonstration of single and multilayer structures was given to show the flexibility of the thick film technology. The wet etching technology revealed the possibility of a great adaptability to pattern and shape innovative devices such as film patterned in thickness. These results lead the way to open a wide range of new industrial application requiring small features and/or multilayer PZT thick film with embedded electrodes. This adaptability concerns as well the shape as physical properties exhibited by the transducer. Such multilayer structure needs to be further investigated and modeled in order to imagine a future multilayer arrays.

References

REFERENCES:

- Abdullah M. J.** and Das-Gupta D. K., Electrical Properties of Ceramic/Polymer Composites, IEEE Transactions on Electrical Insulation Vol. 25 No. 3, 1990 605
- Akhilesh K. S.** ; Pandey D., Krupanidhi S. B., On the discovery of two new monoclinic phases in the morphotropic phase boundary region of $\text{Pb}[(\text{Mg}[1/3]\text{Nb}[2/3])\text{O}[3]]\text{-xPbTiO}[3]$ ceramics, Proceedings of the fourth asian meeting on ferroelectricity (AMF-4), Ferroelectrics, 2005, vol. 326, pp. 91-99.
- Anderson R. W.**, *S-parameters techniques for faster network design*, Hewlett-Packard Journal, Feb 1967, Vol 18, No.6
- Banno H.**, Effects of shape and volume fraction of closed pores on dielectric, elastic, and electromechanical properties of dielectric and piezoelectric ceramics—a theoretical approach, *Am. Ceram. Soc. Bull.* 66 (1987), pp. 1332–1337.
- Bast W.** and Wersing W., “The Influence of Internal Voids with 3-1 Connectivity on the Properties of Piezoelectric Ceramics Prepared by a New Planar Process,” *Ferroelectrics*, 94, 22942 (1989).
- Böttger U.**, Polar Oxides: Properties, Characterization, and Imaging Edited by R. Waser, U. Böttger, and S. Tiedke, Chapter 1, 2005.
- Brown J.A.**, Demore C.E.M., and Lockwood G.R., Design and Fabrication of Annular Arrays for High-Frequency Ultrasound, IEEE transactions on ultrasonics, ferroelectrics, and frequency control, 2004, vol. 51, 8, 1010-1017.
- Brown J.A.**, Lockwood G.R., A Digital Beamformer for High-Frequency Annular Arrays, IEEE transactions on ultrasonics, ferroelectrics, and frequency control, 2005, vol.52, 8, 1262-1269.
- Bruggeman D.A.G.**, The calculation of various physical constants of heterogeneous substances: I. The dielectric constants and conductivities of mixtures composed of isotropic substances, *Ann. Phys.* 1935, 24, pp. 636–664 (in German)
- Burn I.** and Maher G. H., High resistivity BaTiO_3 ceramics sintered in CO-CO_2 atmospheres, *Journal of Materials Science*, 1975, Volume 10, Number 4.
- Cannell D.** and P. Trigg, *Advanced Ceramic Processing and Technology*, chap 4 Processing of electronic ceramics, 1990, p 95
- Cho K.H.**, Lee H.Y., Pore-dependent dielectric and electrical properties of barium titanate ceramic, ISAF '94 Proceedings of the Ninth IEEE International Symposium on Applications of Ferroelectrics, 1995, 566-571
- Cianci E.**, Minotti A., Foglietti V., Caliano G., Pappalardo M., One dimensional capacitive micromachined ultrasonic transducer arrays for echographic probes, *microelectronic engineering*, 2004, 73-74, 502-50.
- Corker D. L.**, Zhang Q., Whatmore R. W., Perrin C., PZT ‘composite’ ferroelectric thick films, *J. Eur. Cer. Soc.*, 2002, 22, (3), 383-390.
- Corkovic S.**, Zhang Q., Whatmore R.W., the investigation of key processing parameters in fabrication of $\text{Pb}(\text{Zr}_x\text{Ti}_{1-x})\text{O}_3$ thick film for MEMS application, *J. Electroceramic*, 2006.

- Dauchy F.**, Dorey R.A., Patterned multilayer thick film electroceramic structures for micro electromechanical systems, 4M conference, 2005
- Dorey R.A.**, Duval F.F.C., Haigh R.D., Wathmore R., effect of repeated sol infiltration on the microstructure and electrical properties of PZT composite sol-gel film, *ferroelectrics*, vol.267, 373-378, 2002.
- Dorey R.A.**, Stringfellow S.B., Whatmore R.W., Effect of sintering aid and repeat sol infiltration on the dielectric and piezoelectric properties of a composite thick film, *Journal of European societies*, 2002, (22) 2921-2926
- Damjanovic D.**, Ferroelectric, dielectric and piezoelectric properties of ferroelectric thin films and ceramics, *Rep. Prog. Phys.*, 1998, vol.61, 1267–1324.
- Dunn L.M.** and Minoru T., Electromechanical properties of porous piezoelectric ceramics, *J. Am. Ceram. Soc.* 76, 1993, vol.7, pp. 1697–1706.
- Duval F.F.C.**, Thesis, “PZT Thick films for high frequency transducers”, Cranfield University, sept 2003.
- Duval F.F.C.**, Dorey R.A., Wright R.W., Huang Z., Whatmore R.W., Fabrication and modelling of high frequency PZT composite thick film membrane, 2004.
- Fang L.**, Meng S.S., Chang-Zheng Hu, High permittivity and low loss dielectric ceramics BaLnNiNbO(Ln = La, Nd and Sm), *Journal of Alloys and Compounds*, 2007, vol.429, 280–284
- Feynman R. P.**, *The Feynman Lectures on Physics 'Mainly Electromagnetism and Matter'*, Calif. Addison-Wesley, Redwood City, 1989.
- Fernandez J.F.**, Nieto E., Moure C., Duran P., Processing of porous and dense PZT thick films on Al₂O₃ substrates., ISAF 1994: proceedings of the ninth IEEE International Symposium on Applications of Ferroelectrics, New York, 1994, 49-52.
- Fousek J.**, Permissible domain walls in ferroelectric species, *Czechoslovak Journal of Physics*, 1971, Vol.21, Number 9, 955-968.
- Foster F.S.**, Ryan L.K. and Turnbull D.H., Characterization of Lead Zirconate Titanate Ceramics for Use in Miniature High-Frequency (20-80 MHz) Transducers, *IEEE international ultrasonics, ferroelectrics, and frequency control*, 1991, Vol. 38., 5, 445-453.
- Fujito K.**, Wakiya N., Shinozaki K., Mizutani N., Change of residual stresses and electrical properties of Pb(Zr,Ti)O₃ thin films upon introducing various bottom electrodes, *Journal of the Ceramic Society of Japan*, 2002, vol110 [5], 421-427.
- Fukuda M.**, NI SHI HI RA M. and I MANO K., Real Time Extraction System Using Double-Layered Piezoelectric Transducer for Second-Harmonic Ultrasonic Pulse Waves *Japanese Journal of Applied Physics*, 2006, Vol.45, 5B, pp. 4556–4559.
- Gurevich V.L.** and Tagantsev A. K., Intrinsic dielectric loss in crystals, *Advances In Physics*, 1991, vol. 40, No. 6, 719-767
- Gaucher P.**, Thales research and technology, piezoelectric micro-electro-mechanical systems for acoustic applications, <http://www.teaser.fr/~pgaucher/Publications.html>

- Gottlieb E.J.**, Cannata J.M., Hu C-H., and Shung K.K., Development of a High-Frequency (> 50 MHz) Copolymer Annular-Array, Ultrasound Transducer *IEEE transactions on ultrasonics, ferroelectrics, and frequency control*, 2006, vol.53, 5, 1100-1110.
- Harris, N. R.**, Hill, M., Torah, R., Townsend, R., Beeby, S. P., White, N. M. and Ding, J., A multilayer thick-film PZT actuator for MEMs applications. *Sensors and Actuators A* 2006, Vol.132, 1, pp. 311-316.
- Harwood M.G.**, Variation with time of the electrical conductivity of rutile, *J. Appl. Phys.*, 1965, vol. 16.
- Heerens W. C.** Application of capacitance techniques in sensor design, *J. Phys. E: Sci. Instrum.* 1986, vol 19.
- Herbert J. M.**, Ceramic dielectrics and capacitors, Gordon and Breach Science Publishers, 1985.
- Houssa M.**, Afanas'ev V.V., Stesmans A. and Heyns M.M. Defect generation in Si/SiO₂/ZrO₂/TiN structures: the possible role of hydrogen, *Semicond. Sci. Technol.* 16 No 12, December 2001, L93-L96, PII: S0268-1242(01)128047-X
- Hu C-H.**, Snook K.A., Cao P., and Shung K.K., High-Frequency Ultrasound Annular Array Imaging. Part II: Digital Beamformer Design and Imaging, *IEEE transactions on ultrasonics, ferroelectrics, and frequency control*, 2006, vol.53, 2, 309-313.
- Huang C.L.**, Chen B.H., Wu L., Application feasibility of Pb(Zr,Ti)O₃ ceramics fabricated from sol-gel derived powders using titanium and zirconium alkoxides, *Materials Research Bulletin* (2004)
- Hrovat M.**, Holc J., Drnovsek S, Belavic D., Cilensek J., Kosec M., PZT thick films on LTCC substrates with an interposed alumina barrier layer, *Journal of the European Ceramic Society*, 2006, 26, 897–900.
- IEEE** Standard on Piezoelectricity, American National Standards Institute, ANSI/IEEE Std 176-1987
- IMASONIC**, <http://www.imasonic.com/Medical/IMHighFreq.php>,
- Jonscher A.K.**, Physical basis of dielectric loss, *Nature*, 1975, vol 253, 717 – 719.
- Kino G.S.**, Acoustic waves, Prentice-Hall, Englewood Cliffs, NJ (1987).
- Kwona T.Y.**, Parka J.H., Kima Y.B., Yoona D.S., Cheonc C., Leeb H.L., Tae Song Kim Preparation of piezoelectric 0.1Pb(Zn0.5W0.5)O₃–0.9Pb(Zr0.5Ti0.5)O₃ solid solution and thick films for low temperature firing on a Si-substrate, *Journal of Crystal Growth*, 2006, 295, 172–178
- Kornev K.V.** and Neimark A.V., Spontaneous Penetration of Liquids into Capillaries and Porous Membranes Revisited, *Journal of Colloid and Interface Science*, 2001, Vol.235, 101-113.
- Leclerc B.**, Process Optimization for Sol-Gel PZT Films, Master thesis, Queen's University, Kingston, Ontario, Canada, 1999.

- Lethiecq M.**, Berson M., Feuillard G., Patat F. Principles and applications of high-frequency medical imaging." Advances in acoustic microscopy (ed. A. Briggs and W. Arnold), 1996, Plenum Press 2: 39-102.
- Lethiecq M.**, Levassort F., Tran-Huu-Hue L-P., New Acoustic Impedance Piezoelectric Material for broadband transducer application, IEEE international ultrasonics, ferroelectrics, and frequency control, 2004.
- Levassort F.**, Tran-Huu-Hue L.P., T. Bove J. Holc., Kosec M. and Lethiecq M., High performance piezoceramic films on substrates for high frequency imaging, *Proceedings of IEEE International Ultrasonics Symposium*, 2001, pp.1035–1038.
- Liliehorn T.**, and Stefan Johanson, Fabrication of multilayer 2D ultrasonic transducer microarrays by green machining, J. of Micromachining and Microengineering, 2004, Vol.14, 702-709
- Livage J.**, and Sanchez C., Sol-gel chemistry, Journal of Non-Crystalline Solids, 1992, Vol.145, 5, 120-130.
- Love, E. R.** "The Electrostatic Field of Two Equal Circular Conducting Disks." Quart. J. Mech. Appl. Math. 1949, vol 2, 428-451.
- Lukacs M.**, Sayer M., and Foster S., Single Element High Frequency (<50 MHz) PZT Sol Gel Composite Ultrasound Transducers IEEE Transaction on Ultrasonics, Ferroelectrics, and Frequency control, 2000, Vol.47, 1, 148-159.
- Madou M.J.**, Fundamentals of microfabrication the science of miniaturisation, second edition, CRC press, 2002
- Mahan G.D.** and Subbaswamy K.R., Local Density Theory of Polarizability (Physics of Solids and Liquids), Springer; 1 edition, 1990.
- Marechal P.**, Levassort F., Holc J., Tran-Huu-Hue L.P., Kosec M., and Lethiecq M., High Frequency Transducer Based on Integrated Piezoelectric Thick Films for Medical Imaging, IEEE transactions on ultrasonics, ferroelectrics, and frequency control, 2006, Vol. 53, 8, pp. 1524-1533.
- Mason W.P.**, Electromechanical Transducers and Wave Filters, Published D. Van Nostrand Co, 1948.
- Meyerhofer D.**, Characteristics of resist films produced by spinning, J. Appl. Phys., 1978, 49(7), 3993-3997
- Morosov M.**, PhD dissertation: softening and hardening transitions in ferroelectric Pb(Zr,Ti)O₃ ceramics, EPFL, These N° 3368, 2005.
- Moulson A.J.** and Herbert J.M., Electroceramics, second edition, Ed: Wiley 2003.
- Murali P.**, Ledermann N., Baborowski J., Barzegar A., Gentil S., Belgacem B., Petitgrand S., Bosseboeuf A., and Setter N., Piezoelectric Micromachined Ultrasonic Transducers Based on PZT Thin Films, IEEE transactions on ultrasonics, ferroelectrics, and frequency control, 2005, vol.52, 12, 2276-2288.
- Nicholson J.W.**, the electrification of two parallel circular discs, Philosophical Transaction of Royal Society of London, serie A, vol.224. 1924, 303-369

- Noguera C.**, Physics and chemistry at oxide surfaces, Cambridge University Press, 1996.
- Nye J F**, Physical Properties of Crystals, Oxford University Press, 1985.
- Onga R.J.**, Berfield T.A., Sottos N.R., Payne D.A., *Sol-gel derived Pb(Zr,Ti)O₃ thin films: Residual stress and electrical properties* *Journal of the European Ceramic Society* (2005)
- Ong R.J.**, Payne D.A., Densification and stress development for the chemical-solution deposition of PZT thin layers on silicon, IEEE, 2001, 0-7803-5940-2/01.
- Ong R.J.**, Payne D.A., Sottos N.R., Processing Effects for Integrated PZT: Residual Stress, Thickness, and Dielectric Properties, J. Am. Ceram. Soc., 2005, vol88 [10], 2839 – 2847.
- Ohring M.**, The Materials Science of Thin Films, Academic Press, San Diego, 1992.
- Palmer H. B.**, Capacitance of a parallel-plate capacitor by the Schwartz-Christoffel transformation, Trans. AIEE, March 1927, Vol. 56, pp. 363.
- Padmini P.**, R. Krawietz, R. Köhler, G. Gerlach: Preparation and stress evaluation of ferroelectric thin films of PZT based pyroelectric sensors, *Ferroelectrics*, 1999, Vol. 228, pp. 79-89
- Pang G.**, Sayer M., Lockwood G.R., and Watt M., Fabrication of PZT Sol Gel Composite Ultrasonic Transducers Using Batch Fabrication Micromolding, IEEE transactions on ultrasonics, ferroelectrics, and frequency control, 2006, vol.53, 9, 1679-1684.
- Pao S.**, Chao M., Wang Z., Chiu C., K. Lan. Huang Z., Shih L., Wang C., TXC Corp., Taoyuan; Analysis and experiment of HBAR frequency spectra and applications to characterize the piezoelectric thin film and to HBAR design, Frequency Control Symposium and PDA Exhibition, 2002. IEEE International, 2002, 27- 35.
- Park J. H.**, Kwon T.Y., Kim H.J., Kim S.R., Yoon D.S., Cheon C.I., Kim H., Kim T.S., Resonance properties and mass sensitivity of monolithic microcantilever sensors actuated by piezoelectric PZT thick film, J Electroceram, 2006, 17, 565–572.
- Poynting J.H.**, J.J. Thomson, Text book of physics: Sound, Edition: CHARLES GRIFFIN AND COMPANY, (1909) chapter II and VII.
- Preisach F.**, Über die magnetische Nachwirkung, Zeitschrift für Physik, 1935, vol.94, 277-302.
- Rice R.W.**, Porosity of Ceramics. Marcel Dekker, NY, 1998.
- Robert G.**, DamjanoHbvic, D., Setter, N., Turik, A.V., Preisach modeling of piezoelectric nonlinearity in ferroelectric ceramics. J. Appl. Phys., 2001. Vol.89, 9, 5067-5074.
- Rosenbaum J. F.**, Bulk acoustic wave theory and devices, Artech House Boston-London, 1988
- Sakka S.**, Sol-Gel Science and Technology. vol.3, Kluwer academic publisher, 1999.
- Schwarz R.W.**, Bunker B.C., Dimos D.B., Assink R.A., Tuttle B.A., Taillant D.R., and Weinstock I.A., Solution chemistry effects in Pb(Zr,Ti)O₃ thin film processing, Integrate Ferroelectrics, 1992, pp.243-254.
- Schwarz S.L.**, Shrout T.R., Shulze W.A.and Cross L.E., J. Amer. Soc. 1984, 67, 311.
- Scharzer S.** and A.Roosen, Tape Casting of piezo ceramic/polymer composites, j.of the European soc. 1999, (19) 1007-1010.

- Sengupta S.S.**, Park S.M., Payne D.A. Integrated electroceramics: Densification and stress development in sol-gel derived thin layers, *Integrated Ferroelectrics*, 1997, Vol. 14, pp. 193-200
- Sischka F.**, Agilent training,
http://eesof.tm.agilent.com/docs/iccap2002/MDLGBOOK/1MEASUREMENTS/3VNA/3SPAR/1SparBasics_1.pdf
- Sjöström M.**, *Frequency analysis of classical Preisach model*. IEEE Transactions on magnetics, 1999. Vol.35(4): p. 2097-2103.
- Sloggett G J**, Barton N G and Spencer S J, Fringing fields in disc capacitors, *J. Phys. A. Math. Gen.* 1986, vol19, 2725-2736.
- Snook K.A.**, Ritter T.A., Shrout T.R., Shung K.K., Design of a High Frequency Annular Array for Medical Ultrasound, *Ultrasonics*, IEEE Transactions on Ferroelectrics and Frequency Control, 2001, Vol.49, 2, pp.169-176.
- Snook K.A.**, Hu C-H, Shrout T.R., and Shung K.K., High-Frequency Ultrasound Annular-Array Imaging. Part I: Array Design and Fabrication *IEEE transactions on ultrasonics, ferroelectrics, and frequency control*, 2006 vol.53, 2, 300-308.
- Southin J. E. A.**, Wilson S. A., Schmitt D., Whatmore R. W., $e_{31,f}$ determination for PZT films using a conventional 'd33' meter, *J. Phys. D: Appl. Phys.*, 2001, 34, 1456-1460
- Srinivasan G.**, DeVreugd C. P., Hayes R., Bichurin M.I. and Petrov V.M., Magnetolectric effects in ferromagnetic/piezoelectric multilayer composites *Applied Physics A: Materials Science & Processing*, 2005, Vol.80, 4, 891-897.
- Stuart F.**, Kasia, Harasiewicz A., Slicrar D., History of Medical and Biological Imaging with Polyvinylidene Fluoride (PVDF) Transducers, *IEEE transaction on ultrasonics, ferroelectrics and frequency control*, vol 47, n°6, Nov 2000, pp 1363- 1371
- Stoney G.G.**, The tension of metallic films deposited by electrolysis, *Pro. Poy. Soc. London A Mater.* 1909, vol.82, pp. 172–175.
- Tagantsev A. K.**, Mechanisms of polarization switching in ferroelectric thin films, *Ferroelectrics*, 1996, vol.184, n°1-4, pp. 79-88.
- Tagantsev A. K.** and Stolichnov I. A., injection-controlled size effect on switching of ferroelectric thin films, *Applied Physics Letters*, 1999, Vol.74, 9, pp. 1326-1328.
- Tanimoto T.**, Okazaki K., Yamamoto K., Tensile stress-strain behaviour of piezoelectric ceramics, *Japanese Journal of Applied Physics* Vol. 32 (1993) pp.4233-4236
- Timoshenko, S.**, Analysis of bi-metal thermostats, *Journal of the Optical Society of America*, 1925, Vol.11, 233-255.
- Torah R.N.**, Beeby S.P., White N.M., Improving the piezoelectric properties of thick film PZT: the influence of paste composition, powder milling process and electrode material, *Sensors and Actuator A*, 2004, (110), 378-384.
- Von Hippel A. R. (Sir)**, dielectric material and their application. New York,N.Y.:The Technology Press of M.I.T. and John Wiley & Sons. 1954.

- Wathmore R.**, zhang Q., Huang Z., Dorey R.A., Ferroelectric thin and thick films for Microsystems, *Materials science in semiconductor processing* 2003, 5, 65-76
- Weinberg M.S.**, Working equations for piezoelectric actuators and sensors, *Journal of Microelectromechanical Systems*, 1999, Vol.8, 4, 529-533.
- Wingcho Chew** and Jin AU Kong, Effects of Fringing Fields on the Capacitance of Circular Microstrip Disk, *IEEE transactions on microwaves theory and techniques*, 1980, vol 28, No 2.
- Wintle H. J.**, Exactly Soluble Models of Electrothermal Breakdown, *J. Appl. Phys.*, 1981, Vol. 52, p 4181.
- Wolny W. W.**, Piezoceramic thick films—technology and application. State of the art in Europe. In *Proceedings of 12th IEEE International Symposium on Applications of Ferroelectrics 2000*, ed. S. K. Streiffer, B. J. Gibbons and T. Tsurumi. Honolulu, 2001, pp. 257–262.
- Wortman J.J.** and Evans R. A., "Youngs' Modulus, Shear Modulus and Poisson's Ratio in Silicon and Germanium", *J. Applied Physics*, 1965, Vol.36, 1, pp 153-156.
- Zhang H.**, Zhang S., Zheng K., Parameter characterization of high-overtone bulk acoustic resonators by resonant spectrum method, *Ultrasonics*, 2005, Vol.43, pp.635–642.
- Zhao H.**, Ren T.L., She Liu J., Liu L., Li Z., high quality PZT thick films using silicon mold technique for MEMS applications, *IEEE International Conference on Solid State Sensors, Actuators and Microsystems*, Boston, 2003 vol8-12.
- Zheng K.**, Lu J., Chu J., Study on wet-etching of PZT thin film, *Microprocesses and Nanotechnology, Conference International 2003. Digest of Papers*, 2003, 29-31, pp 248-249
- Zheng X.**, Li J., Zhou Y., X-ray diffraction measurement of residual stress in PZT thin films prepared by pulsed laser deposition, *Acta Materialia*, 2004, vol.52, 3313-3322.

Appendix

Appendix:**A-Mason Model**

Frequency variation is defined as :

$$f_n = 0.001 + n.1/10000$$

$$n \in [1,4000]$$

Material properties :

Thicknesses

$l_{Pt}, l_{PZT}, l_{P_t}, l_{ZrO_2}, l_{SiO_2}$ are defined in (m)

Density

$\rho_{Pt}, \rho_{PZT}, \rho_{ZrO_2}, \rho_{SiO_2}$ are defined in (Kg/m³)

Material stiffness

$C_{Pt}, C'_{PZT}, C_{ZrO_2}, C_{SiO_2}$ are defined in (Kg/m³)

with $C_{PZT} = C'_{PZT} + (2\pi \cdot f_n \cdot 10^9) \eta i$ with $\eta = 2.5$

Acoustic velocity

$$v_x = \sqrt{C_x / \rho_x} \quad x = \text{material}$$

Attenuation coefficients

$\alpha_{Pt}, \alpha_{PZT}, \alpha_{ZrO_2}, \alpha_{SiO_2}$

Acoustic impedance

$$Z_x = \rho_x \cdot v_x$$

$$k_{x_n} = 2\pi \cdot f_n \cdot 10^9 / v_x$$

Z_x as function of frequency

$$Z_{Pt_n}(t) = Z_{Pt} \cdot \tanh[(\alpha_{Pt} + k_{Pt_n} i) l_{Pt}] \quad \text{top electrode}$$

$$Z_{SiO_2_n} = Z_{SiO_2} \cdot \tanh[(\alpha_{SiO_2} + k_{SiO_2_n} i) l_{Pt}]$$

$$Z_{ZrO_2_n} = Z_{ZrO_2} \cdot \frac{Z_{SiO_2_n} \cosh[(\alpha_{ZrO_2} + k_{ZrO_2_n} i) l_{ZrO_2t}] + Z_{ZrO_2} \sinh[(\alpha_{ZrO_2} + k_{ZrO_2_n} i) l_{ZrO_2t}]}{Z_{ZrO_2} \cosh[(\alpha_{ZrO_2} + k_{ZrO_2_n} i) l_{ZrO_2t}] + Z_{SiO_2_n} \sinh[(\alpha_{ZrO_2} + k_{ZrO_2_n} i) l_{ZrO_2t}]}$$

$$Z_{Pt_n}(b) = Z_{Pt} \cdot \frac{Z_{ZrO_2_n} \cosh[(\alpha_{Pt} + k_{Pt_n} i) l_{Pt}] + Z_{Pt} \sinh[(\alpha_{Pt} + k_{Pt_n} i) l_{Pt}]}{Z_{Pt} \cosh[(\alpha_{Pt} + k_{Pt_n} i) l_{Pt}] + Z_{ZrO_2_n} \sinh[(\alpha_{Pt} + k_{Pt_n} i) l_{Pt}]} \quad \text{bottom electrde}$$

$$Z_{Load_n} = \frac{Z_{PZT} [Z_{Pt_n}(t) + Z_{Pt_n}(b)] \cos(k_{PZT} l_{PZT} / 2)^2 + Z_{PZT}^2 \sin(k_{PZT} l_{PZT}) i}{Z_{PZT} [Z_{Pt_n}(t) + Z_{Pt_n}(b)] \cos(k_{PZT} l_{PZT}) + [Z_{PZT}^2 + Z_{Pt_n}(t) Z_{Pt_n}(b)] \sin(k_{PZT} l_{PZT}) i}$$

Electrode size

$$A = \pi r^2$$

Capacitance

$$C_0 = \epsilon_r \epsilon_0 \cdot A / l_{PZT}$$

electromechanical coupling coefficient of PZT thick film

k_t defined in Chapter 7,

$$Z'_{Device} = \frac{1}{2\pi f_n 10^9 C_o} \left[\frac{k_t^2 \cdot \tan\left(\frac{k_{PZT} l_{PZT}}{2}\right)}{\left(\frac{k_{PZT} l_{PZT}}{2}\right)} Z_{load_n} \right]$$

$$R = \epsilon_r \tan(\delta)$$

$$Z_{Device} = Z'_{Device} + R$$

$$S_{11}(db) = 20 \log \left| \frac{Z_{Device} - 50}{Z_{Device} + 50} \right|$$

B-Masks design**B-I Etching testing and cylinder device masks**

Chromium masks are made by the Dutch company Delta Masks (335 euros/ masks)

B-I-1 Four chromium masks were design, general overview

- **Silicon etching** (on drawing –purple)
- **PZT etching** (on drawing –green)
- **Top electrodes** (on drawing –red)
- **Bottom electrodes** (on drawing –yellow)

Each mask was divided in four parts: A, B, C, D (Figure C)

Constant distance in the mask

- For A, B, C and D designs, the silicon etching square (purple) is larger than the electrode (top el. (red) bottom el. (yellow)) by 0.300 mm.
- For A, B, and D the PZT etching circle (Green) is larger than the electrodes by 0.300 mm.

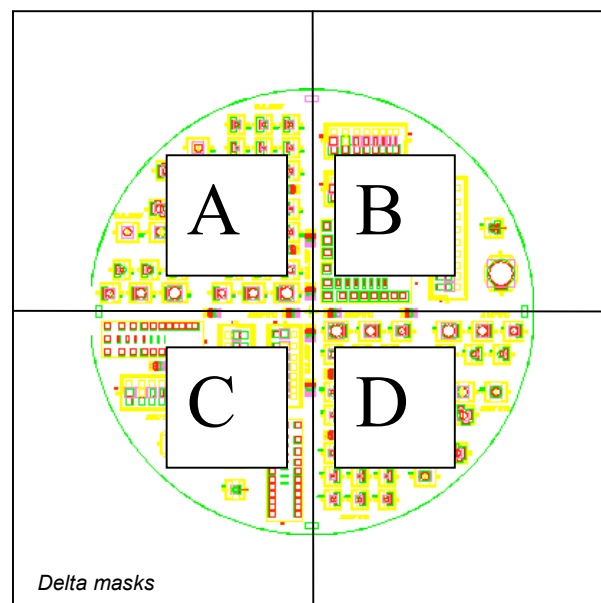


Figure B1: Overview of the mask: the four part A, B, C, D

B-I-2 Parts: A=D: Full cylinder device

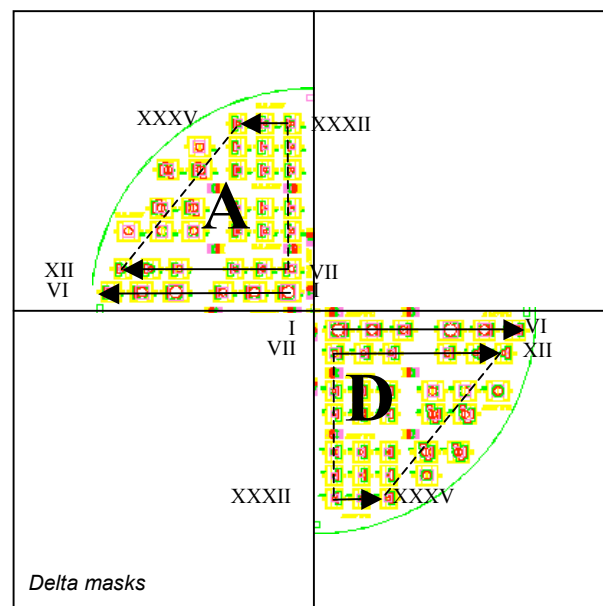


Figure B2: Electrodes number on the part A and D, electrodes radius from 1mm to 50 micrometers

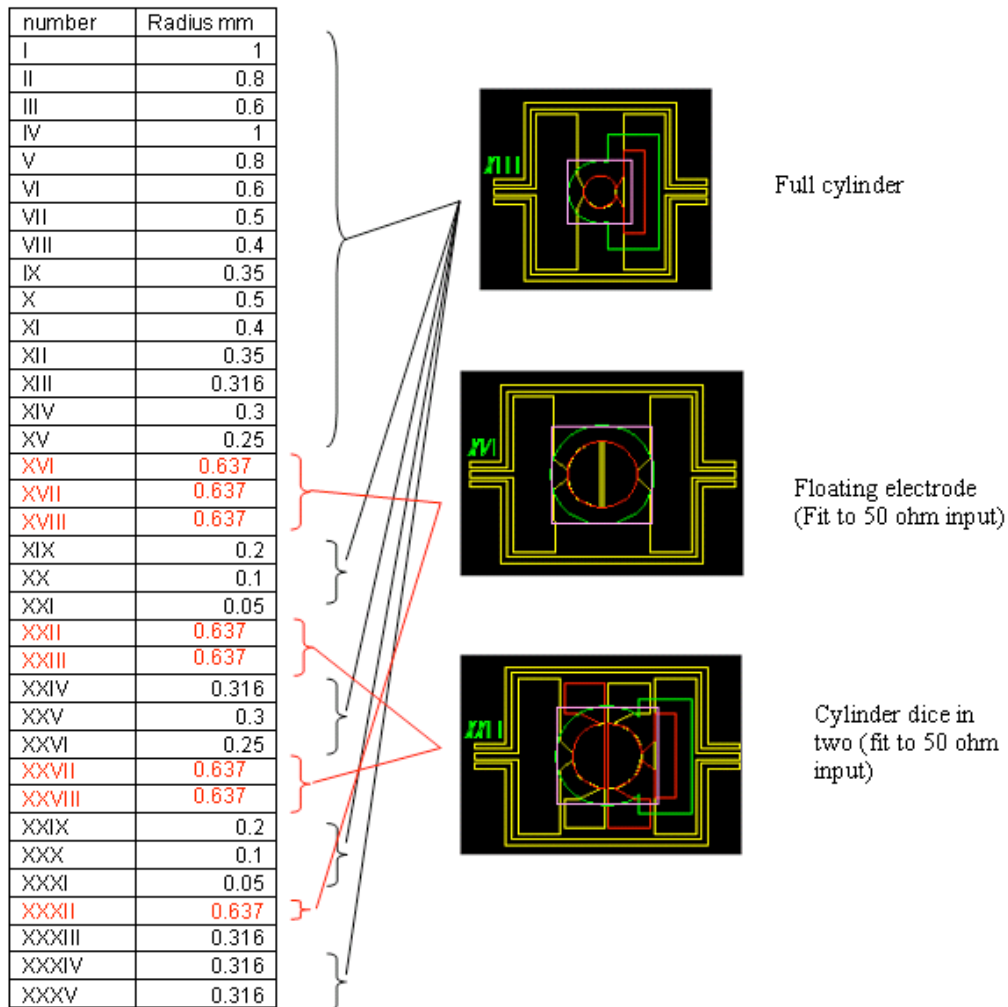


Figure B3: Electrode size, and different design (colours definition see beginning of this chapter)

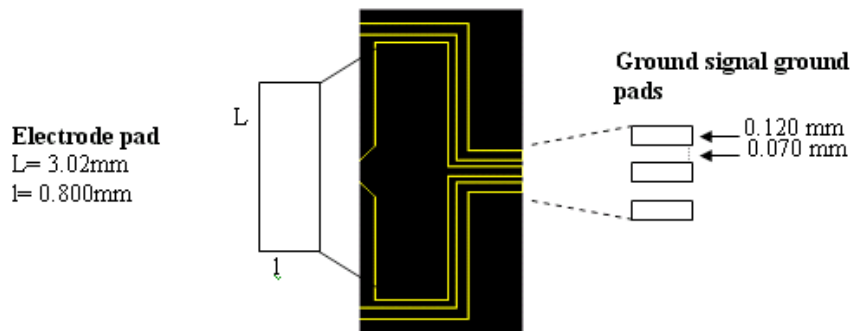


Figure B4: Contact pads size (colours definition see beginning of this chapter)

B-I-3 Parts: B PZT Wet etching

Five designs: I, II and III + annular test+ 2mm cylinder

B-I-3-1 Design I:

Destined to test the etching minimum gap we can achieve between the

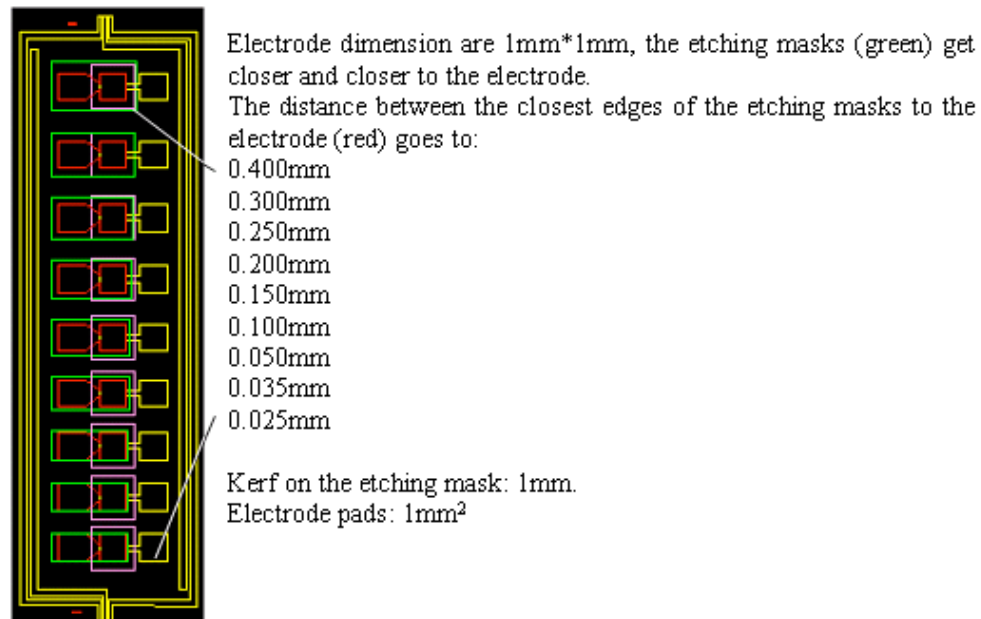
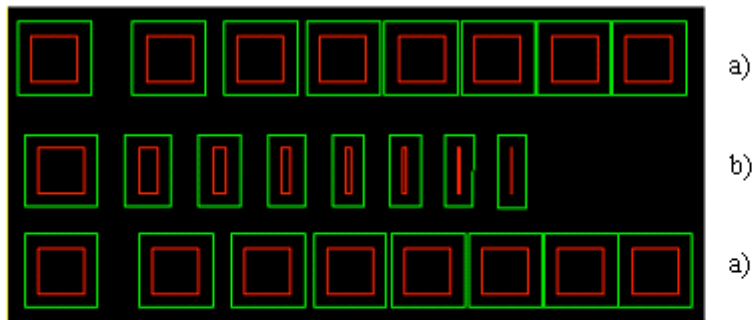


Figure B5: Wet etching undercut experiment mask design (colours definition see beginning of this chapter)

B-I-3-2 Design II:

Destined to test the kerf of etching mask and the electrode side assuming a distance etching mask to electrode fixed at 300 micrometers Figure B6.



a) Kerf (reading sense):

0.900 mm, 0.400mm, 0.200mm, 0.100mm, 0.075mm, 0.050mm, 0.025mm

b) Electrode size (reading sense):

1mm, 0.400mm, 0.300mm, 0.200mm, 0.100mm, 0.080mm, 0.050mm, 0.025mm

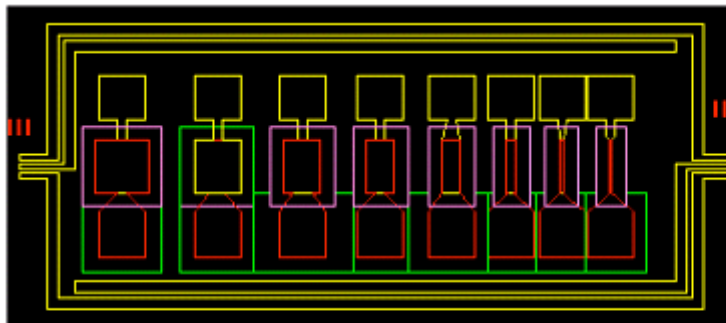
Figure B6: masks to test (colours definition see beginning of this chapter)

B-I-3-3 Design III:

Imasonic design is destined to test the vibration on different electrode geometry than disk.

Figure B7

Pad size: 1*1mm

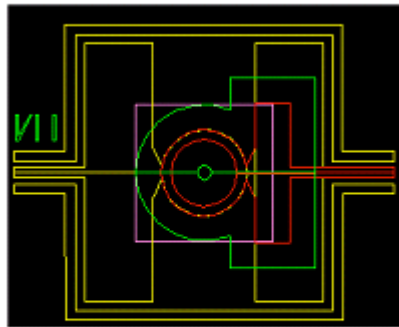


Constant length L of the electrode (red central) = 1mm

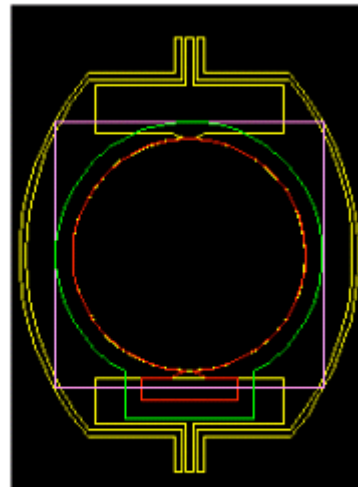
The width if these are ranged to 1mm to 0.025mm: 1.155mm, 1mm, 0.800mm, 0.600mm, 0.400mm, 0.200mm, 0.100mm, 0.035mm

Figure B7: influence of the ratio thickness width (colours definition see beginning of this chapter)

B-I-3-4 Design IV: Annular and cylinder on B:



Annular:
0.113mm width
External radius of the VII design (0.500mm)

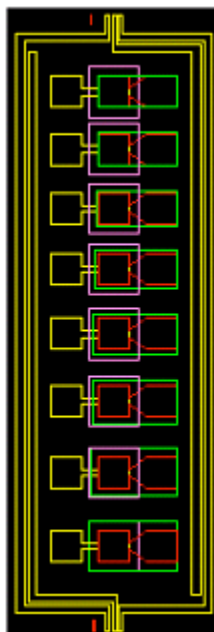


Full cylinder 2mm

Figure B8: Annular and 2mm cylinder (colours definition see beginning of this chapter)

B-I-4 Parts: part C, Dry etching test part

B-I-4-1 Design I:



Design to test how close to the electrodes the powder blaster technique can etch the PZT:

The distance between an edge of the PZT etching square and the electrodes varies:

- 0.300mm
- 0.250mm
- 0.200mm
- 0.150mm
- 0.100mm
- 0.050mm
- 0.025mm
- 0.000mm

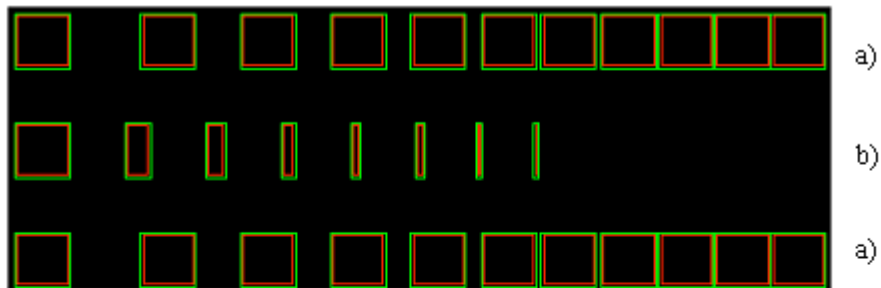
Electrodes pad: 1mm²

Electrodes: 1mm²

Wire connecting electrodes to pad 0.200mm width

Ground signal ground pad: 0.120mm width, 0.070mm kerfs

Figure B9:

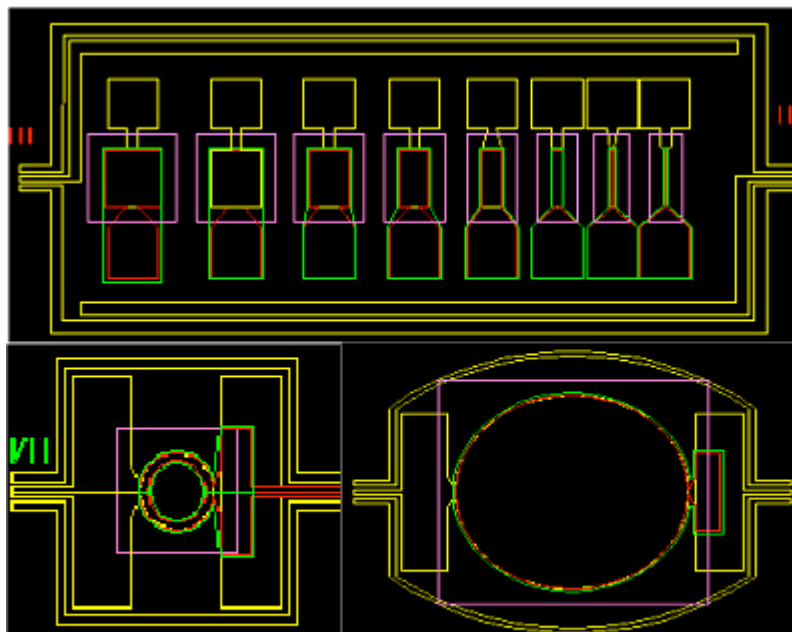
B-I-4-2 Design II:

Powder blaster testing masks: the distance between the PZT etching square (green) and the electrode (red) is 0.050mm for a) and b)

a) 1mm^2 square electrodes, the kerfs is the variable:
1.4mm, 0.900mm, 0.700mm, 0.500mm, 0.300mm, 0.150mm, 0.100mm, 0.050mm,
0.025mm

b) 1mm is the electrode length, 1mm is the kerfs (for the PZT etching square (green)), the electrode width is the variable:
1mm, 0.400mm, 0.300mm, 0.200mm, 0.100mm, 0.080mm, 0.05mm, 0.025mm

Fig B10

B-I-4-3 Design III: Annular, full cylinder

Imasonic designs describe in the part B, only difference is the distance between the etching mask green and the electrodes, which is in this case 0.025mm

Fig B11